HYBRID PRESTRESSED CONCRETE BRIDGE GIRDERS USING ULTRA-HIGH PERFORMANCE CONCRETE

Final Report **December 2020**

Principal investigators:
H. R. Hamilton
Gary R. Consolazio

Research assistant:
Eduardo Torres

Department of Civil and Coastal Engineering
University of Florida
P.O. Box 116580
Gainesville, Florida 32611

Sponsor:
Florida Department of Transportation (FDOT)
Project Manager: William Potter

Contract:
UF Project No. P0086443 & P0086444
FDOT Contract No. BDV31-977-101

University of Florida
Engineering School of Sustainable Infrastructure and Environment
Department of Civil and Coastal Engineering
University of Florida
P.O. Box 116580
Gainesville, Florida 32611

Disclaimer

The opinions, findings, and conclusions expressed in this publication are those of the authors and not necessarily those of the State of Florida Department of Transportation.

Unit of Measurement Conversions

SI* (MODERN METRIC) CONVERSION FACTORS

*APPROXIMATE CONVERSIONS **TO** SI UNITS*

SYMBOL	WHEN YOU KNOW	MULTIPLY BY	TO FIND	SYMBOL
LENGTH				
in	inches	25.4	millimeters	mm
ft	feet	0.305	meters	m
yd	yards	0.914	meters	m
mi	miles	1.61	kilometers	km
AREA				
in^2	square inches	645.2	square millimeters	mm^2
ft^2	square feet	0.093	square meters	m^2
yd^2	square yard	0.836	square meters	m^2
ac	acres	0.405	hectares	ha
mi^2	square miles	2.59	square kilometers	km^2
VOLUME				
fl oz	fluid ounces	29.57	milliliters	mL
gal	gallons	3.785	liters	L
ft^3	cubic feet	0.028	cubic meters	m^3
yd^3	cubic yards	0.765	cubic meters	m^3
NOTE: volumes greater than 1000 L shall be shown in m^3				
MASS				
oz	ounces	28.35	grams	g
lb	pounds	0.454	kilograms	kg
T	short tons (2000 lb)	0.907	megagrams	Mg (or "t")
TEMPERATURE (exact degrees)				
^oF	Fahrenheit	5(F-32)/9 or (F-32)/1.8	Celsius	^oC
ILLUMINATION				
fc	foot-candles	10.76	lux	lx
fl	foot-Lamberts	3.426	candela/m^2	cd/m^2
FORCE and PRESSURE or STRESS				
kip	1000 pound force	4.45	kilonewtons	kN
lbf	pound force	4.45	newtons	N
lbf/in^2	pound force per square	6.89	kilopascals	kPa

*SI is the symbol for the International System of Units. Appropriate rounding should be made to comply with Section 4 of ASTM E380.

SI* (MODERN METRIC) CONVERSION FACTORS

*APPROXIMATE CONVERSIONS **FROM** SI UNITS*

SYMBOL	WHEN YOU KNOW	MULTIPLY BY	TO FIND	SYMBOL
LENGTH				
mm	millimeters	0.039	inches	in
m	meters	3.28	feet	ft
m	meters	1.09	yards	yd
km	kilometers	0.621	miles	mi
AREA				
mm^2	square millimeters	0.0016	square inches	in^2
m^2	square meters	10.764	square feet	ft^2
m^2	square meters	1.195	square yards	yd^2
ha	hectares	2.47	acres	ac
km^2	square kilometers	0.386	square miles	mi^2
VOLUME				
mL	milliliters	0.034	fluid ounces	fl oz
L	liters	0.264	gallons	gal
m^3	cubic meters	35.314	cubic feet	ft^3
m^3	cubic meters	1.307	cubic yards	yd^3
MASS				
g	grams	0.035	ounces	oz
kg	kilograms	2.202	pounds	lb
Mg (or "t")	megagrams (or "metric	1.103	short tons (2000 lb)	T
TEMPERATURE (exact degrees)				
°C	Celsius	1.8C+32	Fahrenheit	°F
ILLUMINATION				
lx	lux	0.0929	foot-candles	fc
cd/m^2	candela/m^2	0.2919	foot-Lamberts	fl
FORCE and PRESSURE or STRESS				
kN	kilonewtons	0.225	1000 pound force	kip
N	newtons	0.225	pound force	lbf
kPa	kilopascals	0.145	pound force per square inch	lbf/in^2

*SI is the symbol for the International System of Units. Appropriate rounding should be made to comply with Section 4 of ASTM E380.

Technical Report Documentation Page

1. Report No.	2. Government Accession No.	3. Recipient's Catalog No.

4. Title and Subtitle	5. Report Date
Hybrid Prestressed Concrete Bridge Girders using Ultra-High Performance Concrete	December 2020
	6. Performing Organization Code
7. Author(s)	8. Performing Organization Report No.
Torres, E., Hamilton, H. R. and Consolazio, G. R.	
9. Performing Organization Name and Address	10. Work Unit No. (TRAIS)
University of Florida Department of Civil & Coastal Engineering P.O. Box 116580 Gainesville, FL 32611-6580	11. Contract or Grant No. BDV31-977-101
12. Sponsoring Agency Name and Address	13. Type of Report and Period Covered
Florida Department of Transportation 605 Suwannee Street, MS 30 Tallahassee, FL 32399	Final Report July. 2018-Dec. 2020
	14. Sponsoring Agency Code

15. Supplementary Notes

16. Abstract

In prestressed bridge girders, end region reinforcement and strand debonding are used to control cracking caused by high tensile stresses that occur due to prestress transfer. In some cases, these measures do not effectively control cracking, resulting in construction delays, potential repairs, additional costs, and potential compromise of long-term durability. Ultra-High Performance Concrete (UHPC) is an attractive solution to prevent end region cracking and potentially increase girder span lengths. This approach consists of producing a hybrid girder in which UHPC is placed at the end of the girder and conventional self-consolidating concrete (SCC) mixture placed in the remainder of the girder. This approach strategically places the higher cost and higher strength material in the portion of the beam with most extreme stress conditions during construction. To evaluate the effectiveness of UHPC, experimental and analytical investigations were conducted.

The experimental program covered five 20-ft-long Florida-I 72 beam (FIB 72) mockups made of SCC and UHPC and two 50-ft-long Florida-I 54 beam (FIB 54) UHPC-SCC hybrid girders used to evaluate end region behavior and strength under applied shear. Cracking and strain data were collected during prestress transfer, and one year after transfer. Variables considered in these specimens included UHPC length from the girder end and amount of end region reinforcement. The experimental results of the FIB 72 mockups indicated that UHPC ends exhibited maximum end region crack widths of 0.003 in., which were ~25% of the crack widths in the SCC ends. Load tests on UHPC-SCC FIB 54 hybrid girder indicated shear strengths significantly higher than comparable SCC girders. Furthermore, the UHPC-SCC interface performed well during load tests, thereby validating the methods of construction.

The analytical program was conducted in three stages: (1) Material model identification and calibration, (2) Development and validation of FIB 72 mockup model for end region evaluation, and (3) development and validation of FIB 54 hybrid girder model under shear loads. The results from the analytical work confirmed that UHPC is a promising approach to reducing end region cracking.

17. Key Words	18. Distribution Statement
UHPC, prestressed girder, hybrid girder, end region, shear strength, concrete cracking	No restrictions

19. Security Classif. (of this report)	20. Security Classif. (of this page)	21. No. of Pages	22. Price
Unclassified	Unclassified	211	

Form DOT F 1700.7 (8-72) Reproduction of completed page authorized

Acknowledgments

The authors acknowledge and thank the Florida Department of Transportation (FDOT) for funding the research presented in this report. The authors thank the project manager William Potter for his technical input and support and for facilitating resources throughout the project. The authors also thank the FDOT Marcus H. Ansley Structures Research Center and personnel, including Christina Freeman, Stephen Eudy, Justin Robertson, Michael Waters, and Miguel Ramirez, for their expertise, assistance, and support with experimental testing.

Standard Concrete Products are acknowledged and thanked for their efforts in planning and fabrication of the research specimens, especially Kurt Podoll, Ryan Cartwright, Klaus Barna, and Sean Alderman.

Finally, the authors appreciate the contributions to this research made by UF undergraduate and graduate students, including Felix Garcia, Carson Gonzalez, Joshua Wasserman, Saul Licona, Gabriela Calana, and Glenda Diaz.

Executive Summary

In prestressed bridge girders, end region reinforcement and strand debonding are used to control cracking caused by high tensile stresses that occur due to prestress transfer. In some cases, these measures do not effectively control cracking, resulting in construction delays, potential repairs, additional costs, and potential compromise of long-term durability. Ultra-High Performance Concrete (UHPC) is an attractive solution to prevent end region cracking and potentially increase girder span lengths. This approach consists of producing a hybrid girder in which UHPC is placed at the end of the girder and conventional self-consolidating concrete (SCC) mixture placed in the remainder of the girder; the higher cost and higher strength material is placed in the portion of the beam with most extreme stress conditions during construction. To evaluate the effectiveness of this use of UHPC, experimental and analytical research was conducted; the research results are described in this report.

The experimental program was divided in two phases. In the first phase, five 20-ft-long Florida-I 72 beam (FIB 72) mockups made of SCC were constructed to evaluate end region behavior. The second phase consisted of constructing two 50-ft-long Florida-I 54 beam (FIB 54) UHPC-SCC hybrid girders to investigate the performance under load testing.

Phase one FIB 72 mockups were constructed to compare end region behavior between UHPC and SCC ends. Additional UHPC-only mockups were constructed with reduced amount of end region steel reinforcement to investigate the behavior of UHPC. These mockups were instrumented with linear strain gages and fiber optic sensors (FOS) to measure strain during prestress transfer. Additionally, the mockups were monitored for one year to document changes in crack width and characteristics. Crack width measurements indicated that SCC ends result in crack widths up to four times greater than those of UHPC. Furthermore, it was found that crack widths measured on UHPC ends do not exceed 0.003 in. regardless of the amount of end region reinforcement.

Phase two FIB 54 UHPC-SCC hybrid girders were load-tested to determine the capacity and behavior of the UHPC-SCC interface under applied shear. A total of four load tests were performed to investigate the effect of UHPC length from the girder end and amount of end region reinforcement. Due to limiting capacity of the strong floor supporting the frame, the specimens were not loaded to failure but to a maximum load of 1,000 kip. Up to this load, the UHPC-SCC interface was able to transfer loads without exhibiting significant damage. Furthermore, the UHPC-SCC hybrid girder carried at least 25% higher superimposed shear without reaching failure compared to past SCC FIB 54 girders.

The analytical program was conducted in three stages: (1) material model identification and calibration, (2) development and validation of FIB 72 mockup model for end region evaluation, and (3) development and validation of FIB 54 hybrid girder model under shear loads. The first stage consisted of calibrating material models available in LS-DYNA to approximate the tensile behavior of UHPC. To accomplish this, finite element models of the Direct Tension Test (DTT) and ASTM C1609 Flexure Beam test were developed to calibrate the material model parameters and approximate the experimental behavior. The calibration showed that MAT_84 Winfrith and concrete damage MAT_72R3 were capable of approximating UHPC tensile behavior.

Using the calibrated MAT_84 material model, the second stage of the analytical work included simulation of the FIB 72 mockups during prestress transfer. Concrete and mild-steel reinforcement strains measured during prestress transfer were used to validate the analytical model. After validation of the analytical model, a parametric study on the FIB 96 was performed

to determine potential benefits of UHPC on larger girder sections. The analytical models showed that SCC develops crack widths at least 3.75 times greater than those of UHPC.

Stage 3 of the analytical work used the calibrated MAT_72R3 model to perform simulations of the FIB 54 hybrid girders during prestress transfer and load tests. Good agreement was found between the experimental and analytical results; however, the model will need further calibration once the experimental failure strengths are available.

Table of Contents

List of Figures

List of Tables

1 Introduction

Ultra-high performance concrete (UHPC) is an emerging class of concrete with enhanced mechanical properties combined with improved durability. These properties make UHPC an attractive material to be used to fabricate bridge components. UHPC is associated with high costs, which has impeded its wide implementation in the United States. This has typically been due to the proprietary nature of the UHPC mixtures developed in recent years.

More interest has been expressed by precast concrete producers in Florida in developing their own UHPC mixtures that can be used to produce targeted products in a cost-competitive manner for such areas as highway bridge components.

The research covered in this report is an example of one such application of UHPC to the production of precast bridge components; the focus is on the use of UHPC at the end of precast bridge girders to improve crack control in the end region caused by the prestressing forces. During prestress transfer, the girder end region is subjected to bursting, spalling, and splitting stresses that result in concrete cracking. A past research project sponsored by the FDOT (Diaz and Hamilton, 2020) evaluated the effectiveness of fiber-reinforced concrete (FRC) to control end region cracking in prestressed girders. The study found that FRC was able to reduce end region crack widths, which improves the serviceability and durability as well as reduce the need for crack repair.

These findings motivated the execution of this project to evaluate the effectiveness of using UHPC to better control cracking than is possible with the use of self-consolidating concrete (SCC) that is currently used to produce bridge girders in Florida. High UHPC cost motivates efficient use of the material; to take full advantage of the improved UHPC mechanical properties, the concept of a UHPC-SCC hybrid girder was developed. The UHPC-SCC hybrid girder concept strategically places the higher cost and higher strength material in the portion of the girder that is subjected to the most extreme stress conditions during construction.

This report presents results from experimental and analytical investigations that were conducted to evaluate the effectiveness of UHPC to control end region cracking and the performance of the UHPC-SCC interface under superimposed shear. Also included in this report are examples of possible span length increase achievable with the UHPC-SCC hybrid girder.

Experimental work included five 20-ft-long Florida-I 72 beam (FIB 72) mockups made of SCC and UHPC and two 50-ft-long Florida-I 72 beam (FIB 72) UHPC-SCC hybrid girders used to evaluate end region behavior and strength under applied shear. Cracking and strain data were collected during prestress transfer and for up to one year after transfer. Variables considered in these specimens included UHPC length from the girder end and amount of end region reinforcement.

Analytical work in this project utilized the finite element analysis (FEA) method. FEA models were validated using the data collected from the experimental program and then were used to investigate end region behavior in a FIB 96.

This report presents the results of research conducted on hybrid prestressed concrete bridge girders using UHPC. The literature review in Chapter 2 provides background of current knowledge of end region behavior, UHPC material properties, UHPC tensile testing, UHPC shear strength, and UHPC modeling. Chapter 3 covers the FIB 72 mockup design, construction, material testing, strain measured during prestress transfer, and end region crack monitoring. Chapter 4 covers the FIB 54 hybrid girder design, construction process, and shear test procedures and results. Chapter 5 covers direct tension test results that were conducted on a number of

different components. Chapter 6 covers the parametric study conducted to determine the possible increases in girder span that might be possible with the use of UHPC-SCC hybrid girders, and Chapter 7 describes the analytical work that was conducted in support of the experimental testing. This report closes with overall summary and conclusions of the research and suggestions for implementation of the results.

1.1 Research Objectives

The main objective of this research project was to evaluate the effectiveness of using UHPC in the reduction or elimination of visible end region cracking after prestress transfer. This objective was achieved by conducting experimental and analytical work designed with the following sub-objectives:

- Investigate, evaluate, and implement construction methods that can be used by precast plants to construct UHPC-SCC hybrid girders
- Test the tensile properties of UHPC specimens to assess the quality of the UHPC mix
- Evaluate the effectiveness of UHPC concrete at controlling end region cracking
- Test the structural performance of the UHPC-SCC interface under superimposed shear
- Evaluate the potential benefits of UHPC on larger girder cross-sections
- Determine possible contribution of UHPC to the structural performance of prestressed bridge girder, in terms of longer span lengths

1.2 Research Organization

The report is divided in three major components:

- Design, construction, testing and monitoring the FIB 72 mockups for end region evaluation. End region evaluation consisted of measuring strains in the concrete and mild-steel reinforcement during prestress transfer, and characterizing end region crack growth overtime.
- Design, construction, and load testing of the FIB 54 hybrid UHPC-SCC girders.
- Analytical investigation focused on evaluating the effectiveness of UHPC at controlling end region cracking in ends with reduced reinforcement and or larger FIBs cross-section.

2 Literature Review

2.1 Background

Ultra-high-performance concrete (UHPC) is a relative new class of concrete that began to develop in the late 1990s. This new class of concrete is able to provide high strength, enhanced ductility and durability. The Federal Highway Administration has been one of the pioneers for the implementation in the United States defining UHPC as a cementitious-based composite with discontinuous fiber that exhibits a compressive strength above 21.7 ksi, pre- and post-cracking tensile strength above 0.72 ksi, and enhanced durability via its discontinuous pore structure (Rusell and Graybeal, 2013). These enhanced properties have steered the application of UHPC to structural components such as joints between deck panels (Figure 2-1), prestressed girders (Figure 2-2), deck slabs, deck overlay, and precast piles (Figure 2-3).

UHPC has generally been available only in the form of proprietary commercially available mixtures since early 2000s (Graybeal 2011). Due to the proprietary UHPC mixes, the cost of UHPC is well above that of conventional ready-mixed concrete and has been reserved only for relatively small volume applications. This has been somewhat of an impediment to the widespread use of UHPC.

Figure 2-1 UHPC used for joints of deck panels

Figure 2-2 UHPC used to fabricate prestressed girders

Figure 2-3 Precast piles made of UHPC

In Florida, the application of UHPC has been limited to repair between existing precast slab units, closure between beam flanges, and prestressed U-beam repair (FHWA, 2017). Recently, however, precast concrete producers in Florida have become interested in producing their own version of UHPC and employing the mixtures in targeted or specialized applications, which may include highway bridge components.

One such application is the end region of prestressed concrete girders. The approach is to produce a hybrid girder in which UHPC would be placed at the end of the girder and conventional FDOT SCC concrete girder mixture placed in the remainder of the girder. This approach strategically places the higher cost and higher performance material in the portion of the beam that has the most extreme stress conditions during construction. However, this approach raises questions that need to be considered during the construction process in terms of SCC-UHPC joint. Up through the conclusion of this research project no studies addressing the SCC-UHPC hybrid girder approach from an experimental perspective were found.
Ronanki et al. (2017) evaluated the concept of UHPC-NC (normal concrete) hybrid girder with a series of Finite Element models developed in ATENA. The study aimed to address end region

cracking and performance of the UHPC-NC interface subjected to shear stresses. The study reported that maximum stresses in the end region reinforcement were 17.5 ksi and that no cracking is expected to occur during prestress transfer. Additionally, the authors did not expect for separation between the NC and UHPC to occur, because the shear stresses at the interface during dead loads and HL-93 loading were less than the shear capacities obtained experimentally from push-off tests.

2.2 End Region

In prestressed concrete girders, end region is typically understood to be the end of the girder over a length approximately equal to their height. During prestress transfer, the girder end regions are subjected to bursting, spalling and splitting stresses that result in concrete cracking (Figure 2-4).

Bursting and spalling stresses form due to the eccentricity between the centroid of the strands and the girder center of gravity. The eccentricity during prestress transfer creates a moment in the girder cross-section, which generates tensile forces from the location of the prestressing strands to the top flange. Concrete cracking occurs when the generated tensile stresses exceed the strength of concrete. In general, these cracks form at the interface between the bottom flange and the web (Figure 2-5). Splitting stresses are generated as a result of Hoyer expansion of strands, which can result in splitting cracks in the bottom flange.

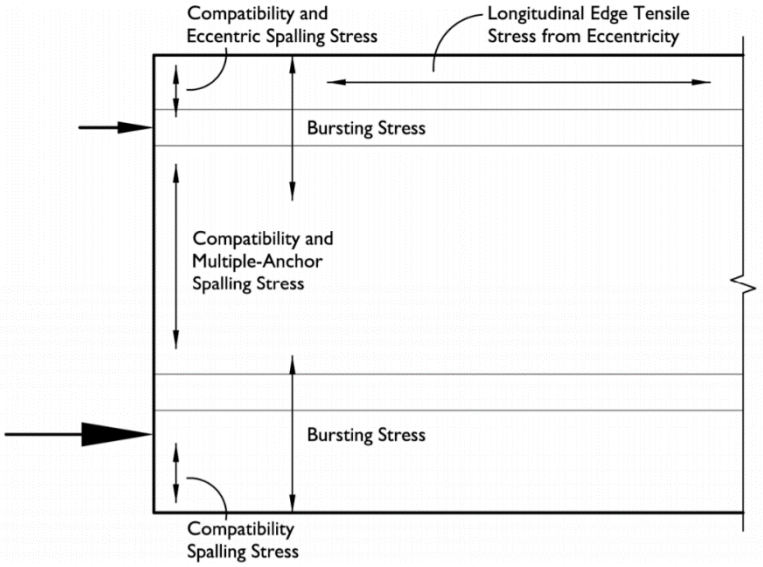

Figure 2-4 Stresses in the end region (Dunkman et al., 2010)

Figure 2-5 End region cracks

2.2.1 End Region Design

Provisions for end region design were developed from research conducted by Marshall and Mattock (1962). This study proposed to calculate the amount of transverse reinforcement using Equation 2-1.

$$A_r = 0.021 \frac{P_i}{f_s} \frac{h}{l_t} \qquad \text{Equation 2-1}$$

where A_r is the required area of transverse reinforcement, P_i is the total prestress force, f_s is the design stress in the reinforcement, h is the depth of the member and l_t is the strand transfer length.

End region design required by AASHTO LRFD Bridge Design Specifications (2017) and the FDOT Structures Design Guidelines (2018) are derived from Marshall and Mattock's proposed equation (1962), by replacing the h/l_t portion of the equation with a factor between 2 and 2.3.

Both design guidelines follow a similar approach, although the FDOT approach is more conservative due to environmental conditions in the state of Florida. The amount of reinforcement in both design guidelines is quantified using Equation 2-2 for the specified end region location. Both design guidelines are summarized below:

AASHTO LRFD 5.9.4.4.1-1 (2017):

- 4% P_u from the end of the beam to h/4

FDOT (2018)

- 3% P_u from the end of the beam to h/8
- 5% P_u from the end of the beam to h/4
- 6% P_u from the end of the beam to 3h/8

$$P_u = f_s A_s \qquad \text{Equation 2-2}$$

where P_u is the total prestress force (without losses) in ksi, f_s is the stress in the steel not to exceed 20 ksi, A_s the total area of reinforcement located within the specified distance from the end of the girder, and h is the overall dimension of precast member in the direction in which resistance is being evaluated. In addition, the FDOT Index 20010 (2012) provides limits for the maximum bonded prestress force for all FIBS as listed in Table 2-1.

Table 2-1 Maximum bonded prestress force

Beam Type	Max. Bonded Prestress Force at Beam End (kip)
FIB 36	1,450
FIB 45	1,670
FIB 54	1,740
FIB 63	1,740
FIB 72	1,980
FIB 78	2,230
FIB 84	2,375
FIB 96	2,375

2.2.2 End Region Crack Control and Repair

Crack control is partly addressed during design by placing mild-steel reinforcement at strategic locations where tensile stresses are developed during prestress transfer. Another common approach is to debond prestressing strands at the end to reduce end region stresses. Tadros et al. (2010) summarizes additional measures that can improve crack control:

a. Adjust method of detensioning from flame cutting to hydraulic release
b. Adjust detensioning sequence to release top straight or draped strands before bottom strands
c. Both ends of the same prestressing strand should be cut simultaneously to prevent uneven forces.
d. Minimize free strand length between abutment and first prestressed member and between prestress members
e. Apply lubricant to the precast bed to reduce friction generated by member shortening during detensioning
f. Increase the length over which the strand is heated during flame-cutting to increase elongation before rupture
g. Design member with low concrete release strength

Recent innovative options for crack control have been developed by (Diaz and Hamilton 2020, and Alireza and Rafic 2020). Diaz and Hamilton (2020) used fiber-reinforced concrete (FRC) for girder fabrication. The study reported that FRC reduced maximum crack widths and

effective crack widths by 50% and 40% respectively. Also, it was found that hooked end fibers were the most effective by maintaining crack widths under 0.006 in.

Alireza and Rafic (2020) evaluated the end region behavior of UHPC prestressed girders with varying depths and web widths. The study estimated that the stresses in the rebar were under the 20 ksi limit based on the strain measured in the concrete surface. Finally, the study recommended that the current design practice in AASHTO LRFD (2017) can be applicable for girder ends made of UHPC, where the benefits of UHPC can be engaged in the design (Equation 2-3). For instance, Alireza and Rafic (2020) specified a UHPC contribution of 1 ksi, which was a conservative approximation of the cracking strength obtained from DTTs.

$$0.04P_u = f_s A_s + f_{UHPC} A_C \qquad \text{Equation 2-3}$$

where $f_{UHPC}$is the UHPC contribution (1 ksi) and A_c is the concrete area of the web thickness by the distance from the girder end to H/4.

When end region cracking does occur, it is typically necessary to evaluate the cracking and determine if repair or some other treatment is necessary. Table 2-2 lists the NCHRP 654 (2010) published crack treatments from a national survey, and recommended treatment from the study. Table 2-3 shows the FDOT Standard Specifications for Road and Bridge Construction (2018) crack repair specifications.

Table 2-2 NCHRP 654 (Tadros et al. 2010) crack treatment during production

National Survey		Recommended Crack Treatment	
Crack Width (in.)	Repair Method	Crack Width (in.)	Repair Method
<0.007	Surface Sealing	<0.012	No action
0.007 – 0.025	Epoxy Injection	0.012 – 0.025	Apply Sealant
>0.025	Reject Beam	0.025 -0.050	Inject epoxy
		>0.05	Reject Girder

Table 2-3 Crack Treatments specified by Standard Specifications for Road and Bridge Construction (FDOT 2018)

Crack Width (in.)	Repair Method
≤ 0.006	Penetrant Sealer*
0.006 – 0.012	Penetrant Sealer or epoxy injection
> 0.012	Engineering evaluation

*Only for extreme environment conditions; otherwise, not treatment needed

2.3 UHPC Material Composition

UHPC is composed of portland cement, supplemental cementitious materials (silica fume), fine sand, high-range water reducing admixtures (HRWR), fibers, and water. Each constituent is carefully selected and proportioned to obtain optimal particle packing and high strength. In addition, to obtain compressive strengths above 20 ksi, the mixture is designed using low water-cement ratios ranging from 0.17-0.22, which is accompanied with high dosages of HRWR.

Steel fibers are the most common fiber type used for UHPC, with fiber dosages ranging from 1% to 3% of the total volume by weight. Wu et al. (2016) studied the effect of steel fibers at varying dosage and shape. The study found that the flowability of UHPC decreases with an increase in fiber volume or when deformed fibers were used (hook-end). The compressive and

flexural strength was higher for the mixtures having high volume of steel fibers, and it was higher for mixtures having hook-end or corrugated fibers as opposed to straight fibers. Finally, it was concluded that the volume or shape of the fibers did not have an effect on the first crack during compressive or flexural loading.

The flowability of UHPC is measured using ASTM C1437 —Standard Test Method for Flow of Hydraulic Cement Mortar. This test method provides a measure of the flowability of fresh UHPC as well as a visual indication of the distribution of the fibers throughout the mortar. Depending of the application, flow tests may be performed before adding the fibers, which allows verification that the mortar flowability is adequate (Figure 2-6). Consider that while UHPC does not have coarse aggregate, the steel fibers can clump or segregate if the mortar has low viscosity as shown in Figure 2-7a.

A UHPC mix with well distributed fibers is shown in Figure 2-7b. ASTM C1856 — Standard Practice for Fabricating and Testing Specimens of Ultra-High performance Concrete provides procedures for the fabrication and testing of UHPC specimens. This standard suggests that UHPC should have a flow varying from 7.8 in. to 9.8 in.

Figure 2-6 Spread test on UHPC without fibers (Photo credit: Torres)

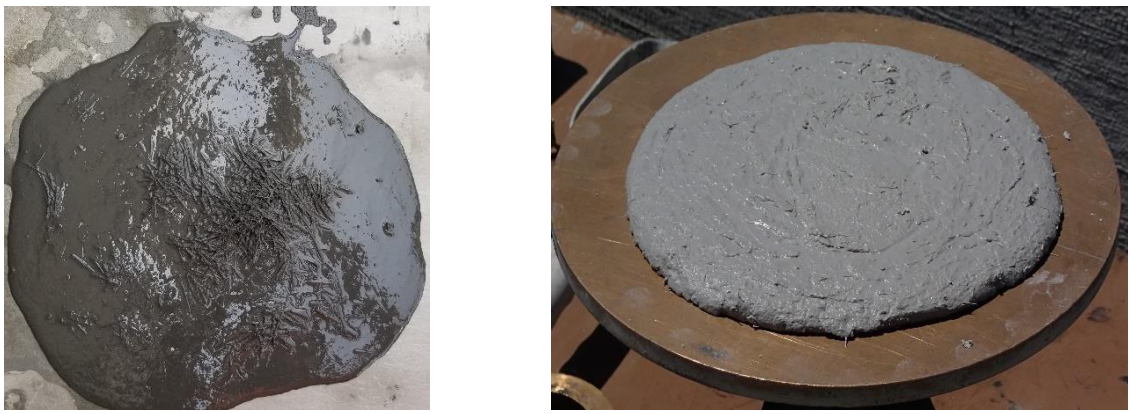

Figure 2-7 Fiber distribution in UHPC: (a) fiber uneven distributed during spread test (Photo credit: Torres); (b) fibers well distributed (Photo credit: Torres)

2.4 UHPC Mechanical Properties

2.4.1 Compressive Strength

UHPC compressive strength test is performed using ASTM C39— Standard Test Method for Compressive Strength of Cylindrical Concrete Specimens, along with some modifications specified in ASTM C1856— Standard Practice for Fabricating and Testing Specimens of Ultra-High performance Concrete. ASTM C1856 is applicable to any UHPC with a compressive strength above 17,000 psi. The modifications to the ASTM C39 include:

1. Only use 3 in. × 6 in. cylinder specimens for compressive testing
2. The ends of the cylinders shall be ground plane to within 0.002 in.
3. The load shall be applied at a rate of 1025 ± 50 psi/s.

Typical compressive stress-strain behavior of UHPC is shown in Figure 2-8a (Singh et al., 2017). At peak strength, compressive strength tests of high strength concrete cylinders often result in an explosive brittle failure. However, in UHPC, the steel fibers prevent the concrete from spalling as shown in Figure 2-8b. Haber et al. (2018) investigated the compressive strength of six commercially available UHPC mixtures. The study reported that the pre-peak compressive stress-strain relationships was similar among all mixtures. However, at peak strength a wide range of strains varying from 0.00274 to 0.00524 (Figure 2-9) were reported among the tested UHPC mixtures.

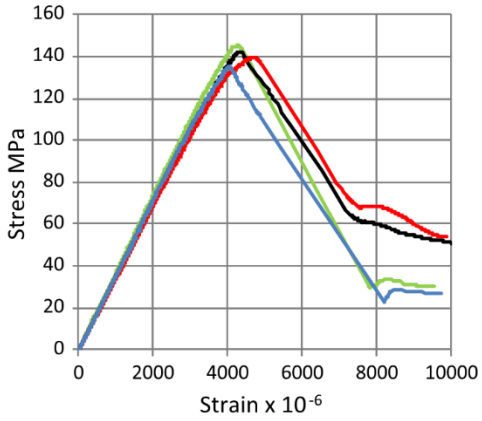

(a)

(b)

Figure 2-8 UHPC compressive strength: (a) experimental results (Singh et al. 2017), and (b) tested cylinder (Photo credit: Torres)

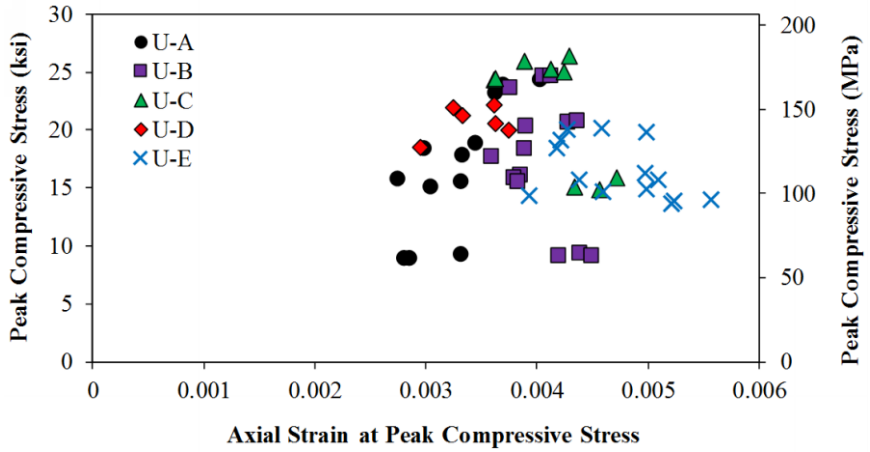

Figure 2-9 Axial compressive strains measured at peak stress (Haber et al. 2018)

2.4.2 Tensile Strength

One of the fundamental assumptions in the strength design of reinforced concrete sections is to ignore the concrete strength in tension. Under service load conditions in prestressed concrete, the tensile strength of concrete is considered when checking service stresses; AASHTO LRFD C5.4.2.7 allowable stress for Service III limit states check is specified based on the modulus of rupture as $0.24\sqrt{f'c}(ksi)$. UHPC, however, generally exhibits tensile strengths 2-3 times higher than that of conventional concrete. Furthermore, the fibers present in UHPC mixtures provide crack control under service conditions and tensile ductility under strength conditions. The enhanced tensile strength and ductility provide an opportunity to optimize structural design of structural components beyond what is typically possible for conventional structural concrete. If the tensile strength is to be considered in the design, however, a convenient and effective method to measure the tensile strength is needed.

Several test methods have been proposed in the literature (Yang et al., 2010, Graybeal and Baby 2014, Voit and Kirnbauer 2014, Yuliarti et al., 2015, Kang et al., 2016, Haber et al., 2018, Graybeal and Baby 2019, Zhou and Qiao 2019) to test for the tensile strength of fiber-reinforced concrete and UHPC; these include splitting tensile test, direct tension test (DTT), flexural beam tests, Barcelona test, among others. One particular challenge that all of these test methods face is the preferential fiber alignment that can occur when casting test specimens. Preferential fiber alignment can result in under- or overestimation of the tensile strength. The mold for casting specimens is typically much smaller and more confined than the formwork used to cast the structural member that is being constructed. Casting of the test specimens may result in very different UHPC flow patterns than that experienced in the formwork used to cast the structural member.

The direct tension test and flexural beam test (ASTM C1609) are methods used to determine the tensile strength of UHPC. The DTT test requires sophisticated equipment that is only available in a few laboratories in the US. This test has the potential to be implemented by agencies as a qualification requirement to approve a UHPC mix. Then, a test with a much simpler setup such as flexural beam tests can be required to be performed on a daily basis as quality control at UHPC production facilities.

In general, the direct tension test is a complicated by the difficulty in obtaining evenly distributed stresses throughout the cross section and controlling a stable load versus displacement

response (Wille et al., 2014). While currently no testing standards are available, the FHWA (Graybeal and Baby 2019), AFGC-SETRA (2002), and JSCE (2008) have provided recommendations on how to perform an uniaxial tensile test.

The Federal Highway Administration (FHWA) performed a large research project to review tensile strength test methods (Graybeal and Baby 2019). From this project, the FHWA developed guidelines for a direct uniaxial tension test known as the direct tension test (DTT). The DTT consists of directly relating the uniaxial tensile properties of UHPC from global elastic behavior through localization of strain within an individual crack (Graybeal and Baby 2019). The study considered specimens of different lengths, different shapes and the effect of adding a notch in the middle. A sample stress-strain curve obtained from a DTT is shown in Figure 2-10. The figure shows the different stages observed during uniaxial tensile loading of UHPC. The initial part of the curve displays the elastic portion of the curve until first crack occurs. The second portion of the curve shows multi-cracking occurring in the middle region (Figure 2-11). Finally, the last region is denoted as crack localization, which consists of the localization of strain in a discrete crack (Figure 2-12).

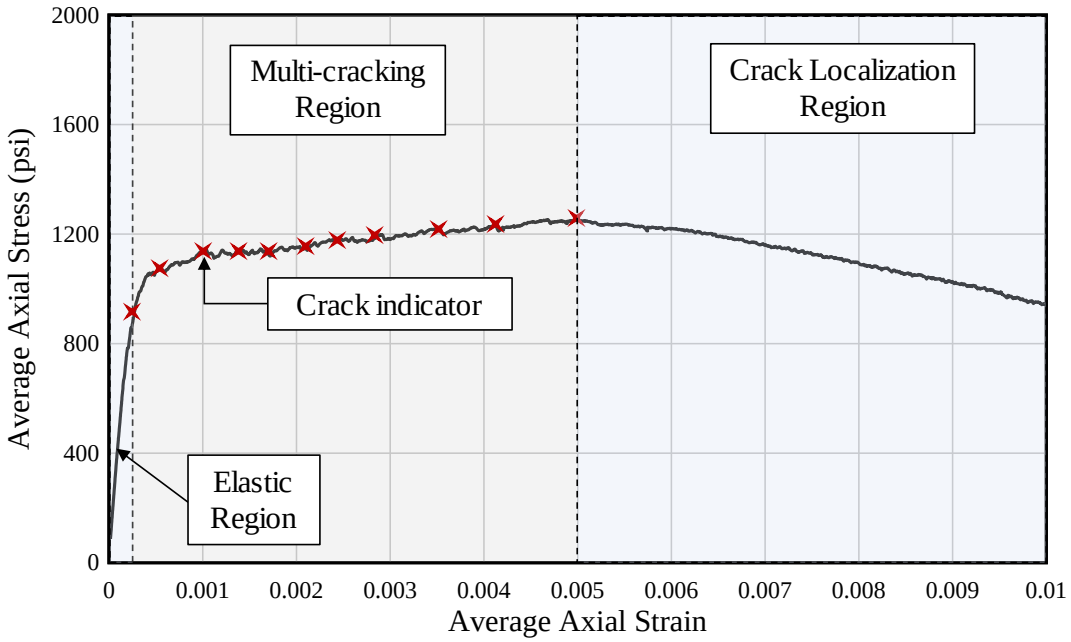

Figure 2-10 Tensile response obtained from Direct Tension Test

Figure 2-11 Multi-cracking during uniaxial tensile loading (Photo credit: Torres)

Figure 2-12 Crack localization during tensile loading (Photo credit: Torres)

Other test setups and sample geometries have been used to perform uniaxial tests on UHPC specimens (Tran and Kim 2013, Nguyen et al., 2014, Wille et al., 2014, Zhou and Qiao 2019). Zhou and Qiao (2019) used finite element analysis (FEA) to assist in the design of a dog-bone-shaped specimen (Figure 2-13) capable of characterizing tensile response by displaying linear elastic, strain hardening, and strain-softening behaviors.

The shape of the developed specimen avoided the necessity of attaching the tapered aluminum plates —needed on the FHWA DTT method— on the side of the specimens. Nevertheless, fabricating specimens with the specified curvature to transition from the thicker section to the thinned middle region can be challenging. In the middle region, the specimen has the same cross section area as the specimens from the FHWA study, but the gage length increases from 4 in. to 6 in.

Nguyen et al. (2014) developed a similar dog-bone shape specimen with square corners in the grip region (Figure 2-14). In this study, the gage length varied from 4.9 in to 9.8 in. It was found that a larger gage length did not affect the post-cracking strength but affected the energy absorption capacity and multi-cracking behavior. In addition, the authors did not report information regarding the development of the specimen geometry or potential drawbacks associated with the square corners.

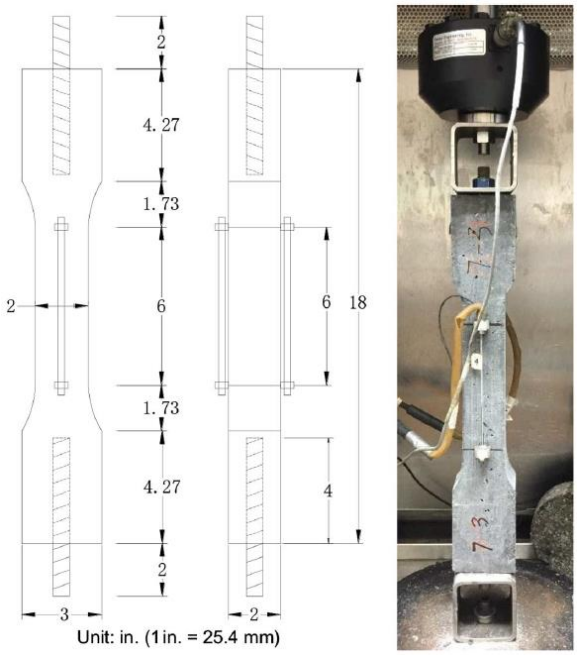

Figure 2-13 DTT dog-bone-shape specimen (Zhou and Qiao, 2019)

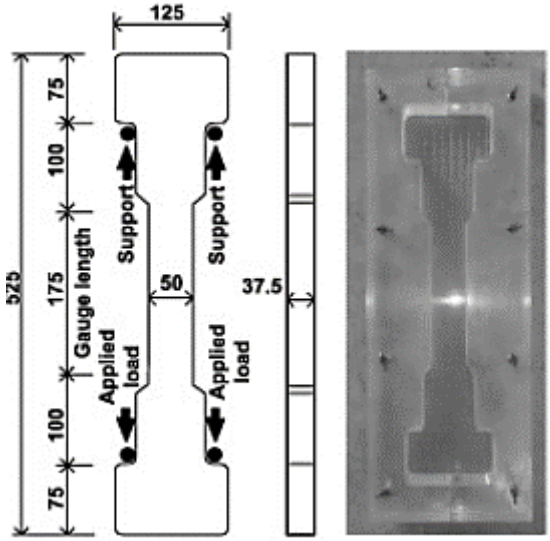

Figure 2-14 Dog-bone shape DTT specimen (Nguyen et al., 2014)

Another test method that can be used to investigate the tensile strength of UHPC is a flexural beam test. This test is performed using ASTM C1609— Standard Test Method for Flexural Performance of Fiber-Reinforced Concrete. The load-deflection curve obtained from

this test (Figure 2-15) is highly dependent on the type and amount of fibers in the concrete. The load-deflection curve should be interpreted based on the application, level of acceptable cracking, and deflection serviceability. In general, the behavior is initially elastic with cracking occurring when the tensile strength is reached. The fibers provide the tensile stiffness that allows more load to be carried beyond cracking up to the ultimate strength. Once beyond the peak load, the load capacity will generally decrease as the displacement increases up to termination of the test. Residual strength can be computed at different deflection levels recommended in the test method such as 0.02 in. or 0.08 in. Residual strength is computed using the formula of the modulus of rupture to determine the notional gross section bending stresses corresponding to a specific load as shown in Equation 2-4:

$$f_r = \frac{PL}{bd^2} \qquad \text{Equation 2-4}$$

where f_r is the residual strength of concrete (psi), P is the load (lbs.), L is the span length (in.), b is the beam width (in.) and d is the beam depth (in.).

However, flexural tests require an inverse analysis to determine the uniaxial stress-strain behavior. Inverse analysis is generally performed using two methods. The first method is point-by-point, which estimates the stress-strain curve based on the equilibrium of moments and forces in a sectional analysis for each value of midspan strain on the tension face. The second method is derived from an inverse analysis from the bending moment versus midspan deflection (Graybeal and Baby, 2014). Several studies have developed inverse analysis methods to obtain the uniaxial stress-strain curve from flexural tests (AFGC-SETRA 2002, JCI 2006, Qian and Li 2008, Rigaud et al., 2011, Mobasher et al., 2014). Mobasher et al. (2014) developed a study to back-calculate an effective uniaxial residual tensile strength of regular and high-performance fiber-reinforced concrete from flexural test results. This study considered a variety of parameters such as notched and un-notched beams, different fiber types, shapes, and volume (Mobasher et al., 2014). The study found that in the case of the ASTM C1609, the back-calculation results in an overestimation of the residual strength and recommends that for design the values must be scaled by a factor of 0.31-0.34. Similarly, the inverse analysis methods developed by JCI (2006), Qian and Li (2008) and Rigaud et al. (2011) overestimate the post-cracking strength by 12 % and underestimate the strain hardening by 30%.

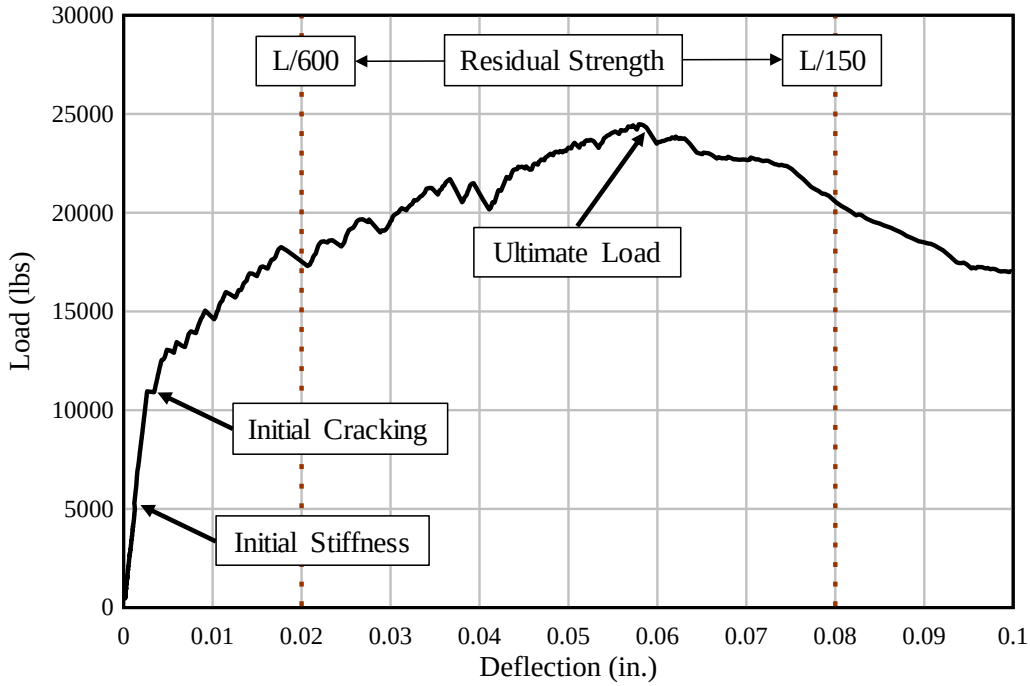

Figure 2-15 Load-deflection curve

2.4.3 Ductility

Ductility is an important property for structures by providing the ability of resisting significant deformation without sudden failure. Ductility is defined as the ratio of post-yield deformation to yield deformation (Wang et al., 2010). In fiber reinforced concrete, ductility is given by the mechanics between the cementitious matrix and the fibers.

The most common failure mode of fiber reinforced concrete and the mode responsible for the ductile behavior is the fiber-bridging-debonding-pullout (Abbas and Khan 2016). This failure mechanism is characterized by the debonding of the fiber with the cementitious matrix and the frictional sliding of the fiber as the crack width increases (Figure 2-16). This mechanism is dependent of the fiber type, fiber dosage and fiber distribution in the direction of the crack propagation (Zollo, 1996). Note that fiber pull-out is the preferred failure mechanism; however, another failure mechanism is fiber rupture, which results in brittle behavior of the structural component.

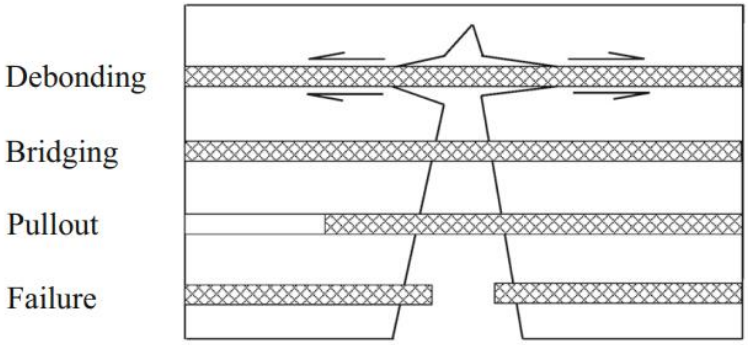

Figure 2-16 Mechanisms of fiber-cementitious matrix interaction (Abbas and Khan 2016)

UHPC enhanced properties allow the cementitious matrix and fiber to develop bond strengths up to four times higher than those observed in normal and high-strength concrete (Wille and Naaman, 2013). Cementitious matrix and fiber bond strength is enhanced in UHPC due to the optimized particle packing. Wille and Naaman (2013) concluded that using Zircon sand and silica fume with small mean particle size enhances the interfacial bond between the fiber and the matrix. Several studies (Banthia and Trottier 1991, Naaman and Najm 1991, Markovic 2006, Kim et al., 2008, Zile and Zile 2013, Soetens et al., 2013, Wu et al., 2016, Xu et al., 2016, and Qi et al,. 2018) suggest that the pull-out mechanism can be enhanced with hook or deformed steel fibers. In general, hook end fibers follow the same debonding and bridging mechanism observed in straight steel fibers; however, the pull-out force its higher due to anchorage effect of the fiber hook end. Qi et al. (2018) investigated the effect of fiber type, fiber orientation (0°, 30° and 45°) and fiber dimension. The study found that fiber dimension is more significant for straight fibers as oppose to hook-end fibers. Also, the authors show that fibers with an inclination of 0° developed the lowest pull-out force and is recommended to be adopted in design as a conservative assumption for both serviceability limit state and ultimate limit state.

2.5 Shear Strength of UHPC Structural Members

Several studies have performed experimental tests to investigate the behavior of UHPC under shear loads (Graybeal 2006, Voo et al., 2010, Xia et al., 2011, Lim and Hong 2016). Graybeal (2006) performed three shear tests on AASHTO Type II beams with no shear reinforcement. The study reported shear strengths up to 500 kips, where the main failure mechanisms were diagonal tension in the web and strand slip. The researchers also compared the UHPC beams experimental results to the expected capacity of a conventional 8 ksi concrete AASHTO Type II with representative shear reinforcement.

The researchers reported that UHPC capacity is twice that of the conventional concrete girder, illustrating the significant contribution of UHPC to girder shear strength. Voo et al. (2010) also performed several shear tests on beams without stirrups. The study concluded that the steel fibers result in a distribution of damage in the web before the main failure crack forms, verifying the strain hardening behavior characteristic of UHPC after tensile cracking. Xia et al. (2011) also reported high post-cracking resistance, outlined by multi-cracking developed parallel to the main shear crack.

Lim and Hong (2016) investigated the synergetic effect of shear reinforcement and UHPC to enhance beam ductility. The study reported an increase of 13% to 19% for beams with reinforcing bar shear reinforcement as opposed to beams relying solely on the UHPC fibers.

Furthermore, the study also recommended that UHPC beams not be restricted to the maximum bar spacing of 0.75d in ACI 318-19.

The Japan Society of Civil Engineers (JSCE), French Standard NF P18-710, Australian Design Guidelines and the Federal Highway Administration provide guidelines to predict the shear capacity for structures made of UHPC as indicated in Equation 2-5 by dividing the contribution to shear in four components: concrete (V_c), UHPC steel fibers (V_f), mild-steel reinforcement (V_s) and prestressing strands (V_p).

$$V_f = V_C + V_f + V_s + V_p \quad \text{Equation 2-5}$$

All of these terms are generally addressed by several design guidelines, except for the fiber contribution. Fiber contribution is addressed differently by design codes and continues to be investigated.

The JSCE (2008) estimates the contribution of the fibers using Equation 2-6, where V_{fd} is the shear contribution of the fiber, f_{vd} is the design tensile yield strength of UHPC, β_u is the angle of the diagonal crack (45°), $b_w$is the width of the member, z is the effective depth divided by 1.15, and γ_b is a factor with a value of 1.3.

$$V_{fd} = (\frac{f_{vd}}{tan\beta_u})b_w\frac{z}{\gamma_b} \quad \text{Equation 2-6}$$

The NF P18-710 (2016) estimates fiber contribution using Equation 2-7 where V_{Rdf} is the shear fiber contribution, b_w is the effective width, z is the lever arm of internal forces computed by multiplying the effective depth by 0.9, σ_{Rdf} is the average post-cracking strength up to a crack opening of 0.011 in. and θ is the shear angle of inclination.

$$V_{Rdf} = b_w z\sigma_{Rdf}cot\theta \quad \text{Equation 2-7}$$

The Australian Design Guidelines for Ductal Prestressed Concrete Beams (Gowripalan and Gilbert, 2000) developed design requirements specifically for the Ductal UHPC mix. Due to the limited amount of research, shear strength is limited to a principal tensile stress of $0.5 + 0.13\sqrt{f_c}$.

The FHWA (Graybeal and Rafic 2019) estimated shear strength using Equation 2-8, where V_{UHPC} is the shear resistance offered by UHPC, γ_f is a reduction factor accounting for fiber orientation, d_v is the lever arm between tensile and compressive forces, θ is the angle of shear cracking and $f_{cr}$is the is the tensile cracking strength of UHPC. The tensile cracking strength is defined as the stress intercept of a line with slope equal to the elastic modulus with an offset of 0.02%.

$$V_{UHPC} = \gamma_f b_w d_v f_{cr} cot\theta \quad \text{Equation 2-8}$$

Zheng et al. (2019) performed an experimental study to investigate the shear behavior of prestressed I-girders made of UHPC. In this study the experimental results were compared to the predictions computed using the JSCE (2008), NF P18-710 (2016) and the Swiss Society of

Engineers and Architects (SIA) code. The study reported that all code provisions resulted in an underestimation of the shear resistance. The JSCE (2008) was found to be the closest predictor of the shear strength.

2.6 UHPC Finite Element Model

The superior mechanical properties of UHPC have resulted in the interest of several researchers to search for possible structural applications. Conducting experimental studies of potential applications is costly. A combination of finite element analysis (FEA) simulations with the results of experimental work provide an attractive and cost-effective alternative to investigate the performance of UHPC.

FEA software packages offer material models capable of simulating the behavior of conventional concrete; however, the development of material models capable of representing the behavior of UHPC is limited. Hence, several researchers have proposed modifications to existing material models to approximate the behavior of UHPC. The most common material models include the concrete damaged plasticity model from ABAQUS, the concrete damage model from LS-DYNA, and the total strain-based crack model in DIANA.

Previous studies have been able to approximate the behavior of UHPC using the aforementioned material models. For instance, Graybeal (2010) showed that the concrete damaged plasticity model is capable of approximating the structural performance of I-girders and Pi-girders made of UHPC by adjusting the tension stiffening definitions within the material model.

Similarly, Bahij et al. (2018) and Zagon and Zoltan (2016) developed finite element models to investigate the shear behavior of UHPC beams. The studies were able to develop models capable of matching the crack propagation and failure type observed in experimental tests.

In addition, Liu et al. (2017) evaluated the impact response of UHPC under projectile penetration. The study showed that manually calibrating parameters of the concrete damage model in LS-DYNA can well characterize the compression and flexural behavior of UHPC. The material model calibration approach used by Liu et al. (2017) consisted of using flexural test results along with a FEM of the flexural test to calibrate the material model by trying to match the experimental results as shown in Figure 2-17.

(a)

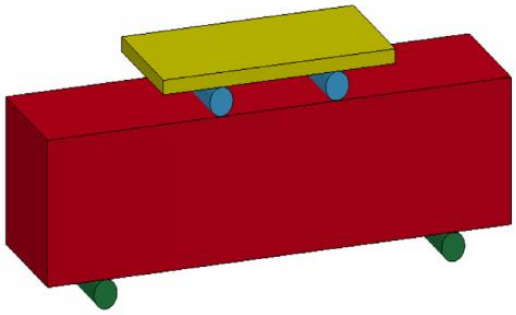

(b)

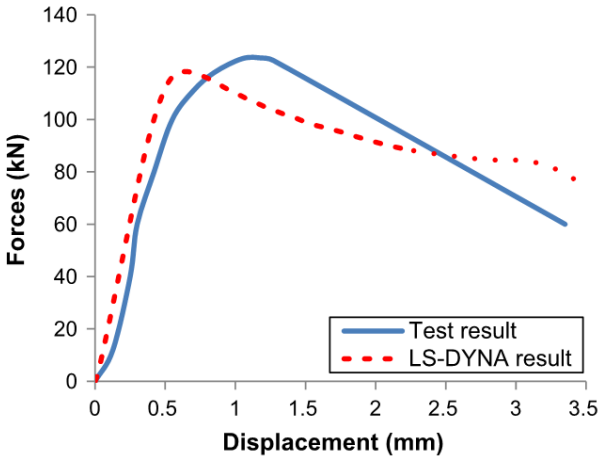

(c)

Figure 2-17 Concrete damage model material calibration (Liu et al., 2017): (a) ASTM C1609 experimental test, (b) FEM of ASTM C1609, and (c) Comparison of FEM and experimental results

One of the material models further discussed in this study is the LS-DYNA Concrete Damage Model MAT_CONCRETE_DAMAGE_REL3. The concrete damage model developed by Karagozian & Case (K&C) is a three-invariant model with three shear failure surfaces that includes damage and strain-rate effects (LSTC, 2016). The failure surfaces and compression meridians in this model were defined based on available data of unconfined compression tests and triaxial compression tests with different levels of confinement (Malvar et al., 1997). The variables used to define the failure surfaces are automatically generated based on the specified unconfined compressive strength.

However, for materials with different behavior such as UHPC, the automatically generated parameters may not adequately characterize the desired behavior. Nevertheless, with the growth of interest in UHPC finite element modeling, the developers of the concrete damage model released an update to model UHPC based on experimental data from compression and tension tests of UHPC specimens (Crawford et al., 2016). Release III includes parameters that allow the model to distinguish between compression and tension damage, and to approximate residual tensile strength. With the improvements of release III of the material model, Crawford

et al. (2016) performed a study of multi severe loading with blast or projectile penetration to demonstrate the difference in features between the UHPC enhanced properties and those of normal strength concretes.

The release III of the concrete damage model was found to accurately predict the ultimate strength, stiffness, hardening and softening behavior of UHPC under flexural loading (Yin, et al., 2019). In this study, the authors performed three-point flexural tests in accordance to EN 12390 to calibrate the material model. The authors used a similar approach to Liu et al. (2017), where the material model was calibrated using a flexural test. However, the calibration approach performed by Yin, et al. (2019) covered additional modeling parameters such as single-element behavior, mesh size, loading rate and strain rate effects. Once those parameters were understood, the authors started manually calibrating the material model to match their experimental results. The authors found that the parameters having more influence were the concrete softening parameter, the localized width parameter and the concrete tensile strength as shown in Figure 2-18.

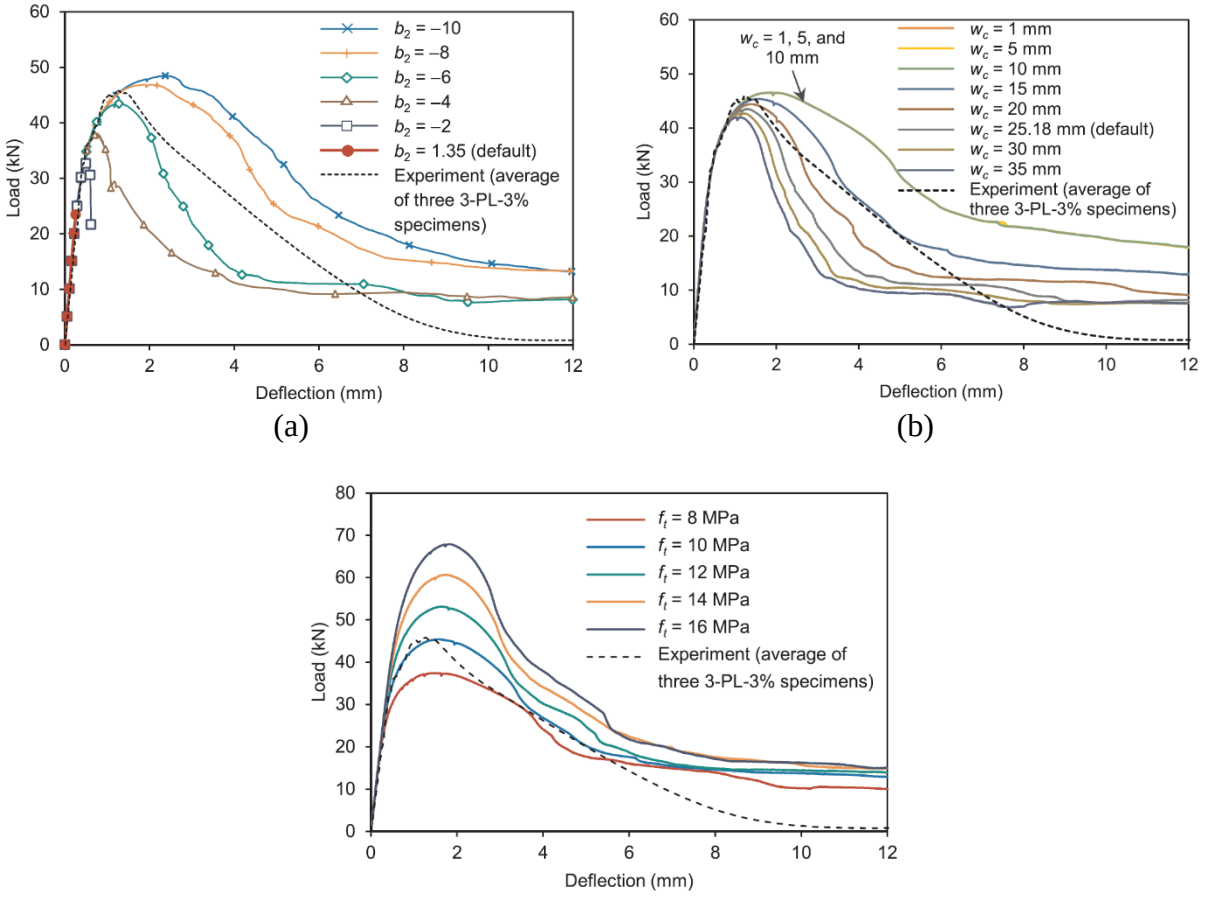

Figure 2-18 Calibration of concrete damage model using flexural test results: (a) softening parameter, (b) localized crack width parameter and (c) tensile strength of concrete (Yin et al., 2019)

3 FIB 72 Mockups

3.1 Specimen Design

Five FIB 72 girder mockups having either UHPC/SCC or only UHPC were designed to evaluate the behavior of UHPC (Figure 3-1). These specimens were devised with varying end region detailing schemes, while including the maximum number of prestressed strands allowed by the FIB strand pattern; this maximized the prestressing force to which the mockups would be subjected during prestress transfer. The variables considered in the detailing schemes included varying the quantities of bundled bars 5Y, 5K and 5Z, confinement reinforcement, and shear reinforcement (Table 3-1).

The control specimen G1 was detailed with the typical FIB end region reinforcement as recommended by FDOT Design Specifications. This specimen was constructed with both UHPC and SCC to provide a control for both classes of concrete. To test the effectiveness of UHPC in controlling bursting, spalling, and splitting stresses, vertical bar and confinement spacing was increased in mockups G2 through G5 (Figure 3-2), which significantly reduced the quantity of bar reinforcement available for end region crack control.

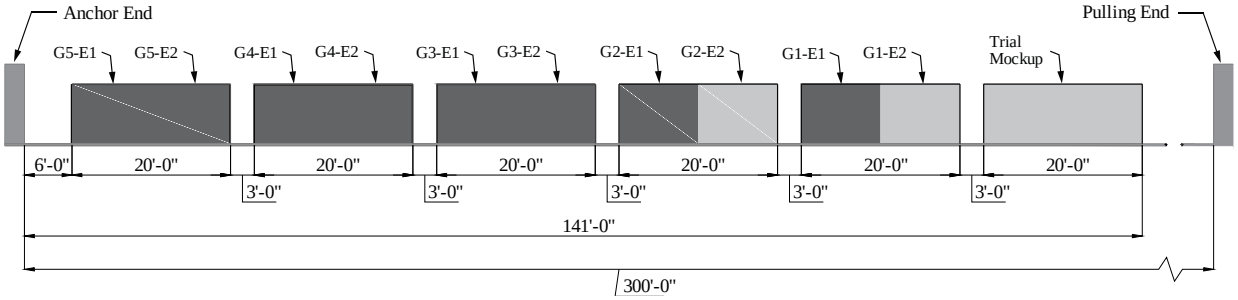

Figure 3-1 Layout of FIB 72 girders in prestress bed

Table 3-1 End-zone detailing

Girder No.	End	Bundle spacing (in.)	Confinement Spacing End region (in.)	Confinement Spacing Middle Region (in.)	Vertical Reinforcement End region (in.)	Vertical Reinforcement Middle Region (in.)
1	1	3.5	3.5	6.0	3.5	3.0
	2	3.5	3.5		3.5	
2	1	7.0	7.0	9.0	7.0	9.0
	2	7.0	7.0		7.0	
3	1	-	7.0	9.0	7.0	9.0
	2	-	14.0	18.0	7.0	
4	1	-	-	-	7.0	9.0
	2	9.0	9.0	9.0	9.0	
5	1	-	9.0	9.0	9.0	9.0
	2	-	-	-	9.0	

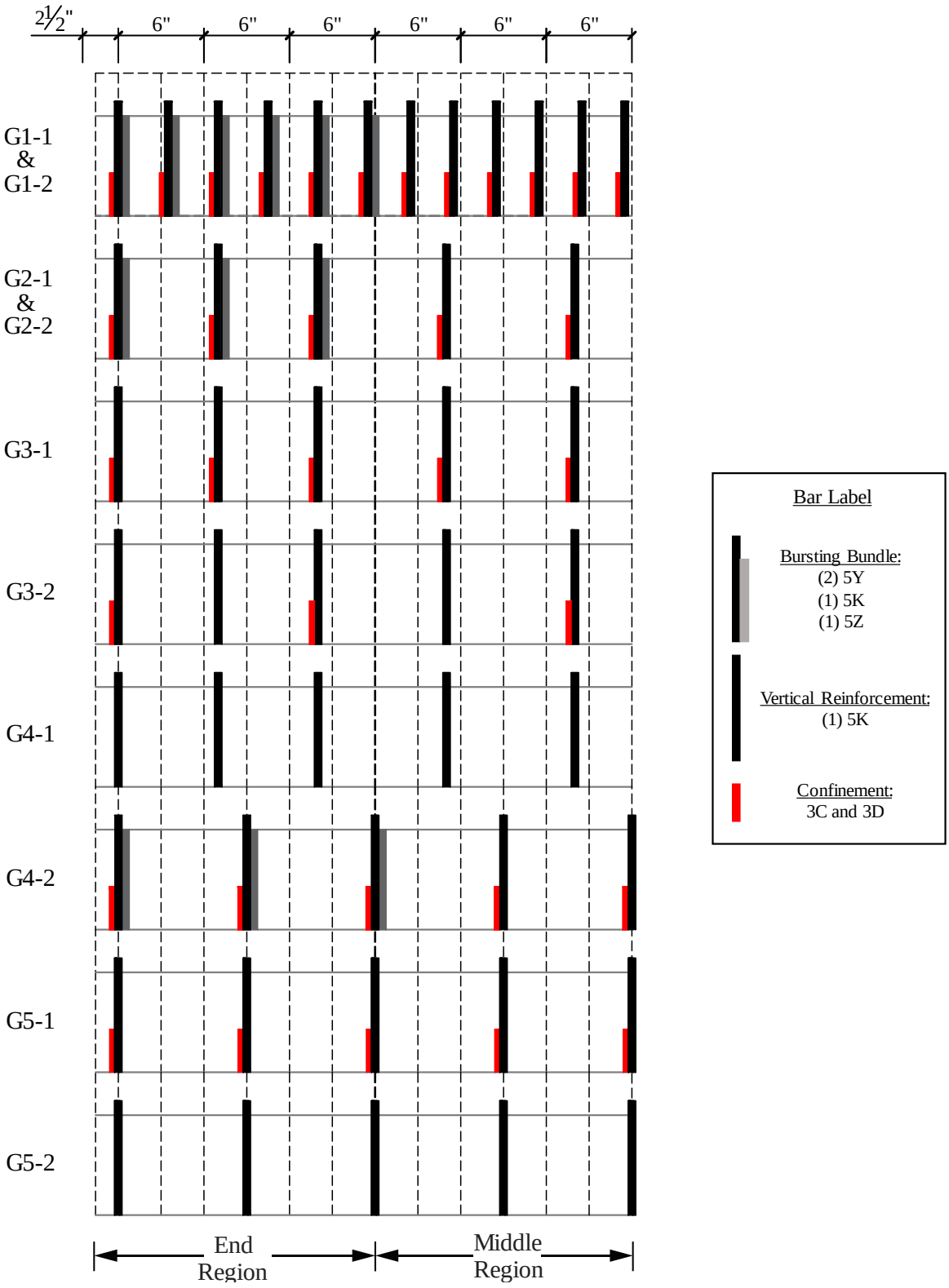

Figure 3-2 Sketch of end region detailing

The number of the strands was selected to maximize the prestress force that was applied to the mockups. The current FIB strand pattern allows the use of a maximum of 70 0.6-in. diameter seven-wire prestressing strands in the bottom flange, which results in a total prestress force at transfer of 3,066 kip.

During mockup design, it was found that for G1 and G2 the limiting factor to use all 70 strands was the SCC allowable compressive stresses. The concrete compressive stresses, immediately after release, exceed the limits specified by AASHTO LRFD Bridge Design Specifications (2017) and FDOT (2018) for SCC with a compressive strength (at release) of 6,000 psi (Figure 3-3.).

FDOT (2018) references AASHTO LRFD 5.9.2.3.1a (2017), which specifies that compressive stresses before losses should not exceed 65% of the concrete compressive strength. Including all 70 strands was desired to have a direct comparison between UHPC and SCC. Rather than debonding strands in the SCC mockups, to comply with the limits, prestress transfer was delayed until the mockups with SCC developed a compressive strength of 7,500 psi

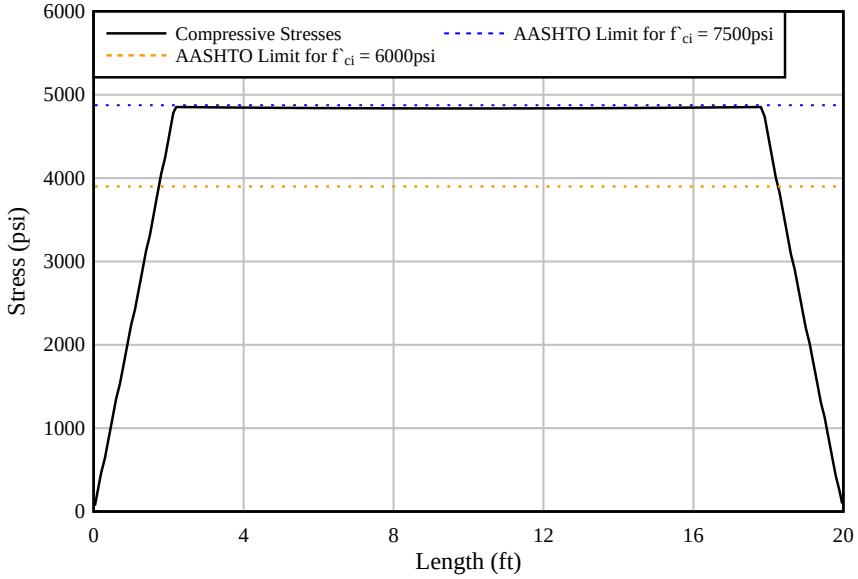

Figure 3-3 Compressive stresses for G1 and G2 having SCC and UHPC

Figure 3-4 and Table 3-2 indicate the parameters that were used for the design of reinforcement to control cracking caused by end region stresses in the mockup specimens. AASHTO LRFD requirements indicate that the end region should be designed using 4% of the total bonded prestress force (no losses) for a length of H/4 from the end. The provisions further specify that the stress in the reinforcement should not exceed 20 ksi to control crack widths. For example, the design stress for a commonly used reinforcing bar such as ASTM A615 Gr60, the design stress is limited to $0.33f_y = 0.33(60 \text{ ksi}) \sim 20 \text{ ksi}$.

For this study, the researchers used AASHTO LRFD recommendations to design the mockups with SCC in G1 and G2. G1 had typical FDOT reinforcement detailing. For the SCC end of the G1 (G1-E2), the calculated stress in the bursting reinforcement was 19.8 ksi. In G2, which had a reduced area of bursting reinforcement, the calculated stress was 33.1 ksi.

It has been shown in previous testing (Alireza and Rafic, 2020) that the UHPC fibers will contribute significantly to crack control in structural elements subjected to tension in general and

to bursting stresses in particular. To calculate this contribution, direct tension test results of tests conducted on other similar UHPC material were used.

Average measured tensile strength in these DTT was approximately 1,200 psi; initial cracking occurred at approximately 800 psi. Contribution of the UHPC was limited to a working stress required to cause cracking to provide a working stress approach similar to that used for the steel bars. UHPC was assumed to contribute an average stress of 800 psi over the thickness of the web (7 in.) times H/4. Thus, UHPC is assumed to resist a force of 100 kip.

The relative contribution of the bars and fibers in resisting bursting stresses is unknown. It is expected, however, that as cracking occurs, the steel reinforcement and UHPC will share the bursting stresses in some proportion. To gage the contribution of the bars, they were assumed to contribute to resisting the remainder of the bursting force beyond that resisted by the UHPC (23 kip). These stresses are presented in Table 3-2. Bar contributions vary among mockups because of the varying quantities of bar reinforcement used in the mockups.

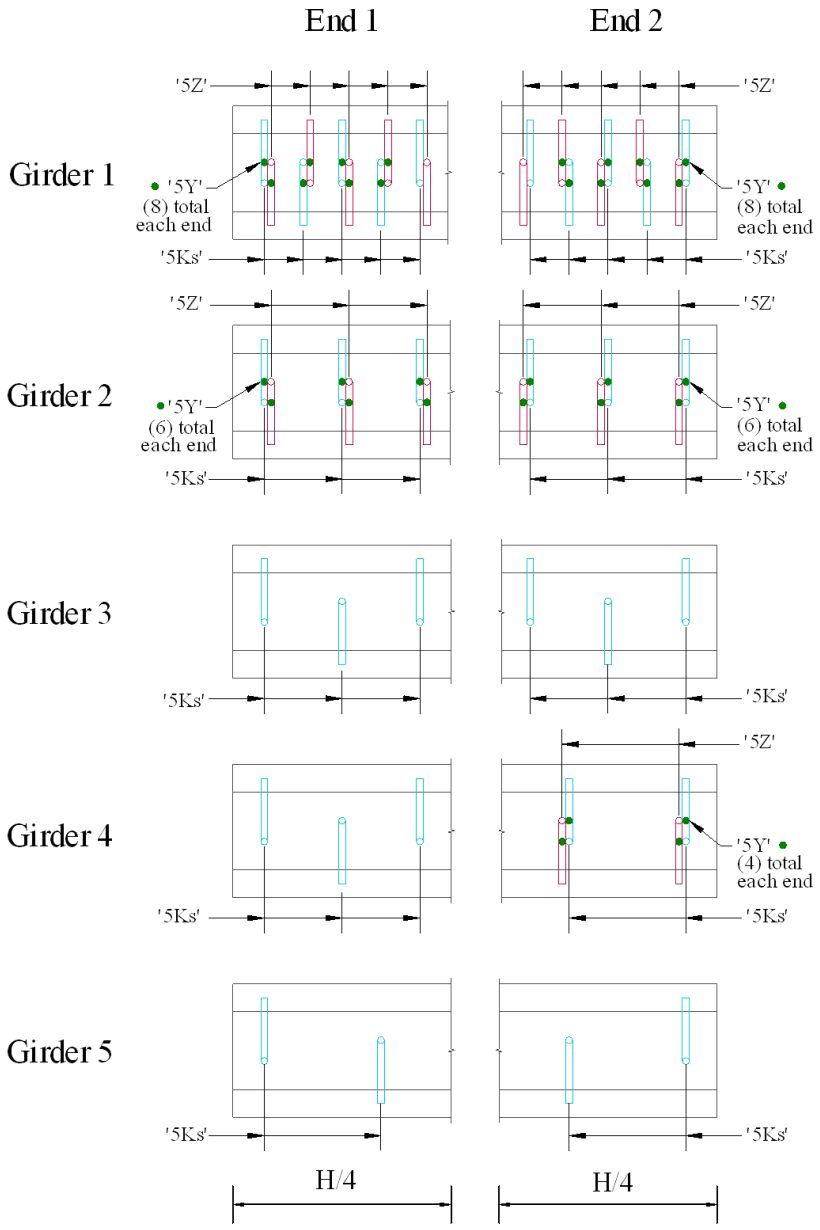

Figure 3-4 Top view of reinforcement steel along H/4 for each mockup

Table 3-2 Bursting stresses design parameters

Girder End	Concrete Type	Total A_s (in^2)	$0.04P_u$ (kip)	UHPC Resistance (kip)	Steel Stress* [f_s] (ksi)
G 1-1	UHPC	6.2	123	100	4
G 1-2	SCC	6.2		NA	20
G 2-1	UHPC	3.72		100	7
G 2-2	SCC	3.72		NA	33
G 3-1	UHPC	0.93		100	25
G 3-2	UHPC	0.93		100	25
G 4-1	UHPC	0.93		100	25
G 4-2	UHPC	2.48		100	10
G 5-1	UHPC	0.62		100	37
G 5-2	UHPC	0.62		100	37

*UHPC is assumed to carry 800 psi working stress for H/4 from end of web. Reinforcing bars are assumed the carry the remaining bursting stress.

3.2 Specimen Construction

Five FIB 72 20-ft-long mockups were constructed between October 10th, 2019 and October 18th, 2019 at Standard Concrete Products in Tampa. The construction events are listed in Table 3-3.

Table 3-3 Construction schedule of FIB 72 mockups

Construction Events	Days						
	1	2	3	4	5	6	7
Install strands	X	X					
Pull Strands		X					
Tie reinforcement		X	X				
Pour SCC			X				
Interface Surface Preparation			X				
Pour UHPC					X		
Strip steel forms						X	
Install Instrumentation						X	X
Detensioning							X

Construction began by marking the precast bed to denote the ends of each mockup and the SCC and UHPC locations for G1 and G2.

Once the mockup locations were marked, the base of the steel bulkheads was placed at the ends of the SCC locations of G1 and G2 and at the ends of each mockup for G3, G4 and G5. The SCC sections were cast before the UHPC sections.

The next step was to place the prestressing strands. Once placed, the strands in the top flange were tensioned first followed by the strands in the bottom flange. The bottom strands were tensioned starting with bottom layer and working up to the topmost strand layer. After strand tensioning, mild reinforcement was installed in the SCC section of G1 and G2, and for the entire length of G3, G4 and G5 (see Figure 3-5 through Figure 3-9).

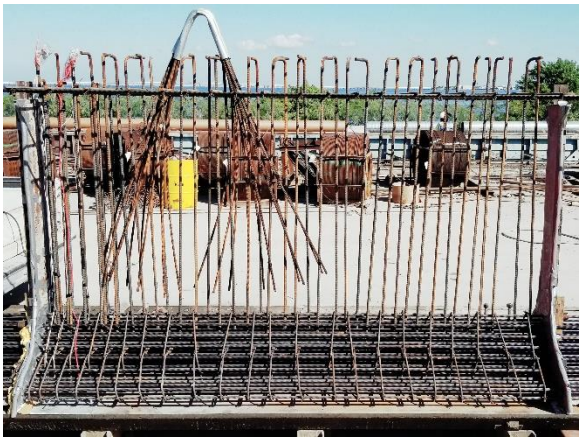

Figure 3-5 Mild-steel reinforcement in SCC portion of G1

Figure 3-6 Mild-steel reinforcement in SCC portion of G2

Figure 3-7 Mild-steel reinforcement in G3

Figure 3-8 Mild-steel reinforcement in G4

Figure 3-9 Mild-steel reinforcement in G5

Prior to attaching the steel forms, the bulkheads at the UHPC-SCC interface in G1 and G2 were covered with a retarder admixture (Master Finish HV) to prevent the surface SCC paste from hardening at that location (Figure 3-10). Water blasting of the SCC surface, created a uniform roughened surface against which the UHPC was cast. The retarder was applied using a

paint brush on top of duct tape that was previously taped to the bulkhead surface. Steel forms were squared and set in place using cross-ties.

G1-E2 and G2-E2 were cast with SCC using FDOT Class VI concrete (f'c =8,500psi), which is typical for precast girder production in Florida. The SCC sections were allowed to cure for one day before stripping the forms. Then, the bulkheads were shifted to the mockup end to allow the installation of the remaining reinforcement in the UHPC sections (Figure 3-11 and Figure 3-12).

Figure 3-10 Application of concrete retarder admixture to bulkhead

Figure 3-11 G1 before UHPC pour

Figure 3-12 G2 before UHPC pour

The remaining UHPC sections of G1 and G2, in addition to the entire length of G3, G4 and G5 were then cast.

The UHPC mixing procedure consisted of filling the mixer with all the cementitious materials, sand, water, and admixtures (Figure 3-13a). The ingredients were then mixed for approximately seven minutes; a sample was then extracted from the mixer to perform a cone flow test. If the mortar spread was found to be between 8 in. and 10 in., then steel fibers were added (Figure 3-13b).

The steel fibers were manually added through a mesh in a plywood board attached to a mechanical vibrator that facilitated fiber dispersion, which worked well to prevent the formation of fiber clumps (Figure 3-14). The time to complete the mixing process varied from 20 to 25 minutes.

UHPC was mixed in loads of 3.2 cubic yards, which was enough volume to fill one-half of a single mockup and collect sufficient materials testing samples.

Single loads were batched and delivered to G1 and G2, respectively. For G3, G4, and G5, however, two loads were batched sequentially and discharged to the buggy, which stayed by the batch plant waiting for both batches to be prepared. Once the Tuckerbilt had a load of 6 cubic yards of UHPC, it was directed to the precast bed to pour an entire mockup (Figure 3-15).

After the pour was finished, the precaster used a hand roller to prevent the UHPC from forming a continuous “elephant skin.” This action resulted in a rougher surface that would be beneficial for future bond with the concrete deck (Figure 3-16).

Figure 3-17 shows G1 completed after stripping the forms. Finally, all mockups were allowed to cure for two days before prestress transfer (Figure 3-18).

(a) (b)

Figure 3-13 UHPC mixing: (a) Mixing mortar and (b) mortar spread test

Figure 3-14 Steel fibers added to UHPC through a steel wire mesh

Figure 3-15 UHPC pour using Tuckerbilt buggy

Figure 3-16 UHPC surface finishing

Figure 3-17 G1 completed

Figure 3-18 Construction crew in position for detensioning

Detensioning sequence is shown in Figure 3-19. The strands were individually flame cut starting in the top layer and continuing downward to the bottom of the tendon. Each strand was simultaneously cut between each mockup and between the end mockups and abutment.

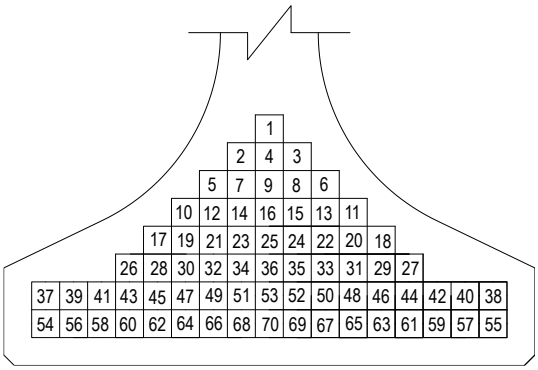

Figure 3-19 Detensioning sequence

Detensioning of the last layer of strands was interrupted by a sudden rupture of the remaining thirteen strands (Figure 3-20 and Figure 3-21), which resulted in an abrupt shift of four mockups in the precast bed. The displaced mockups included G1, G2, G3 and an additional SCC specimen, which was not part of this research (Figure 3-22). No outward damage was noted visually upon inspection. Unfortunately, however, instrumentation was damaged, which terminated the data logging.

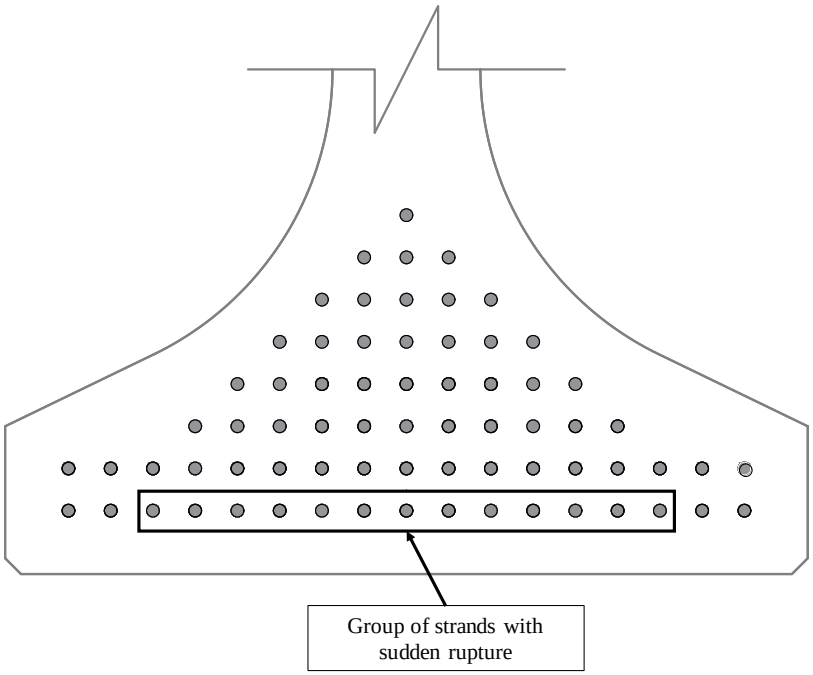

Figure 3-20 FIB strand pattern showing ruptured strands

Figure 3-21 Photo of prestressing strands after strand rupture

Figure 3-22 Specimens displaced during detensioning

3.3 Material Testing

3.3.1 Fresh Properties

Fresh properties of SCC were tested to verify that the batches complied with the FDOT requirements listed on Table 2. A single SCC batch was produced to fill each SCC halve in G1 and G2. Testing of the UHPC mixes was performed following the recommendations of ASTM C1856—Standard Practice for Fabricating and Testing Specimens of Ultra-High Performance Concrete, along with practices used by the precaster such as measuring the diameter of the cone flow with and without steel fibers (Figure 3-23). Samples of SCC and UHPC were collected at the batch plant and tested in the quality control station before the concrete truck directed towards the precast bed. A summary of the fresh properties results of all five UHPC batches are given in Table 3. Note than in the case of G3-G5, the results are of samples collected after two UHPC batches loaded inside the Tuckerbilt truck.

The method used to evaluate the fresh properties of UHPC consisted of measuring the flow-cone spread diameter of the mortar only. If the spread diameter was between 8 in. and 10 in., fibers were added to the mortar. The values shown in Table 3 indicate a small increase in spread diameter with the addition of the fibers.

(a)

(b)

(c)

Figure 3-23 UHPC fresh properties testing: (a) flow cone test, (b) spread test without fibers, and (c) spread test with fibers

Table 3-4 FDOT fresh properties requirements for SCC

Test Method	FDOT Requirements	Results
ASTM C1611- Slump Flow	27 ±2.5 in.	24.5 inches
ASTM C1611- T-50	2-7 seconds	3.8 seconds
ASTM C231- Air Content	0%-6%	2.4%
ASTM C138- Unit Weight	-	139.9 lbs./ft^3
Temperature	-	82°F

Table 3-5 UHPC fresh properties

Mockup Name	Flow cone spread (in.)		Temperature (°F)
	Without Fibers	With Fibers	
G1	9.75	10.50	89
G2	8.75	10.00	90
G3	9.00	9.25	91
G4	9.75	9.25	93
G5	9.25	9.37	93

3.3.2 Compressive Strength

Compressive strength cylinders (4 in. × 8 in.) were prepared from a sample collected immediately after mixing; cylinders were cured using two methods. One method was to store the cylinders at ambient temperature along the girder bed. The other method used match-curing, which employs a thermocouple to measure the temperature inside the mockup below the top strand layer in the bottom flange and controls the temperature of the cylinder sample to match that of the mockup (Figure 3-24).

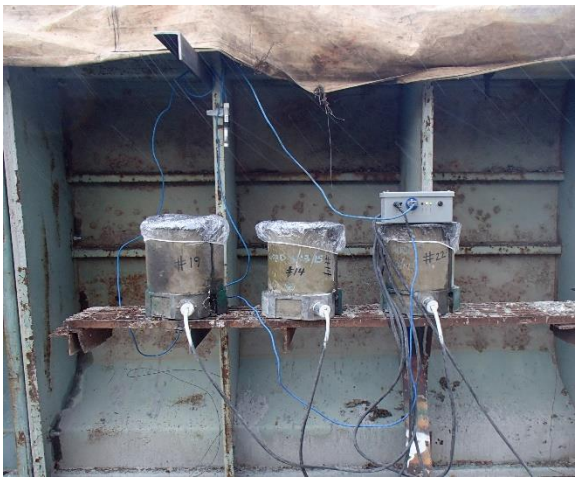

Figure 3-24 Match-cure system used for mockup cylinder samples

Compressive strength tests were performed at the precaster quality control lab following the guidelines given by ASTM C39— Standard Test Method for Compressive Strength of Cylindrical Concrete Specimens. SCC cylinders were loaded in compression with neoprene pads on the top and bottom surfaces to provide uniform load transfer.

UHPC cylinders were transported to the FDOT District 1 office to grind the top and bottom surface to obtain uniform surfaces for load transfer before testing in compression at the precaster quality control lab. Both SCC and UHPC tests were performed at the age of detensioning and 28 days. Table 3-6 and Table 3-7 list the compressive strength results of SCC and UHPC respectively. Recall that in the mockup design section, it was specified for both concretes to obtain a compressive strength above 7,500 psi at age of detensioning to withstand the compressive stresses induced by the prestress force, both the SCC and UHPC satisfied this requirement.

UHPC compressive strength results presented in Table 3-7 showed that the 48-hr match-cured compressive strength was slightly higher than the 28-day bed cured (ambient temperature) strength. In addition, G1 through G4 exhibited approximately 30% higher 48-hr compressive strength values using match-cured system than the bed cured specimens at 28 days. This behavior has been noted by other researchers (Ishi et al. 2008, and Ahlborn et al, 2008) where the effect of temperature and moisture on the strength development of UHPC can be significant. For instance, Ishi et al. (2008) showed a decrease of 32% when curing temperature was decreased from 90°C to 70°C.

Table 3-6 Compressive strength results of SCC

Age of Specimens	Compressive Strength (psi)
Detensioning	9,080
28 days	10,760

Table 3-7 Compressive strength results

Batch Number	Compressive strength (psi)		
	Detensioning (48 hr.)		28 days
	Match-cured	Bed-cured	Bed-cured
G1-E1	23,920	18,030	22,910
G2-E1	23,980	17,690	22,810
G3	25,030	18,100	23,190
G4	24,800	19,410	22,100
G5	22,200	19,790	23,690

3.3.3 Tensile Strength

Direct tension test and flexure beam test were used to determine the tensile strength of UHPC. Background and details of these test methods were covered in the Literature Review section 2.4.2. UHPC collected from the Tuckerbilt once mixing was complete. The beam molds were filled with UHPC using the funnel shown in Figure 3-25. Six (2 in. × 2 in. × 17 in.) beams were prepared from each batch to conduct DTTs at age of detensioning and 28 days. Similarly, six (4 in. × 4 in. × 14 in.) beams were prepared for FB tests.

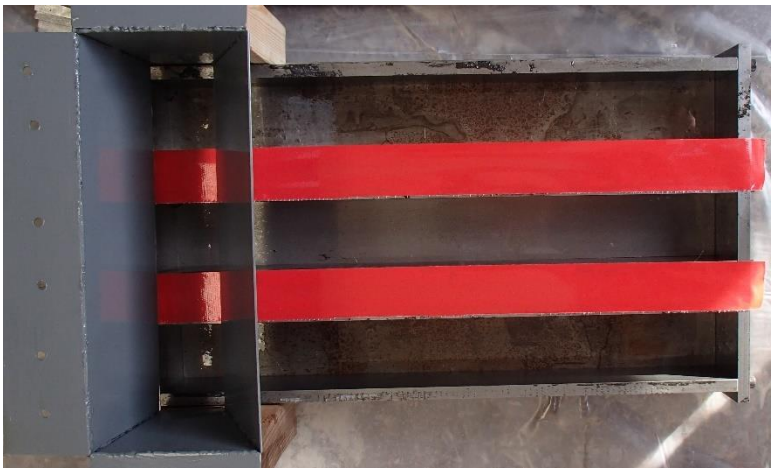

Figure 3-25 DTT and FB sample preparation

DTT was performed at the University of Florida Materials Testing Laboratory using a closed-loop hydraulic system used for tensile testing along with a gripping mechanism capable of gripping the specimen without inducing bending strains exceeding 10% of the axial strains.

FB tests were performed at the University of Florida Materials Testing Laboratory following the guidelines of ASTM C1609— Standard Test Method for Flexural Performance of Fiber-Reinforced Concrete (Using Beam with Third-Point Loading).

The results of both the DTT and the FB tests for age of detensioning and 28 days are shown in Figure 3-26 and Figure 3-27. Three DTT and FB specimens were tested at age of detensioning and 28 days. In addition, Table 3-8 summarizes strength values of the specimens at age of detensioning. Due to the number of specimens and the short time window to obtain results representative of age at detensioning, some of the DTT were terminated at lower strain levels. For this research, the residual stress values in the multi-cracking region are of interest to the end region cracking behavior of UHPC.

According to Graybeal and Baby (2014), the cracking strength of UHPC can be estimated from DTT results in one of two ways. The first method determines the stress at the first slope discontinuity from the elastic response. This method, however, can underestimate the cracking strength due to the bending induced during gripping.

The second method consists of averaging the stress in the multi-cracking phase. This method, however, requires some qualitative assessment in the process used to identify the multi-cracking region. Graybeal and Baby (2014) proposed the average stress during multi-cracking as the most reliable estimate for the UHPC cracking strength.

For comparison, cracking strength was calculated from DTT results using both methods for G1 through G5 (Table 3-8). The results of cracking strength agree with the findings of Graybeal and Baby (2014), where the slope discontinuity method underestimates the cracking strength compared to the method that uses averaging of the multi-cracking phase.

The DTT results indicated that G3-G5 developed higher tensile strengths than G1 and G2. The same trend is observed in the FB results where G4 and G5 exhibited average maximum loads between 21,581 lbs. and 21,618 lbs., while G1 and G2 had a maximum load between 15,732 lbs. to 17,371 lbs. Based on the larger diameter spreads exhibited by G1 and G2, it is thought that these mixes had higher water content, which may have resulted in lower strengths.

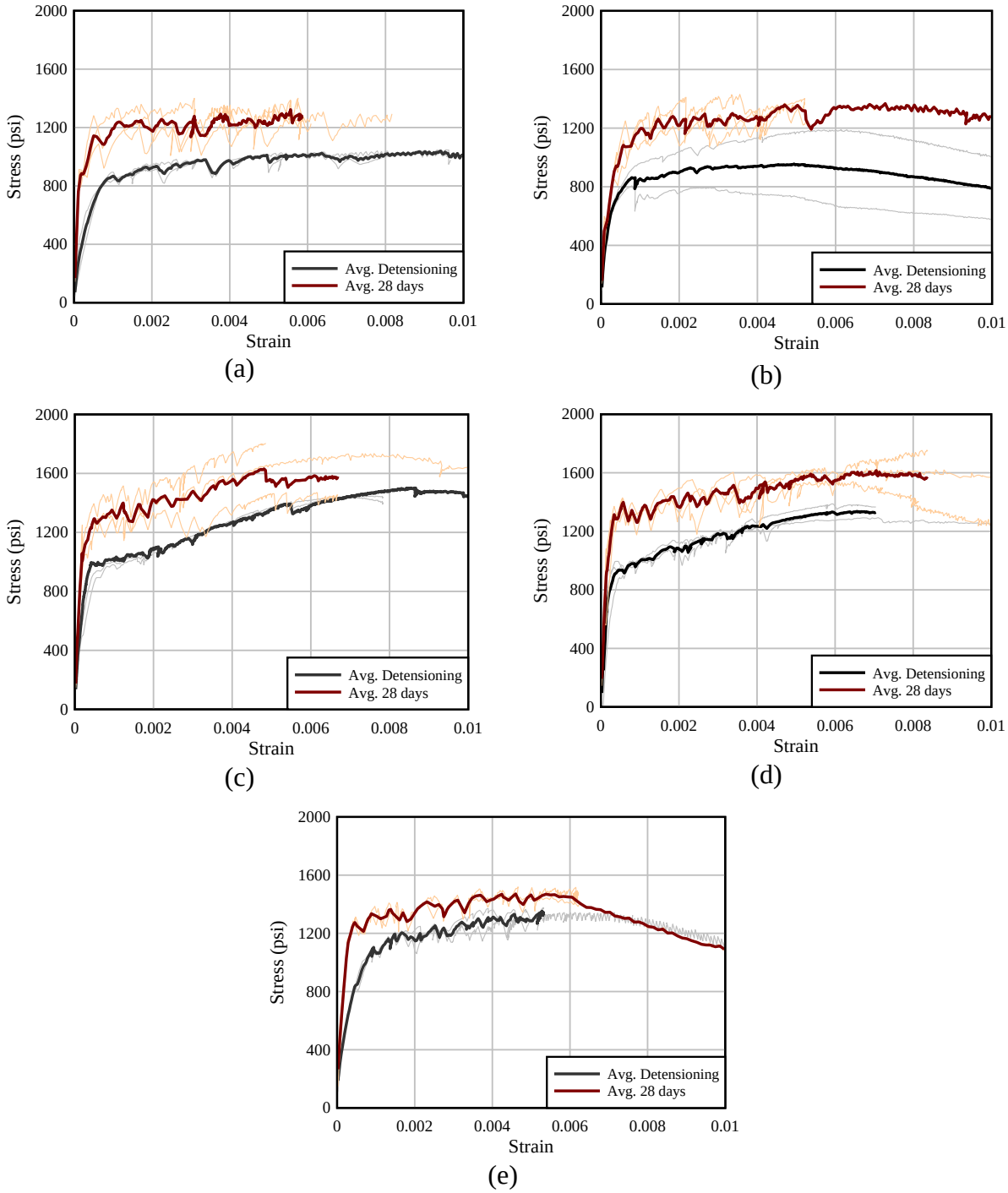

Figure 3-26 Results of the DTT for all batches: (a) G1, (b) G2, (c) G3, (d) G4 and (e) G5

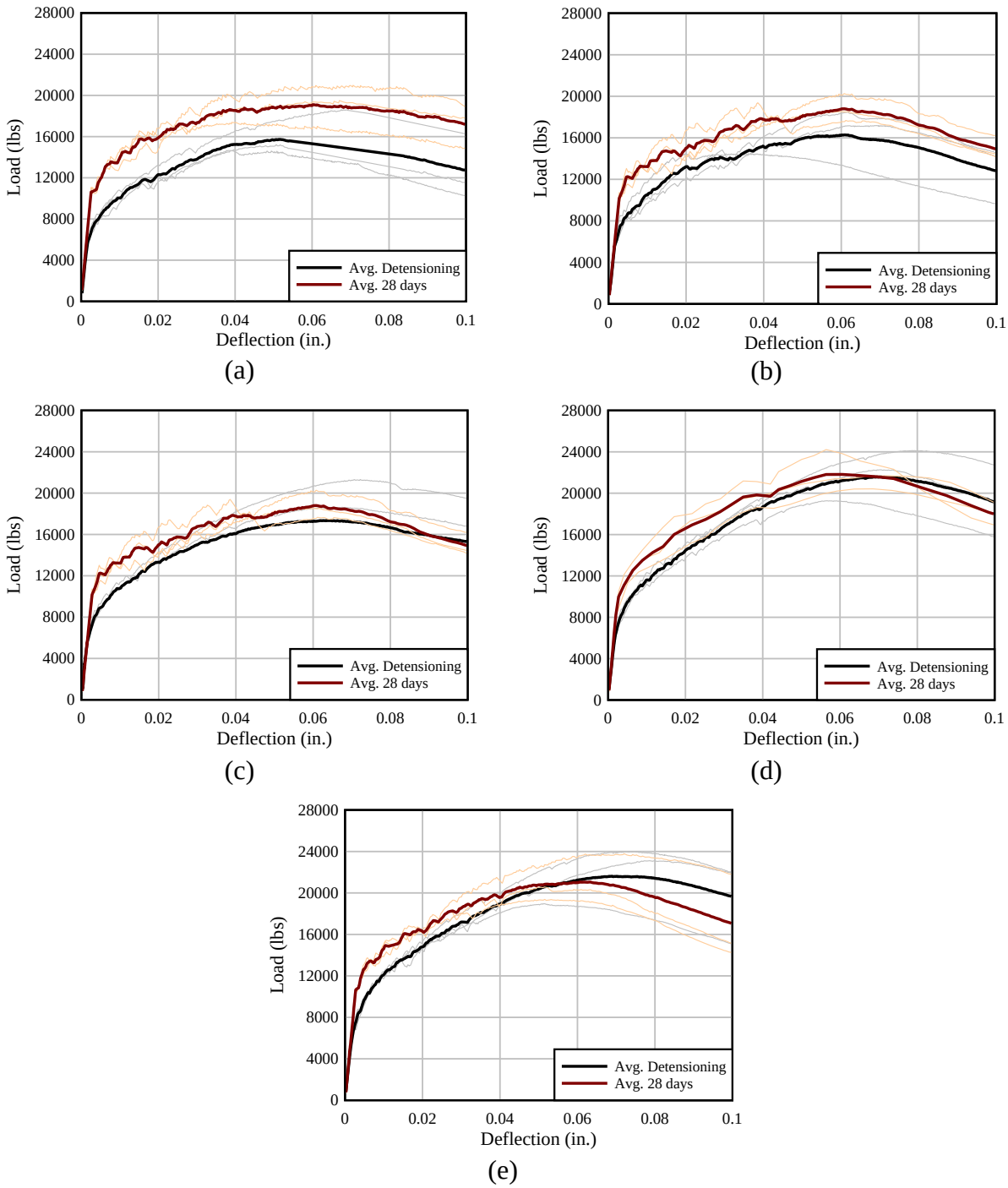

Figure 3-27 Results of the FB for all batches: (a) G1, (b) G2, (c) G3, (d) G4 and (e) G5

Table 3-8 Summary of average tensile testing results at age of detensioning

Batch Number	DTT Results			FB Results	
	Cracking Strength (psi)		Peak Strength (psi)	Cracking Load (lbs.)	Peak Load (lbs.)
	Method 1: Slope Discontinuity	Method 2: Multi-cracking average stress			
G1	220	928	1,079	5,626	15,730
G2	695	896	955	4,929	17,180
G3	752	1,106	1,501	5,903	17,370
G4	868	1,129	1,335	6,301	21,580
G5	963	1,205	1,350	7,140	21,620

3.4 Detensioning Results

Each mockup was instrumented to measure strains during prestress transfer. The instrumentation included vibrating wire gages, linear-strain gages, and fiber optic sensors (FOS), which were used to determine the transfer length and concrete strains in the end region.

3.4.1 Transfer Length

Transfer length was measured with fiber optic sensors bonded to the bottom flange concrete surface at eight mockup ends (Figure 3-28). Not all ends were instrumented due to limited number of FOS channels and FOS length. Measured strain was used to calculate transfer length using the 95% AMS method developed by Russell and Burns (1996).

Table 3-9 lists a summary of the measured transfer length values. Figure 3-29 shows the measured transfer length for each end, which resulted in transfer lengths ranging from 17.0 in. to 20.5 in. for UHPC and between 30.5 in. to 31.8 in. for SCC. Transfer length was calculated based on the strain measured up to the point of strand rupture when data-logging was interrupted due to the sudden rupture of strands during detensioning. See Section 3.2 for details regarding the incident during detensioning.

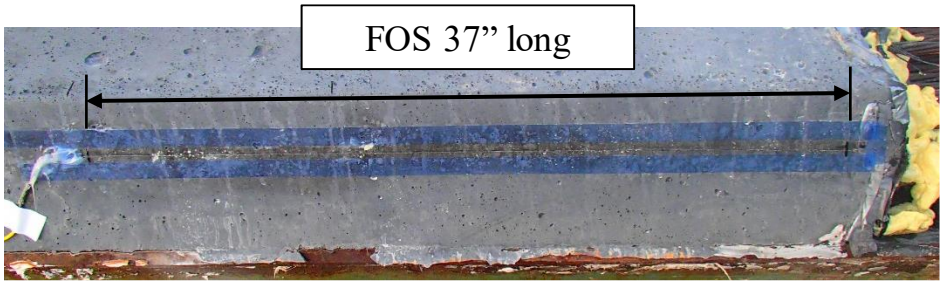

Figure 3-28 Installed FOS to measure transfer length

Figure 3-29a shows a comparison between UHPC and SCC ends in G1. Microstrain plateau on the UHPC end occurred at approximately 608 με; the SCC plateau occurred at 789 με. Figure 3-29b shows the measured strain in G2-E2 made of SCC. Microstrain in G2-E2 plateau occurred at 806 με, which was similar to the measured value in G1-E1, also fabricated using SCC. Figure 3-29c shows the transfer length of G3-E1 and G3-E2. Microstrain plateau measured in G3 was 634 με and 532 με for G3-E1 and G3-E2, respectively. Figure 3-29d shows

the transfer length of G4-E1 and G4-E2. Measured microstrain plateau at 595 με for G4-1 and 388 με for G4-2.

Strain in G4-E2 was lower than in G4-E1 by 207 με, which is surprising as both ends are made of UHPC and the data was extracted at the same prestress level. One reason for the lower measured strain could have been incomplete adhesion of the fiber-optic cable; this is based on the variation in measured strains over the cable length with some of the peaks close to 600 με, which is near the strain level observed in the other UHPC ends. Another explanation is a variation in modulus between the ends of the specimen, which in this case is unlikely as both ends were cast with the same UHPC batch.

Figure 3-29e shows the transfer length of G5-E2. Measured strain in G5-E2 plateaus at 449με, which was also below the 600 με observed in the previous UHPC ends except for G4-E2.

Table 3-9 Summary of measured transfer lengths

Mockup	End	Concrete	Transfer Length (in.)	AASHTO LRFD
G1	End1	UHPC	20.5	36 in.
	End2	SCC	31.8	
G2	End 1	UHPC	-	
	End 2	SCC	30.5	
G3	End 1	UHPC	20.25	
	End 2		19.75	
G4	End 1		20.5	
	End 2		17.0	
G5	End 1		-	
	End 2		18.3	

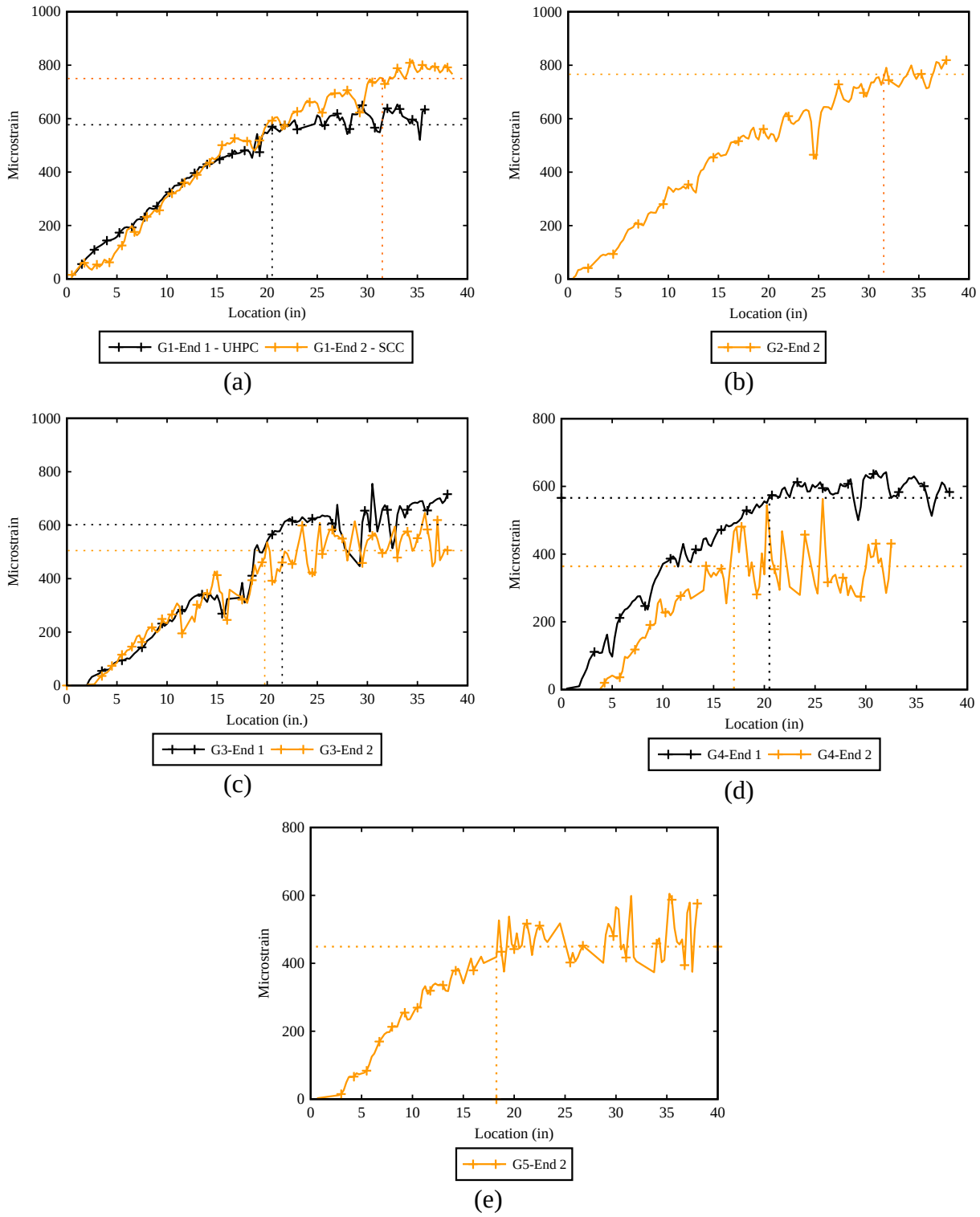

Figure 3-29 Measured transfer length using FOS: (a) G1, (b) G2, (c) G3, (d) G4 and (e) G5

3.4.2 Concrete Strain

Fiber optic sensors (FOS) were installed on the girder web to measure the vertical strain during detensioning (Figure 3-30). FOS were distributed in two vertical lines to measure the tensile strains created near the end of the girder (Line 1 and 2). Line 1 was installed between the end of the girder and the first bundle of vertical steel reinforcement. Line 2 was installed on the opposite side of the first bundle of steel reinforcement. In addition to measuring the strains during detensioning, the data showed the location of insipient web cracks. This enabled the researchers to use a microscope to find narrow cracks in the regions of high strain, that would have otherwise been invisible and likely not detected.

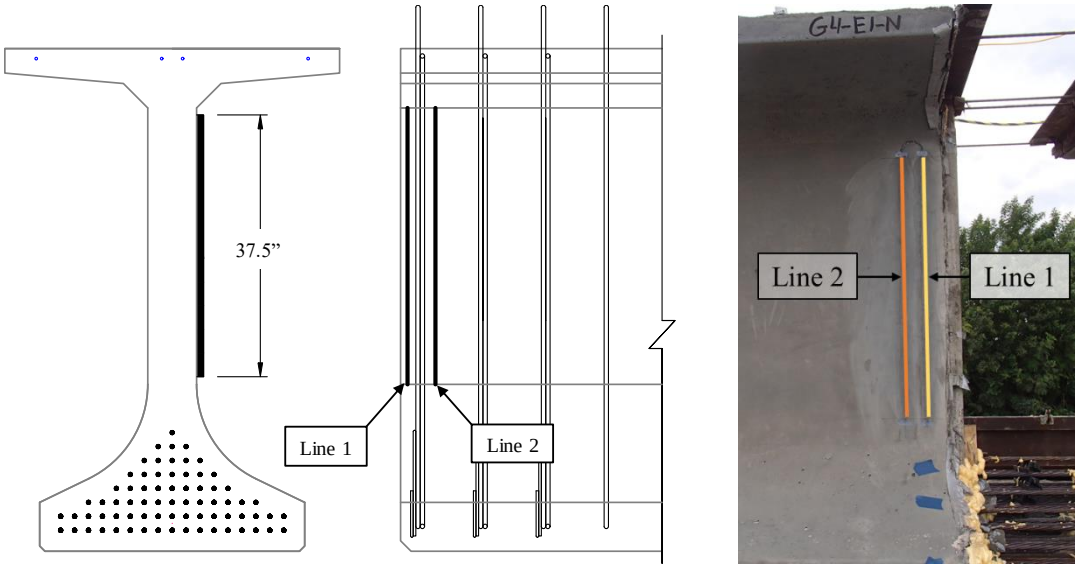

(a) (b)

Figure 3-30 Layout of FOS installed on girder web surface

Concrete strain was recorded with FOS until sudden unexpected rupture of the 13 strands occurred, thus abruptly terminating the detensioning and strain monitoring. Figure 3-31 through Figure 3-35 show the average strain of the last five seconds recorded with the FOS on each girder end before strand rupture. These figures show the strain measured against the girder height. In general, all UHPC end regions behaved similarly exhibiting peak strains at a height ranging from 25 in. to 35 in. above the bottom of the girder.

UHPC end regions, however, did not exhibit sharp increases in strain that can be associated with crack formation. In fact, the maximum level of strain (~150με) was well below the crack localization but near the initial cracking strength based on DTT observations. In addition, during inspection (spraying acetone on the concrete surface and with a crack microscope) after prestress transfer no cracks were found on the UHPC ends. Meanwhile, SCC ends exhibited sharp peaks in strain, which indicated incipient cracking. For instance, Figure 3-36 shows the FOS readings of G1-E2 having three peaks, which matches the cracks identified in that girder.

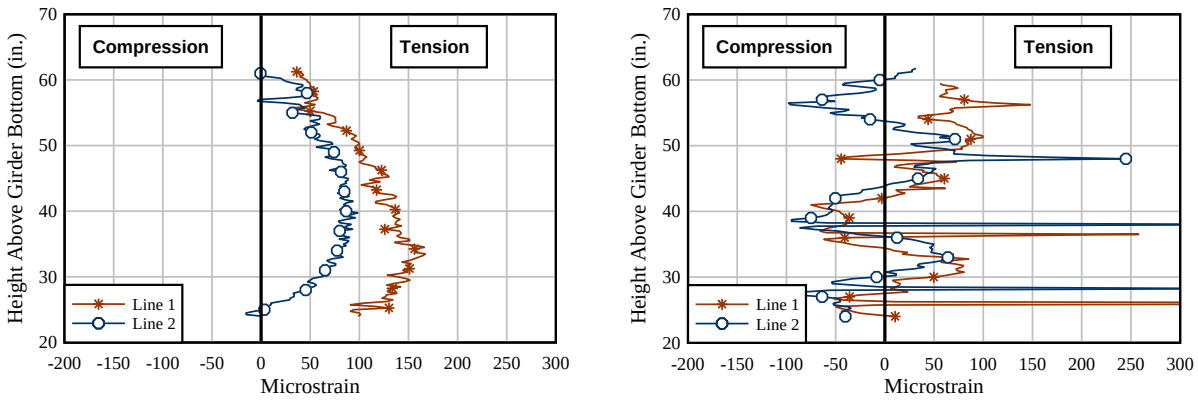

Figure 3-31 G1 concrete strain measured with FOS: (a) G1-E1 (UHPC) and (b) G1-E2 (SCC)

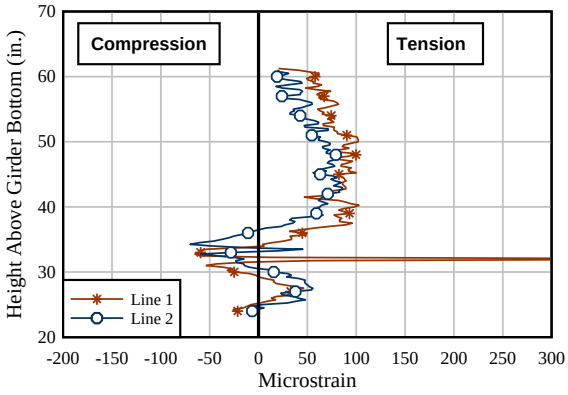

Figure 3-32 G2-E2 (SCC) concrete strain measured with FOS

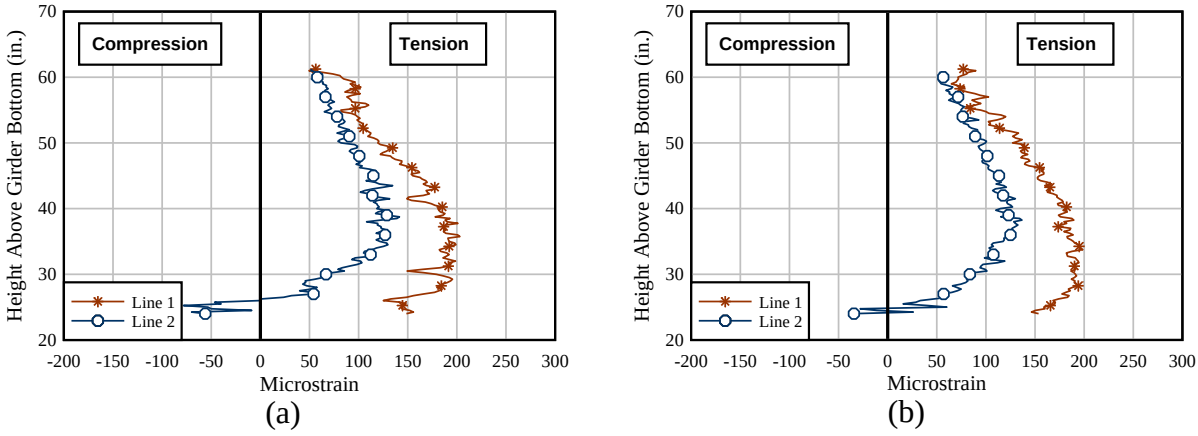

Figure 3-33 G3 concrete strain measured with FOS: (a) G3-E1 and (b) G3-E2

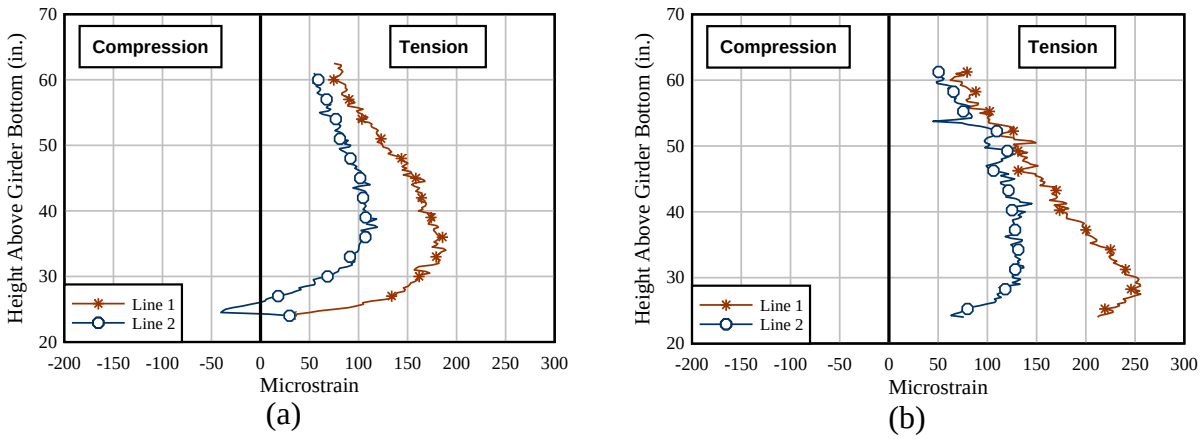

Figure 3-34 G4 concrete strain measured with FOS: (a) G4-E1 and (b) G4-E2

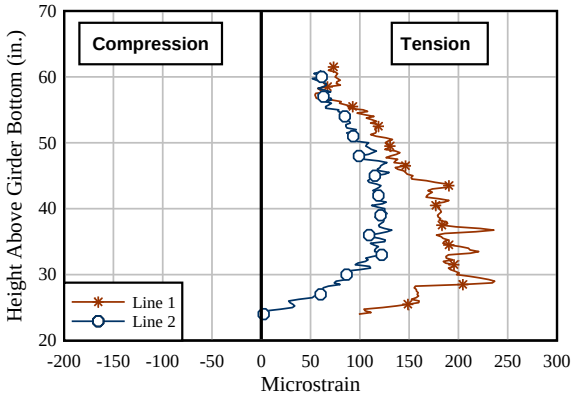

Figure 3-35 G5 concrete strain measured with FOS

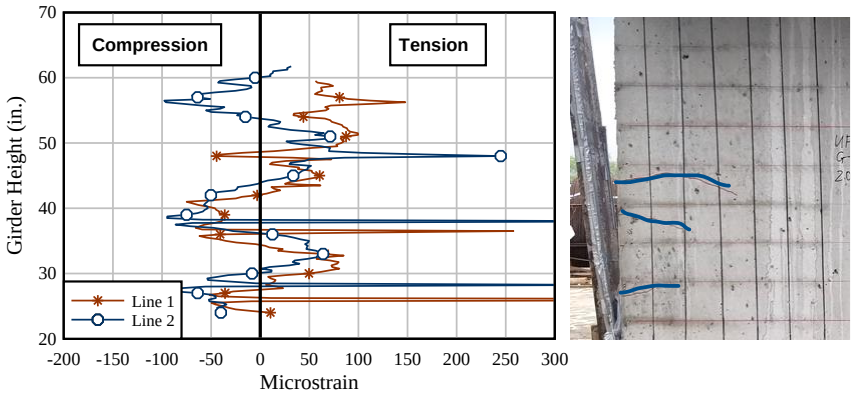

Figure 3-36 FOS strain peaks associated with cracking on the SCC

3.4.3 Mild-steel Reinforcement Strain

Strain gages were installed on vertical mild-steel reinforcement to measure strain during detensioning (Figure 3-37). Peak strains in reinforcement occur at crack locations in the concrete; because it is impossible to know where these cracks will occur when the strain gages are placed, the peak strains are not likely to be captured. Nevertheless, the strain data collected from the mild-steel reinforcement are valuable for validation of FEA models and were used as such.

Strain gages were installed at varying heights of the #5 K-bar placed in the first two bundles closest to the girder end. Strain gage "A" was installed 45 in. from the girder bottom, and strain gage "B" was installed 30 in. from the bottom (Figure 3-37). Consider that in the opposite end the strain gage name is followed by either the number 3 or 4, where 4 represents the strain gage closest to the end.

Figure 3-38 through Figure 3-42 show the measured strain data during the detensioning process. Note that the data represents the strain in the rebar at the point when 57 strands had been cut and before the sudden unexpected rupture of multiple strands. In these figures, positive strain represents tension and negative strain is compression. In general, vertical strain in the web was highest for the rebar near the end of the girder and decreased as the distance from the girder end increased. The highest strain was measured on G5-E2, which was the girder end with the least amount of reinforcement.

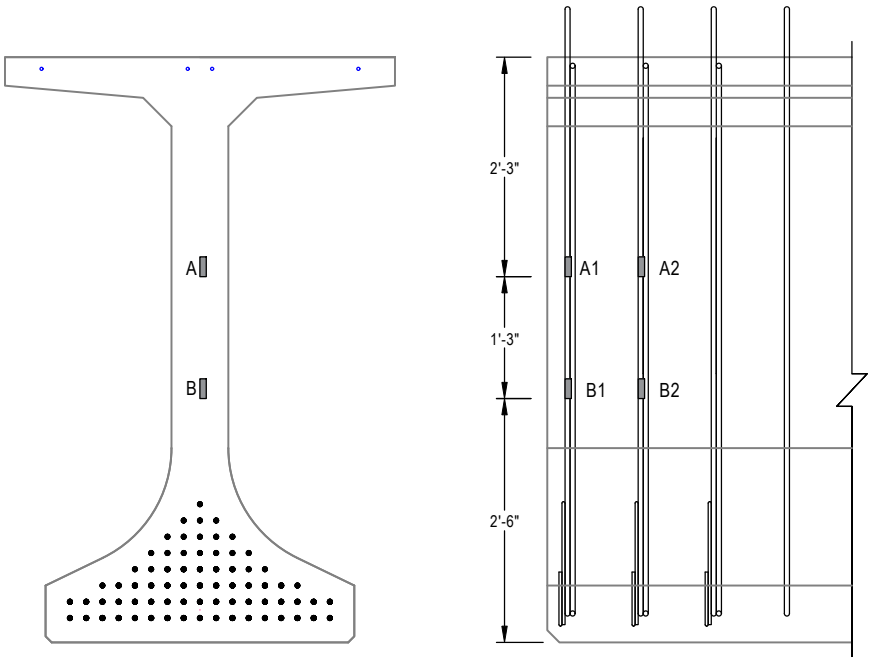

Figure 3-37 Location of strain gages installed on mild-steel reinforcement

Figure 3-38 shows the measured strain in the steel rebar for both ends of G1. Recall that G1 had typical FDOT end region detailing. G1-E1 was cast using UHPC and G2-E2 was cast with SCC. At the end of detensioning, strain gage A1 and B1 in G1-E1 showed strain values of 162 με and 236 με, respectively. These values are higher than the strain in the concrete surface measured by the FOS at the same girder height as was shown in Figure 3-31a. The difference in strains can be attributed to microcracking occurring in the UHPC. The same comparison was not possible for G1-E2 because the SCC exhibited extensive cracking which affected FOS

measurements (Figure 3-31b). Furthermore, the rebar strain in both the SCC and UHPC were surprisingly similar, except for B4, which exhibited 10% higher strain than B1.

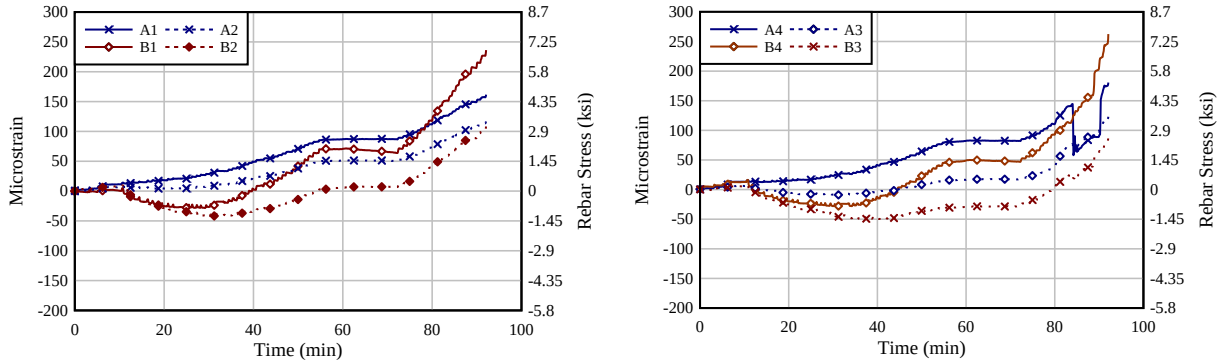

(a) (b)

Figure 3-38 Mild-steel reinforcement strain: (a) G1-E1 (UHPC) and (b) G1-E2 (SCC)

Figure 3-39 shows the measured strain in the steel rebar for both ends of G2. This specimen had the same reinforcement detailing on both ends, but the reinforcement was reduced by 50% compared to G1. The reduced reinforcement was implemented by doubling the space between vertical reinforcement. Surprisingly, the strains recorded in G2 were lower than those in G1 except for B3. This behavior was not expected because G2 had less reinforcement than G1. Furthermore, when comparing between G2 ends, strain gages A3 and B3 (SCC) exhibited strain at least 23% higher than A2 and B2 (UHPC), showing the contribution of steel fibers to carry stress.

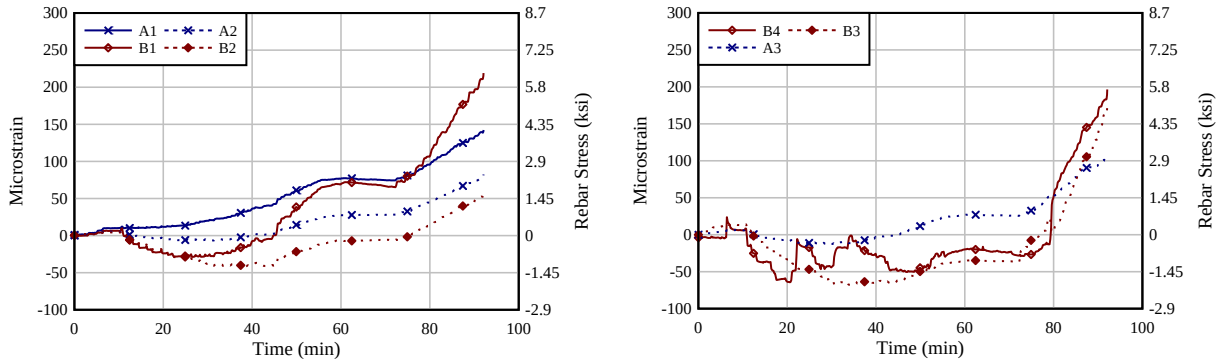

(a) (b)

Figure 3-39 Mild-steel reinforcement strain: (a) G2-E1 (UHPC) and (b) G2-E2 (SCC)

Figure 3-40 shows the measured strain in the steel rebar for both ends of G3. This mockup had the same vertical reinforcement detailing on both ends, but the confinement was reduced by 50% on G3-E2. Also, both ends of G3 did not have the bundle of four #5 bars that G1 and G2 had, but instead a single #5 K-bar. A comparison between G2-E1 with G3-E1 to evaluate the effect of removing the reinforcement bundles might be misleading because the UHPC in G3 exhibited 8% higher tensile cracking strength than the UHPC in G2.

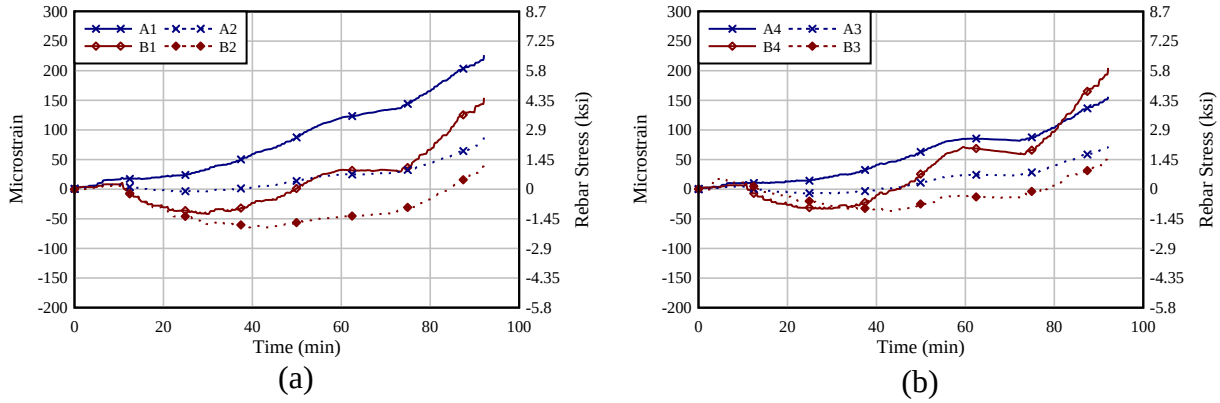

Figure 3-40 Mild-steel reinforcement strain: (a) G3-E1 and (b) G3-E2

Figure 3-41 shows the measured strain in the mild-steel rebar for both ends of G4. Vertical reinforcement in G4-E1 consisted of a single #5 K bar spaced at 7 in. with no confinement. G4-E2 vertical reinforcement had the typical bundle of 4 #5 bars, but spaced at 9 in. Comparison between both ends of G4 show that E1 had higher maximum strain. For instance, A1 had 25.6% higher strain than A4, and B1 had 3.5% higher strain than B4. The effect of increasing the spacing between reinforcement bundles from 3.5 in. (G1), 7 in. (G2) to 9 in. (G4) remains unclear due to the different cracking strength in the UHPC. UHPC in G4 exhibited 125% and 34% higher cracking tensile strength than G1 and G2 respectively.

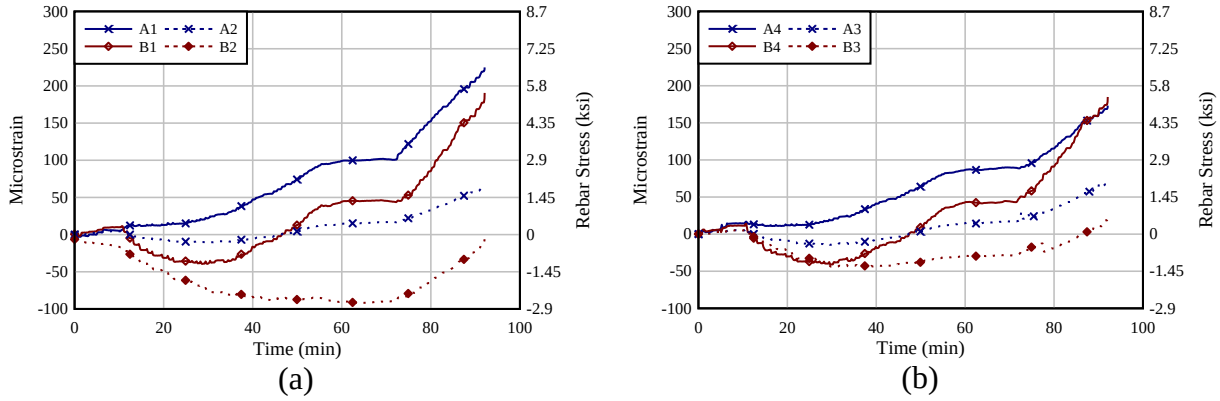

Figure 3-41 Mild-steel reinforcement strain: (a) G4-E1 and (b) G4-E2

Figure 3-42 shows the measured strain in the mild-steel rebar for both ends of G5. In general, both ends have the same vertical reinforcement detailing but G5-E2 does not have confinement. G5 had the lowest amount of steel reinforcement, but also had the highest cracking tensile strength among all UHPC batches, based on the tensile test coupons.

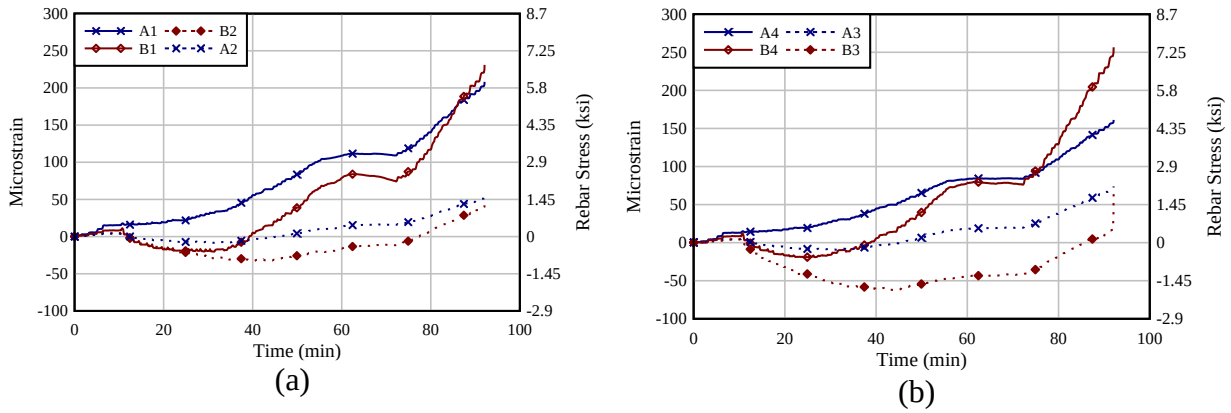

Figure 3-42 Mild-steel reinforcement strain: (a) G5-E1 and (b) G5-E2

3.5 End Region Cracking

Crack mapping and crack width measurements were performed on each mockup after prestress transfer and periodically for one year.

A 5 in. × 5 in. gridline reference system was applied to the beam to facilitate crack mapping and improve the consistency of crack width measurements over time (Figure 3-43). The grid covered the height of the web and 30 in. from the girder end. The distance from the end was selected to comply with the 2018 FDOT Structures Design Guidelines, which requires splitting resistance reinforcement to be included at distances of h/8, h/4, and 3h/8 from the end. The grid line labels shown in the figure were used to record and track crack width and length.

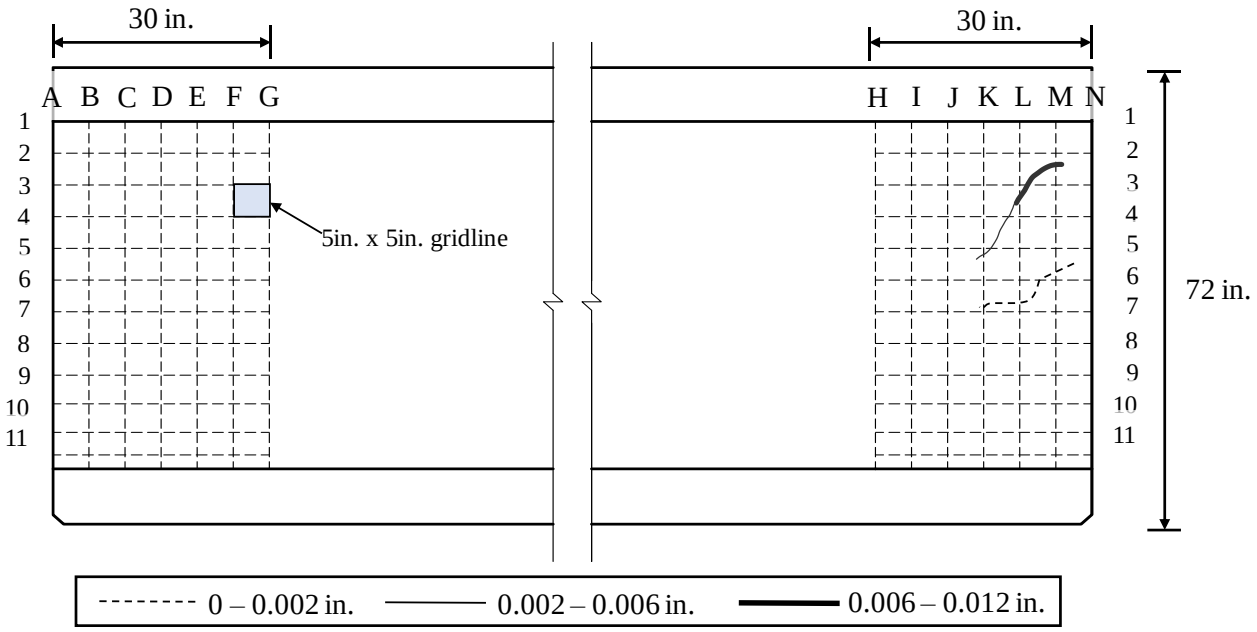

Figure 3-43 Reference gridline used for crack monitoring

3.5.1 Crack Monitoring

All five mockups were inspected for cracking immediately after prestress transfer and at different intervals during the subsequent months. Figure 3-44 through Figure 3-48 show sketches of the cracks formed at the following times: immediately after prestress transfer, one week after transfer, and three months after transfer. Crack width measurements were also taken at one year after transfer; because reference gridlines and crack marks had faded completely, change in crack length could not be recorded. Crack width data, however, are presented in the following sections.

The cracks in these figures were separated in three categories based on the crack widths (Figure 3-43). The first category includes cracks from 0 in. to 0.002 in. and is represented with a dash line. The second category includes cracks with widths between 0.002 in. to 0.006 in. and is represented with a solid black line. Finally, the third category includes cracks with a width above 0.006 in. and is represented with a thick solid black line.

An overall crack length was estimated for each end based on the intersection between the cracks and gridline (Figure 3-49). As expected, the number of cracks, crack length, and measured crack widths increased over time. Horizontal web cracking was identified on the SCC ends immediately after prestress transfer. UHPC ends showed minimal cracking after transfer, which was very difficult to visually observe even by spraying ethanol on the surface. Bottom flange cracking due to the Hoyer effect and diagonal cracking due to creep and thermal effects started appearing on the SCC within the first week after prestress transfer. UHPC ends, however, did not show any bottom flange or diagonal cracking until 20 days after prestress transfer. In general, there was no correlation between the amount of steel reinforcement and the cracks found. In fact, it appears that UHPC tensile cracking strength is the controlling factor, as G4 and G5 exhibited the lowest number of cracks and the highest tensile cracking strength (Table 3-8).

Figure 3-44 shows a schematic of the cracks formed in G1. This mockup was made of UHPC (G1-E1) and SCC (G1-E2). Immediately after prestress transfer, G1-E2 exhibited horizontal cracks in the web and a few diagonal cracks in the top section of the web. Crack widths after detensioning were below 0.006 in. One week after detensioning, the number of cracks and crack length increased on the SCC side, and small horizontal cracks appeared on the UHPC end. Three months after detensioning, cracks in the SCC exceeded 0.006, which would require the application of sealant or epoxy filling. UHPC mockups, however, exhibited diagonal cracking with widths less than 0.002 in., likely formed due to creep or thermal effects.

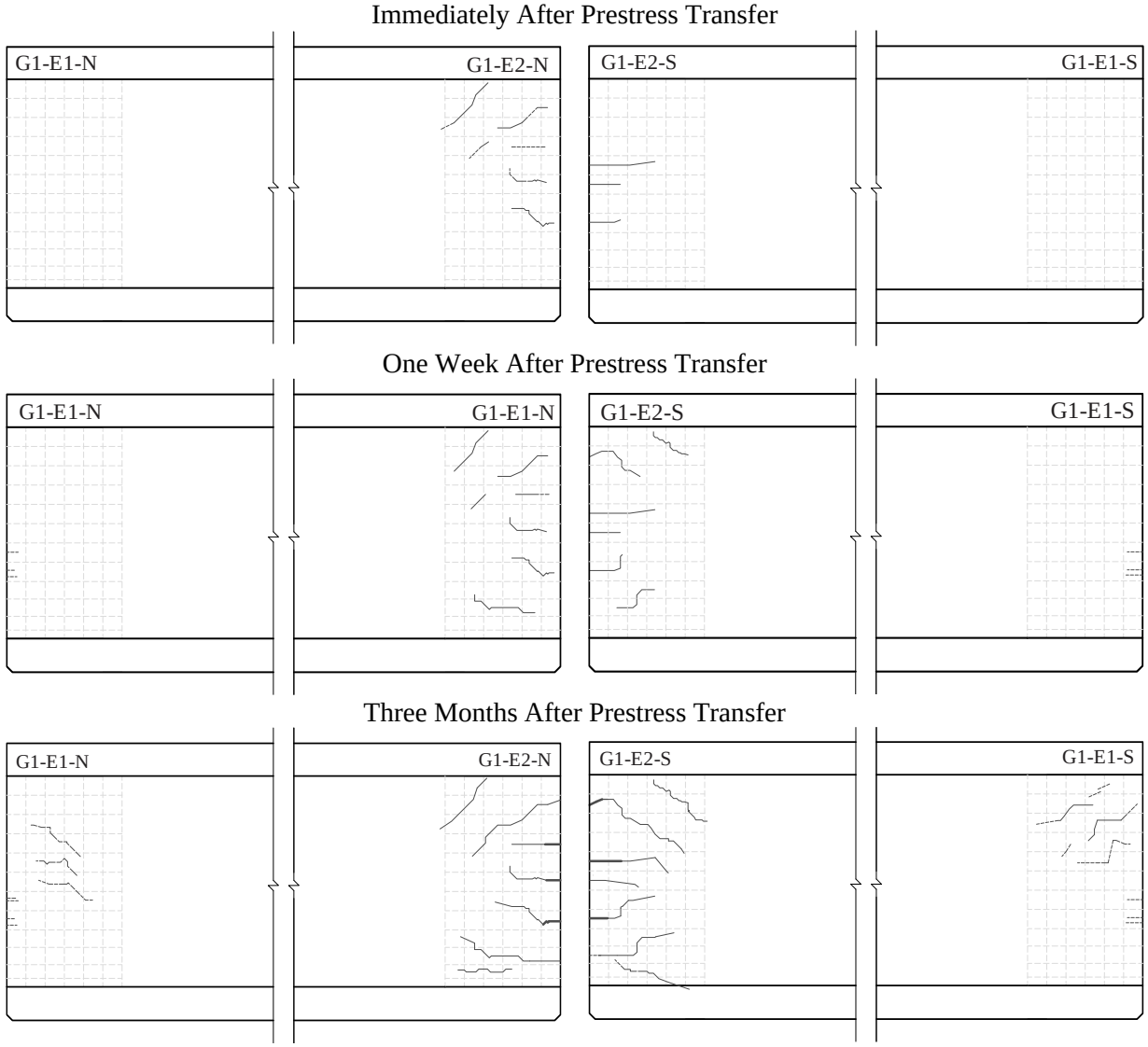

Figure 3-44 Crack monitoring of G1

Figure 3-45 shows a schematic of the cracks formed in G2. This mockup was made of UHPC (G2-E1) and SCC (G2-E2). Immediately after prestress transfer G2-E2 exhibited horizontal cracks in the web and diagonal cracks in the top section of the web. Mockup G2 exhibited more cracking on the SCC side than G1, which was expected due to the lower amount of reinforcement. Cracking was quantified based on the crack length at each end and is discussed at the end of this section. Crack widths after detensioning were below 0.006 in. One week after detensioning, the number of cracks and crack length increased on the SCC side, and small horizontal cracks appeared on the UHPC end. Three months after detensioning, cracks in the SCC exceeded 0.006 in., which would require the application of sealant or epoxy filling. UHPC mockups, however, exhibited diagonal cracking with widths less than 0.002 in., likely formed due to creep or thermal effects.

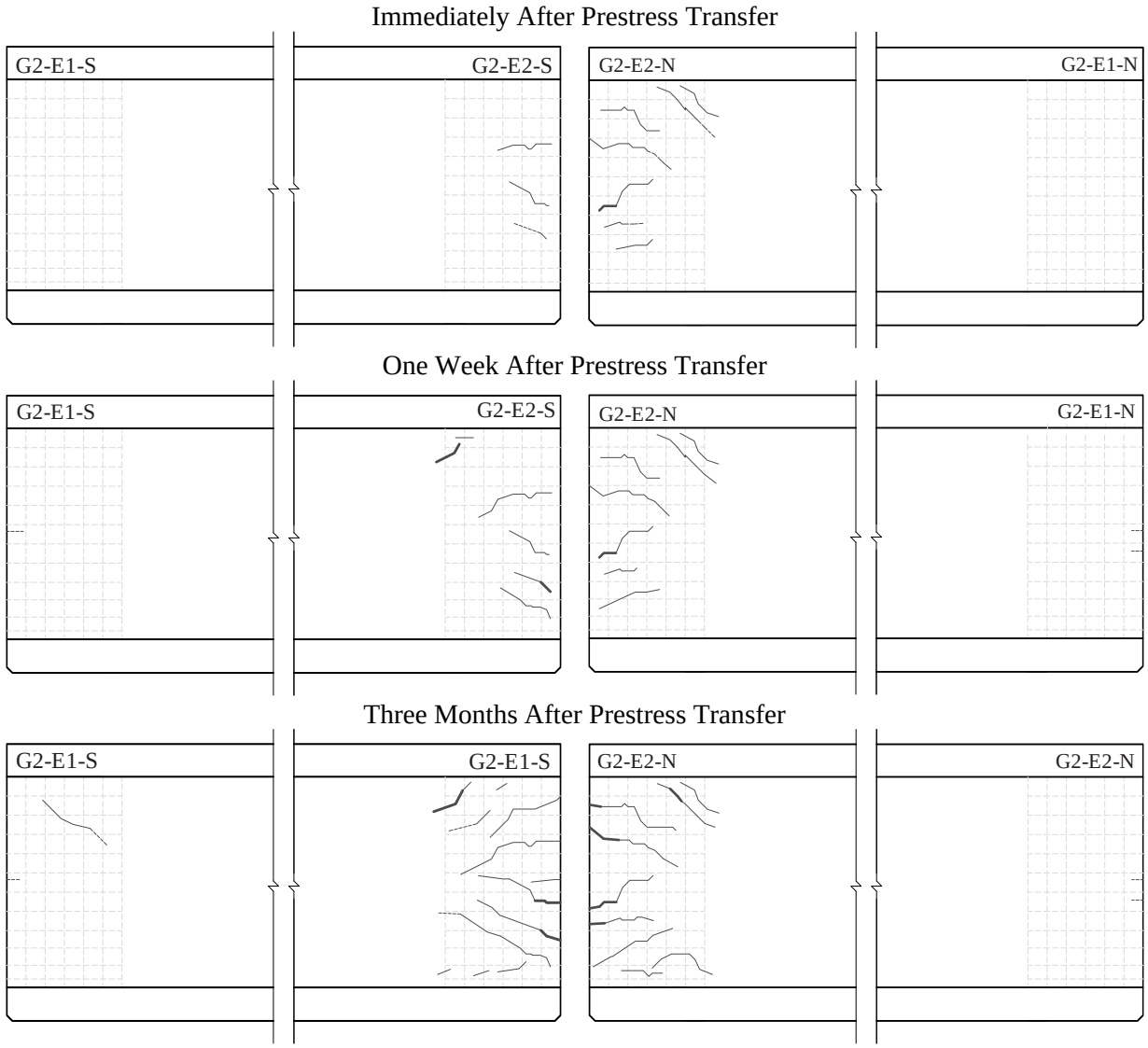

Figure 3-45 Cracks monitoring of G2

Figure 3-46 shows a schematic of the cracks formed in G3. This mockup was made entirely of UHPC. Small horizontal cracks were found immediately after prestress. Crack widths immediately after detensioning were below 0.002 in. One week after detensioning, the number of cracks, crack length and crack width remained the same. Three months after detensioning the mockup exhibited diagonal cracking with widths less than 0.002 in., likely formed due to creep or thermal effects.

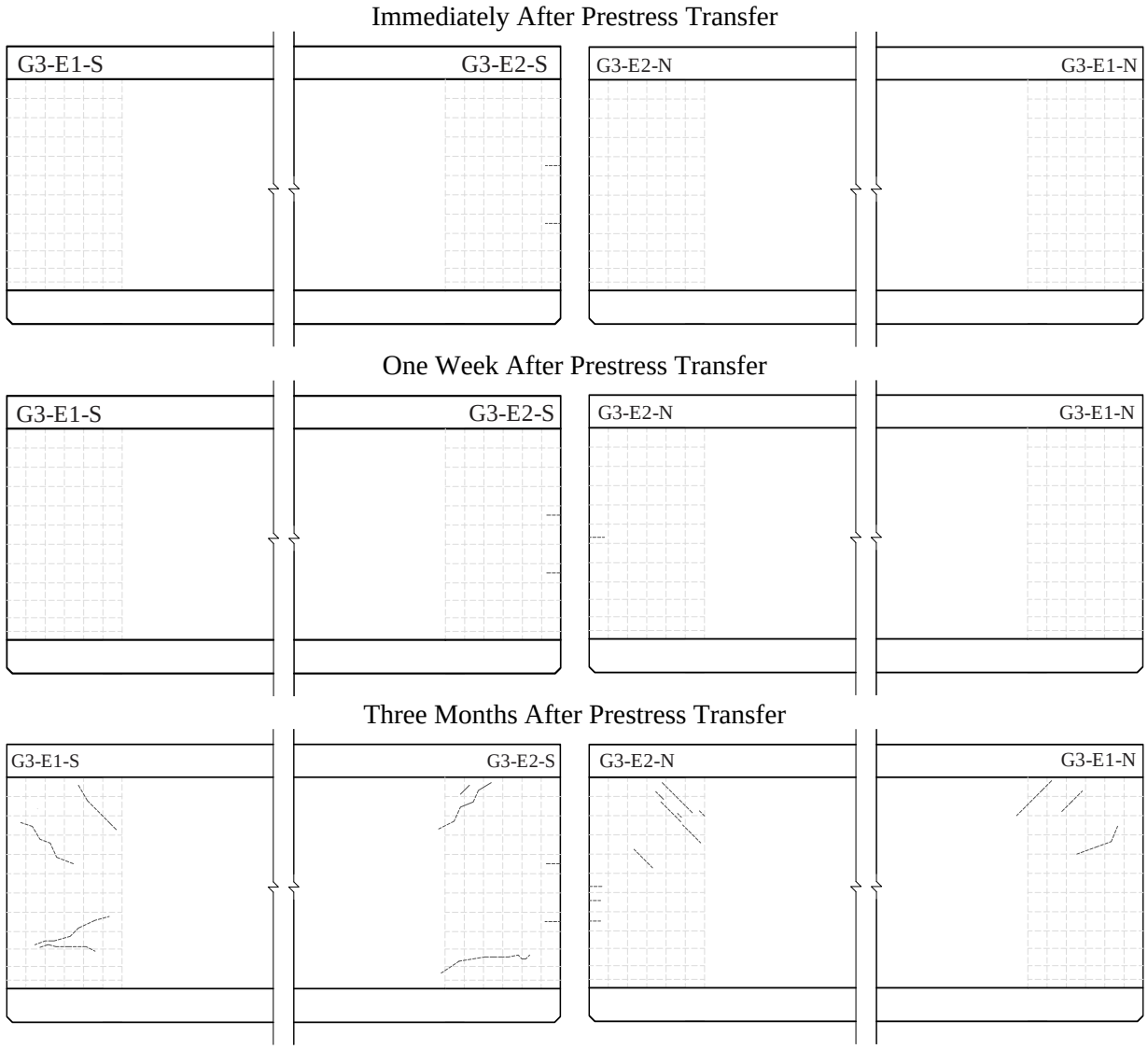

Figure 3-46 Cracks monitoring of G3

Figure 3-47 shows a schematic of the cracks formed in G4. This mockup was made entirely of UHPC. No cracks were found immediately after prestress. One week after detensioning, small horizontal cracks were found on both ends of the mockup. Measured crack widths were under 0.002 in. Three months after detensioning the mockup exhibited diagonal cracking with widths less than 0.002 in., likely formed due to creep or thermal effects.

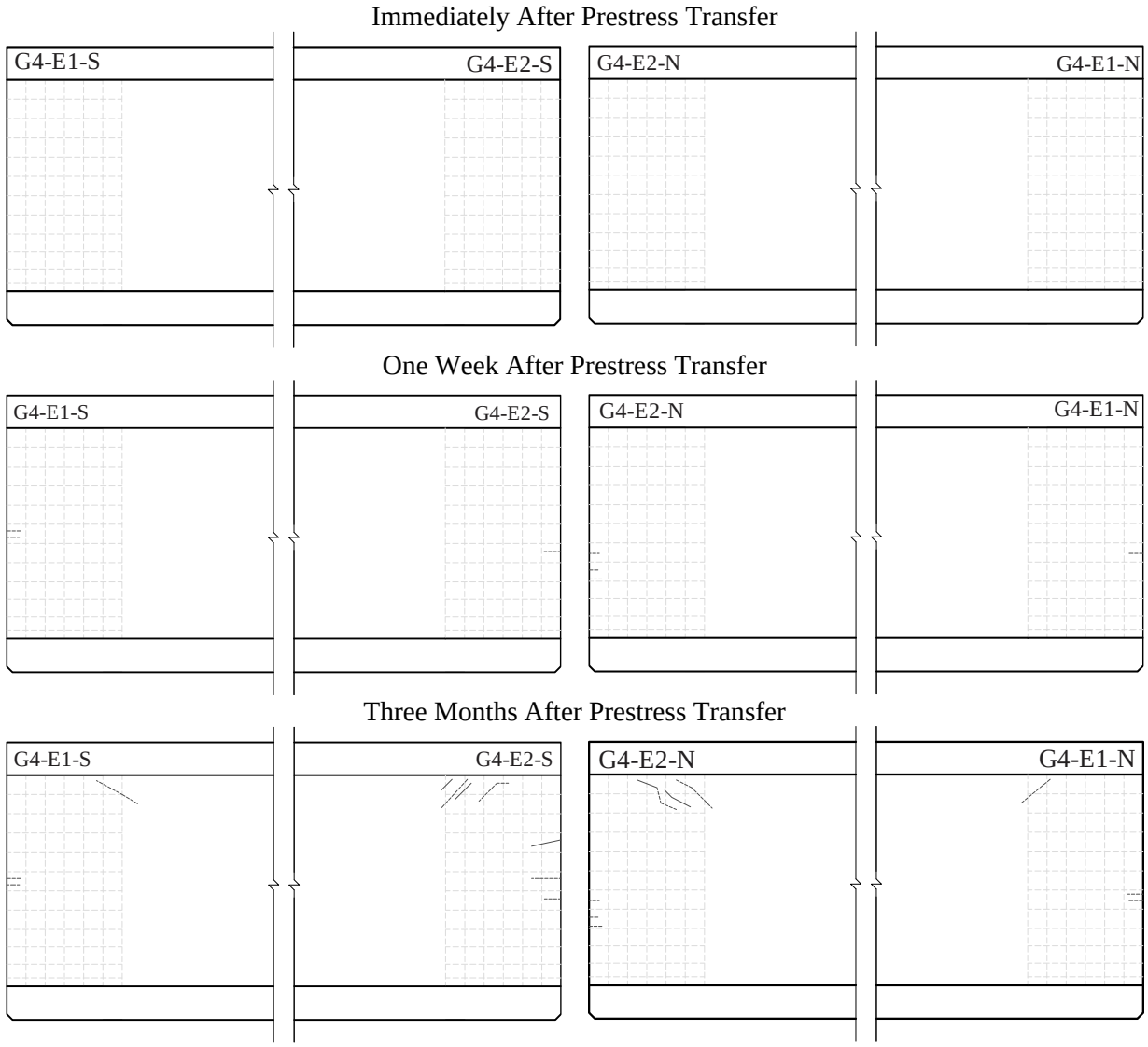

Figure 3-47 Cracks monitoring of G4

Figure 3-48 shows a schematic of the cracks formed in G5. This mockup was made entirely of UHPC. No cracks were found immediately after prestress. One week after detensioning, small horizontal cracks were found on G5-E2 (South). Measured crack widths were under 0.002 in. Three months after detensioning both UHPC ends exhibited light diagonal cracking, likely formed due to creep or thermal effects. Crack widths of these diagonal cracks were under 0.002 in. Recall that G5 had the least amount of reinforcement on end, but also the highest cracking tensile strength as measured by DTT.

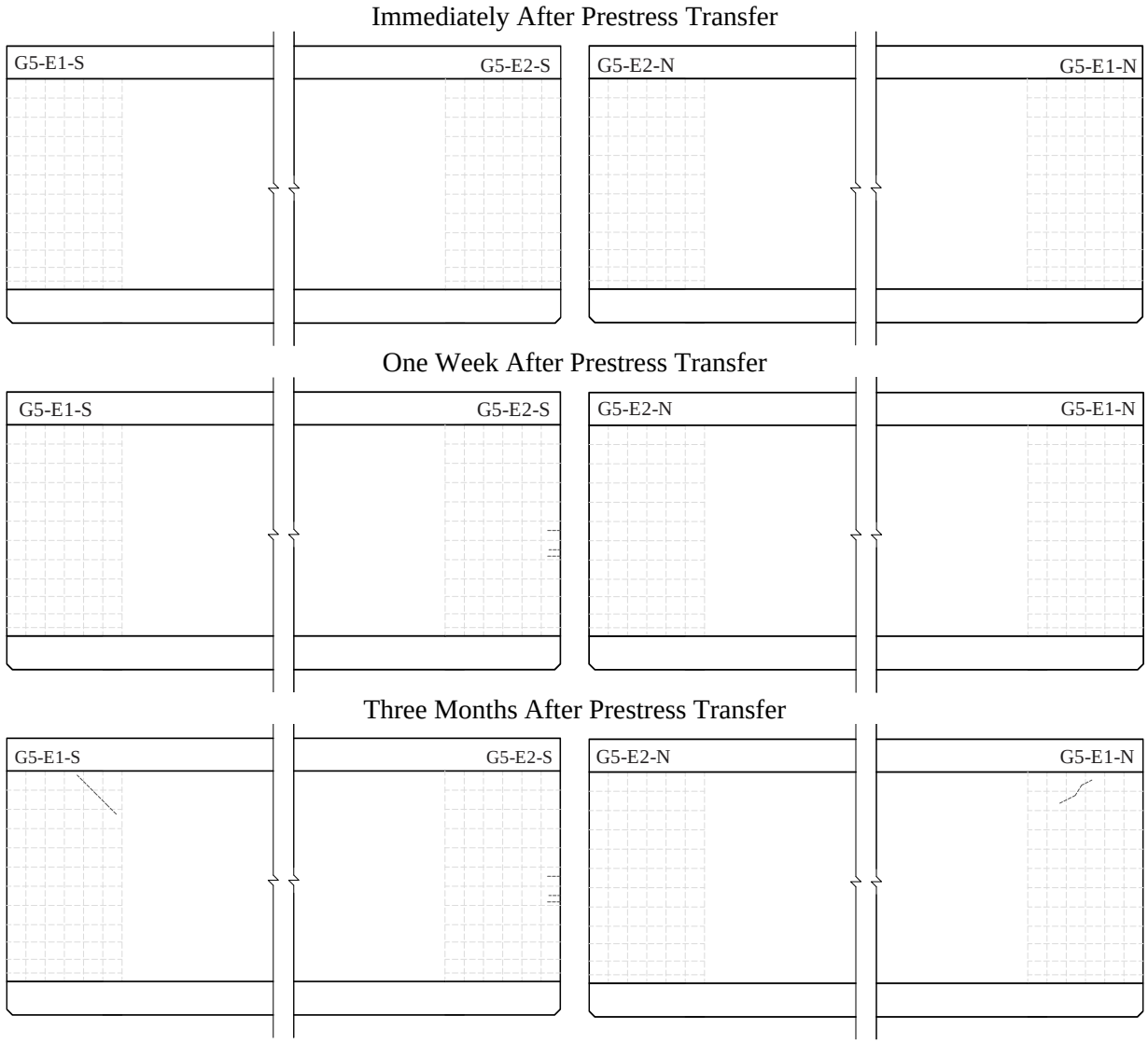

Figure 3-48 Cracks monitoring of G5

Figure 3-49 shows the total crack length at each end. In general, crack length grew overtime. After prestress transfer mockup ends made of SCC exhibited crack lengths ranging from 152 in. to 214 in., while UHPC ends had under 10 in. of crack lengths. One week after prestress transfer the SCC crack lengths varied from 233 in. to 285 in. for G1 and G2 respectively. UHPC ends started to exhibit more cracking to a maximum length of 25 in. measured in G1-E1. Three months after prestress transfer the crack length on the SCC ends increased to 405 in. for G1 and 514 in. for G2. The crack length on the UHPC ends varied from 14.5 in. to 180 in.

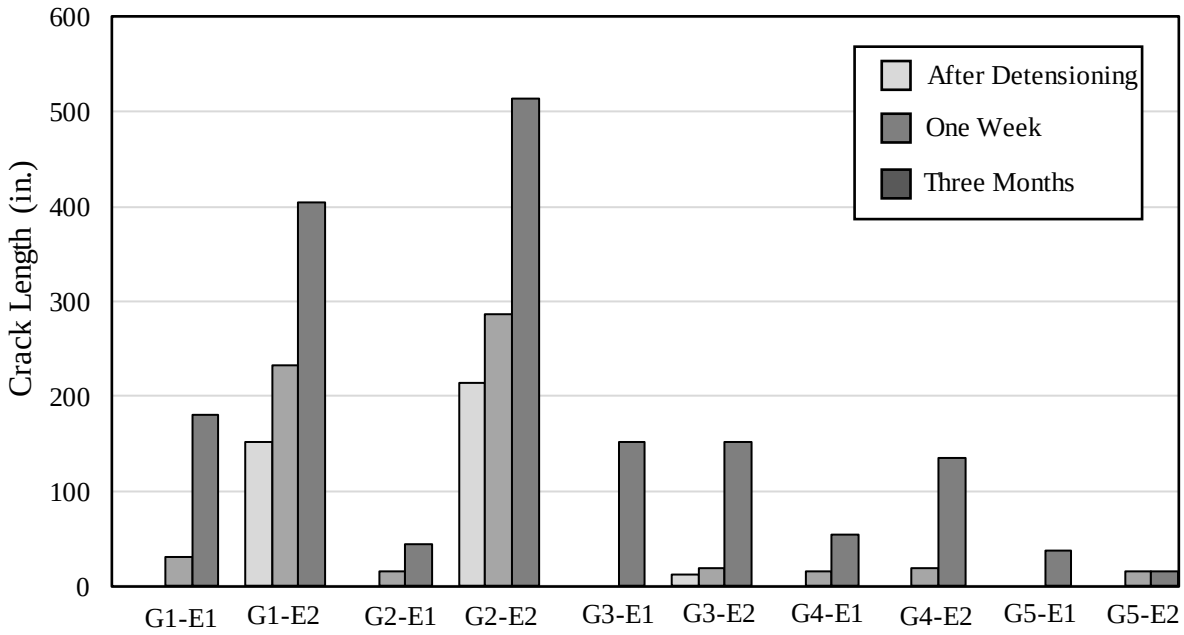

Figure 3-49 Measured crack length

3.5.2 Average Crack Width

Average crack width *(w_a)* is defined as the average of all the crack width measurements taken for each girder end. Figure 3-50 shows the average crack width of the measurements taken from transfer to one year of storing.

In general, w_a increased with time for both SCC and UHPC. SCC w_a was approximately four times greater than that of UHPC. The results indicate that w_a began to plateau after 30 days from prestress transfer. After the plateau, all girders showed a decrease of crack widths, which is attributed to the decrease in temperature during the winter months, and self-healing of the concrete.

Temperature of the concrete surface and ambient were recorded for every crack width measurement. The recorded concrete surface temperature ranged from 57°F to 100°F. Concrete surface temperature varied depending of the ambient temperature and whether the girder face was exposed to the sunlight or in the shadow. Among all mockup ends, G2-E2 exhibited the highest w_a, which was expected because of the reduced amount of reinforcement and presence of SCC. Overall, average crack widths in UHPC ends exhibited remarkable stability with w_a having a peak of 0.001 in. Average crack widths in SCC ends plateaued at 0.0045 in.

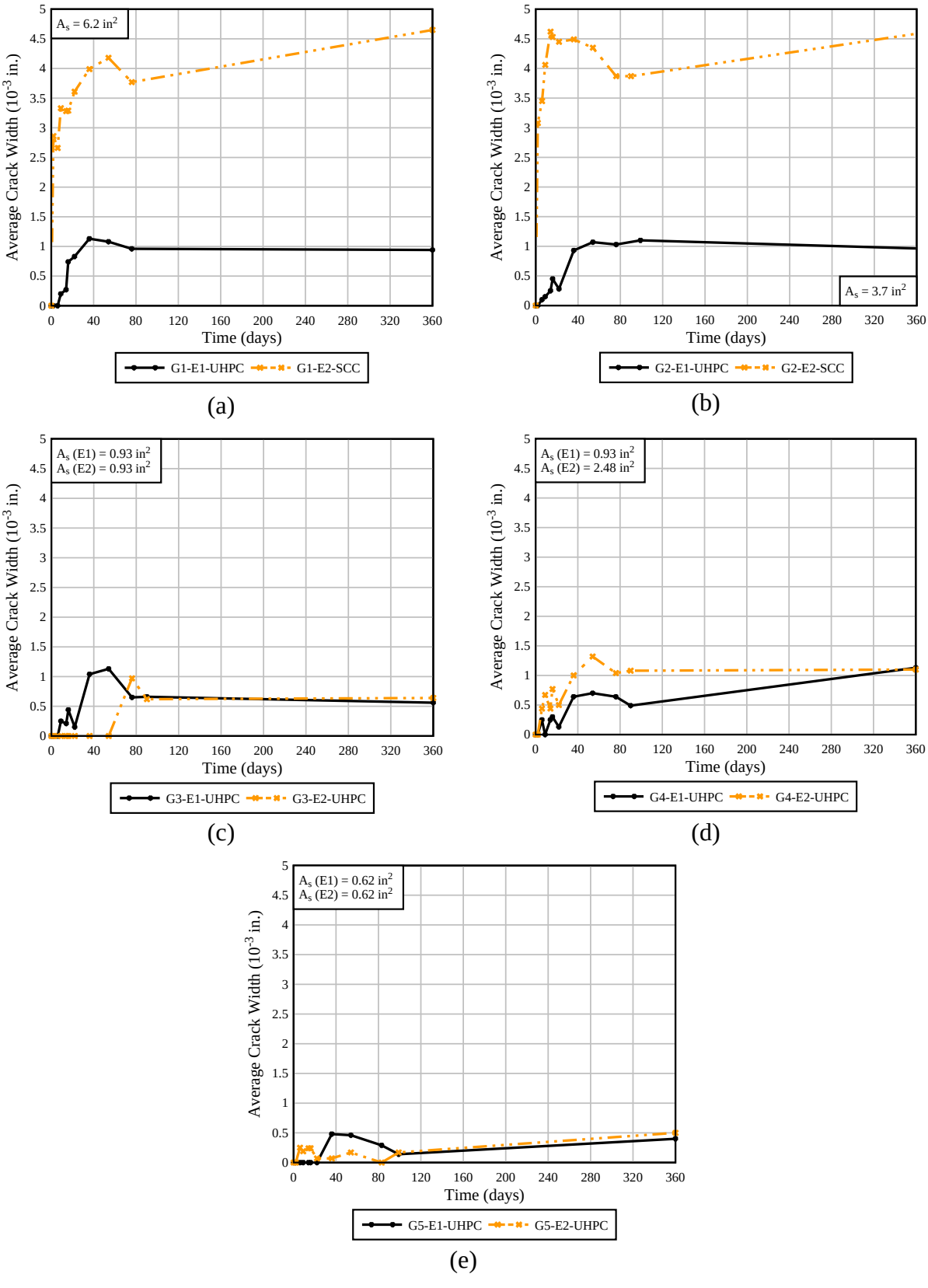

Figure 3-50 Average crack width: (a) G1, (b) G2, (c) G3, (d) G4 and (e) G5

3.5.3 Maximum Crack Width

Maximum crack width (w_{max}) is defined as the single maximum crack width measurement taken on each girder end (Figure 3-51). SCC end exhibited w_{max} 3.66 times greater than those of UHPC. Surprisingly, the UHPC ends exhibiting w_{max} above 0.002 in. were those having four rebar bundles in the end region as reinforcement (G1-E1, G2-E2 and G4-E2). Nevertheless, w_{max} was mostly measured in the diagonal cracks that formed weeks after prestress transfer.

Finally, G5-E2 had the lowest w_{max} and the lowest amount of reinforcement in the end region. This relation, however, is mostly attributed to the cracking tensile strength of G5 which was the highest among all specimens. These results suggest that UHPC needs minimum mild-steel reinforcement to prevent end region cracking that requires patching or other repair technique. In this study minimum reinforcement refers to single #5-k bars distributed longitudinally in the end region at a spacing of 9 in.

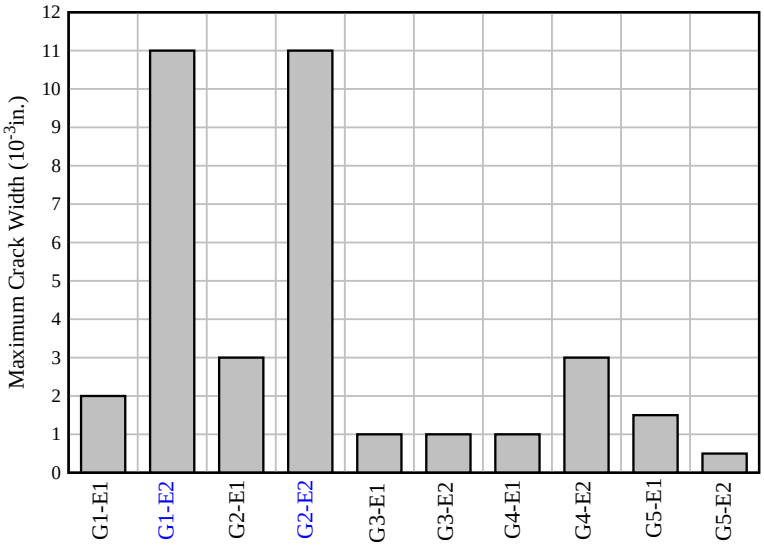

Figure 3-51 Maximum crack width of all specimens.

4 FIB 54 UHPC-SCC Hybrid Girder

Two hybrid FIB 54 girders were designed to determine the structural implications of the hybrid construction technique. The proposed girder configuration and casting plan is shown in Figure 4-1.

The focus of testing was to evaluate the structural performance of the girder when tested with a low shear span-to-depth ratio. It was expected that this loading configuration would highlight possible deficiencies not only the in the UHPC end region, but also at the UHPC-SCC interface. The variables considered in the design of these girders included the length of UHPC at the end of the girder and reduced amount of shear and confinement reinforcement therein. For clarity, the FIB 54 specimens had the same nomenclature used for the mockups, with name G6 and G7 for each specimen.

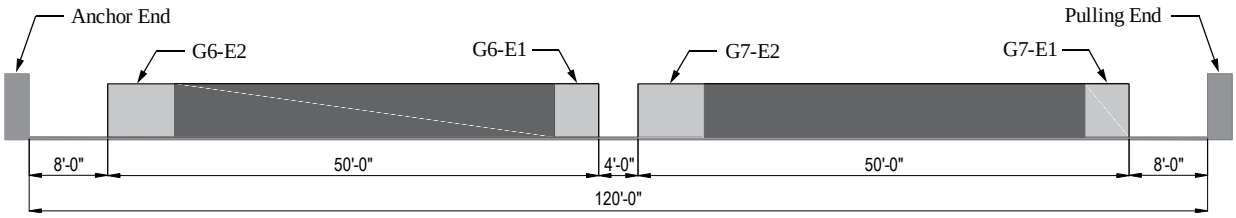

Figure 4-1 Elevation view of FIB 54 girders in casting bed

4.1 Specimen Design

Two different reinforcement detailing configurations shown in Figure 4-2 were used. The first configuration consists of increasing the rebar spacing at the end region to 7.5 in., which is double the spacing of the typical FDOT end zone configuration.

The second detailing configuration had a spacing of 9 in. for the vertical reinforcement and confinement. The second variable considered in the design of the FIB 54 was the length of UHPC at the end zone. For one end, the length of UHPC was equivalent to the height of the girder (54 in.), and the second length was 1.5 times the height of the girder or 81 in. The selected lengths of UHPC were fabricated with similar construction techniques discussed in Section 3.2. Detailed drawings of each specimen are included in Appendix C of this document.

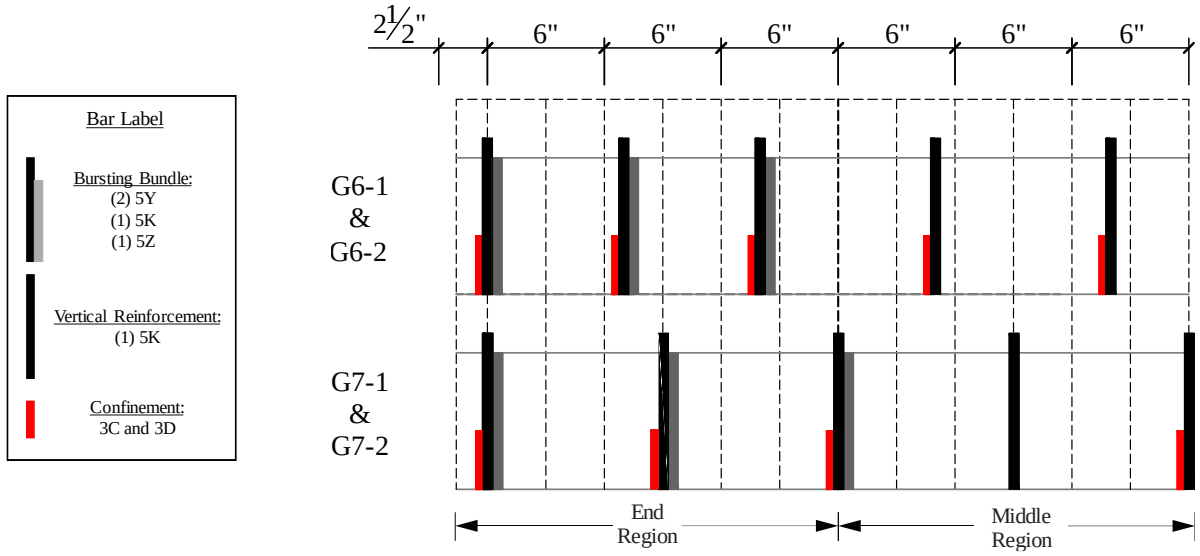

Figure 4-2 Reinforcement detailing used in FIB 54 G6 and G7

Similar to the FIB 72 mockups reported in Section 3, the maximum number of strands allowed by the FDOT strand pattern were used. The strand pattern calls for a maximum of 70 fully bonded strands in the bottom flange. The compressive stresses immediately after release are shown in Figure 4-3.

To prevent excessive micro cracking in the SCC portion that would have compromised shear testing results, prestress transfer was delayed until the SCC compressive strength was above 8,000 psi (Figure 4-3). Note that the limiting forces to prevent vertical splitting specified in SPI Index 450-010 for FIB 54 were ignored because of the enhanced mechanical properties of UHPC.

The contribution of UHPC to the resistance of bursting stresses, however, was calculated using the approach discussed in Section 3.1. In particular, the reinforcement detailing for the FIB 54 in G6 corresponds to G2-E1. Similarly, G7 had the same reinforcement detailing as G4-E2.

Table 4-1 shows the contribution of UHPC and steel reinforcement to the resistance of bursting stresses in both FIB 54 girders.

Table 4-1 Design of bursting stresses based on AASHTO (2017)

FIB 54 Specimens	Total A_s (in^2)	$0.04P_u$ (kip)	UHPC Cont. (kip)	Steel Stress [f_s] (ksi)
G6	6.2	123	100	7
G7	2.4		100	10

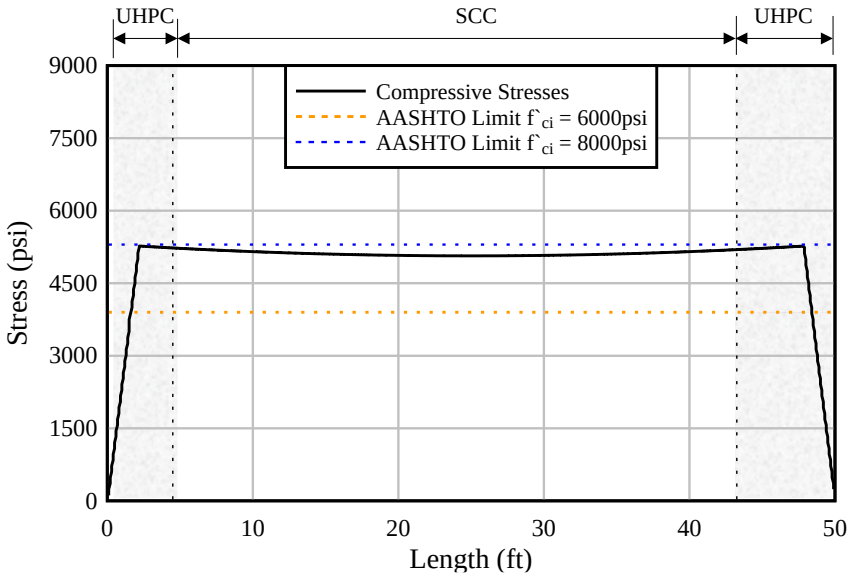

Figure 4-3 Compressive stresses for FIB 54 G6 and G7 immediately after release

4.2 Specimen Construction

This section describes the methods used for the construction of the two 50-ft-long FIB 54 girders constructed between July 9th, 2019 and July 18th, 2019 at Standard Concrete Products in Tampa. The construction events are listed in Table 4-2. In general, the construction followed conventional methods used for typical girder fabrication, with the addition of modifications to fabricate the SCC and UHPC interface.

Table 4-2 Construction schedule

Construction Events	Days							
	1	2	3	4	5	6	7	8
Lay down strands	X	X						
Pull Strands		X						
Tie reinforcement (SCC)		X	X					
Pour SCC			X					
Interface Surface Preparation			X					
Tie reinforcement (UHPC)			X					
Pour UHPC					X	X		
Strip steel forms							X	
Install Instrumentation							X	
Detensioning							X	X

During the specimen design, three techniques were considered for the construction of the UHPC-SCC interface:

1) Removable barrier: Develop a temporary barrier capable of holding the SCC until the UHPC is poured.
2) Polypropylene mesh: Install a mesh supported by the steel reinforcement capable of holding the SCC in one section until the UHPC is poured in the remaining section.
3) Construction joint: fabricate the SCC portion first and shift the bulkheads to pour the UHPC section

Each of the techniques mentioned above had its own benefits and drawbacks. For instance, the removable barrier would be the preferred method because it would likely develop a better bond at the UHPC-SCC interface. The geometry of FIB cross-sections and the strand pattern, however, complicated the fabrication of such a barrier. In addition, the precaster was not comfortable with the concept of removing a barrier during concrete pours because it could result in complications during production and wasted material.

The second alternative was to install a polypropylene mesh to hold the SCC in place and then pour the UHPC. The mesh would be supported by the reinforcement and stay in place for the lifespan of the girder. Several trials in different FIB sections were attempted with reasonable success prior to the construction of the hybrid girder. More details about these trials are given in Appendix E.

The third alternative was to create a construction joint between the SCC and UHPC. This technique is thought to provide the most control over the quality of the interface. This process, however, requires more steps and would likely take more time to fabricate than the other two alternatives; bulkheads must be shifted in place after SCC placement to provide closure to the UHPC forms. Furthermore, UHPC placement must be done at least one day later to ensure that the SCC has set before moving the bulkhead. Finally, the construction joint approach is thought to be the most susceptible to fabrication variations and would give the lowest bond strength of the three candidate methods. The precaster chose this option for fabrication of the test specimens.

Construction began by marking the locations of SCC and UHPC in the precast bed. Once the locations were determined, the steel bulkhead base was placed at the end of the SCC locations of each girder (Figure 4-4). The next step was to place the prestressing strands.

Strands in the top flange were tensioned first. The bottom strands were tensioned starting from bottom layer and working up to the topmost strand layer.

Mild reinforcement was placed in the SCC section after the strands were tensioned (Figure 4-5). In addition, a vibrating wire gage was installed at mid-length to measure long-term prestress losses. Prior to attaching the steel forms, the bulkheads were covered with a retarder admixture (Master Finish HV) to prevent the SCC from hardening at that location (Figure 4-6). The application of the retarder was done using a paint brush on top of duct tape that was previously taped to the bulkhead surface. Forty-foot-long modular steel forms were used for the construction. The steel forms were squared and set in place using crossties.

Figure 4-4 Placement of temporary bulkhead

Figure 4-5 Installation of mild-steel reinforcement in SCC section

Figure 4-6 Application of concrete retarder on bulkheads

The SCC concrete mixture, which was placed first, was FDOT Class VI concrete (f'_c=8,500psi). SCC was poured in the middle sections of the girders (see Figure 4-1 for location) and was allowed to cure for one day before removing the steel forms.

After form stripping, the bulkheads were shifted to the end-girder location. The surface of the SCC end was cleaned using pressurized water to remove the unhardened SCC and expose the coarse aggregate roughened surface, which provided an improved bond with the UHPC (Figure 4-7).

The remaining mild steel reinforcement including the instrumented rebar were then installed in the UHPC portion of the girder (Figure 4-8). To avoid undue influence on the shear testing, the lifting hoops were placed so that the hoop legs were outside of the region expected to have high shear demand. Finally, the steel forms were secured to the precast bed for casting of the specimens.

(a) (b)

Figure 4-7 SCC surface preparation: (a) Priot to water jetting and (b) After water jetting

Figure 4-8 Installation of mild-steel reinforcement on UHPC section of the girder

Because of the cost and technical challenges during mixing and placing, widespread use of UHPC for production in precast yards is still in its infancy. Given this lack of experience, the precast plant elected to move more slowly with the UHPC production than was typical with conventional concrete.

The precaster used a 6-cy mixer for UHPC. The large proportion of cementitious materials used, however, limited the volume of any single UHPC batch to 3.2-cy, which was sufficient for both ends of one girder.

The mixing procedure was the same as the FIB 72 mockups discussed in section 3.2.

After mixing, UHPC mixture was placed in the end sections of each girder. After the pour was finished, the precaster used a hand roller to prevent the UHPC from forming a continuous elephant skin, but instead a rougher surface that can be beneficial for future bond with the concrete deck (Figure 4-9).

Figure 4-9 Finalized UHPC section at girder end

4.3 Material Testing

4.3.1 Fresh Properties

Fresh properties of SCC were tested to verify that the mix complied with the FDOT requirements listed in Table 4-3. Testing of UHPC mixes was performed following the recommendations of ASTM C1856—Standard Practice for Fabricating and Testing Specimens of Ultra-High Performance Concrete, along with practices used by the precaster such as measuring the diameter of the cone flow with and without steel fibers. A summary of the fresh properties results of both UHPC mixes are given in Table 4-4.

Table 4-3 FDOT fresh properties requirements for SCC

Test Method	FDOT Requirements	Results
ASTM C1611- Slump Flow	27 ±2.5 in.	24.5 inches
ASTM C1611- T-50	2-7 seconds	3.8 seconds
ASTM C231- Air Content	0%-6%	2.4%
ASTM C138- Unit Weight	-	139.9 lbs./ft^3
Temperature	-	82°F

Table 4-4 UHPC fresh properties

Test Methods	UHPC (G6)	UHPC (G7)
Cone Flow without Fibers (in.)	10	9
Cone Flow with Fibers (in.)	10.75	9
Temperature (°F)	84	84

4.3.2 Compressive Strength

Compressive strength cylinders (4 in. × 8 in.) were prepared from a sample collected immediately after mixing. Compressive strength tests were performed at both Standard Concrete Products and UF. The SCC tests were performed at SCP following the guidelines given by ASTM C39. The UHPC tests performed at SCP followed the same procedure used for SCC, which included the use of neoprene pads to provide a uniform load transfer. Additional tests were performed at UF following the recommendations of ASTM C1856, which included grinding both faces of the cylinders to create a uniform surface. The specimens were cured using three methods which consisted in matching the curing temperature of the girder inside the steel forms, ambient temperature along the girder bed and room temperature. The UHPC cylinders were tested at 24 hours, age of detensioning (72 hours for G6 and 48 hours for G7), and 28 days. The required compressive strength for release was 8,000 psi, which was achieved by the SCC (Table 4-5) and UHPC (Table 4-6) by the release date.

The compressive strengths of the match-cured specimens were found to be significantly lower than those cured at ambient temperature (Table 4-6). The operators suspected that the system used to match-cure the specimens had technical issues that resulted in very high temperatures that did not allow the UHPC to cure properly. This was supported by the type of failure breaks observed in the match-cure cylinders as opposed to those cured at ambient temperature (Figure 4-10). The match-cure cylinders exhibited crushing in the bottom part of the cylinder, and no additional damage throughout the cylinder.

Figure 4-10 Compressive strength tests

Table 4-5 Compressive strength results of SCC

Age of Specimens	Compressive Strength (psi)
Detensioning	8,880
28 days	10,740

Table 4-6 Compressive strength results of UHPC

Age of Specimens	Type of Curing	Girder 6	Girder 7
24 hours	Match-curing	9,230	10,040
	Ambient Temperature	19,730	19,500
	Room Temperature	8,783	7,240
Detensioning	Match-curing	10,060	-
	Ambient Temperature	20,710	20,550
	Room Temperature	13,400	-
28 Days*	Room Temperature (SCP)	20,010	19,890
	Room Temperature (UF)	17,560	18,440

*Tested at the University of Florida Laboratory

4.3.3 Tensile Strength

Direct tension test and flexure beam tests were used to determine the tensile strength of UHPC. Background and details of these test methods were covered in the Literature Review section 2.4.2. The results of both the DTT and the FB tests are shown in Figure 4-11 and Figure 4-12.

In general, the UHPC mixtures used for G6 and G7 exhibited similar results at age of detensioning, but G7 developed higher strength at 28 days. This was observed for both the DTT and the FB test. Lower tensile strength of G6 may be associated with lower water-to-cement ratio between UHPC mixes. Both G6 and G7 had the same mix design, but the actual volume of mix constituents varied due to batching tolerances. The UHPC batch tickets for each girder indicated that G6 had ~6 gallons more water than G7. The difference in water-to-cement-ratio can affect the fluidity of the mix (see flow cone results), the strength of the cementitious matrix and the fiber distribution due to different viscosities. Stiffness increase at 28 days was observed for both tests, which was due to the maturity of the cementitious matrix, which increases the

tensile stress at which the fibers would slip. Once the concrete started cracking, all samples from G6 and G7 were able to sustain the cracking load up to an ultimate strain of 1% (Figure 4-11).

In practice, one of these test methods could be selected for qualification or quality control of UHPC mixtures; therefore, it was important to determine if the precaster was able to produce several batches of the same UHPC mixture and maintain consistent tensile strength results. Further analysis of the tensile testing collected in the construction of the FIB 54's and the FIB 72's is discussed in Section 5.

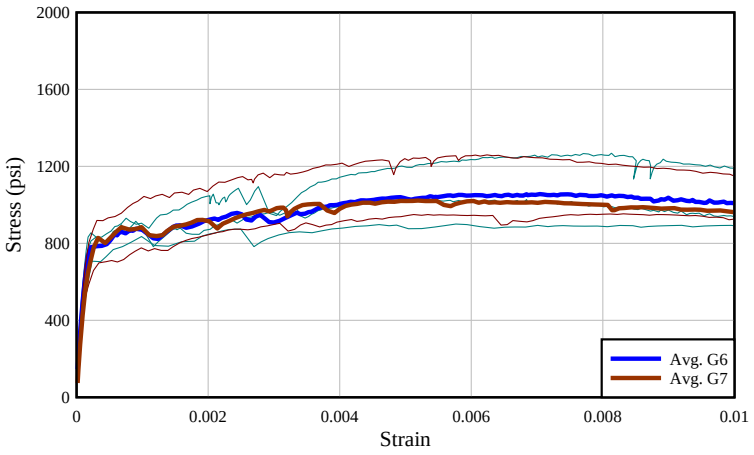

(a)

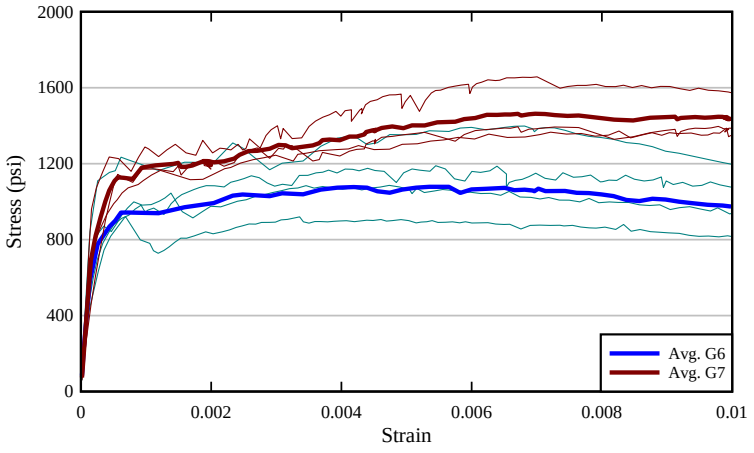

(b)

Figure 4-11 Results of the DTT test for G6 and G7: (a) G6 = 3 days and G7 =2 days (detensioning) and (b) 28 days

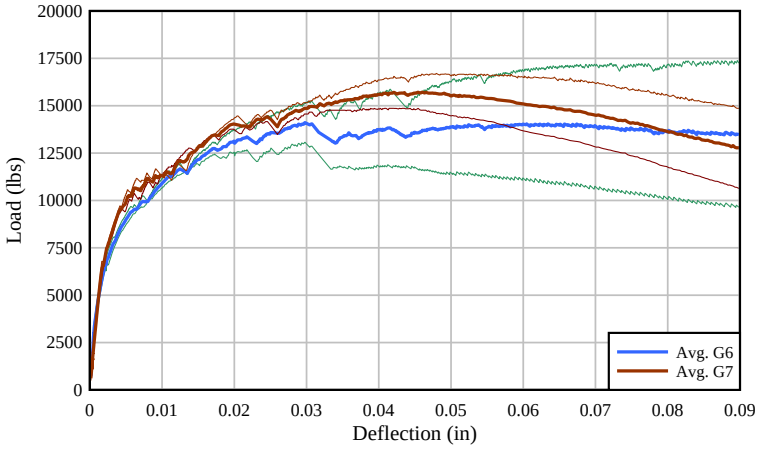

(a)

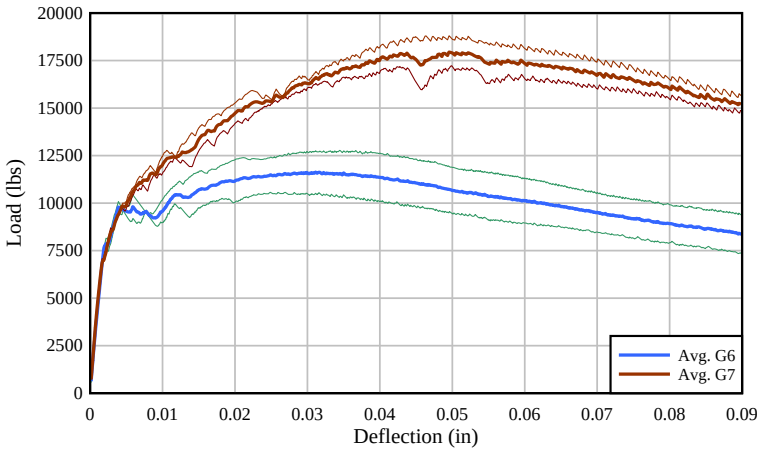

(b)

Figure 4-12 Results of the FB test for G6 and G7: (a) G6 = 3 days and G7 =2 days (detensioning) and (b) 28 days

4.4 Detensioning Results

Each girder was instrumented to measure strains during the detensioning. The instrumentation included vibrating wire gages, demec points and fiber optic sensors, which were used to determine the transfer length and concrete strains in the end region.

End region strain was measured to determine if cracking occurred during the detensioning of the strands. While most of the end region investigation was covered by the FIB 72 specimens, some groundwork was performed with the FIBs 54. The FDOT in the SPI Index 450-010 specifies that for a FIB 54 the maximum bonded applied prestress force is 1,740 kip; however, for the girders in this project the total applied prestress force is 3,080 kip. Excessive vertical tensile stresses may result in cracking, which, if large enough, may require repairs. Therefore, instrumentation was used to measure strain in the concrete and mild-steel reinforcement. FOS were installed vertically in the girder web to measure the strain in the concrete. Bonded electrical resistance strain gages were attached to the mild-steel reinforcement to determine the amount of stress carried by the steel reinforcement at specific locations.

4.4.1 Transfer Length

Transfer length was measured with three different methods including vibrating wire gages, demec points, and fiber optic sensors. For all three methods, transfer length was calculated using the 95% AMS method developed by Russel and Burns (1996). A summary of all the transfer length results is given in Table 4-7. In addition, the values are compared to the AASHTO (2017) equation for transfer length of 60 times the strand diameter. The measured values are about half of the computed value using AASHTO, meaning that this equation is not applicable to UHPC. Figure 4-13 shows the strain measured using vibrating wire gages, this method resulted in transfer length of 17.2 in. and 18.3 in. for G7 and G6, respectively.

Table 4-7 Summary of measured transfer lengths

Girder End	Transfer length (in.)			
	VW Gages	FOS	Demec	AASHTO
G6 – End 1	-	20.1	-	36
G6 – End 2	18.3	18.7	15.0	
G7 – End 1	17.2	17.7	-	
G7 – End 2	-	19.5	10.7	

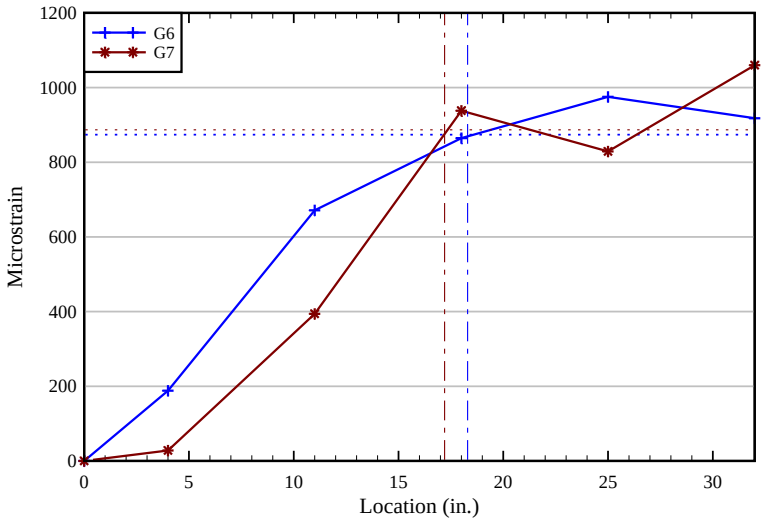

Figure 4-13 Measured transfer length using vibrating wire gages

Fiber optic sensors (FOS) were adhered to the bottom flange concrete surface at the same height as the second row of strands in the FIB strand pattern. The fiber sensor started 0.5 in. from the girder end and extended for approximately 28 in. (Figure 4-14).

Figure 4-15 shows the transfer length of all girder ends measured with FOS. FOS is a very powerful tool to measure transfer length as it provides more data points as opposed to other traditional methods such as demec points, vibrating wire or linear strain gages. In this case, FOS was set to record strain at each 0.25 in. of fiber length at 20Hz. The data collected for G6 and G7 clearly display the distance from the end of the girder to the point at which the strain readings have plateaued; this is the transfer length. The transfer length values obtained from the FOS data ranged from 17.7 in. to 20.1 in.

Local variations in strain readings are thought to be lack of contact between the concrete and FOS that may have occurred during installation.

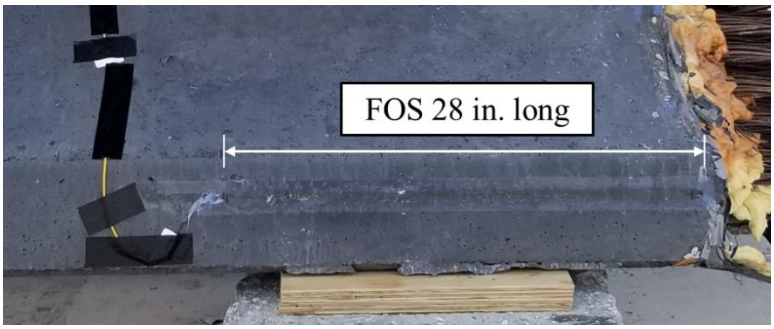

Figure 4-14 FOS installed on bottom flange to measure transfer length

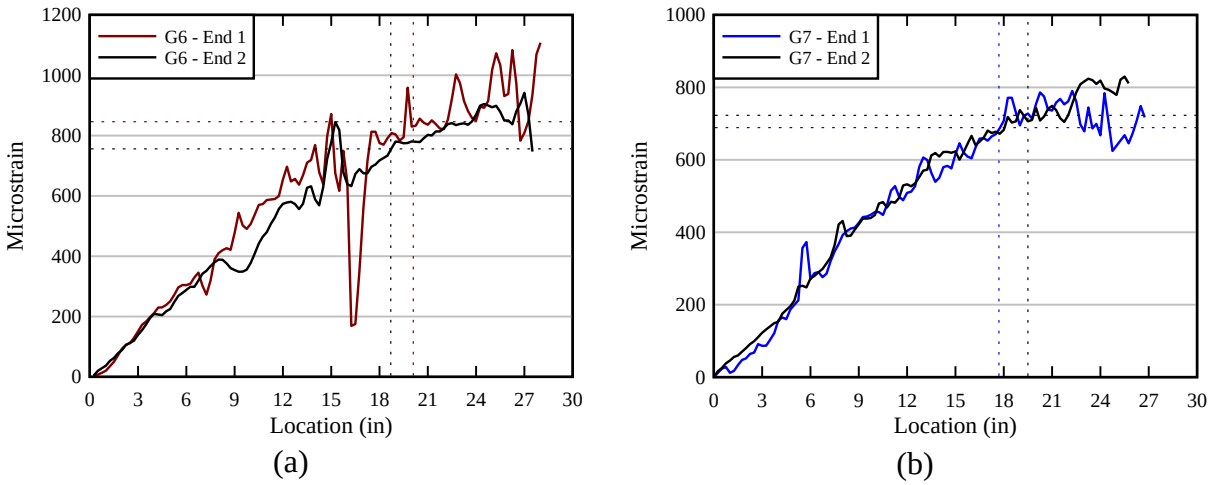

Figure 4-15 Measured transfer length using FOS: (a) G6 and (b) G7

Another method to measure transfer length was using demec points and a digital length comparator (Figure 4-16). Demec points were glued to the surface of the FIB girder bottom flange the day before detensioning. The first demec point was placed 0.5 in. from the girder end, continued with seven additional points 4 in. apart. Figure 4-17 shows the transfer length results of two ends. The transfer length of G6 – End 2 was of 15 in. and for G7 – End 2 the transfer length was 10.7 in.

Note that measurements in two ends were not possible because the points detached from the concrete surface. This occurred because the UHPC surface was still warm during installation of the demec points and the glue possibly dried before the demec point was pressed against the concrete surface, resulting in a weak bond between the demec point and the concrete. This method appears to underestimate the transfer length based on the values measured with the vibrating wire gages and fiber optics.

Figure 4-16 Transfer length measured using demec points and a digital length comparator

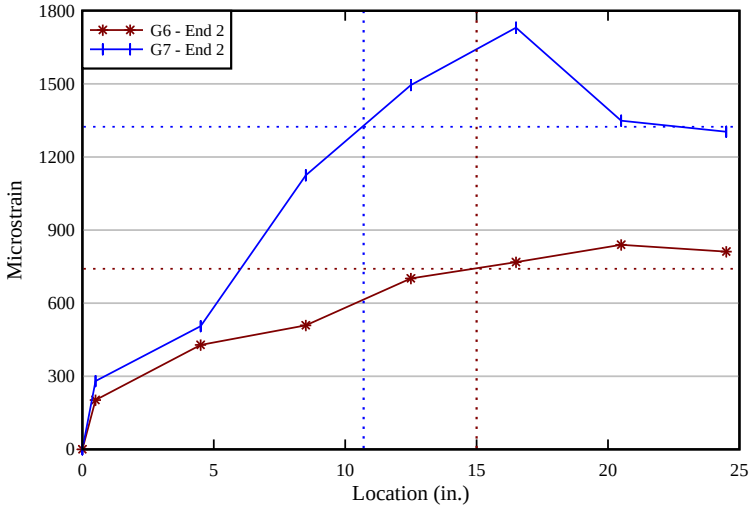

Figure 4-17 Transfer length measured with demec points

Table 4-7 shows a summary of the transfer length measured with all three methods. In addition, the values are compared to the AASHTO (2017) equation for transfer length of 60 times the strand diameter. The measured values are about half of the computed value using AASHTO (2017), meaning that this equation is not applicable to UHPC.

4.4.2 Prestress Losses

Prestress losses were measured by installing a vibrating wire gage at the midspan of the girder (Figure 4-18). Measurements were taken periodically after construction. Table 4-8 lists the measured prestress losses for G6 and G7.

Figure 4-18 Vibrating wire gages used to measure losses

Table 4-8 Effective stress after losses

Girder	*75% f_{pu} (ksi)*	After Detensioning (ksi)	7 days (ksi)	1 month (ksi)
G6	202	176	172	169
G7	202	169	163	159

4.4.3 End Region Concrete Strain

Fiber optic sensors were installed on the girder web to measure the vertical strain during detensioning (Figure 4-19). FOS were distributed in three vertical lines to measure the tensile strains created near the end of the girder (Line 1 and 2) and the compressive strains at a distance away from the end (Line 3). An overall schematic of the measurements is shown in Figure 4-20.

Line 1 was installed one inch prior to the first bundle of vertical steel reinforcement and Line 2 was glued one inch after the first bundle. Line 3 was installed 12 in. away from Line 2 to measure the balancing compressive strains. In addition to measuring the strains during detensioning, the FOS measurements were sensitive enough to identify micro-cracks, which facilitated detection (either visually or with the aid of a microscope) and mapping of cracks.

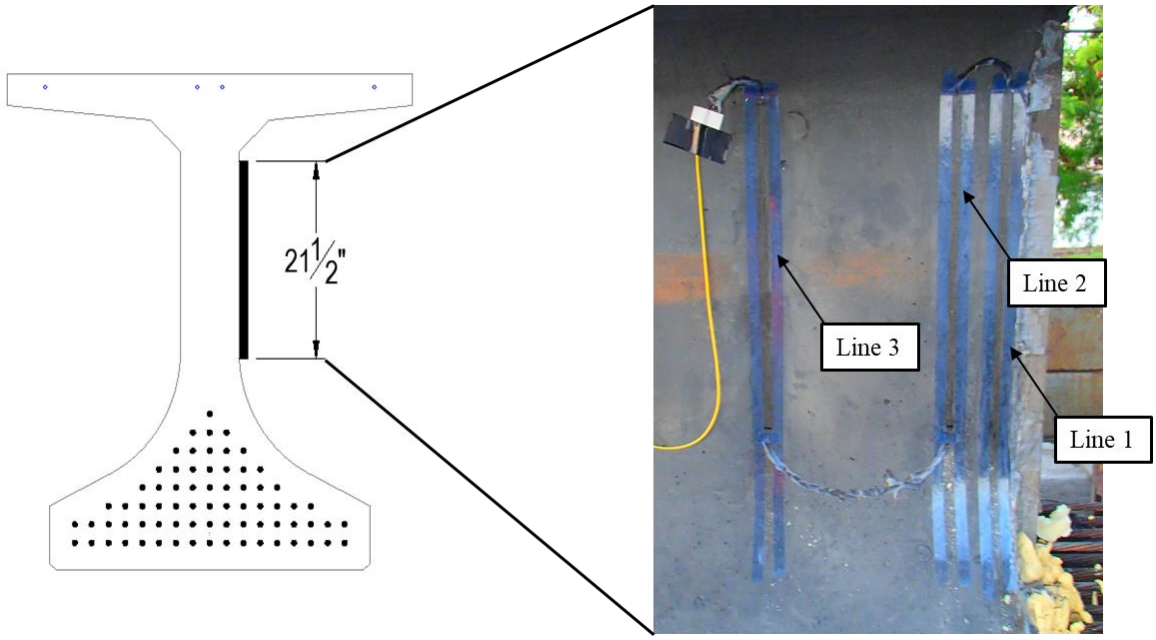

Figure 4-19 FOS installed at the girder ends

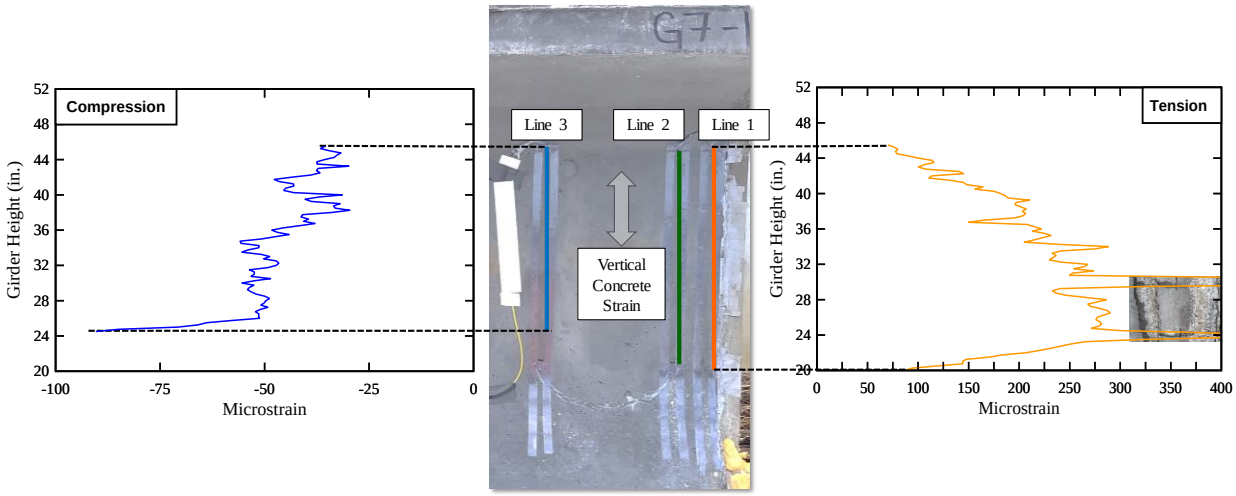

Figure 4-20 Schematic of strain measurements using FOS

Figure 4-21 shows the measured strain for all girder ends at the end of detensioning. In general, all girder ends exhibited similar strain level and distribution. This was expected because the reinforcement layout was similar for G6 and G7 at the location of Line 1 and Line 2 of the fiber optics. However, it is observed that G7 exhibits less compressive strains than G6 (based on Line 3). This difference is associated with the lower amount of vertical steel reinforcement in that region, which due to lower stiffness, it requires more length of concrete to balance the tensile forces. This results in a larger moment arm between the resultant tensile and compressive forces. An illustration of the overall behavior due to the prestress force is shown on Figure 4-22.

The data collected with the FOS provided the location of very high strains that were associated with cracks, which eventually became visible under a microscope. Cracks would typically be visible when the concrete tensile strain measured with FOS exceeded 300 microstrain. The crack width values measured with a microscope in these cases, however, were

usually less than 0.001 in., which was the resolution of the microscope. Finally, the FOS measurements were used to validate FEA models.

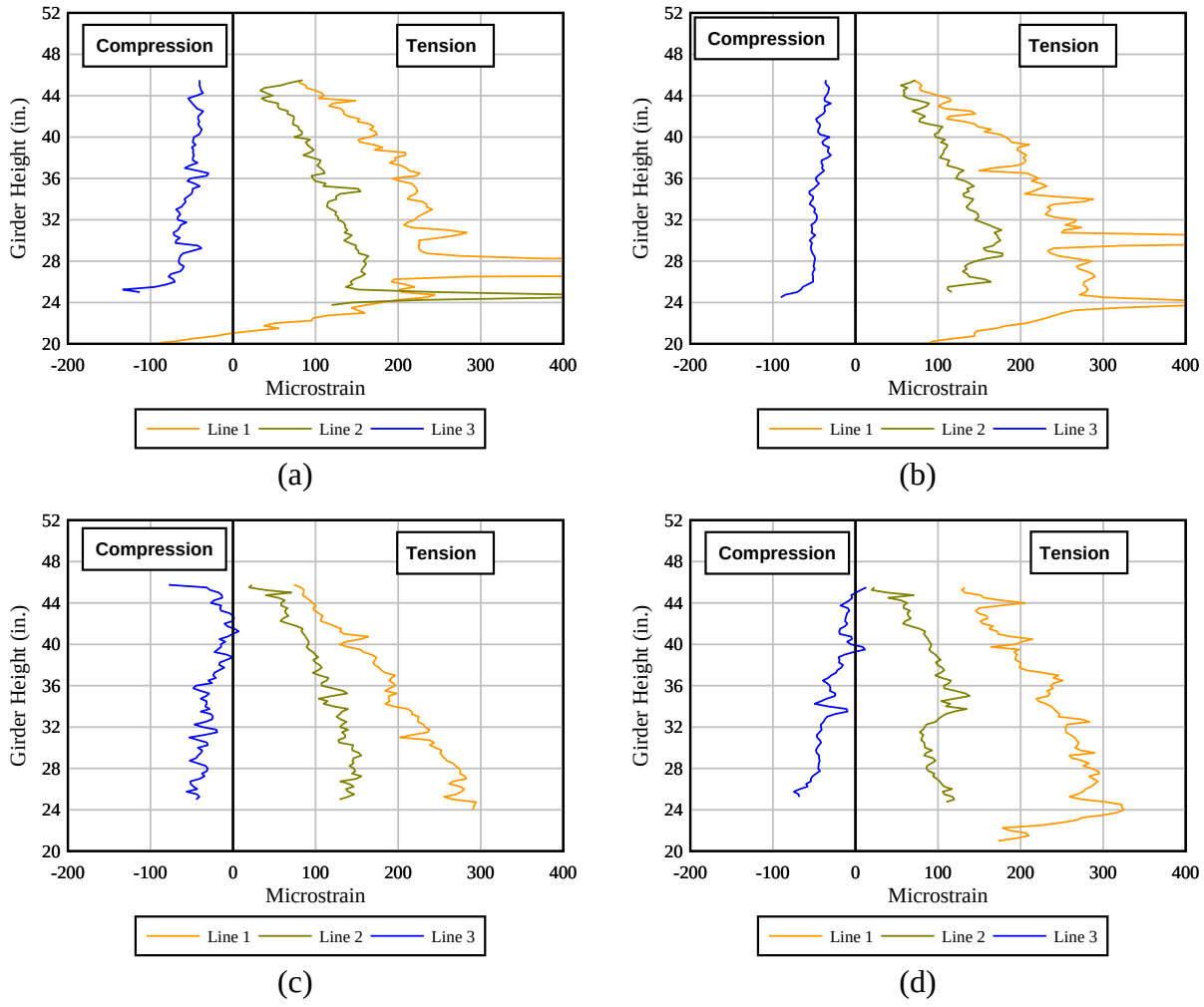

Figure 4-21 Concrete strain measured with FOS: (a) G6 – End1, (b) G6 – End2, (c) G7 – End1, and (d) G7 – End2.

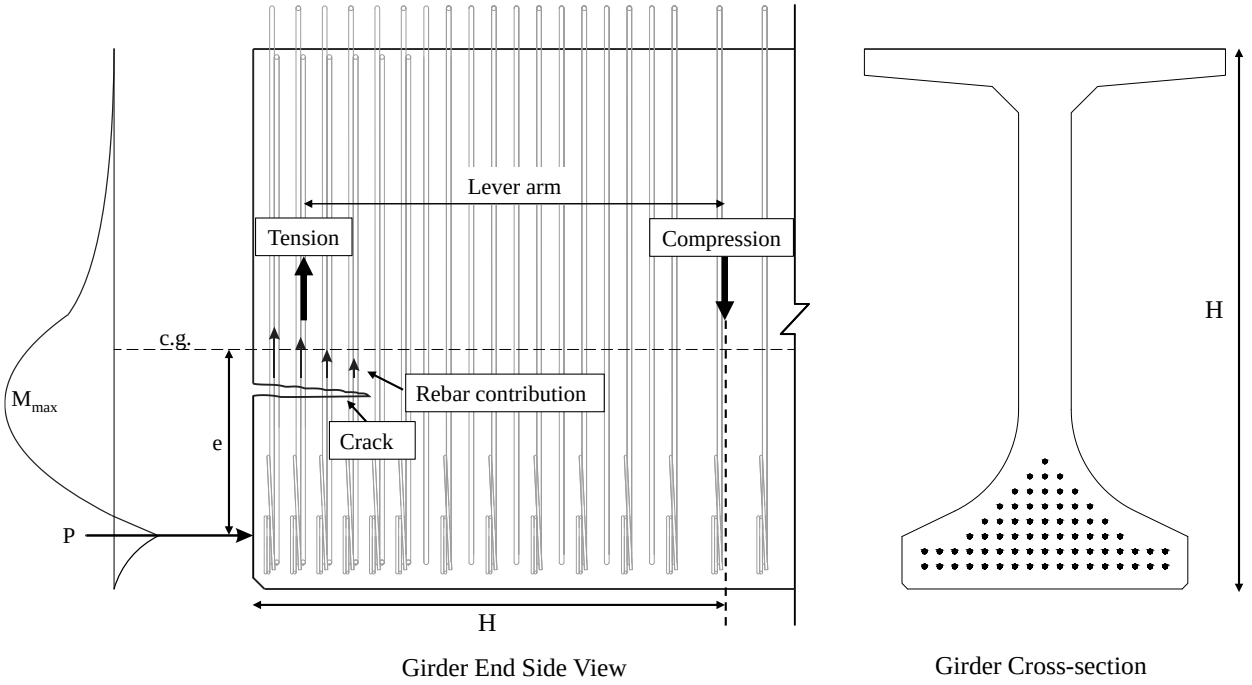

Figure 4-22 End region free body diagram

4.4.4 Mild-steel Reinforcement Strain

Strain gages were installed on vertical reinforcement (Figure 4-23) to measure strain in the steel during detensioning. If the formation of concrete cracks did not coincide with the strain gage location, then the peak steel stresses were not recorded. Nevertheless, the data collected from the mild reinforcement was used to validate FEA models.

In this study, strain gages were installed at varying heights on the two bundles of bars closest to the girder end. Strain gage "A" was installed 39 in. from the bottom, and strain gage "B" was installed 27 in. from the bottom of the girder. Figure 4-24 shows the measured strain data during the detensioning process. The time required to cut all 70 strands was approximately 45 minutes.

In Figure 4-24, positive strain is tension and negative strain is compression. Figure 4-24a and Figure 4-24b show the strain data from strain gage "A" for End 1 and End 2. The maximum strain measured with strain gages "A" was 145 με, which corresponds to a stress in the rebar of 4.2 ksi.

Similarly, Figure 4-24c and Figure 4-24d show the strain measured by strain gage "B" for both End 1 and End 2. The maximum strain measured by strain gage "B" at the end of detensioning was 277 με, which corresponds to a rebar stress of 8.0 ksi.

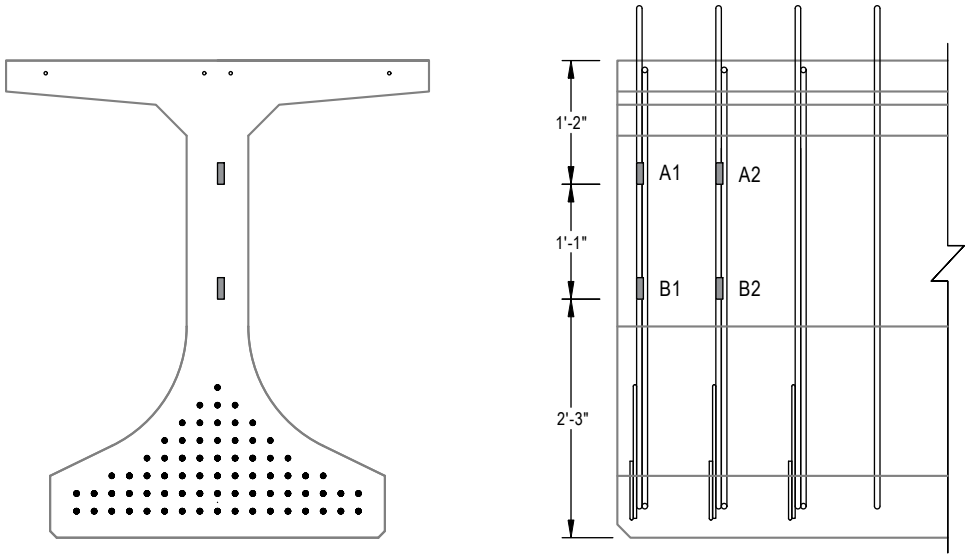

Figure 4-23 Location of strain gages installed on mild-steel reinforcement

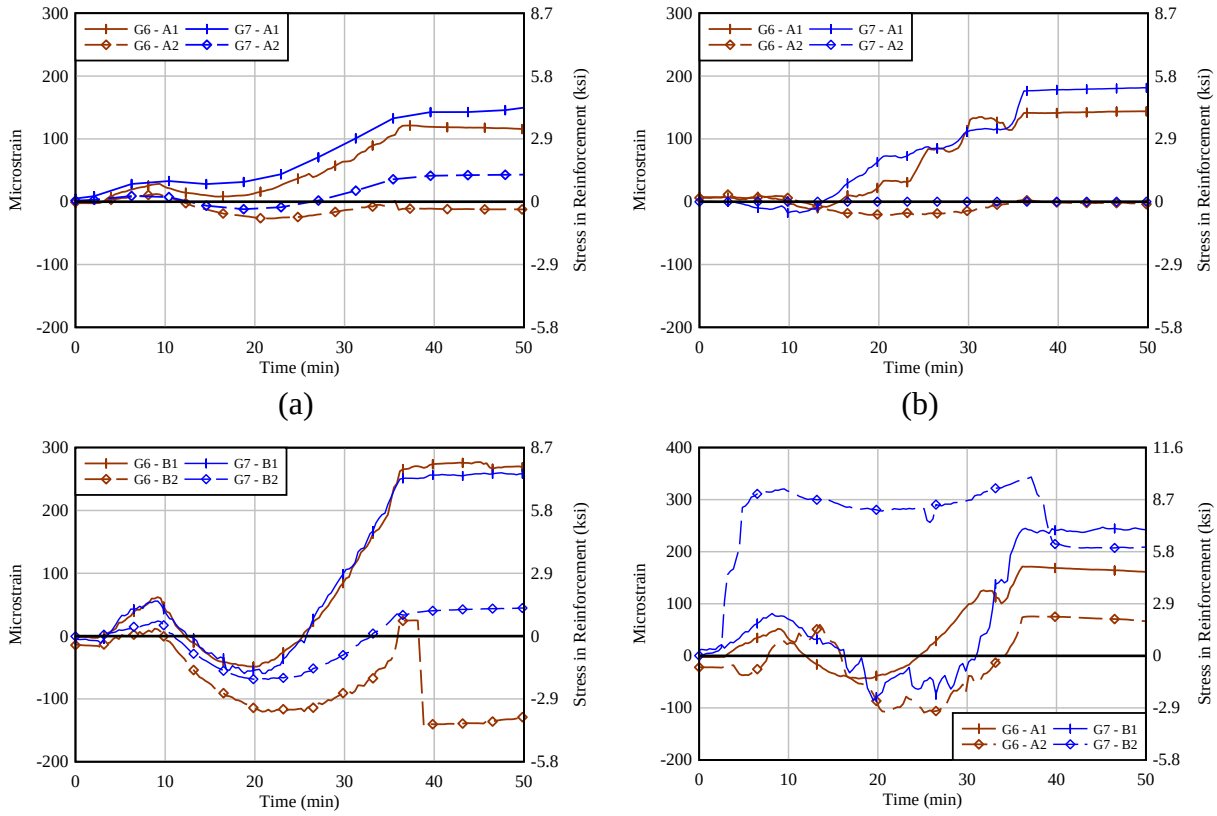

Figure 4-24 Mild-steel reinforcement strain: (a) Gage A-End 1, (b) Gage A-End 2, (c) Gage B-End 1, and (d) Gage B-End 2.

4.5 Deck Construction

Both FIB 54's were shipped to the FDOT Marcus H. Ansley Structures Research Center to perform the shear testing. After unloading of the girders in Tallahassee, cracks were monitored to determine if the crack widths grew or if any damage occurred during transport.

Deck construction was initiated with the installation of wood forms and reinforcement on the top of the precast section for the 8 in. concrete deck. Wood forms were attached to the top flange and held in place using clamps (Figure 4-25).

FDOT class II concrete (f'_c = 4,500 psi) was prepared by a local ready-mix plant in two separate trucks each having 5 cubic yards. Each concrete truck contained enough volume of concrete to pour one deck. Casting of the decks occurred inside the FDOT Structures Laboratory main floor, concrete was poured from the ready mix truck to the girder via a bucket and crane (Figure 4-26). Vibrators were used to consolidate the concrete after the pour and the decks were troweled to provide a smooth finish (Figure 4-27).

Figure 4-25 Deck construction

Figure 4-26 Method for concrete placement

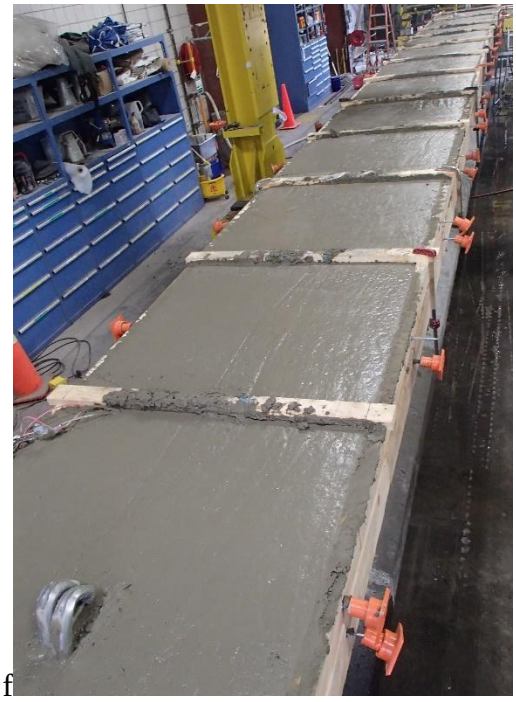

f

Figure 4-27 Finished deck construction

4.6 Shear Tests

4.6.1 Test Setup

This section describes the methods used for the shear testing of the two FIB 54 50-ft-long girders. Figure 4-28 shows a schematic depiction of the test setup including support and loading conditions. The support and load arrangement provides a shear span-to-depth ratio of 2.07.

Each specimen was loaded twice, with the load point placed near one end for the first test and near the opposite end for the second test. This approach generated four tests. Two variables were evaluated during load testing.

The first variable was the amount of shear reinforcement in the critical shear region. G6 and G7 had a total area of vertical reinforcement either 38% or 45% of that used in the typical FDOT shear reinforcement detailing. These percentages were calculated assuming that the FDOT shear detailing specifies a maximum of 6 in. spacing in the S1 region of the girder.

The second variable was the length of UHPC from the near end to the interface. End 1 of G6 and G7 had a UHPC length equal to the girder height (54 in.). End 2 of G6 and G7 had a UHPC length 1.5 times the girder height (83 in.).

Table 4-9 lists the average compressive strength of cylinders tested at the FDOT Marcus H. Ansley Structures Research Center. The reported compressive strength results are the average of three cylinders tested the same day as the shear tests.

During each load test, loading was applied twice to each specimen. The first loading simulated service load, which was estimated assuming a FIB 54 spanning 137 ft with a spacing of 6 ft. The simulated service load was approximately 280 kip. After reaching the service load, the load was held constant to identify and mark cracks. The specimens were unloaded after crack inspection.

The second loading was intended to proof test the girders to a load of 1000 kip, which is equivalent to a superimposed shear load of 809 kip. The 1000 kip load was determined from the capacity of the strong floor supporting the load frame. Past shear testing on FIB 54 girders resulted in failures below 700 kip. In addition, preliminary computations indicated failure in the SCC region at approximately 590 kip. After reaching 1000 kip, the load was then lowered to 700 kip and held to allow for safe crack inspection.

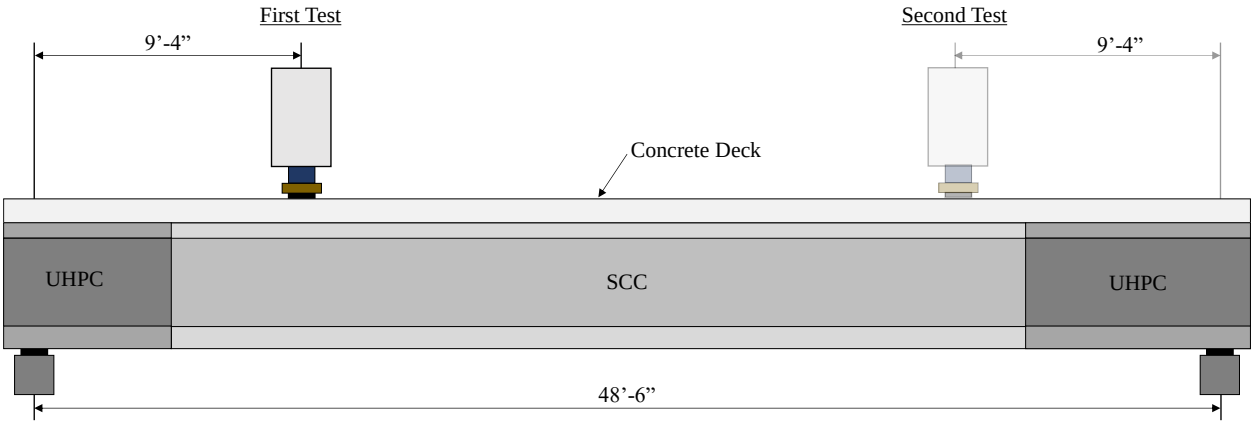

Figure 4-28 Layout of shear test

Table 4-9 Concrete compressive strength using 4 in. × 8 in. cylinders

Girder	Compressive Strength (psi)		
	Deck	UHPC Ends	SCC
G6	7,200	21,070	11,160
G7	5,920	20,670	

4.6.2 Instrumentation

Each specimen was instrumented with displacement transducers, fiber optic sensors (FOS), LVDTs and rosette gages, which are shown in the instrumentation drawings in Appendix D — Instrumentation Drawings of FIB 54 Hybrid UHPC-SCC Girder. Figure 4-29 shows a schematic of the installed instrumentation. Laser displacement transducers were used to record the deflection of the girder during loading. FOS were installed to identify cracking during loading and for finite element model validation. Displacement transducers were installed to measure displacement at the UHPC/SCC interface and strand slip at the end near the load point. Rosette gages were installed at locations of high strains during loading to calculate principal stresses and the principal strain angle.

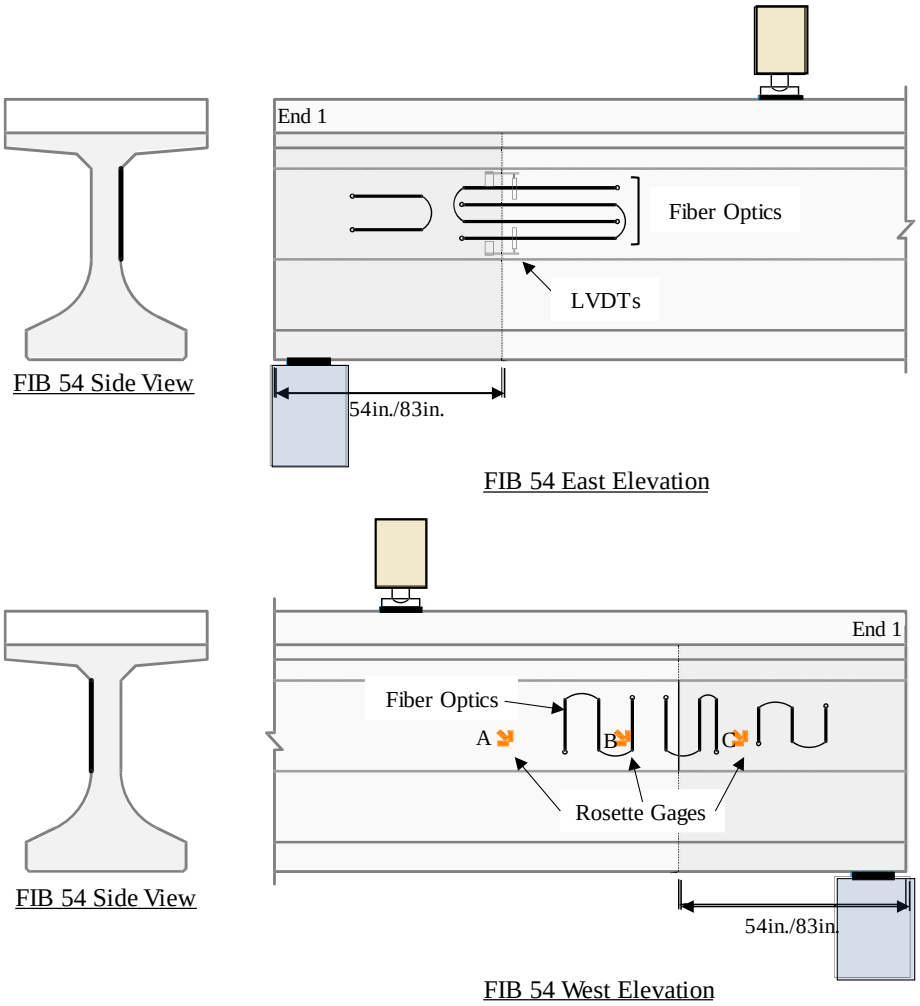

Figure 4-29 Summary of instrumentation for each load test

4.6.3 G6-End 1

G6-E1 shear load test was performed on March 5, 2020. The purpose of this test was to investigate the performance of UHPC placed at the end of the girder. In addition, vertical reinforcement was reduced by 38% from the typical FDOT detailing.

This specimen was first loaded to the service load, unloaded, inspected for cracks, and then loaded to the maximum load permitted by the test equipment. Load-displacement behavior of G6-E1 was linear-elastic during service loading (Figure 4-30). No visible cracks were found to have formed during service loading.

During the final loading, the specimen exhibited fluctuations of unknown cause in the displacement measurements; this made identification of nonlinearity difficult to identify during the test. Nevertheless, the fiber optic sensors installed on the web showed cracking initiating at 328 kip in the SCC portion of the girder. A curve fit shown in Figure 4-30 was plotted using the data prior to cracking (determined with the FOS) to identify the start of non-linearity. It appears that at a load of 765 kip the beam started to exhibit a decrease in stiffness.

Figure 4-31 shows the cracks that had formed in the front face when a maximum load of 1000 kip was reached. For safety reasons, the load was dropped and held at 700 kip to perform crack inspection and to measure crack widths. Figure 4-32 shows a schematic of the crack

patterns observed on both faces of the girder at the end of loading. The maximum crack width found on the SCC was 0.05 in. The UHPC end region, however, exhibited several diagonal cracks with a maximum crack width of 0.01 in. The SCC region exhibited four main diagonal cracks that extended from the top flange to the web, at the UHPC-SCC interface all cracks reduced in width and divided in several cracks. At least twelve cracks were marked on the UHPC continuing the path of the SCC cracks.

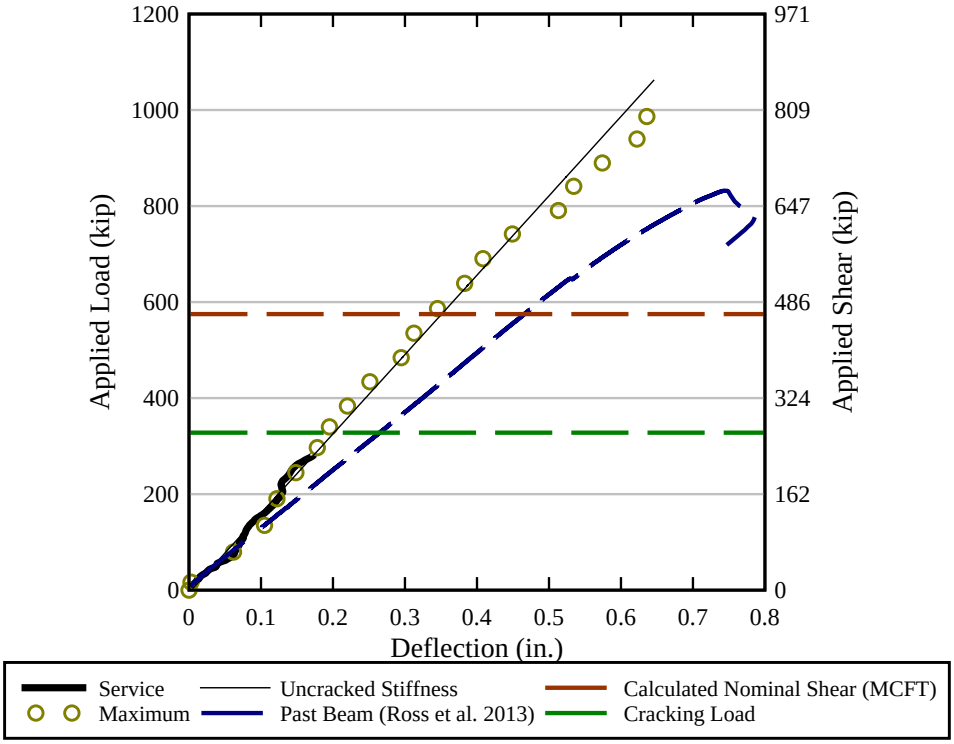

Figure 4-30 Load displacement

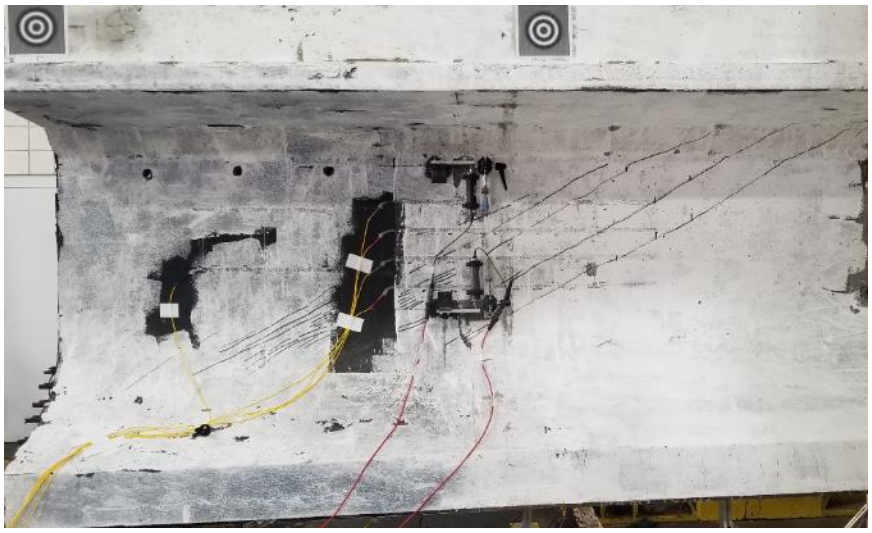

Figure 4-31 Cracking of G6-E1

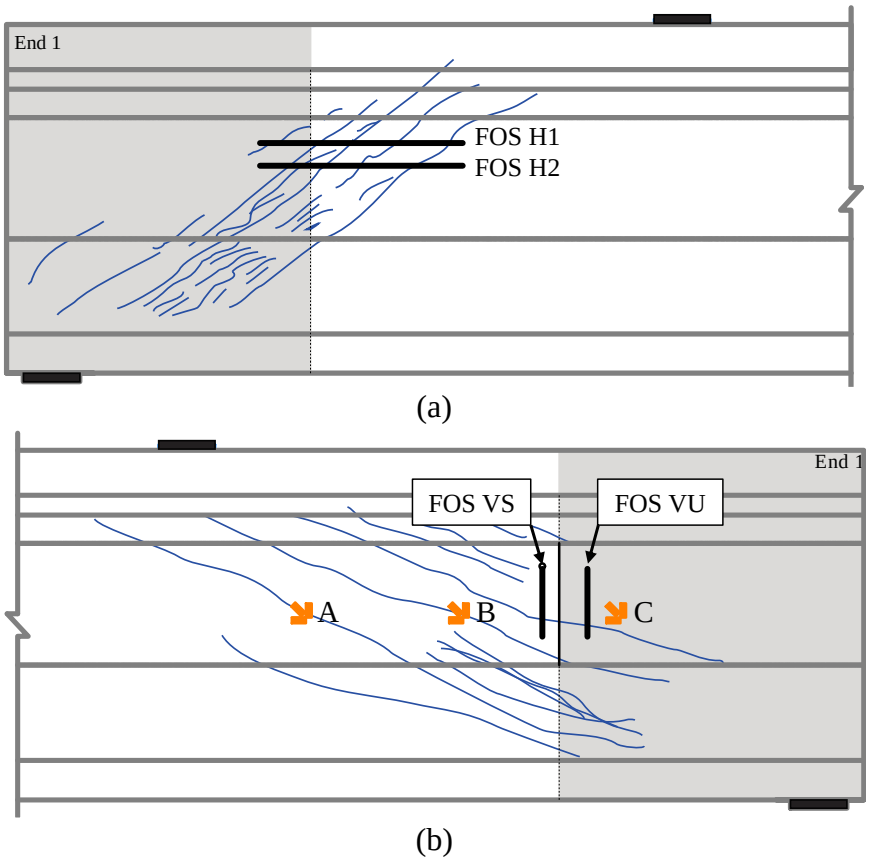

Figure 4-32 Crack patterns at final load on (a) front face and (b) back face

Figure 4-33 shows the measured strain at four increasing load levels using FOS H2 from the front face in Figure 4-32. Figure 4-33 displays the location of the three main cracks that intercepted the FOS during load application. It was observed that the girder exhibited minimal damage at loads below 250 kip, but all three main cracks had formed by the 500 kip mark.

Figure 4-34 shows strain measurements at selected load levels from FOS VS and FOS VU; Figure 4-32b shows their location on the web of the girder. FOS were placed on each side of the SCC-UHPC interface to compare the transfer of stresses between the both concretes. FOS measurements showed no indication of cracking when the load was under 250 kip; however, at 500 kip multiple cracks were observed on both sides of the interface. The UHPC region (Figure 4-34b) displayed more distributed damage as the FOS measurements show more discontinuity at high loads.

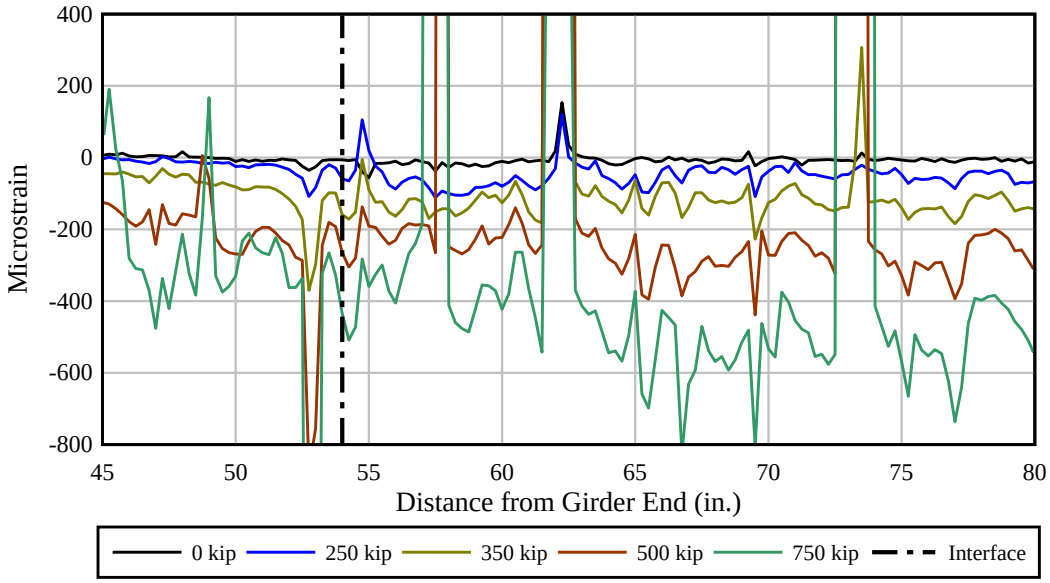

Figure 4-33 FOS H2 strain measurements

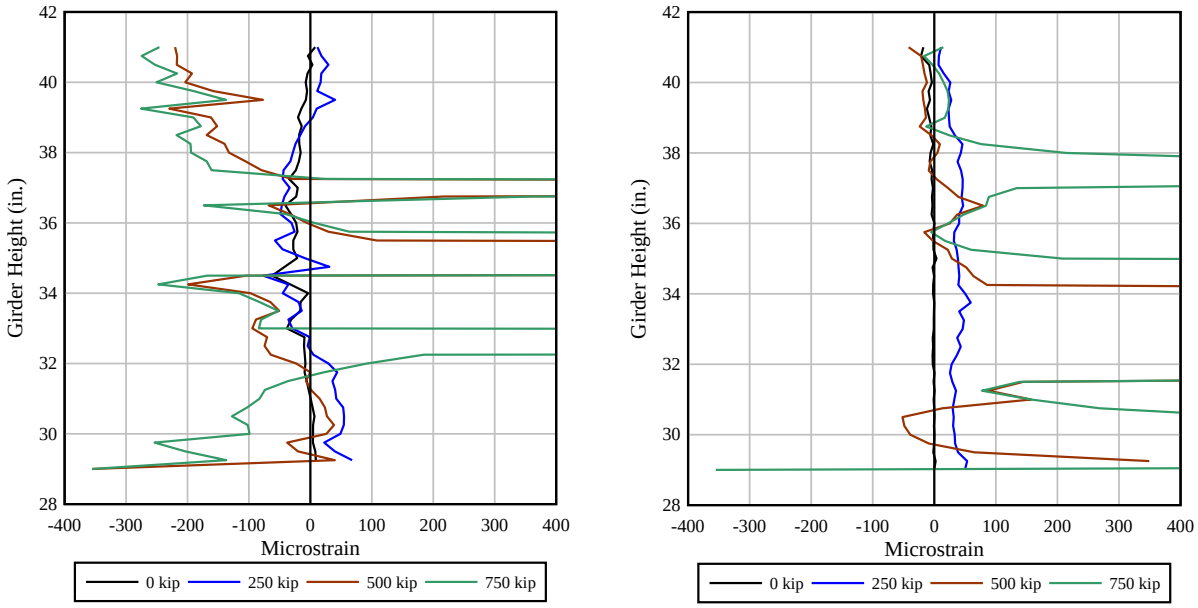

Figure 4-34 Vertical FOS strain comparison: (a) FOS VS (SCC region) and (b) FOS VU (UHPC region)

Figure 4-35 shows the displacements measured by two LVDTs to determine if slip occurred at the UHPC-SCC interface. The maximum measured displacement was 0.029 in., which was measured by LVDT 2 in the bottom portion of the web. The difference between LVDT 1 and LVDT 2 is attributed to cracking occurring at the location of the LVDT fixture, which may have caused unwanted movement. No damage was observed surrounding the interface during loading, indicating that no relative slip had occurred.

Strand slip was measured with ten LVDTs attached to the strands on the end near the load point. Figure 4-36 shows the strand slip measured during loading. Strand slip was considered negligible compared to the results reported by Ross et al. (2012) with similar test specimens, which was expected because failure did not occur. Furthermore, the strand slip results agree with previous UHPC beam tests (Graybeal, 2006), where bonded strands with slip under 0.001 in. were ignored due to negligible slip.

Figure 4-37 shows the minimum and maximum principal strains calculated with the three rosettes gages installed on the girder web. Minimum and maximum principal strains started to exhibit nonlinear behavior due to cracking at approximately 328 kip. At 600 kip, the strain gages stopped recording strain because of cracks formed on the concrete surface. Rosette A was the only one to record data throughout the loading because it was outside of the cracked region.

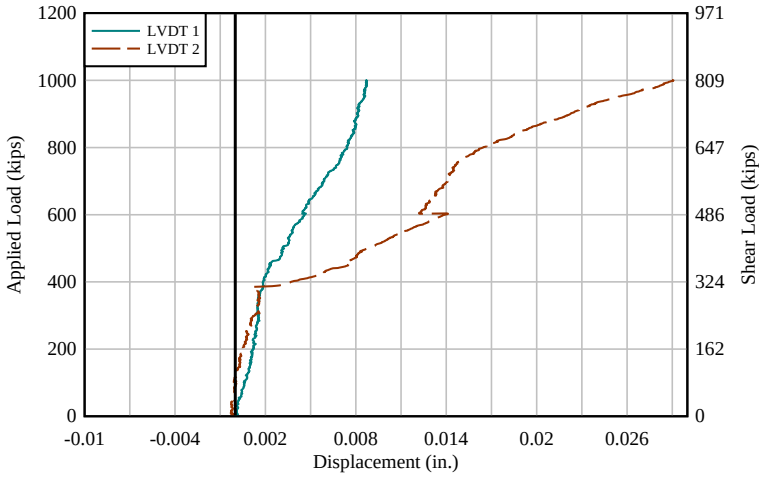

Figure 4-35 Measured interface displacement

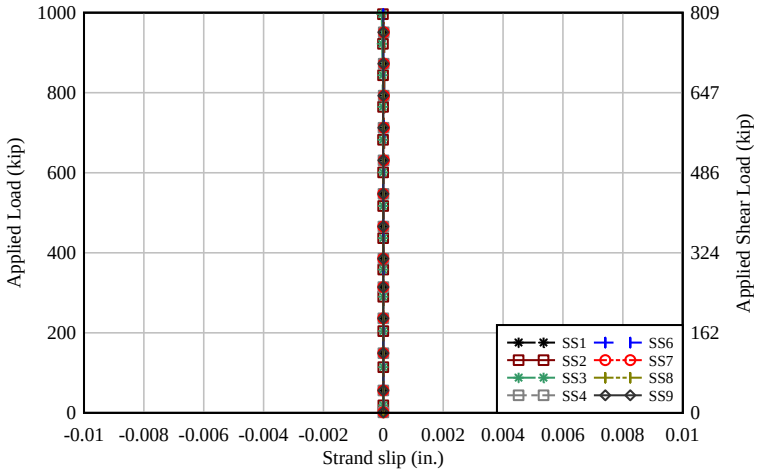

Figure 4-36 Measured strand slip

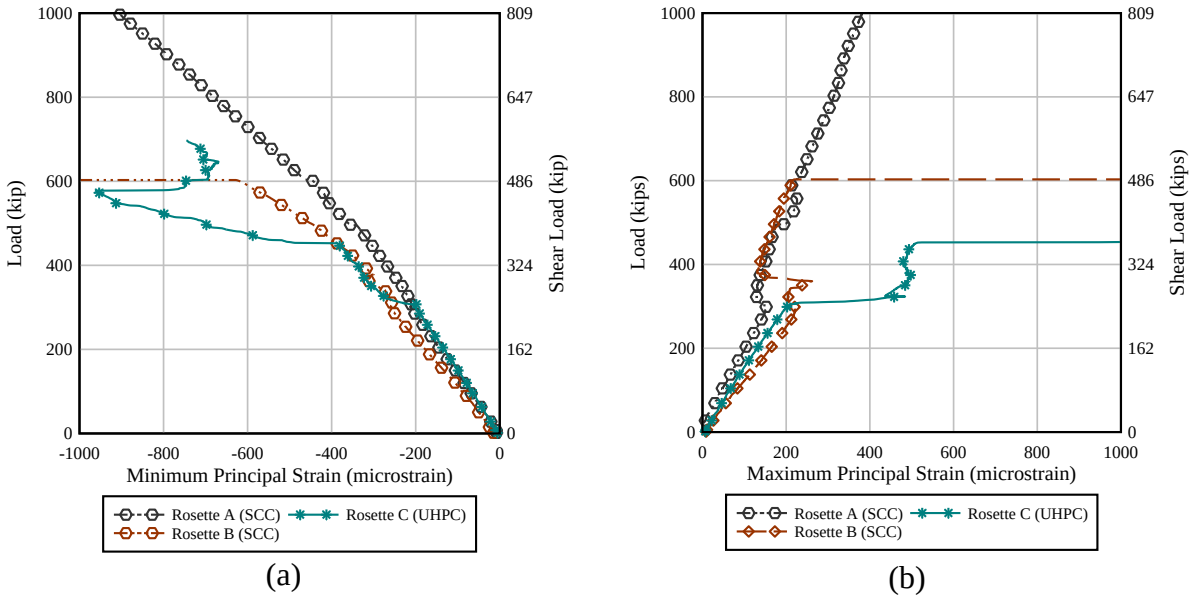

Figure 4-37 Load vs. (a) minimum principal strain and (b) maximum principal strain

4.6.4 G6-End 2

G6-E2 shear load test was performed on March 6, 2020. The primary purpose of this test was to investigate the use of a longer UHPC end region (1.5 times the girder depth) compared to End 1 (equal to the girder depth). G6-E2 had a UHPC length of 83 in. and the same vertical reinforcement detailing as G6-E1.

Figure 4-38 shows the load displacement behavior for G6-E2. This specimen was first loaded to the selected service load (noted as service in plot), unloaded, inspected for cracks, and then loaded to the maximum load permitted by the test equipment (noted as maximum in plot). Load-displacement behavior of G6-E2 was linear-elastic during service loading. At the end of service loading, the load was held for crack inspection. No cracks were found during service loading.

The specimen was then loaded up to the maximum floor capacity (Figure 4-38). The curve fit shown in Figure 4-38 was plotted using the data prior to cracking; strain measurements with the FOS indicated that cracking began to form at a load of 454 kip, which is 126 kip higher than the crack initiation load in G6-E1, suggesting that this end had higher cracking strength.

Figure 4-39 shows the front face cracking that occurred at the maximum load of 1,000 kip. For safety reasons the load was dropped and held at 700 kip to perform crack inspection and to measure crack widths.

Figure 4-40 shows a schematic of the crack patterns observed on both faces of the girder at the end of loading. The SCC region exhibited two primary diagonal cracks that extended from the top flange to the web, at the UHPC-SCC interface all cracks split in several cracks of smaller widths. The maximum crack width found on the SCC was 0.03 in. The UHPC end region exhibited several diagonal cracks with a maximum crack width of 0.005 in. Cracks found on the SCC and UHPC had smaller widths than G6-E1 at the end of testing. Crack distribution suggests that increasing the length of UHPC to 1.5D allowed the girder to distribute the damage along the height of the girder (multiple cracking), likely resulting in more engagement of the steel fibers and mild-steel reinforcement.

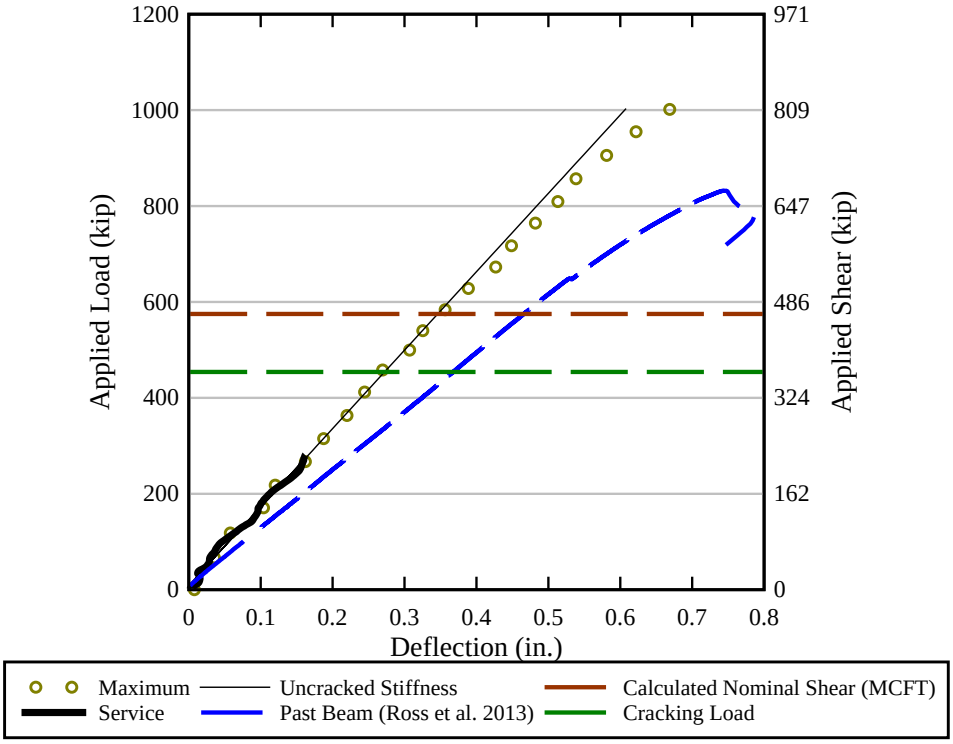

Figure 4-38 Load displacement

Figure 4-39 Cracking of G6-E2

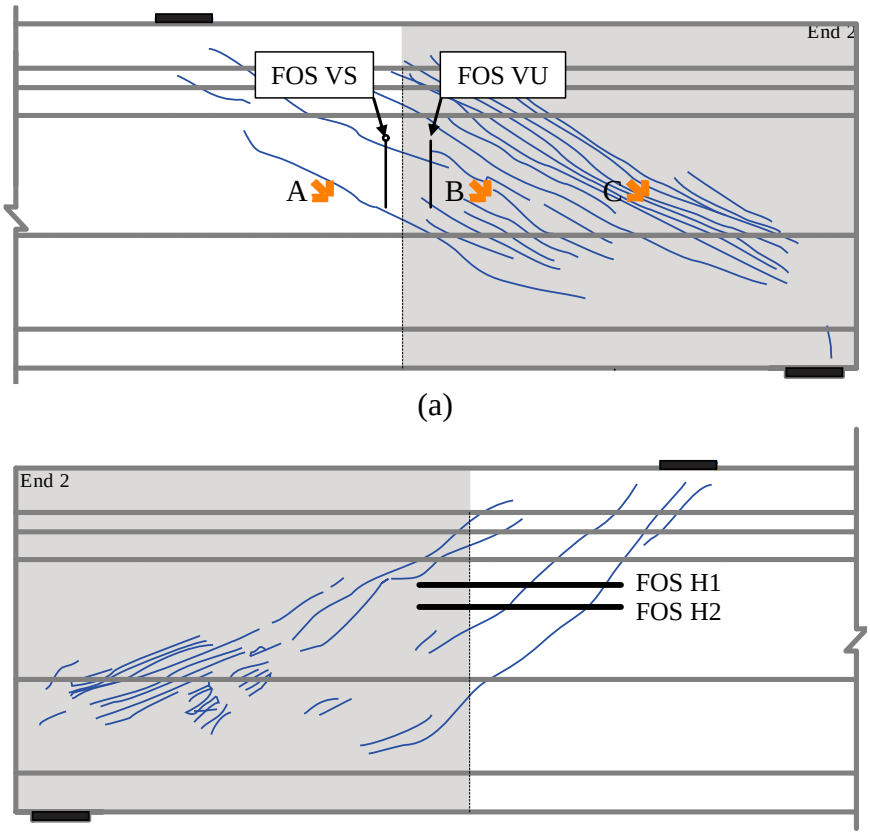

Figure 4-40 Crack patterns at final load on (a) back face and (b) front face

Figure 4-41 and Figure 4-42 shows the measured strain at different load levels using FOS H1 and H2 from the front face in Figure 4-40. Both FOS horizontal lines show similar strain levels on the SCC and UHPC, indicating that no slip occurred at the interface. The FOS was able to measure strain during the entire loading, indicating less damage than G6-E1.

Figure 4-43 shows strain measurements at selected load levels from FOS VS and FOS VU; Figure 4-40a shows their location on the web of the girder. FOS were placed on each side of the SCC-UHPC interface to compare the transfer of stresses between both concretes.

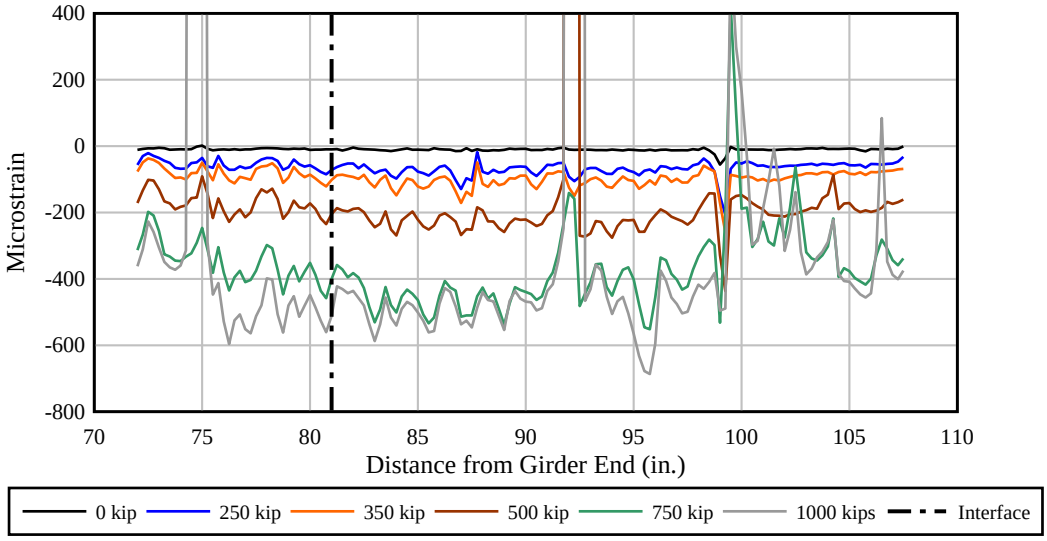

Figure 4-41 Line 1 horizontal FOS strain measurements

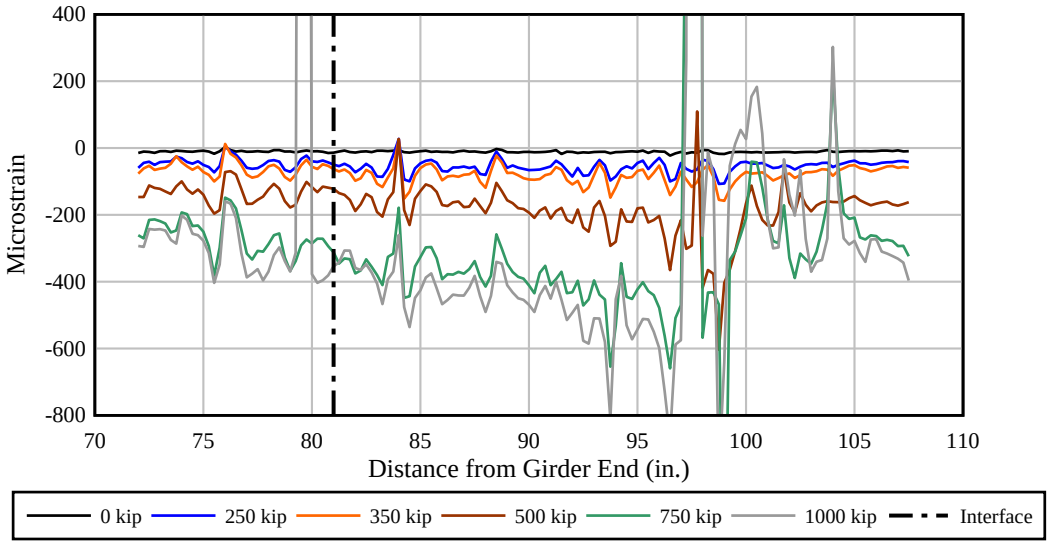

Figure 4-42 Line 2 horizontal FOS strain measurements

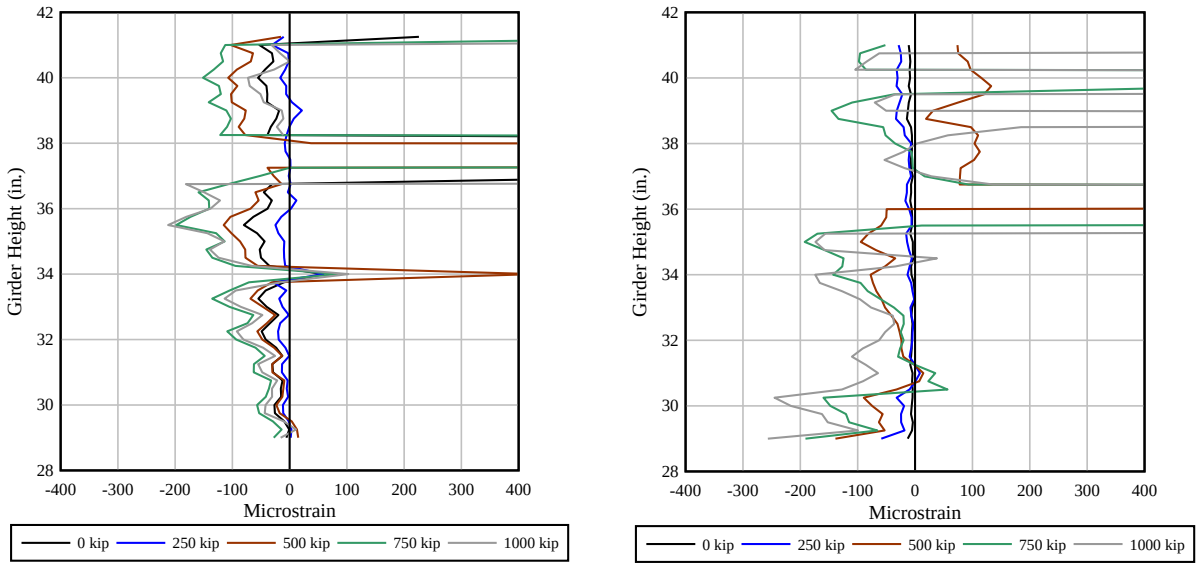

Figure 4-43 Vertical FOS strain comparison: (a) SCC region and (b) UHPC region

Figure 4-44 shows the displacements measured by two LVDTs to determine if slip occurred at the interface. The maximum displacement was 0.017 in., which was measured by LVDT 2 in the bottom portion of the web. However, the sudden change in slope suggests that the LVDT fixture may have moved due to cracking at approximately 700 kip and 780 kip. No damage was visually observed at the interface during loading, indicating that the interface was capable of transferring loads between SCC and UHPC.

Strand slip was measured with ten LVDTs attached to the strands on the end near the load point. Figure 4-45 shows the strand slip measured during loading. Strand slip was negligible because it did not exhibit a sustained increase in slip with load, which was expected because failure did not occur and no cracks were observed near the bottom flange.

Figure 4-46 shows the minimum and maximum principal strains calculated with the three rosettes gages installed in the girder web. Minimum and maximum principal strains of all rosette gages started to exhibit nonlinear behavior due to cracking at approximately 450 kip or 300 microstrain.

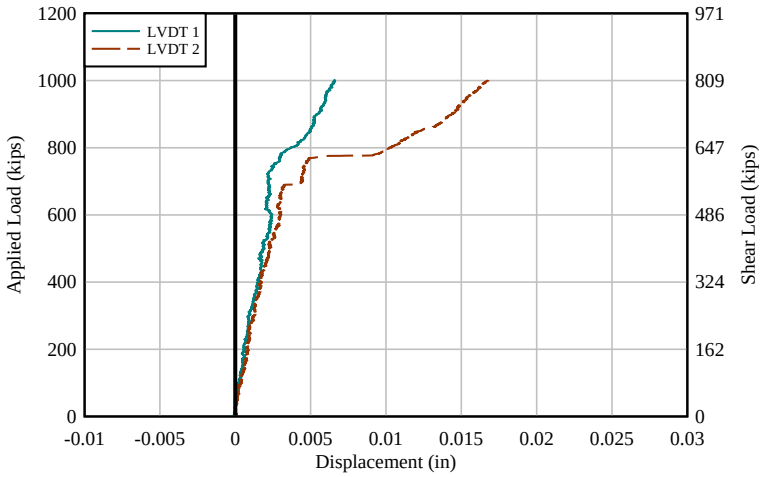

Figure 4-44 G6-E2 interface displacement

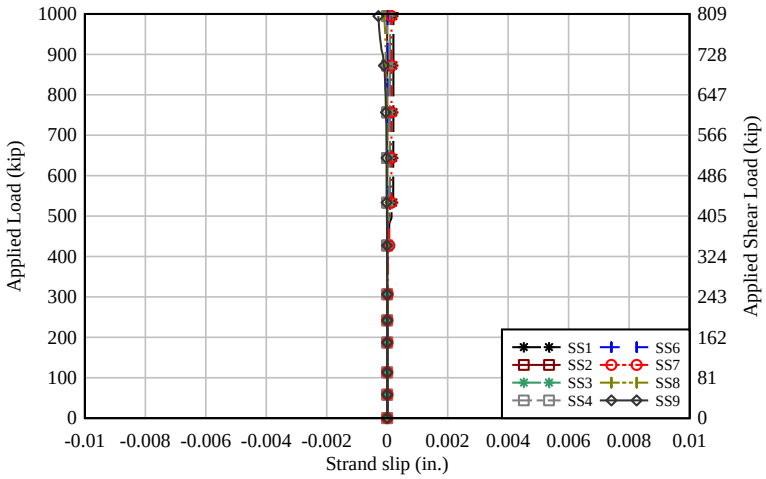

Figure 4-45 G6-E2 measured strand slip

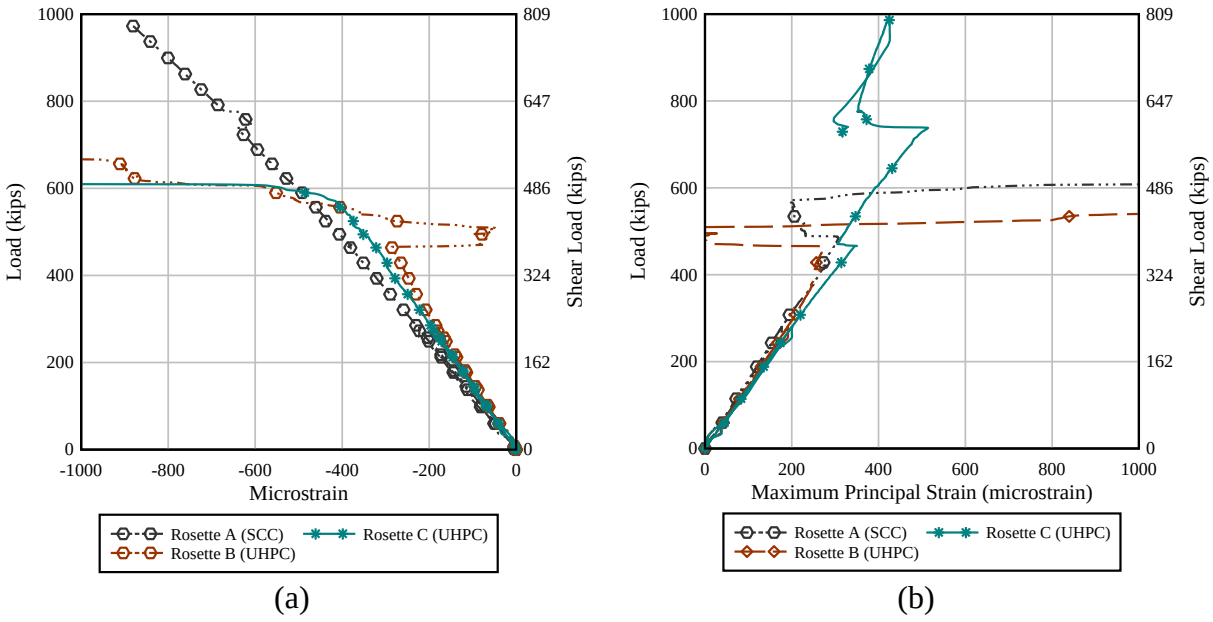

Figure 4-46 Load vs. (a) minimum principal strain and (b) maximum principal strain

4.6.5 G7-End 1

G7-E1 shear load test was performed on March 2, 2020. The purpose of this test was to investigate a further reduction in end region reinforcement. This girder end had UHPC length equal to the girder depth. Vertical reinforcement was reduced by 45% from the typical FDOT detailing.

G7-E1 was the first specimen to be tested, thus it was the first test to show that the girder strength exceeded the structural floor rated capacity. Initially, the test setup used a span of 38.9 ft, which at a load of 1,000 kip resulted in a superimposed shear of 760 kip. After the initial loading to the floor capacity, the distance between supports was increased to 48.5 ft to increase the shear on the test area. The new distance between supports utilized the entire length of the girder and resulted in a maximum superimposed shear load of 809 kip, which was insufficient to reach the girder strength.

Figure 4-47a shows the load-displacement behavior of G7-E1 using the initial distance between supports. During service loading, the behavior was linear elastic. During the second loading, the specimen started to exhibit nonlinear behavior after 475 kip of shear load (Figure 4-47a). Strain collected with the fiber optic sensors indicated that the first crack was generated at 312 kip of load.

The second test having a greater distance between supports consisted of only loading the specimen once until 1,000 kip. Service loading was not performed because the specimen was already cracked from the loading with the initial support layout. The loss of stiffness is noticeable by comparing the load-deflection results to the curve fit of the uncracked specimen.

Figure 4-48 shows cracking that occurred at the maximum load of 1,000 kip. For safety reasons, the load was dropped and held at 700 kip to perform crack inspection and to measure crack widths. Figure 4-49 shows a schematic of the crack patterns observed on both faces of the girder at the end of loading. The SCC region exhibited six diagonal cracks with a maximum crack width of 0.02 in. In general, the crack pattern was similar to G6-E1, but with two

additional cracks on the SCC likely due to the reduction of vertical reinforcement. The UHPC end exhibited multi-cracking with the same orientation as the SCC cracks. Crack widths in the UHPC ranged from 0.001 in. to 0.003 in.

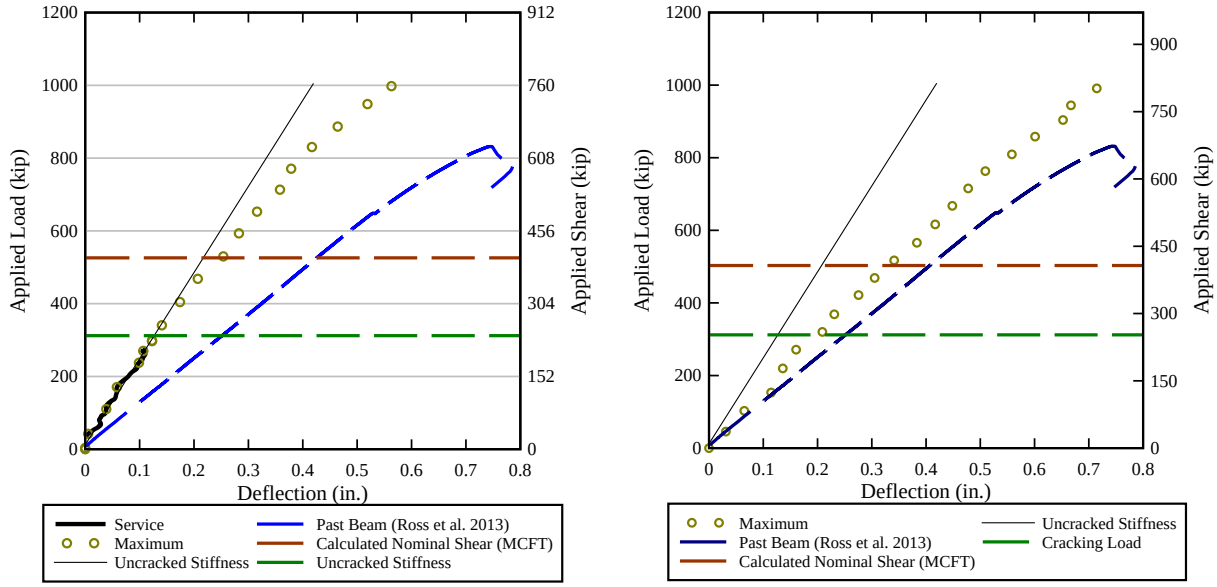

(a) (b)

Figure 4-47 Load vs. deflection results: (a) initial supports layout, and (b) modified supports layout

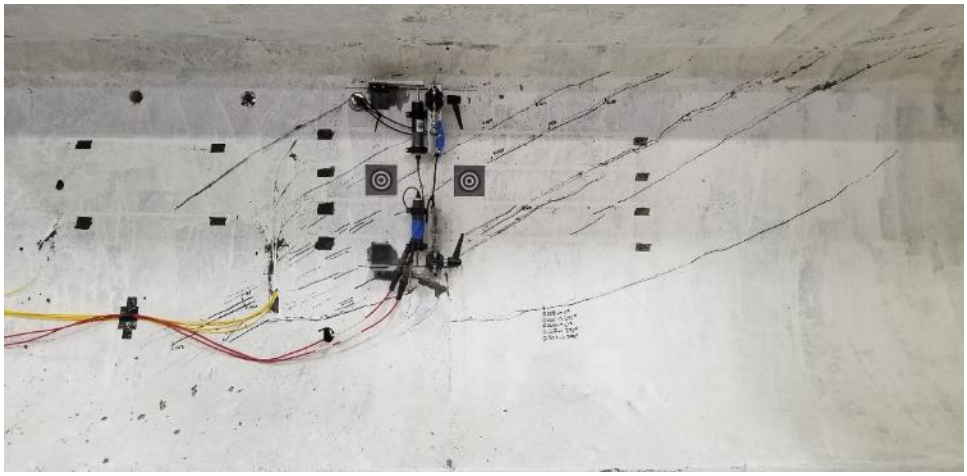

Figure 4-48 Cracking of G7-E1

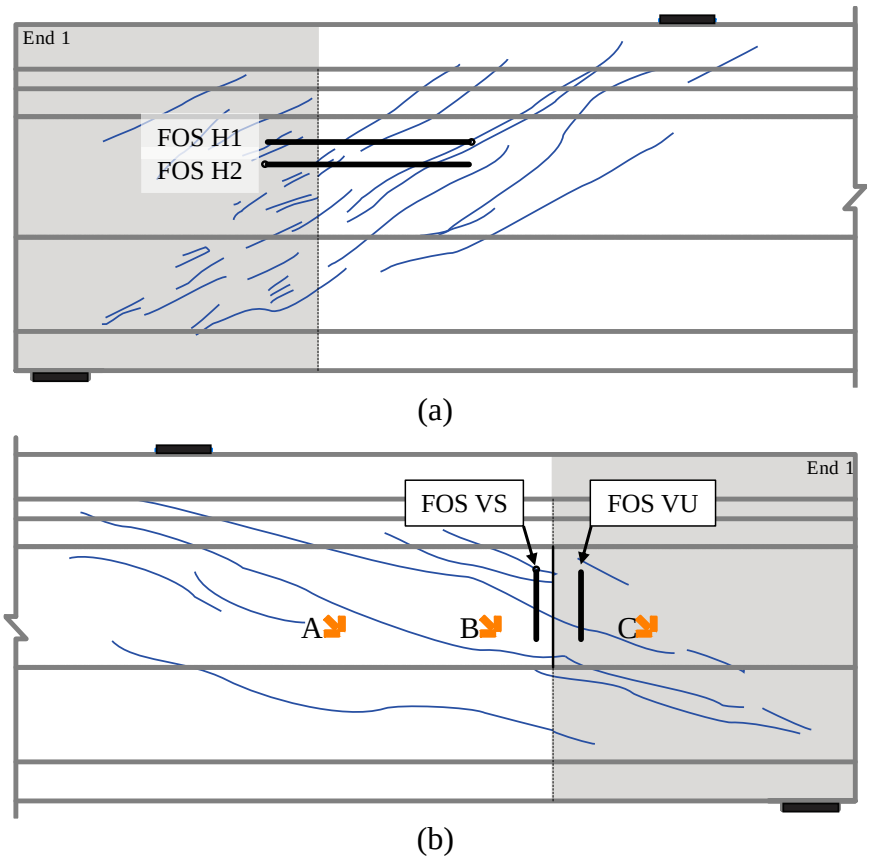

Figure 4-49 Crack patterns at final load on (a) front face and (b) back face

Figure 4-50 and Figure 4-51 shows the measured strain at different load levels using FOS H1 and H2 from the front face in Figure 4-49. Both FOS display the location of the main cracks that intercepted the FOS during load application. It can be observed that the girder exhibits minimal damage at loads below 250 kip, but all three main cracks began to form by the 350 kip mark. Also, both FOS channels exhibit higher microstrain at the location of the interface compared to the previous specimens.

Figure 4-52 shows strain measurements at selected load levels from FOS VS and FOS VU; Figure 4-49b shows their location on the web of the girder. FOS were placed on each side of the SCC-UHPC interface to compare the transfer of stresses between both concretes. Both FOS lines show peaks associated cracks intercepting the FOS channel at 500 kip. The FOS was damaged before reaching 750 kip, confirming that this end exhibited the most damage among all tests.

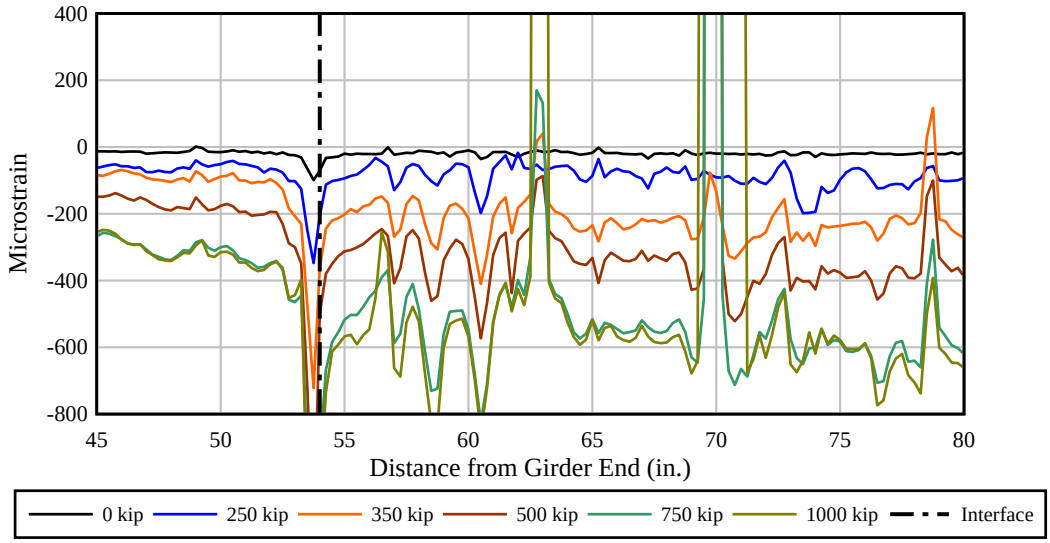

Figure 4-50 Line 1 horizontal FOS strain measurements

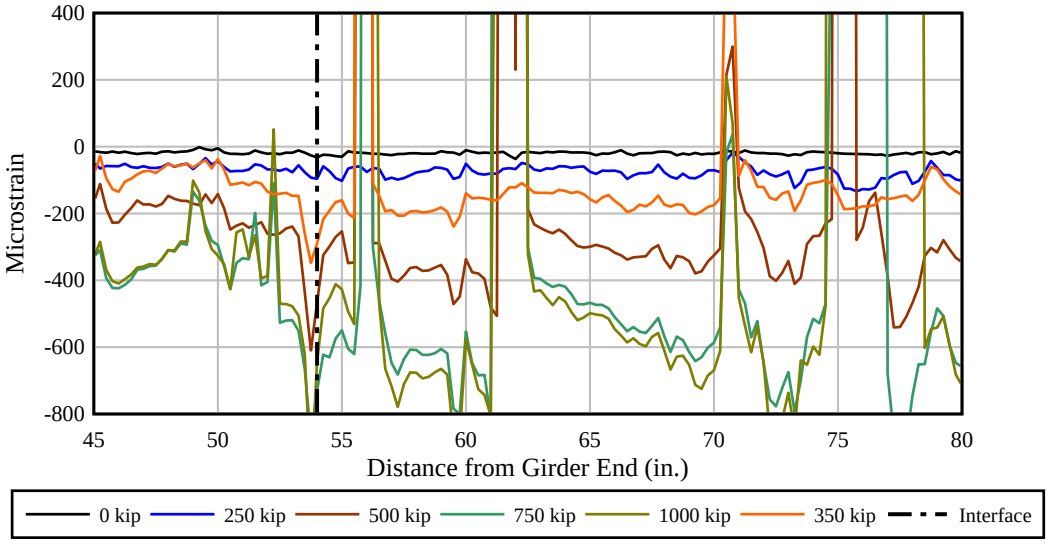

Figure 4-51 Line 2 horizontal FOS strain measurements

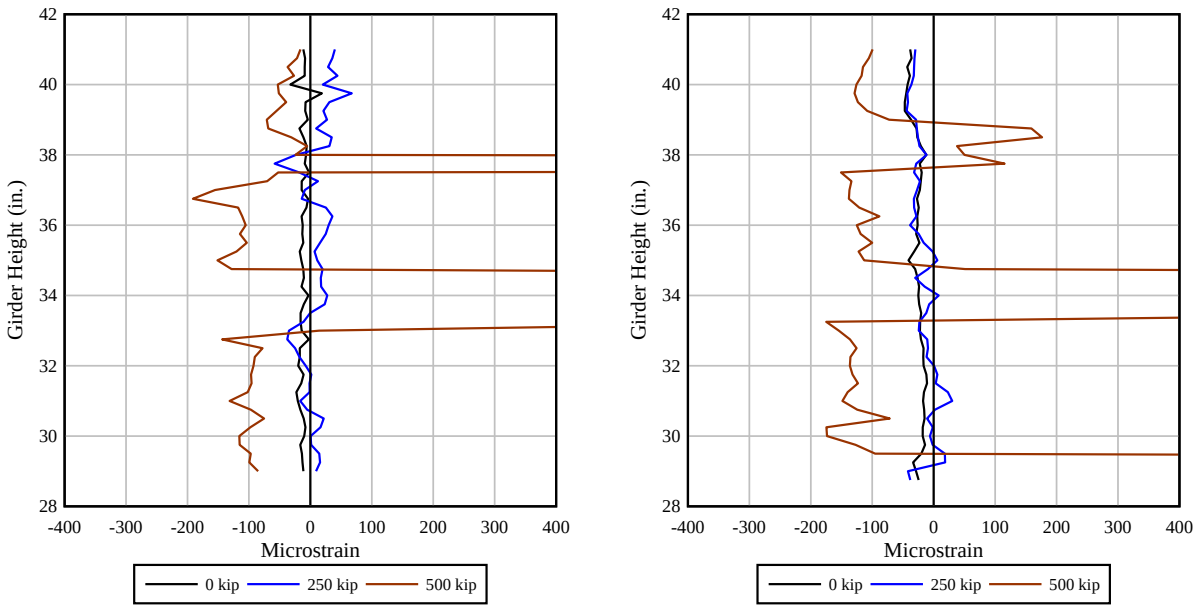

Figure 4-52 Vertical FOS strain comparison: (a) SCC region and (b) UHPC region

Figure 4-53 shows the displacements measured by two LVDTs to determine if slip occurred at the interface. The maximum displacement was 0.015 in., which was measured by LVDT 2 in the bottom portion of the web. Both LVDTs exhibited a continue increase in displacement with load. This behavior was a consequence of the cracks already in place from the first test. Recall that in previous specimens, LVDT 2 exhibited sudden shifts due to cracks forming at the location of the LVDT holder.

Strand slip was measured with ten LVDTs attached to the strands on the end near the load point. Figure 4-54 shows the strand slip measured during loading. Strand slip was negligible because it did not exhibit a sustained increase in slip with load, which was expected because failure did not occur and no cracks were observed near the bottom flange.

Figure 4-55 shows the minimum and maximum principal strains calculated with the three rosettes gages installed in the girder web. Minimum and maximum principal strains of all rosette gages started to exhibit nonlinear behavior due to cracking at approximately 375 kip or 150 microstrain.

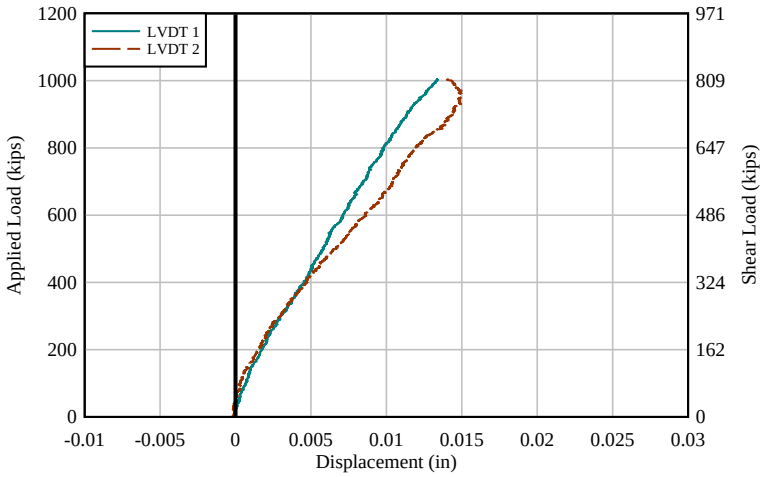

Figure 4-53 G7-E1 interface displacement

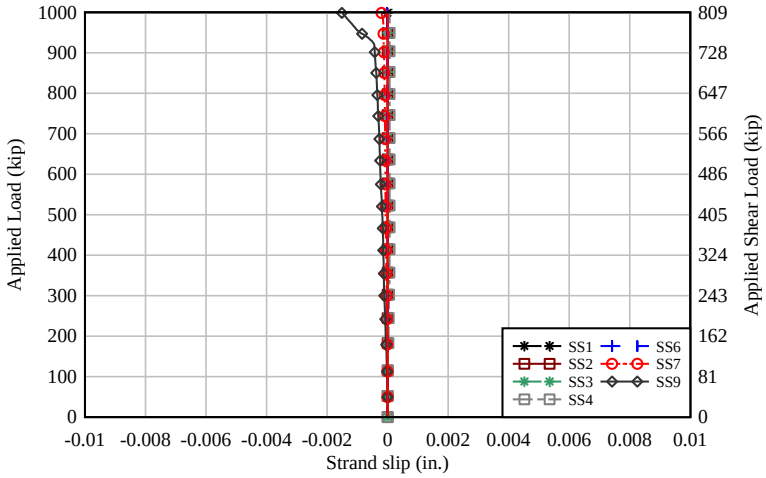

Figure 4-54 G7-E1 measured strand slip

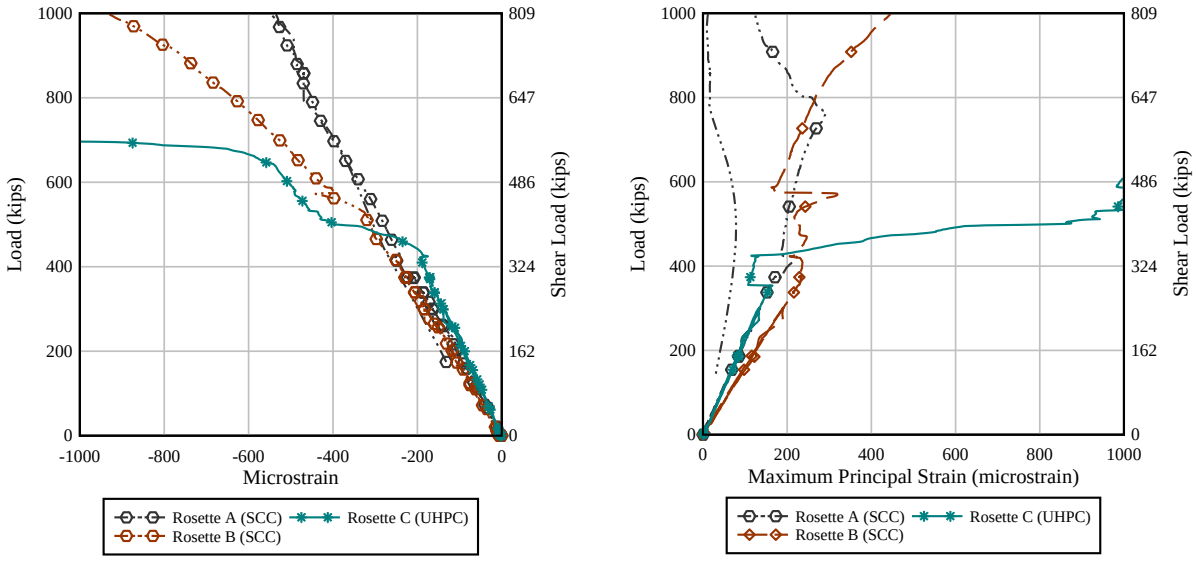

Figure 4-55 Load vs. (a) minimum principal strain and (b) maximum principal strain

4.6.6 G7-End 2

G7-E2 shear load test was performed on March 3, 2020. The primary purpose of this test was to investigate the effect of the use of a longer UHPC end region and reduced reinforcement. G7-E2 had a UHPC length of 83 in. and the same vertical reinforcement detailing as G7-E1.

This specimen was first loaded to the service load, unloaded, inspected for cracks, and then loaded to the maximum load permitted by the test equipment. Load-displacement behavior of G7-E2 was linear-elastic during service loading (Figure 4-56). At the end of service loading, the load was held for crack inspection. No cracks were found during service loading.

The specimen was the loaded up to the floor capacity. Figure 4-56 shows the load-displacement results up to 809 kip of superimposed shear. Strain collected with the FOS indicate that the first crack formed in the SCC at a load of 380 kip, which exceeds End 1 by 60 kip. The data before cracking was used to plot a curve fit to identify non-linearity as load increases. A slope comparison indicates that the beam began to lose stiffness at 654 kip.

Figure 4-57 shows cracking that occurred at the maximum load of 1,000 kip. For safety reasons the load was dropped and held at 700 kip to perform crack inspection and to measure crack widths. Figure 4-58 shows a schematic of the crack patterns observed on both faces of the girder at the end of loading. The SCC region exhibited four diagonal cracks with a maximum crack width of 0.006 in. The decrease in crack width is attributed to the longer section of UHPC, which limited the length available on the SCC for crack propagation. Similar to the previous tests, the cracks on the SCC stopped at the interface transitioning to multi-cracking on the UHPC. Crack widths on the UHPC side ranged from 0.001 in. to 0.002 in.

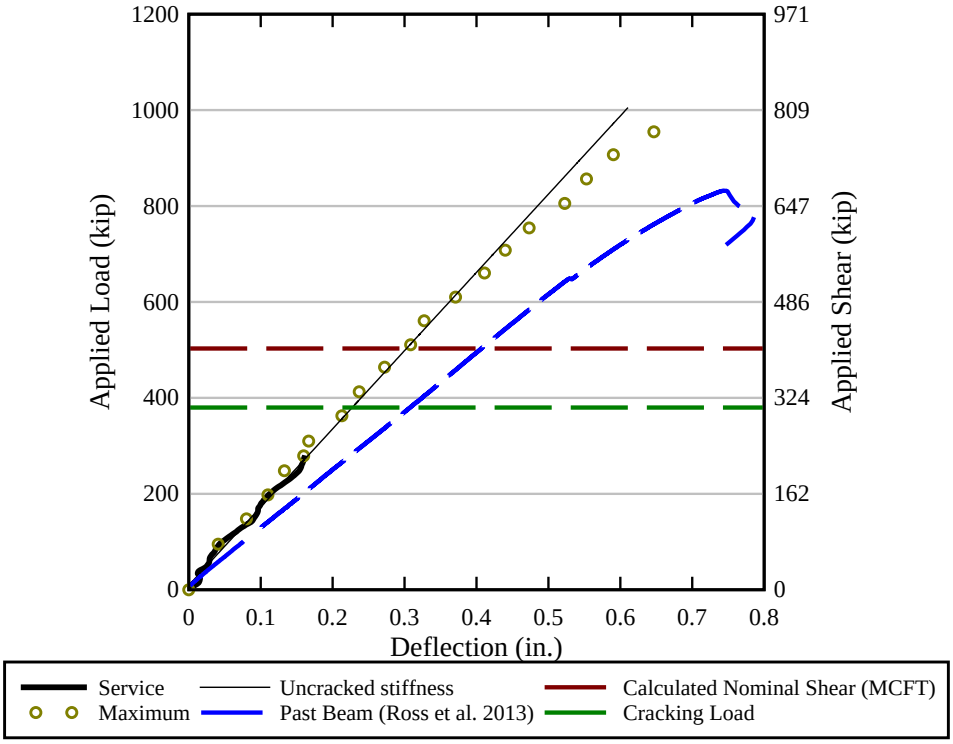

Figure 4-56 G7-E2 load-displacement behavior

Figure 4-57 Cracking of G7-E2

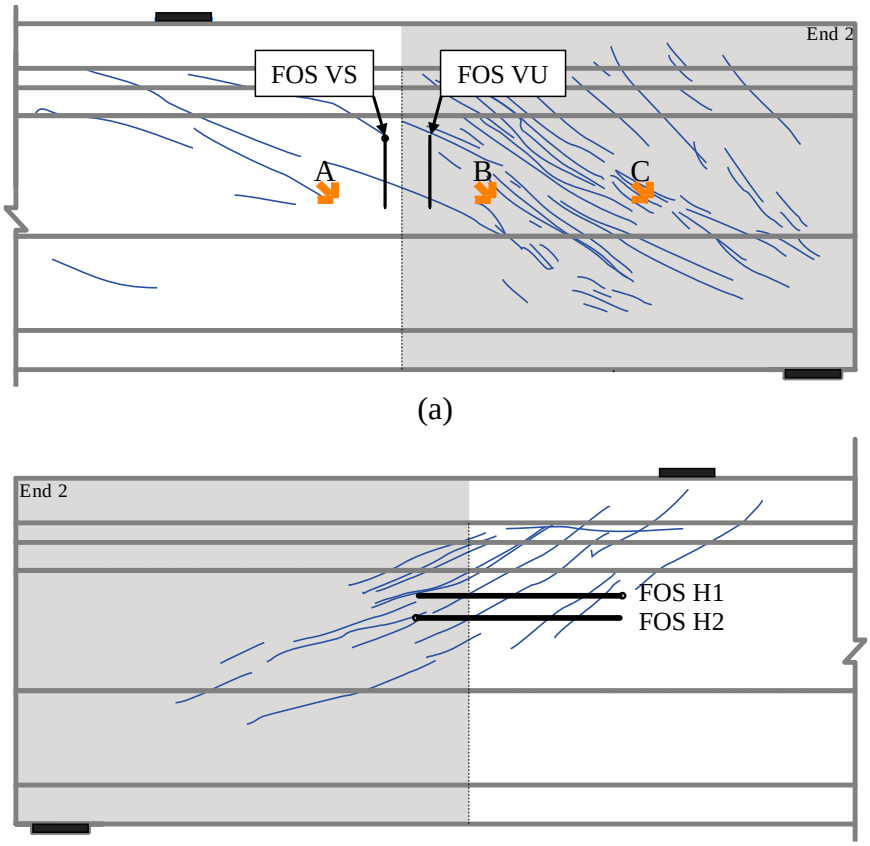

Figure 4-58 Crack patterns at final load on (a) front face and (b) back face

Figure 4-59 and Figure 4-60 shows the measured strain at different load levels using FOS H1 and H2 from the back face in Figure 4-58. FOS H1 shows similar strain levels on the SCC and UHPC, meaning that both concretes had similar damage near the interface. FOS H1 and H2 were able to measure strain during the entire loading, indicating less damage than G7-E1.

Figure 4-61 shows strain measurements at selected load levels from FOS VS and FOS VU. FOS were placed on each side of the SCC-UHPC interface (Figure 4-58a) to compare the transfer of stresses between both concretes. FOS VS installed on the SCC exhibits strain peaks associated with three cracks crossing the interface. FOS VU, however, exhibits more variation in strain at high loads due to cracking, which resulted in the FOS recording strain values exceeding 1,000 με.

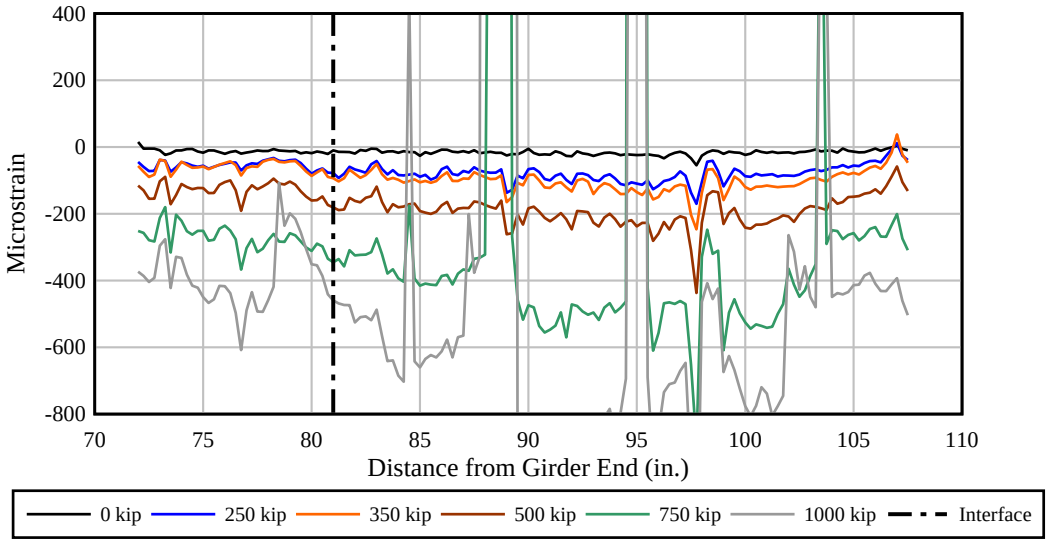

Figure 4-59 Horizontal FOS H1 strain measurements

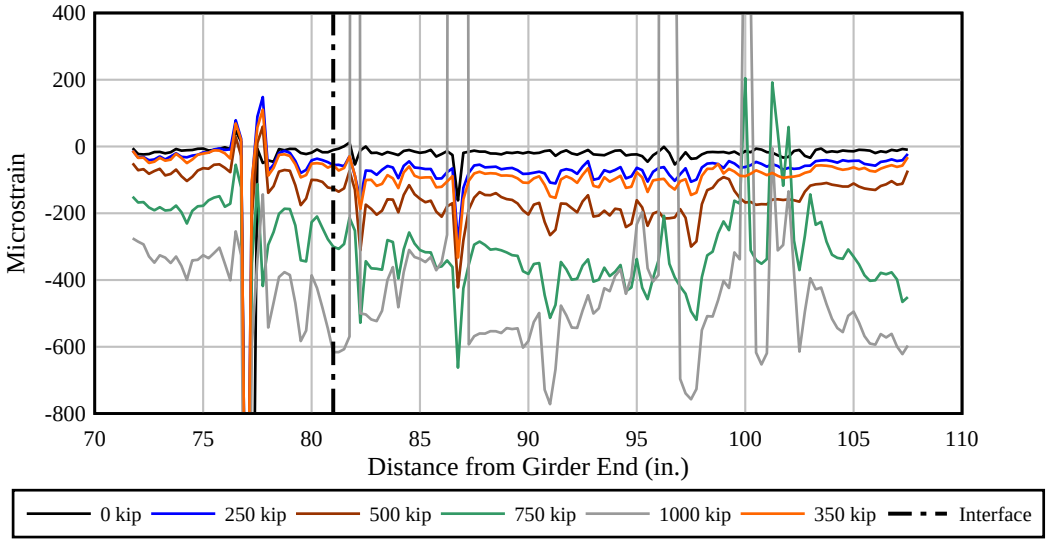

Figure 4-60 Horizontal FOS H2 strain measurements

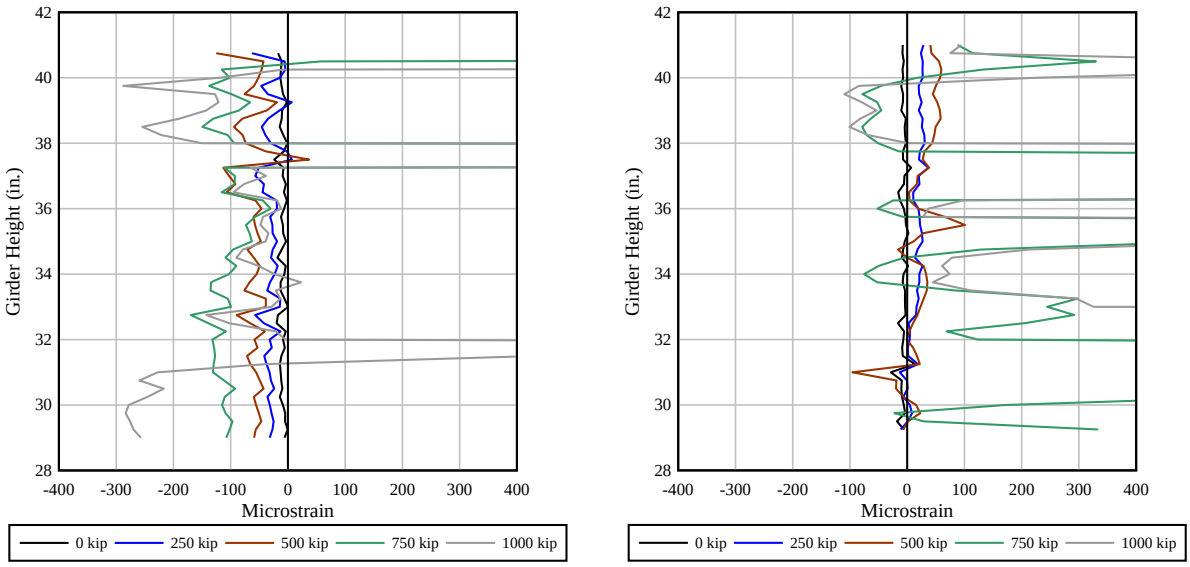

Figure 4-61 Vertical FOS strain comparison: (a) FOS VS in SCC region and (b) FOS VU in UHPC region

Figure 4-62 shows the displacements measured with two LVDTs to determine if slip occurred at the UHPC/SCC interface. The maximum displacement was 0.015 in., which was measured by LVDT 1 in the upper portion of the web. No damage was observed at the interface during loading, suggesting that the interface was capable of transferring loads between SCC and UHPC.

Strand slip was measured with ten LVDTs attached to the strands on the end near the load point. Figure 4-63 shows the strand slip measured during loading. Strand slip was negligible because it did not exhibit a sustained increase in slip with load, which was expected because no damage was observed in the bottom flange.

Figure 4-64 shows the minimum and maximum principal strains calculated with the three rosettes gages installed in the girder web. Minimum and maximum principal strains of all rosette gages started to exhibit nonlinear behavior due to cracking at approximately 380 kip or 230 microstrain.

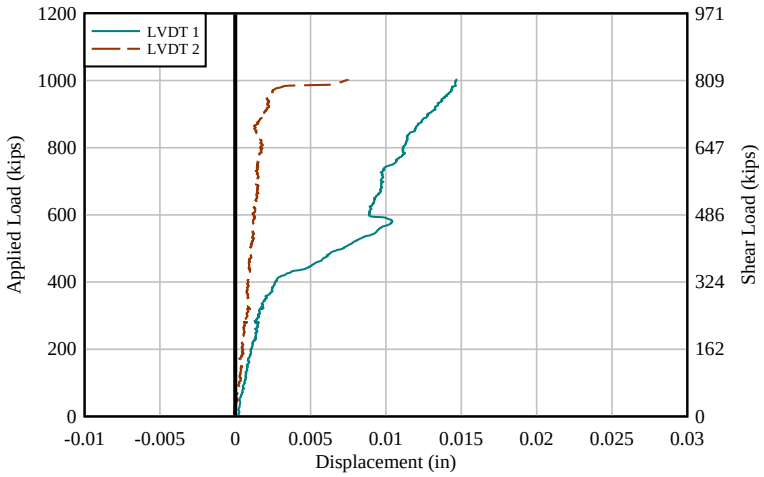

Figure 4-62 G7-E1 interface displacement

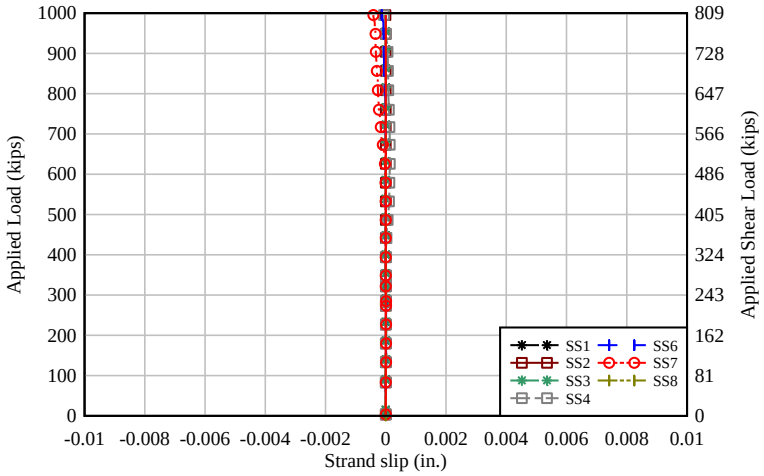

Figure 4-63 G7-E1 measured strand slip

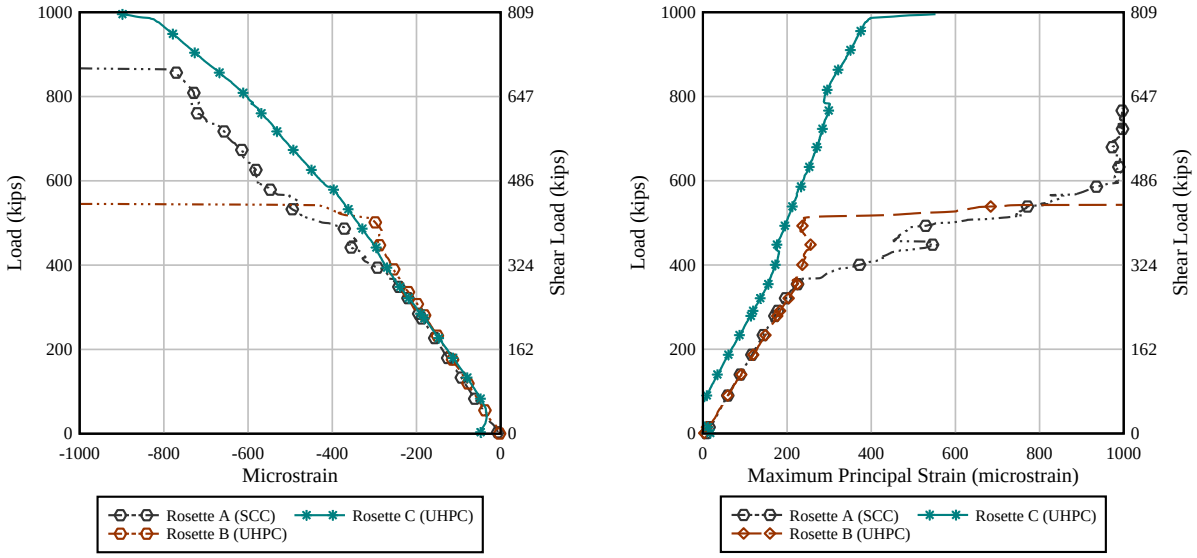

Figure 4-64 Load vs. (a) minimum principal strain and (b) maximum principal strain

5 Overall DTT Results

Successful use of UHPC at precast plants is dependent on quality control methods that ensure consistent fresh and hardened properties among various batches. To test this consistency, DTT specimens were collected during the construction of the FIB 72 mockups and the FIB 54 girders. DTT specimens were fabricated from batches produced using the same UHPC mix design and mixing procedures; batches were produced at different times, however, to suit the fabrication schedule of the FIB specimens.

DTTs were performed at age of detensioning – generally three days– and at 28 days. Recall from section 2.4.2 and Figure 2-10 the key points of the stress-strain curve obtained from DTT that were used for comparison. End region design of the test specimens considered the contribution of UHPC at service load conditions with particular focus on end region cracking. Therefore, cracking strength was the most important point in the stress-strain curve.

Six DTT specimens were cast for each batch to test at both age of detensioning and at 28 days. Recall from Section 3.3 and 4.3 that separate batches were used for the construction of each specimen, resulting in a total of seven batches; the first two batches for the construction of G6 and G7 were produced on July 2019, and the remaining five batches for G1 through G5 girder were produced on October 2019.

Figure 5-1 shows the cracking strength and peak strength with the respective standard deviation for both age of detensioning and 28 days. In addition, Table 5-1 lists a summary of the data collected. Note that during testing, several specimens exhibited crack localization in the region outside the LVDT sensors, resulting in invalid tests that were not included in this analysis.

Cracking strength was computed using two methods recommended by Graybeal and Baby (2014). The first method determines the stress at the first slope discontinuity from the elastic response. This method can underestimate the cracking strength due to the bending induced during gripping.

The second method consists of averaging the stress in the multi-cracking phase. This method, however, requires some qualitative assessment in the process used to identify the multi-cracking region. Graybeal and Baby (2014) proposed the average stress during multi-cracking as the most reliable estimate for the UHPC cracking strength. This recommendation agrees with the results in this study as method 2 resulted in a lower coefficient of variation at both age of detensioning and at 28 days. Furthermore, it was found that cracking strength and peak strength increased by 17%-23% from age of detensioning to 28 days. The increase in strength is attributed to the maturity of the cementitious matrix, which affects the cracking strength and the slip friction between the fiber and the cementitious matrix.

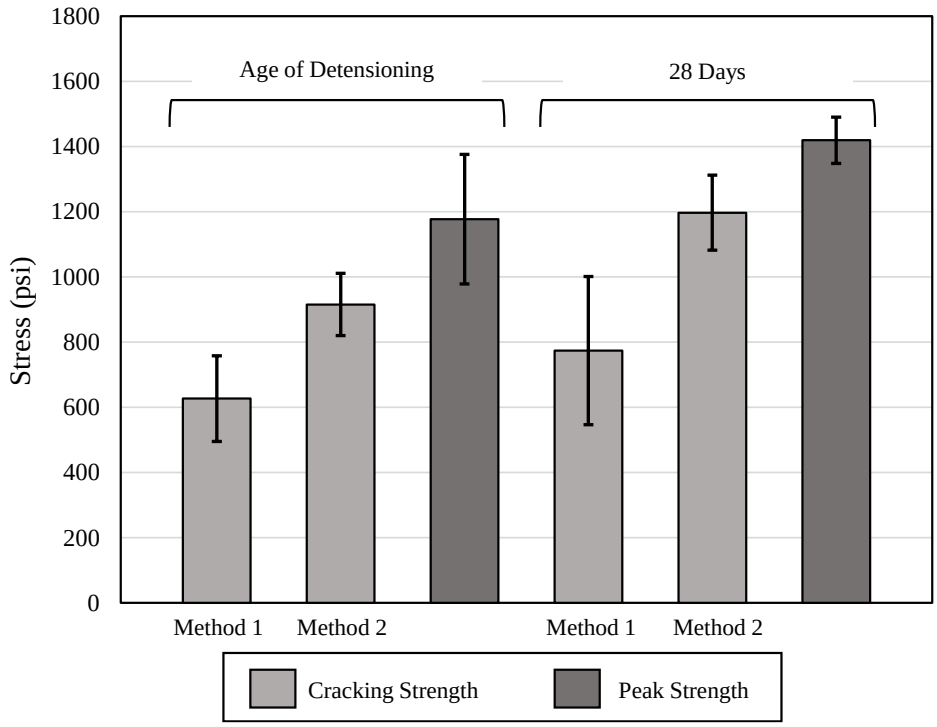

Figure 5-1 Overall DTT results

Table 5-1 Summary of overall DTT results

Variables		Age of Detensioning (3 Days)*			28 Days**		
		Average Stress (psi)	COV (%)	Average strain (με)	Average Stress (psi)	COV (%)	Average strain (με)
Cracking Strength	Method 1	626	21.4	252	774	29.3	180
	Method 2	915	10.3	448	1,197	9.60	689
Peak Strength		1,177	16.9	5,337	1,419	14.9	5,263

*Summary of 16 valid tests

**Summary of 19 valid tests

6 Span Lengths of UHPC-SCC Hybrid Girder

One advantage of UHPC use in precast girders is the possibility that the spans can be increased over those that are typically used in girders fabricated with SCC. To explore the implementation of UHPC in precast girder production, FIB 54 and FIB 96 were designed using UHPC at the girder ends to determine the maximum possible span length that could be attained. The current design criteria were obtained from the FDOT Index 20010 (FDOT, 2012). The index specifies maximum span lengths for all FIBs based on the beam spacing varying from 6 ft to 12 ft. In general, span lengths are limited by allowable stresses at release and under service load conditions. The design assumptions call for a concrete compressive strength of 6 ksi at release and 8.5 ksi minimum 28-day strength.

At release, tension stresses are calculated at the top of the girder and the compressive stresses at the bottom of the girder over the span length. Service limit state includes self-weight of the deck, wall barriers, sacrificial surface, stay-in-place formwork weight, and miscellaneous additional dead loads. Live loads include the HL-93 truck load.

Both FIB 54 and FIB 96 were assumed to be spaced at 12 ft. The use of UHPC at the ends of the girder ensures that the release stresses at that location will not control the amount of prestressing force that can be used. One consequence is that the compressive stresses in the SCC will likely control the design. This was shown to be true in preliminary calculations. Consequently, it was necessary to increase the SCC compressive strength to 8 ksi at release and 10 ksi at 28 days to withstand the higher prestress force necessary to lengthen the girder span.

UHPC-SCC hybrid girder fabrication will likely require at least one additional day in the bed prior to detensioning, which would allow the SCC the necessary time to reach the required compressive strength. Details about the construction process were discussed in Section 4.2.

Furthermore, based on the results of the mockup testing reported in this research, bursting stresses will be resisted by the fibers in the UHPC and present mild-steel reinforcement.

Figure 6-1 shows the stresses at top and bottom of the FIB 54 at prestress transfer and under Service III. The standard FIB 54 design calls for a total of 51 strands, with 39 strands fully bonded and 12 strands with a debonding length varying from 5 ft to 35 ft. The maximum expected shear load during service is 400 kip. The design is controlled by the bottom tension stresses in the girder.

Similarly, Figure 6-2 shows the stresses at release and during service of the modified UHPC-SCC hybrid girder. This design accounts for 70 strands, which is the maximum allowed by the FIB geometry. The tension and compressive stresses limits in the figure were calculated with the modified compressive strengths. It is expected that the UHPC develops higher strengths, and therefore a different limit would apply for UHPC. The modified design allowed to increase the span length by 10% or 12 ft. Note that the location of UHPC at 1.5 times the depth of the girder or at 81 in. from both ends is shown in the figure. Figure 6-2a shows that in the modified design, the SCC does not comply with the allowed compression stresses in the bottom of the girder. Therefore, it is necessary to extend the length of UHPC to 15ft from both ends, debond strands or specify a higher compressive strength at release. For the purposes of this example, the current length of UHPC and the release compressive strengths were maintained. Figure 6-2b shows the stresses at service. The design of the girder was controlled by the allowed compression stresses in the top of the girder. Furthermore, with the new span length the maximum shear force is 430 kip.

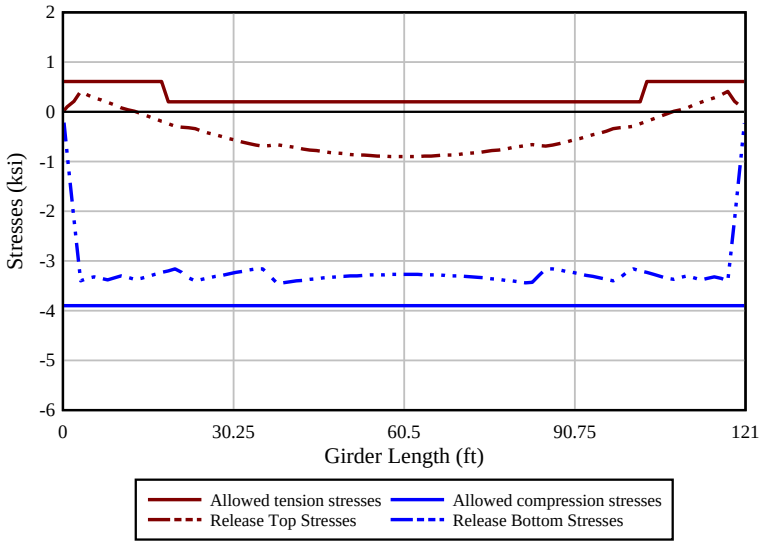

(a)

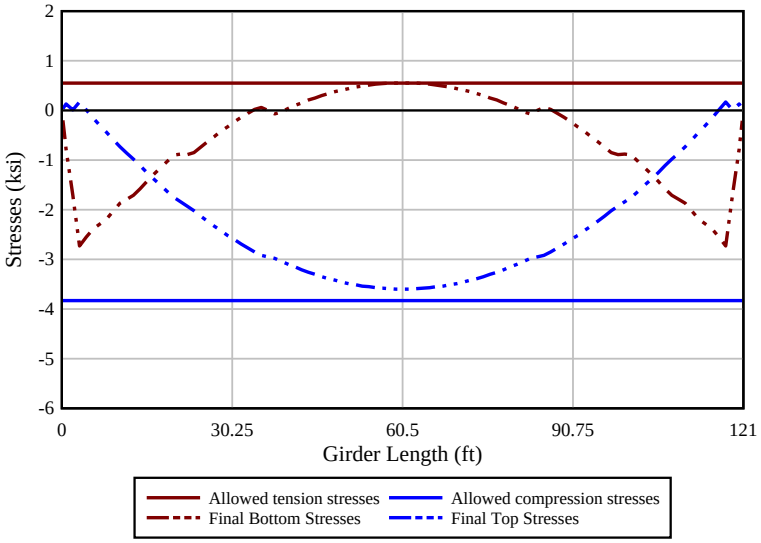

(b)

Figure 6-1 FIB 54 with current design guidelines: (a) stresses at release, and (b) final stresses

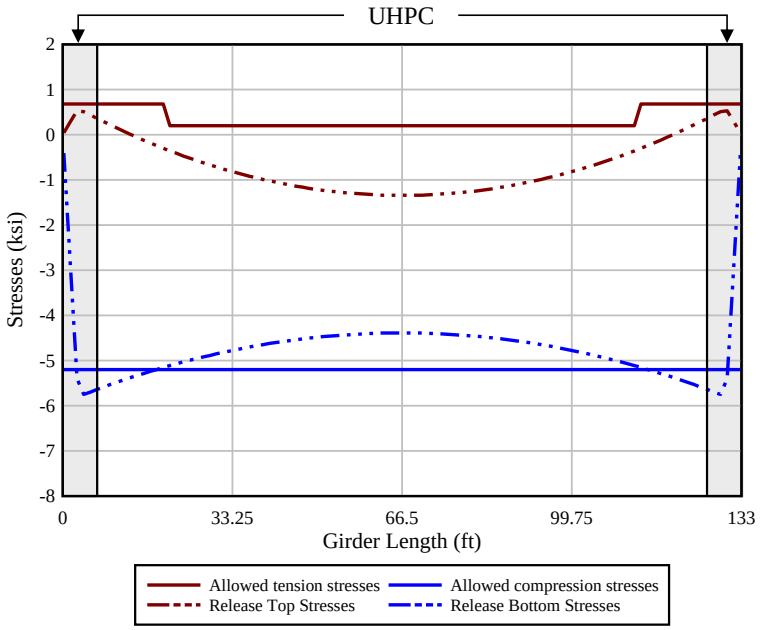

(a)

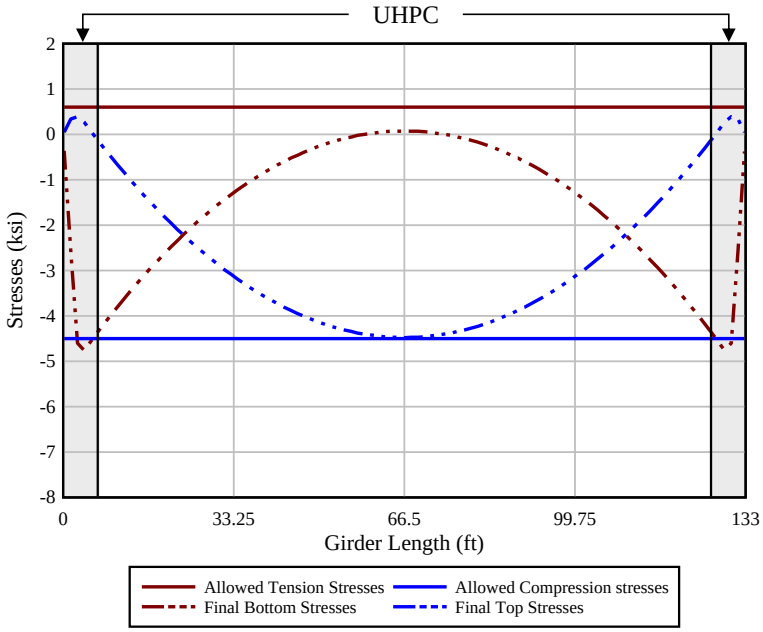

(b)

Figure 6-2 FIB Hybrid FIB 54 with modified design: (a) stresses at release, and (b) final stresses

The same process was repeated for the FIB 96 with a beam spacing of 12 ft. Figure 6-3 shows the stresses that the girder experiences during release and service. Note that typical FIB 96 design calls for a total of 51 strands, with 39 strands fully bonded and 12 strands with a debonding length varying from 5ft to 35 ft. The maximum expected shear load during service is 550 kip. The design is controlled by the bottom tension stresses in the girder.

Similarly, Figure 6-4 shows the stresses at release and during service of the modified UHPC-SCC hybrid girder. Recall that for this example the release and final compressive strengths were increased to withstand the prestress force of 70 fully bonded strands. The modified design allowed to increase the span length by 6.7% or 12 ft. Note that the location of UHPC at 1.5 times the depth of the girder or at 144 in. from both ends is shown in the figure. Figure 6-4a shows that the modified design complies with the stresses at release due to the increased self-weight compared to the FIB 54 in the previous example. Figure 6-4b shows the stresses at service. The design of the girder was controlled by the tension stresses in the bottom of the girder. Furthermore, with the new span length the maximum shear force is 588 kip.

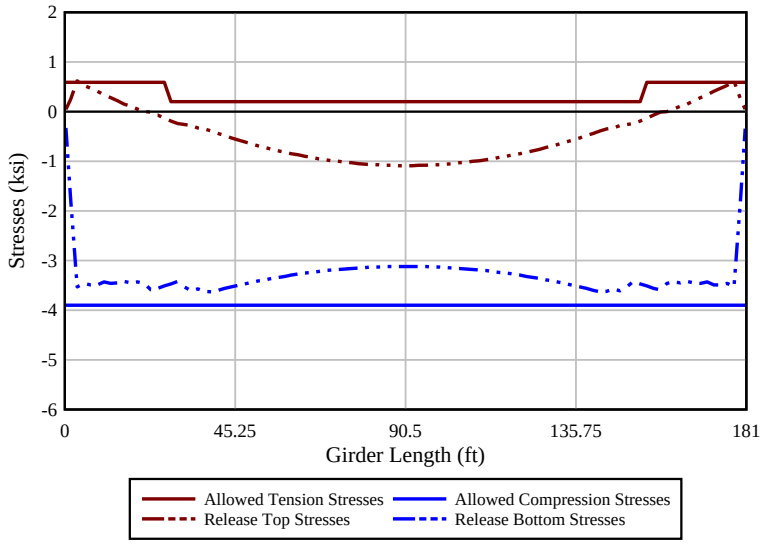

(a)

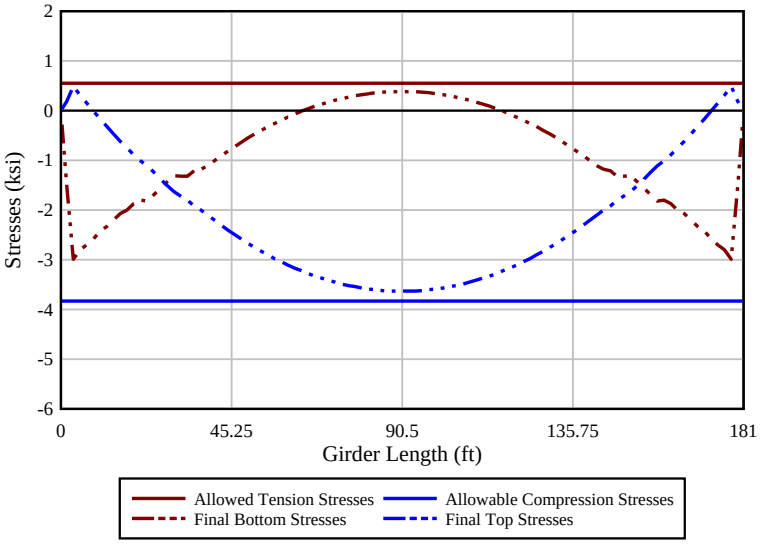

(b)

Figure 6-3 FIB 96 with current design guidelines: (a) stresses at release, and (b) final stresses

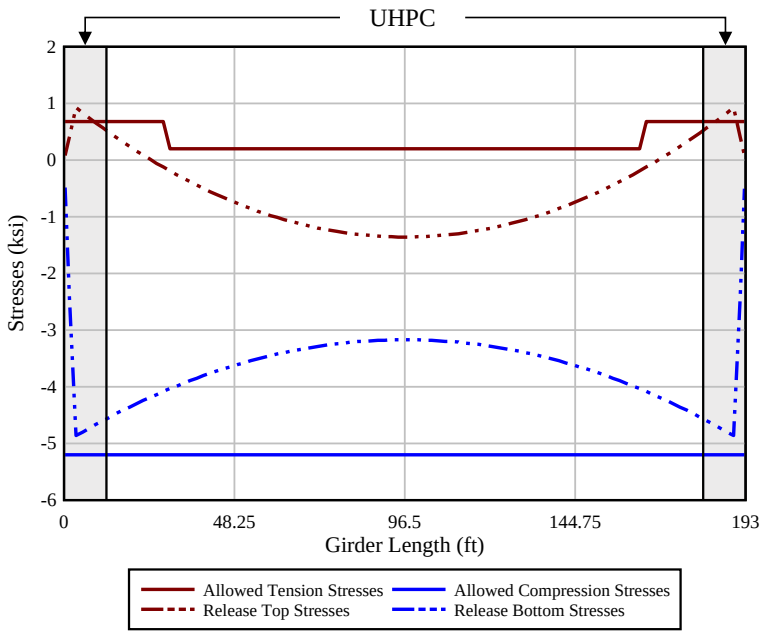

(a)

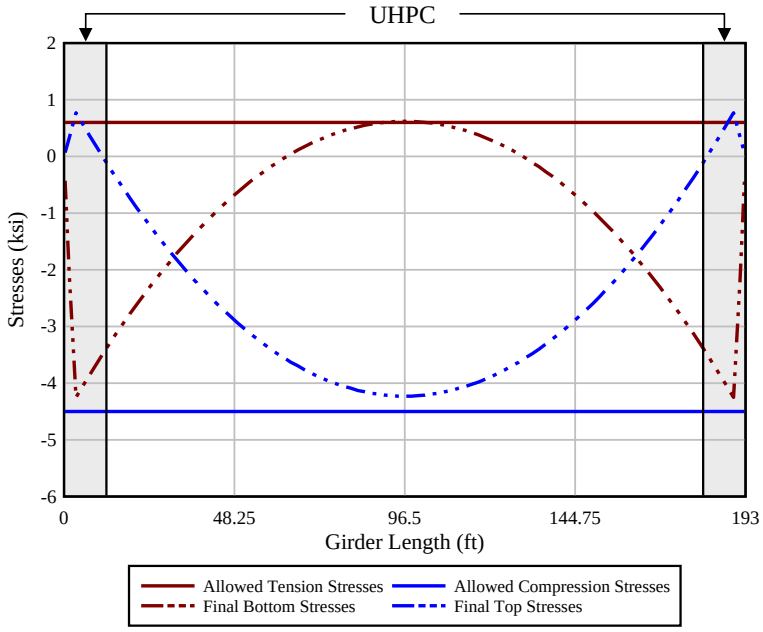

(b)

Figure 6-4 FIB 96 with modified design assumptions: (a) stresses at release, and (b) final stresses

7 Finite Element Analyses of Hybrid Girder

7.1 Overview

Finite element models of the FIB 72 mockups and FIB 54 beams were developed to complement the experimental data. LS-DYNA was the software selected to model both sets of FIBs.

LS-DYNA has several concrete material models capable of approximating the nonlinear behavior of concrete. According to Winkelbauer et al. (2016), LS-DYNA currently has fourteen concrete material models with different numbers of input parameters, strain rate effects, and damage-tracking capabilities. These material models also include unique features of concrete behavior such as evolution of failure surface, representation of material damage under loading, softening, dilation, and shear responses (Winkelbauer, 2016). In addition, researchers (Magallanes et al., 2010, Xu et al., 2014, Crawford et al., 2016, Guo et al., 2017 and Yin et al., 2019) have shown that the compression and tension behavior of FRC or UHPC can be approximated by adjusting parameters within the available material models.

In general, the process used to develop the models in this study was to select the material model for concrete, calibrate the selected material model to approximate UHPC behavior, and model the boundary and loading conditions of prestress transfer and load tests.

7.2 Methods for Material Calibration

Different concrete material models were selected for the FIB 54 and FIB 72 models. For instance, MAT_WINFRITH_CONCRETE was selected to model the FIB 72 mockups for end region evaluation because this material model can generate crack data by defining the crack width parameter or fracture energy. The crack width parameter is used to define a point where the tensile strength of concrete becomes zero. The crack opening width parameter can be useful when evaluating the service strength of structural components. This material model, however, is only applicable for cases where small deformations are expected, making it inadequate for the shear models.

MAT_CONCRETE_DAMAGE_REL3 (MAT_72R3), also known as the K&C (Karagozian & Case) model, was selected to model the FIB 54 girders during shear loading. This material model is generally used to analyze concrete structures subjected to impulsive loadings (Winkelbauer, 2016). The K&C model is not explicitly capable of modeling fibers in concrete; however, the model offers parameters that can be adjusted to distinguish between compression and tension damage and to approximate residual tensile strength after cracking.

The calibration of both material models consisted of modifying the parameters to fit the post-cracking behavior observed during the Direct Tension Test (DTT) and the ASTM C 1609 flexure beam tests (FB). The subsequent subsections describe the characteristics of the finite element models that were used to represent the two test methods.

7.2.1 Direct Tension Test

The concrete specimen dimensions, loading, and boundary conditions were established based on DTT guidelines given by Graybeal (2019). An overview of the FEA model of the DTT specimen is shown in Figure 7-1. The DTT specimen is a 2 in. × 2 in. × 17 in. coupon modeled with 8-node 3D solid elements. The solid elements have a size of 0.25 in. in all directions (Figure 7-2). Aluminum plates attached to the DTT specimen were modeled using solid

elements of the same dimensions as the specimen. Aluminum properties were defined using an elastic material (MAT_001). Assumed properties for the aluminum plates were modulus of elasticity of 10,000 ksi, and Poisson's ratio of 0.33.

The aluminum plates were connected to the concrete specimen using node compatibility, i.e. nodal merging. The hydraulic grips were modeled with an elastic material (MAT_001) using steel properties. Assumed properties for steel were modulus of elasticity of 29,000 ksi, and Poisson's ratio of 0.33. The hydraulic grip model consisted of solid elements in a rectangular mesh with elements measuring 0.5 in. on all sides.

At the start of each simulation, the geometry was defined such that a gap of 0.01 in. was located between the grips and the aluminum plates. Then, pressure was gradually applied to the steel blocks until matching the experimental gripping pressure of 3,000 psi (Figure 7-2). Contact between the grips and the aluminum plates was defined by introducing an automatic surface-to-surface contact with a static friction coefficient of 0.61 and a sliding friction coefficient of 0.47. In addition, the node centered in both top and bottom face of the DTT specimen was restrained from translation in all directions to maintain stability of the specimen during gripping.

Uniaxial tensile force was applied by prescribing a displacement rate (Figure 7-3) to nodes in the top grips along the Z-direction, while restraining the bottom grips from displacement. This approach simulates the experimental approach used to induce uniaxial force on the specimen.

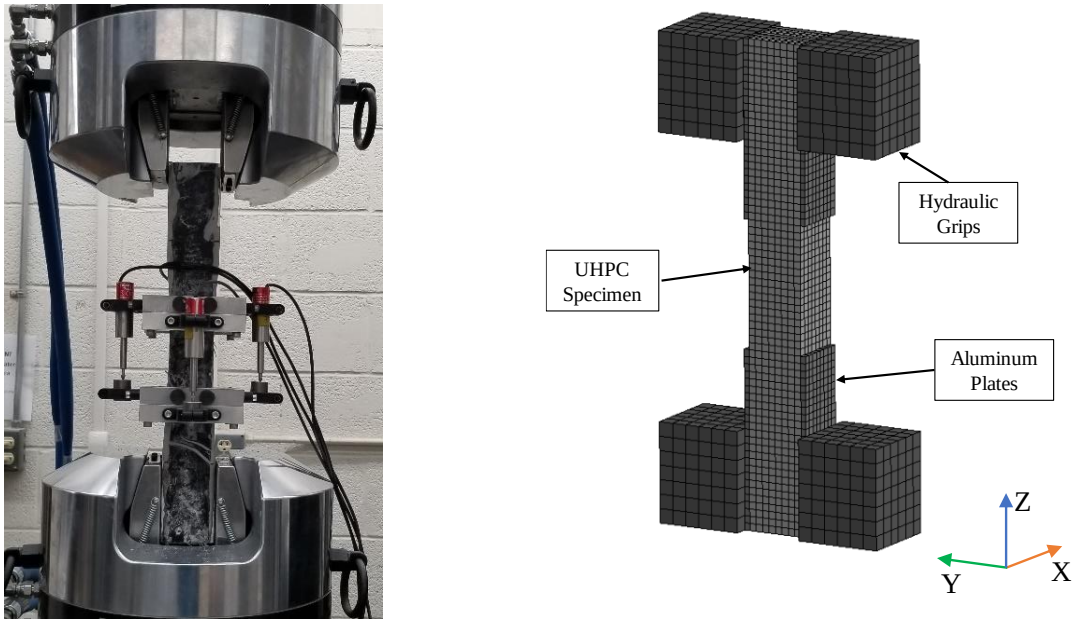

Figure 7-1 Overview of experimental and FEA model of DTT specimen

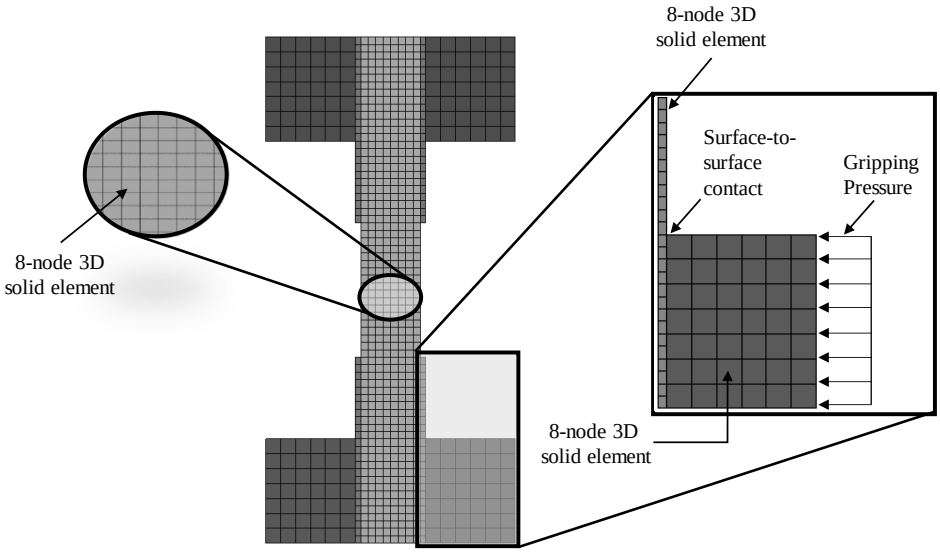

Figure 7-2 DTT model details

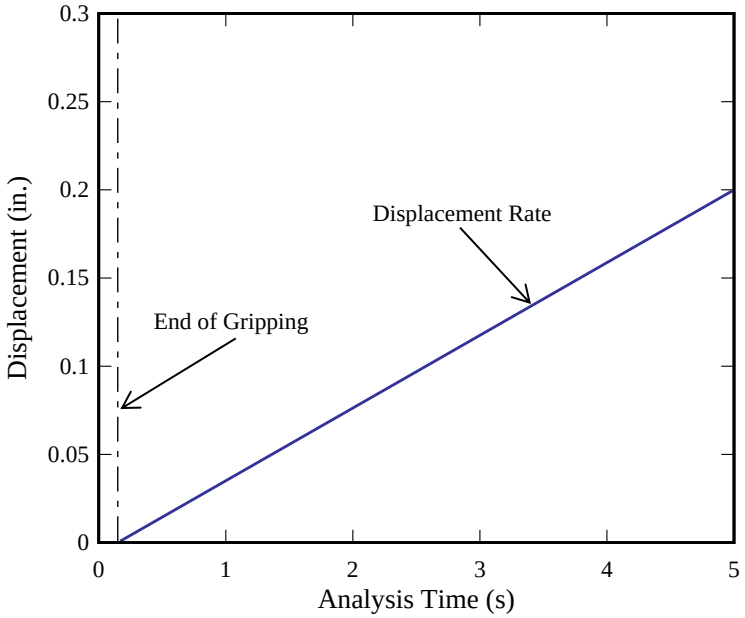

Figure 7-3 Displacement rate for tensile loading in analytical model

7.2.2 Flexure Beam Test

The concrete specimen dimensions, loading and boundary conditions were established based on the ASTM C1609 Standard Test Method for Flexural Performance of Fiber-Reinforced Concrete (2012). Figure 7-4 shows an overview of the flexure beam model. The concrete specimen with dimensions of 4-in. × 4-in. × 14-in. was modeled using 8-node 3D solid elements. A rectangular mesh was used for analysis. Element sizes were varied based on the stress and damage expected to occur in that region; 0.125-in. cubes were used in the middle third where moment is maximum and 0.25-in. cubes for the remaining two-thirds of the specimen (Figure 7-5). Since the beam cross-section, boundary conditions and loading are symmetric about the Y-

Z plane, a half-symmetry model was used. Nodes on the plane of symmetry were constrained along the X-direction to model a symmetric deformation pattern.

Support and loading conditions were modeled using half-cylinders to represent the rollers used in the experimental test. These rollers were also modeled using 8-node 3D solids with assumed steel mechanical properties similar to those used in the DTT for the machine grips. Contact between the rollers and the concrete specimens was defined with an automatic surface to surface contact with a friction coefficient of 0.55 for static friction and 0.45 for dynamic friction. Loading of the specimen was performed by assigning a prescribed displacement to the loading rollers. ASTM C 1609 specifies different displacement rates before and after L/900 (estimated cracking deflection). Figure 7-6 shows the specified displacement rate before and after L/900 (0.013 in.) net deflection.

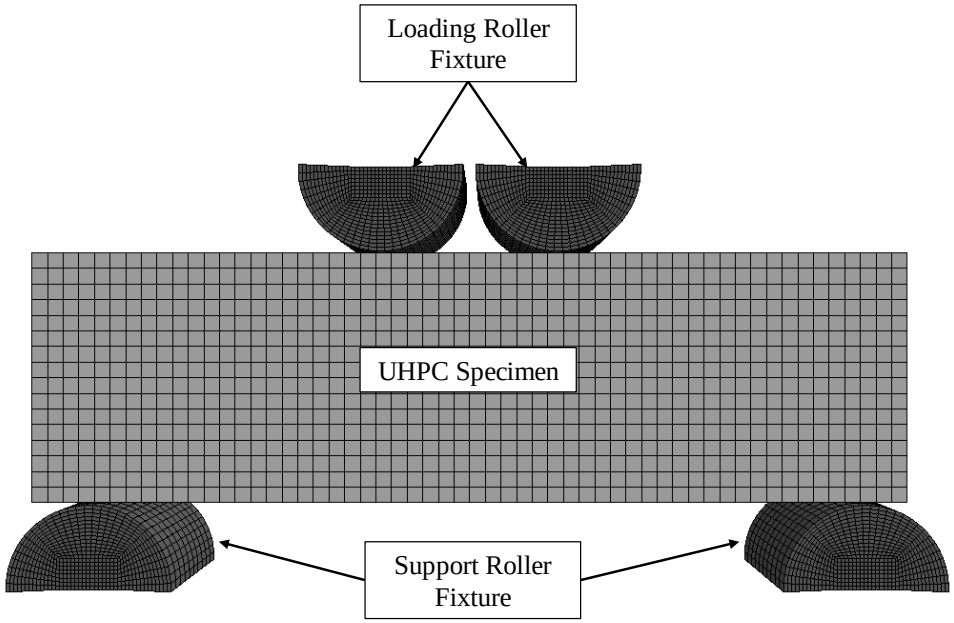

Figure 7-4 Overview schematic of ASTM C1609 flexure beam model

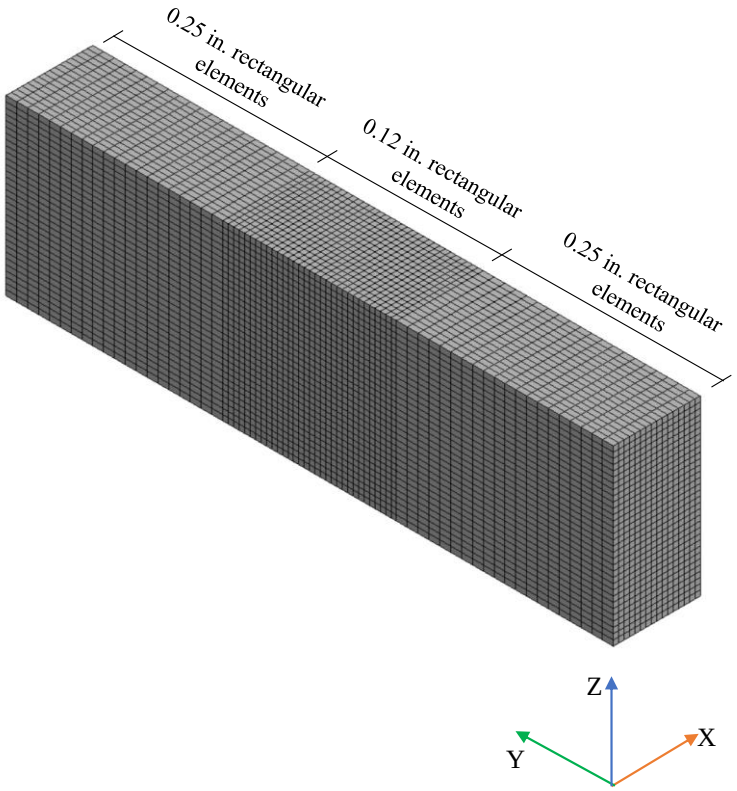

Figure 7-5 Mesh of solid elements in flexure beam model

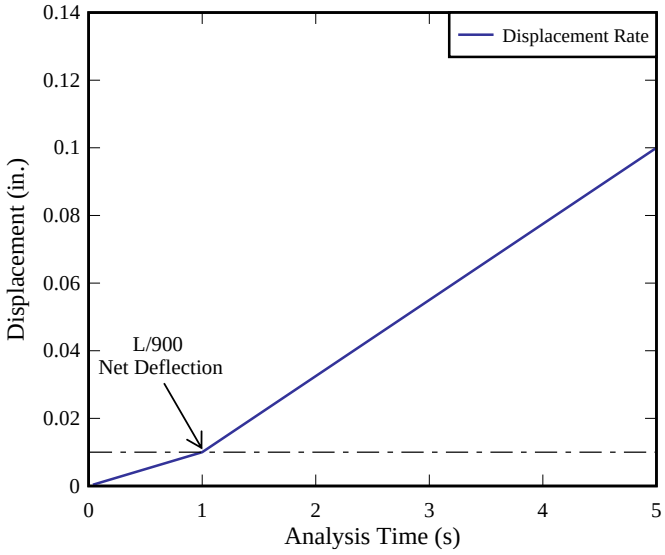

Figure 7-6 Displacement rate for loading rollers

7.3 FIB 72 End Region Models

The FIB 72 FEA model was developed to evaluate end region behavior during prestress transfer. The FIB geometry, strand detensioning procedures, and overall boundary conditions in the FEA model were based on the experimental mockups. For example, Figure 7-7 shows a

schematic of the 20-ft-long G1 mockup having half of the beam made of SCC and the other half made of UHPC. The concrete beam and precast bed were modeled using 8-node 3D solid elements. The shape of the concrete solid elements was devised to minimize the difference between side dimensions of the element, while still accommodating the curved geometry of the bottom flange (Figure 7-8).

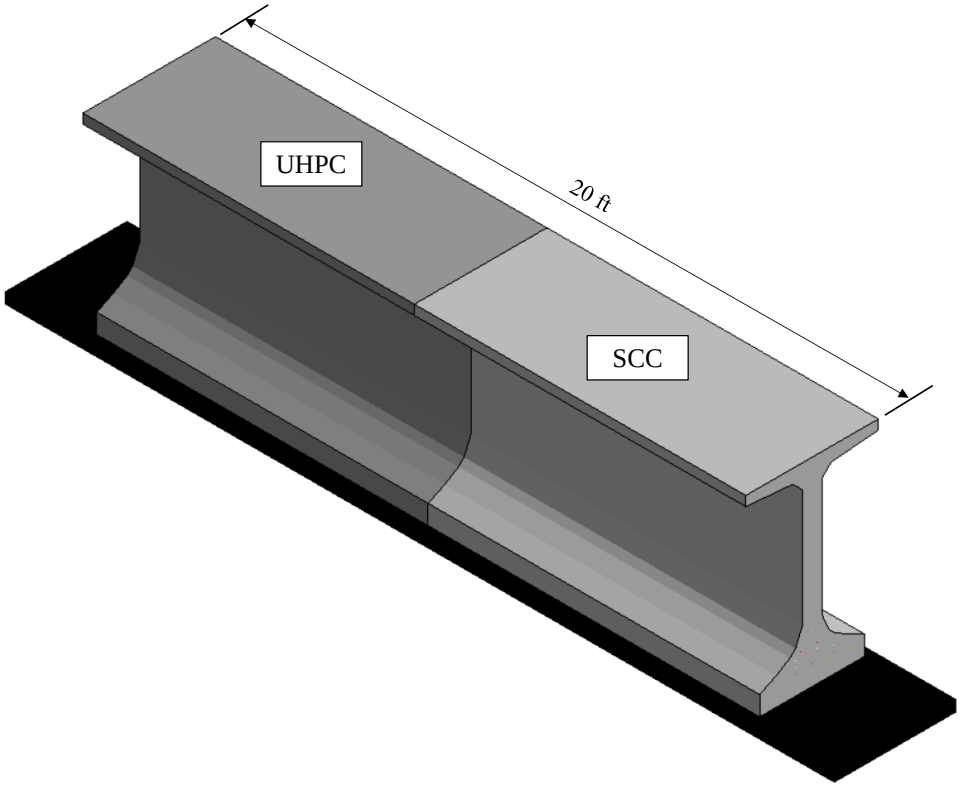

Figure 7-7 FIB 72 mockup model

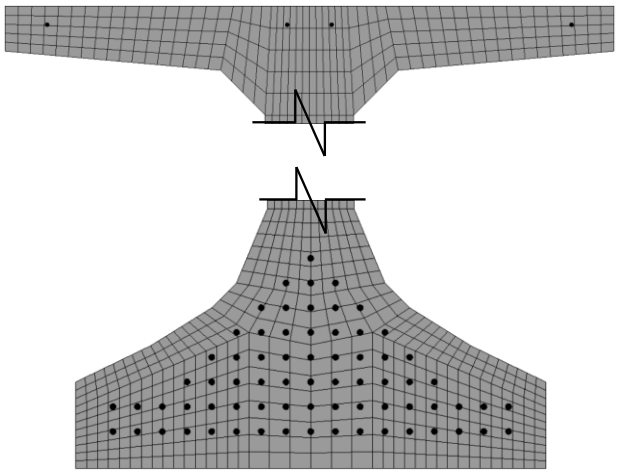

Figure 7-8 FIB 72 mockup model concrete solid elements mesh and strand layout

Mild-steel reinforcement was modeled using discrete beam elements. MAT_PLASTIC-KINEMATIC was selected to model the steel reinforcement, as it allows for the modeling of bilinear kinematic hardening after yielding. Steel properties such as 29,000-ksi modulus of

elasticity, 0.33 Poisson's ratio, and 60-ksi yield stress were defined based on the specified values for Grade 60 rebar (ASTM A615, 2020). The analysis was focused on the transfer of prestress, which is a service load condition. Consequently, it was assumed in this model that the stresses generated in the reinforcement during prestress transfer remained in the elastic range. This was confirmed when evaluating results of the simulation.

Bond between concrete solid elements and the reinforcement discrete beam elements was modeled by incorporating coupling points at the beam ends and surrounding solid element nodes. The lengths of discrete beam elements were modeled as having the same lengths as the surrounding solid elements to ensure that the model had enough coupling points.

This approach also aided in generating the mesh because the discrete beam elements did not need to have nodal compatibility with the concrete solid elements. Figure 7-9 shows examples of the reinforcement layout of G1 (typical FDOT reinforcement) and G5 (lowest amount of reinforcement). In general, the same reinforcement detailing used for the experiment mockups was used for models. Section 3.1 provides the full reinforcement detailing of each mockup.

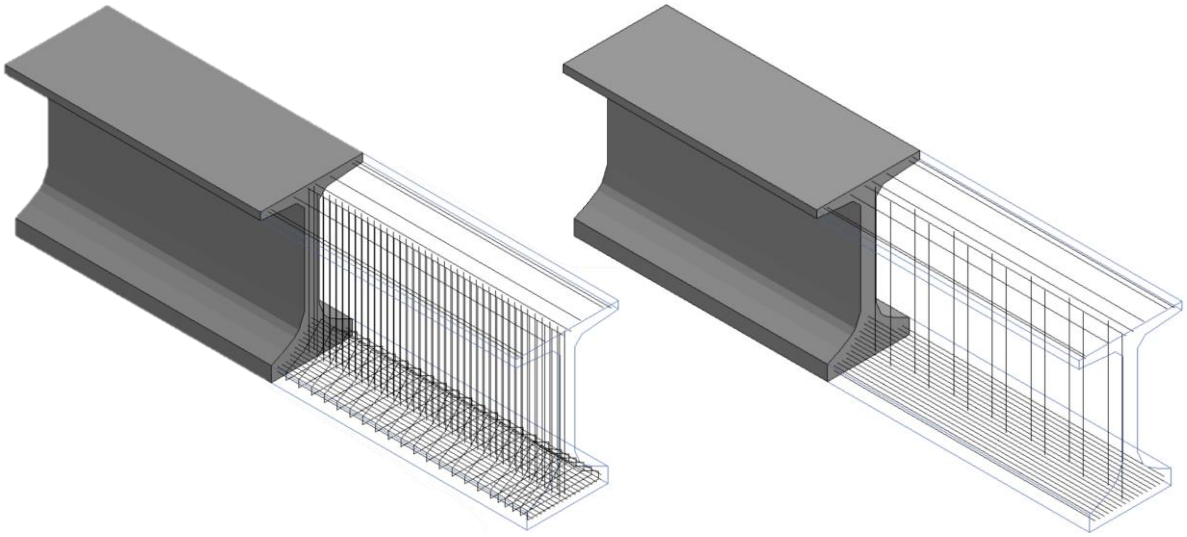

Typical Reinforcement Detailing Reduced Reinforcement

Figure 7-9 Examples of amount of reinforcement on FIB 72 mockup models

Prestressing strands were modeled using discrete cable elements. The length of the cable elements was divided in two groups. The first group consisted of the elements in the transfer length region, which had a length of one inch. The second group consisted of the strands located outside of the transfer length at both ends; these elements had a length of 3 in.

Different cable element lengths were used to optimize computational time, while appropriately representing the transfer length of each mockup. Table 7-1 lists the transfer length values experimentally measured on each mockup and specified in the model.

MAT_CABLE_DISCRETE_BEAM (MAT_071) was used to model the prestressing strands. This material model allows properties of prestressing strands such as modulus of elasticity and initial tensile force to be specified.

Table 7-1 Defined transfer length in finite element models

Mockup	Transfer length End 1 (in.)	Transfer length End 2 (in.)
G1	32*	22
G2	32*	22
G3	20	19
G4	21	17
G5	18	18

* Transfer length for SCC ends

Bond between the prestressing strands and concrete elements was modeled by coupling the beam element nodes to the concrete solid element nodes. The concrete solid element dimensions were adjusted to match the length of the prestressing strand elements.

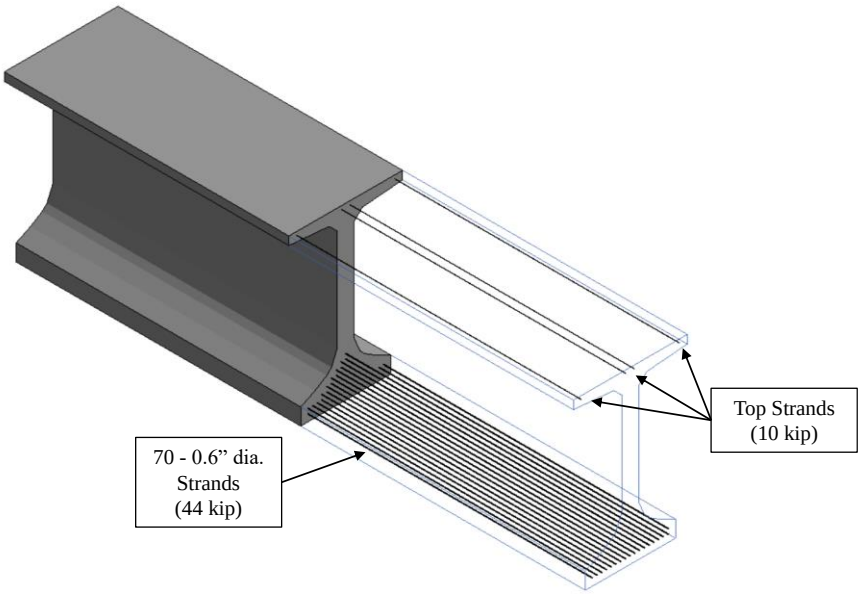

Figure 7-10 FIB 72 mockup prestressing strands details

The detensioning sequence in the model was divided in stages following the process used in the field. Figure 7-11 shows the detensioning sequence in the field and in the FEA model. Because of the excessive computation time required to model the release of each individual strand, detensioning was divided into groups based on the strand positioning levels. Figure 7-12 shows the time of release of each strand group.

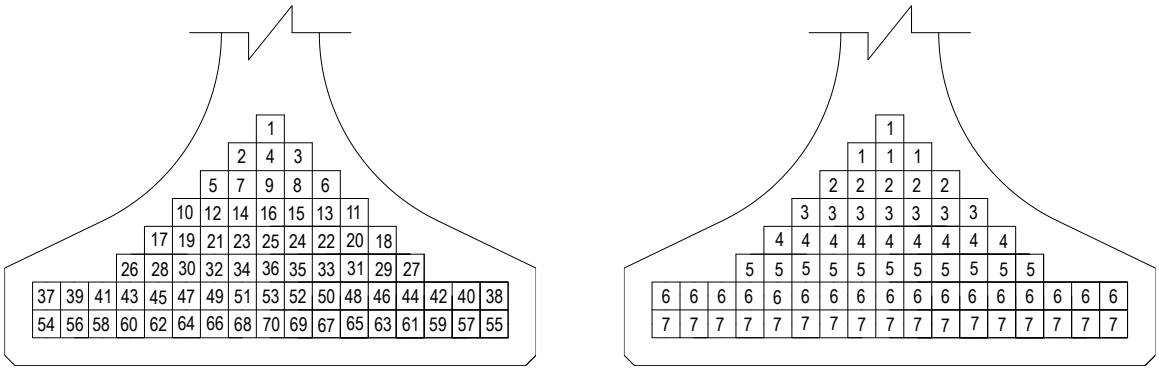

Field Detensioning Sequence FEA Detensioning Stages

Figure 7-11 Detensioning sequence in the field and FEA

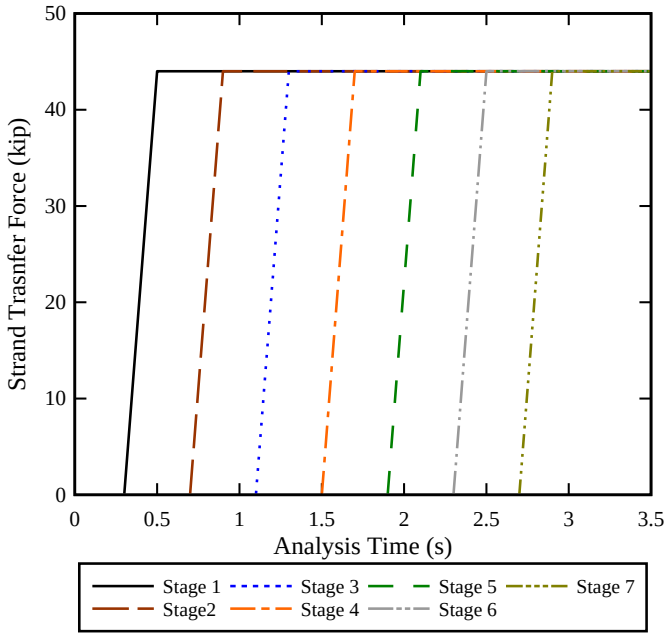

Figure 7-12 Analytical model prestress transfer by stages

7.3.1 Winfrith Concrete Material Model Calibration

The focus of this portion of the research project was to determine the extent and intensity of cracking in UHPC end regions. Such information will help evaluate the potential use of this material in reducing the cracking that currently occurs in FIB girders constructed with SCC. To effectively model the end region behavior of FIB 72 mockups, it was important to accurately represent the post-cracking behavior of UHPC.

As discussed in section 7.1, MAT_WINFRITH_CONCRETE material model was selected to model both SCC and UHPC. This material model was selected because it allows UHPC tensile behavior to be modeled using a smeared reinforcement approach. Smeared reinforcement consists of modeling reinforcement as a fraction of the solid element in all three orthogonal directions. In addition, this material model calculates crack widths that can be graphically represented in the post-processing stage of the analysis.

MAT_WINFRITH requires the user to specify parameters characteristic of concrete including: mass density, Poisson's ratio, ultimate compressive strength, ultimate tensile strength, modulus of elasticity, maximum aggregate size, and crack width at which concrete tensile strength goes to zero. Furthermore, to use smeared reinforcement, the user needs to define modulus of elasticity, yield strength, and the ratio of cross-sectional area of steel relative to the cross-sectional area of concrete in the element plane.

MAT_WINFRITH was calibrated to approximate the behavior of UHPC using the experimental results obtained from DTT at three days of curing, or at the age of detensioning. Experimental results were used to define parameters such as compressive strength, tensile strength (cracking strength using method 2), and crack width at which the tensile strength goes to zero. Concrete modulus of elasticity was calculated using an expression based on the compressive strength proposed by Graybeal (2006) for UHPC (Equation 7-1). Fiber properties were specified based on the fiber data sheet included in the paper bag that corresponded to the fibers used during the mockup construction.

The reinforcement ratio was defined by manually counting fibers in the failure plane of a DTT specimen. After testing, the failed DTT specimens were stored to visually count fibers. The process consisted of taking photos of both surfaces at the location of failure (see Figure 7-13) and counting the fibers on both pieces of the specimen. Among all twelve specimens the average number of fibers at the location of failure was 780 with a standard deviation of 83 fibers. With known geometries of the steel fiber and concrete specimen the fiber volume fraction was calculated to be 0.9 percent. This percent only includes fibers that were pulled in the direction of the tensile force. It is expected that depending on the angles of inclination and direction of the cracks, some fibers do not contribute to bridging the cracks. Additionally, the direction of the crack path is governed by weak areas within the cross-section of the specimen, which results in a non-uniform failure surface with a lower percent of fibers compared to the 2% accounted for in the mix design.

The material calibration process to model the post-cracking behavior consisted of adjusting the material parameters until the analysis results were in reasonable agreement with the DTT experimental results. Most parameters were obtained experimentally; the only parameter that had to be modified was the fiber yield strength. Recall that the ductile behavior of UHPC occurs due to fiber pull-out rather than fiber yielding. Therefore, using the actual fiber yield strength without consideration of bond slip would result in an overestimation of the post-cracking strength. Fiber yield strength was instead computed using the peak strength from DTT tests divided by the fiber volume fraction, as estimated from fiber counting.

Table 7-2 shows the material model parameters after calibration, used to model each FIB 72 mockup. Because end region cracking is a service issue, the focus of the material calibration was crack initiation and residual strength in the multi-cracking region before strain-hardening, which corresponds to a tensile strain of approximately 0.002 in DTT.

$$E_c = 46{,}200\sqrt{f'_c}$$ (Graybeal, 2006) Equation 7-1

(a) (b)

Figure 7-13 Opposing fracture surfaces from DTT specimen used for fiber counting: (a) Side 1 and (b) Side 2

Table 7-2 UHPC properties used in material definition

	Compressive Strength (ksi)	Tensile Strength (ksi)	Percent of fiber area per plane	Fiber Yield Strength (ksi)
G1	23.92	0.91	0.9	116
G2	23.98	0.89	0.9	114
G3	25.03	1.10	0.9	160
G4	24.80	0.97	0.9	148
G5	22.20	1.20	0.9	160

Figure 7-14 shows a comparison of the stress-strain curves from experimental and analytical DTT. The experimental curve was generated from the average of the specimens tested at three days of curing for each batch. Comparisons between the experimental and analytical curves show good agreement in terms of initial stiffness and post-cracking behavior. These results indicate that the material model along with the smeared reinforcement approach was capable of simulating the tensile behavior of UHPC for cases with small deformations.

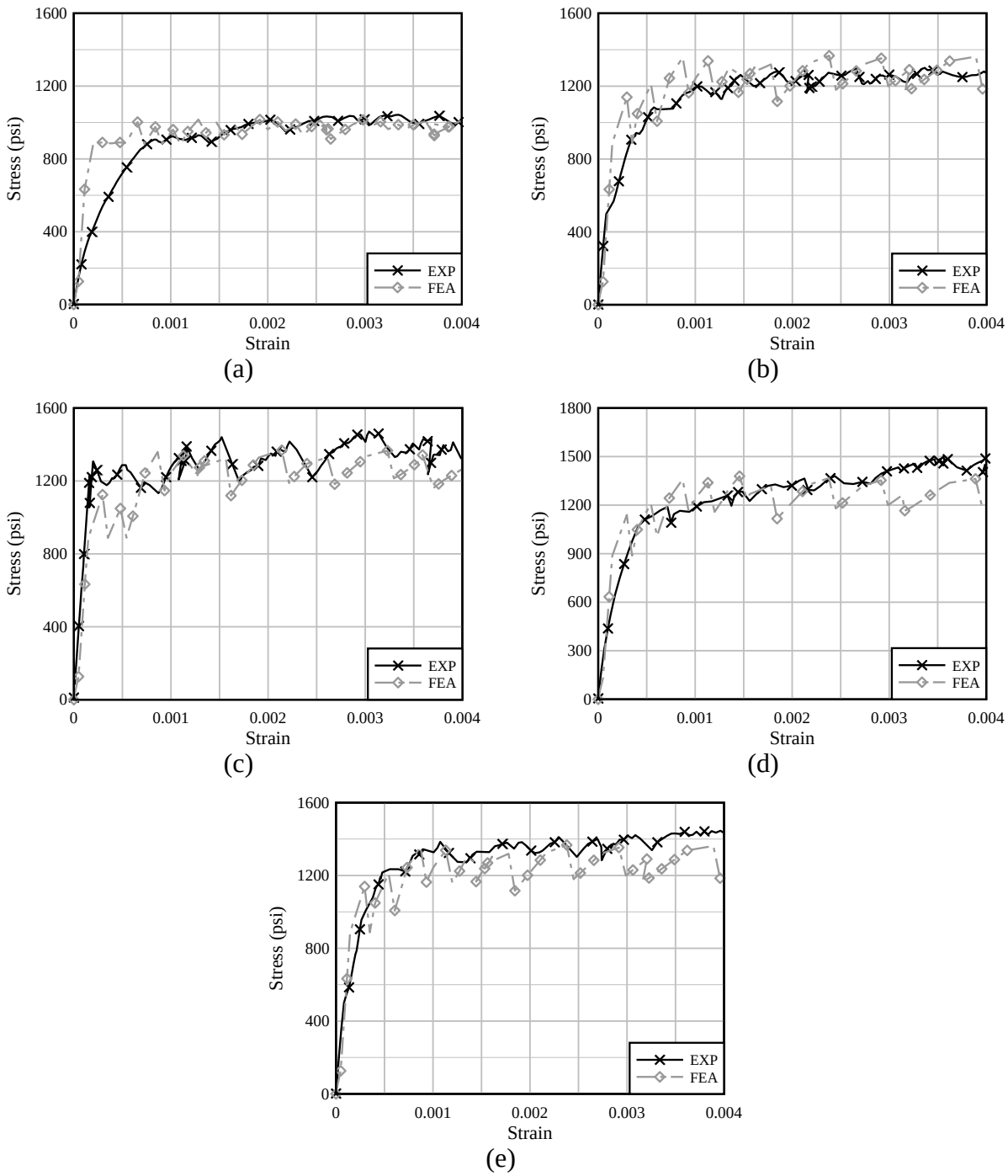

Figure 7-14 Comparison of experimental and analytical DTT results for: (a) G1, (b) G2, (c) G3, (d) G4 and (e) G5

7.3.2 Validation within Elastic Range

Validation of the FIB 72 mockup FEA model in the elastic range consisted of comparing the concrete and mild-steel reinforcement strains from the model to those measured experimentally during prestress transfer.

Figure 7-15 shows the location of the fiber optic sensors (FOS) installed on the concrete surface. Instrumentation limitations restricted the FOS strain measurements to eight ends. FOS Line 1 was placed approximately one inch from the girder end, while FOS Line 2 was 3 in. apart. Validation in the elastic range consisted of comparing the measured concrete strains to the FEA results for up to 35% of the total transferred prestressing force.

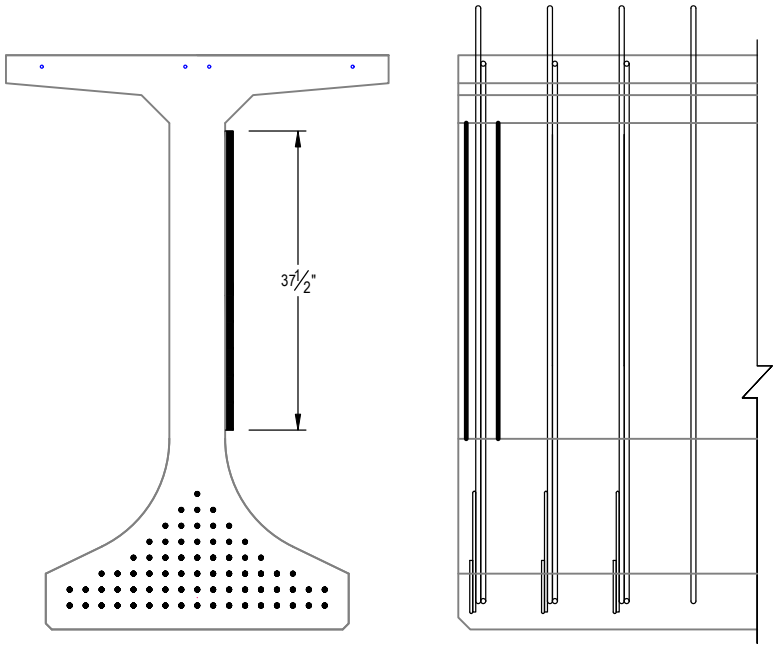

Figure 7-15 FOS used for validation of FIB 72 mockup analytical model

Figure 7-16 through Figure 7-20 show a comparison of the measured concrete strain to the FEA results. These figures show the average strain measured with FOS for 5s, immediately after the transfer of 35% of the prestress force (25 strands released). In general, FOS concrete strain patterns for Line 1 and Line 2 have similar shape, with compressive strains in the lower part of the web and tension strains starting at ~30 in. of girder height. The analytical model shows similar microstrain level for Line 1 in all mockups, while it overestimates Line 2. Figure 7-16 shows the FOS results of G1 having SCC on End-1 and UHPC on End-2. Experimental results showed similar strain levels for both UHPC and SCC; however, the SCC end begins to show more microstrain variation (peaks) that later result in cracking. The analytical model shows that the SCC had almost double the tensile strain of the UHPC end, mainly due to the difference in stiffness. This resulted in the analytical model providing a good approximation of the UHPC deformation but overestimating both FOS lines in the SCC.

At 35% prestress transfer, the decrease in end region mild-steel reinforcement installed in G1 to G5 did not result in significant increase of deformation on the experimental mockups or the analytical model.

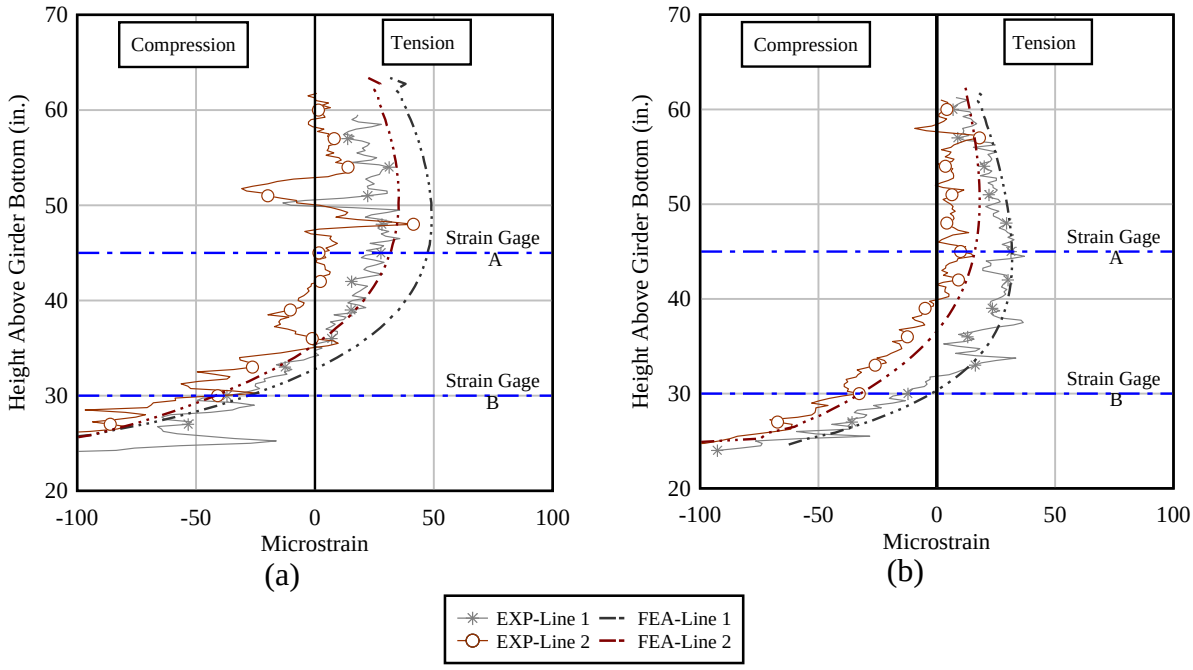

Figure 7-16 Concrete strain at 35% prestress transfer of G1: (a) E1-SCC and (b) E2-UHPC

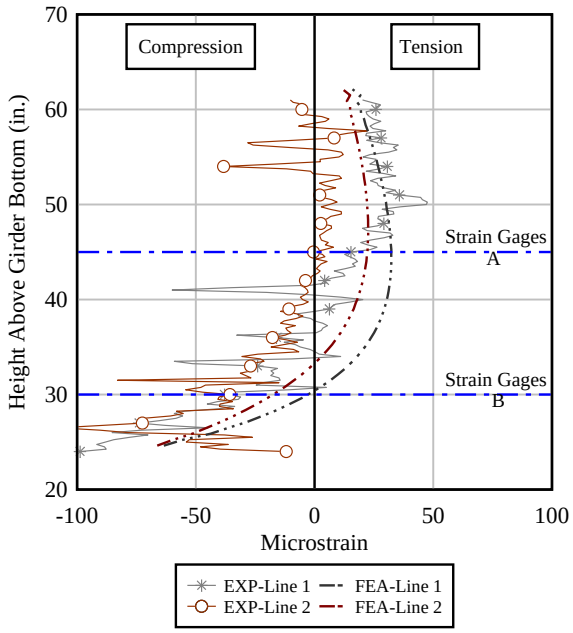

Figure 7-17 Concrete strain at 35% prestress transfer of G2-E2

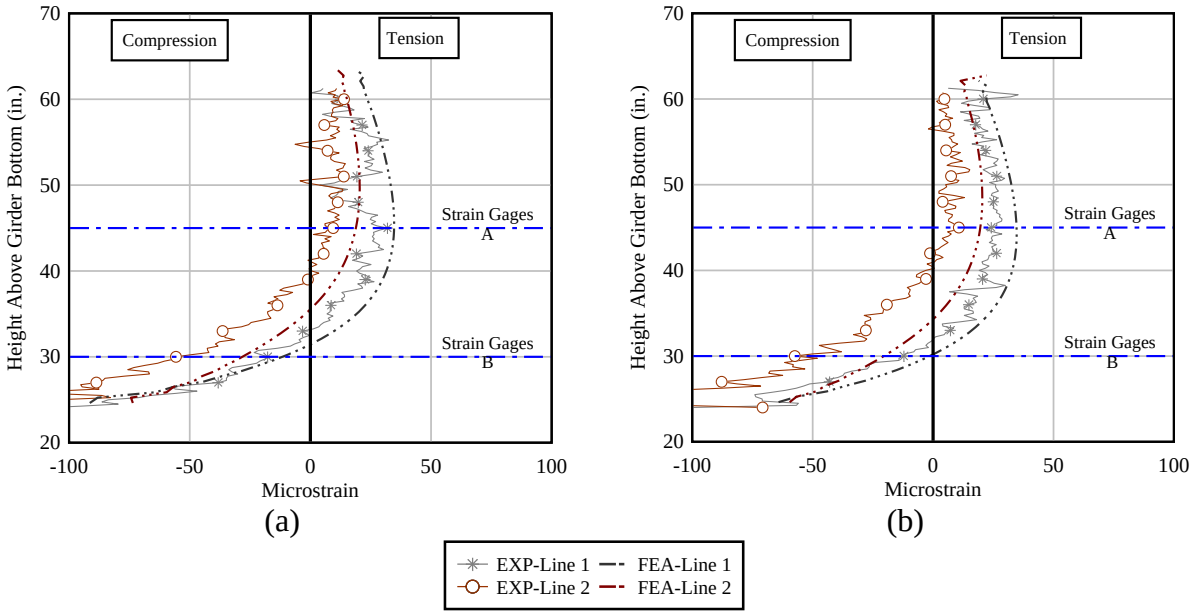

Figure 7-18 Concrete strain at 35% prestress transfer of G3: (a) E1 and (b) E2

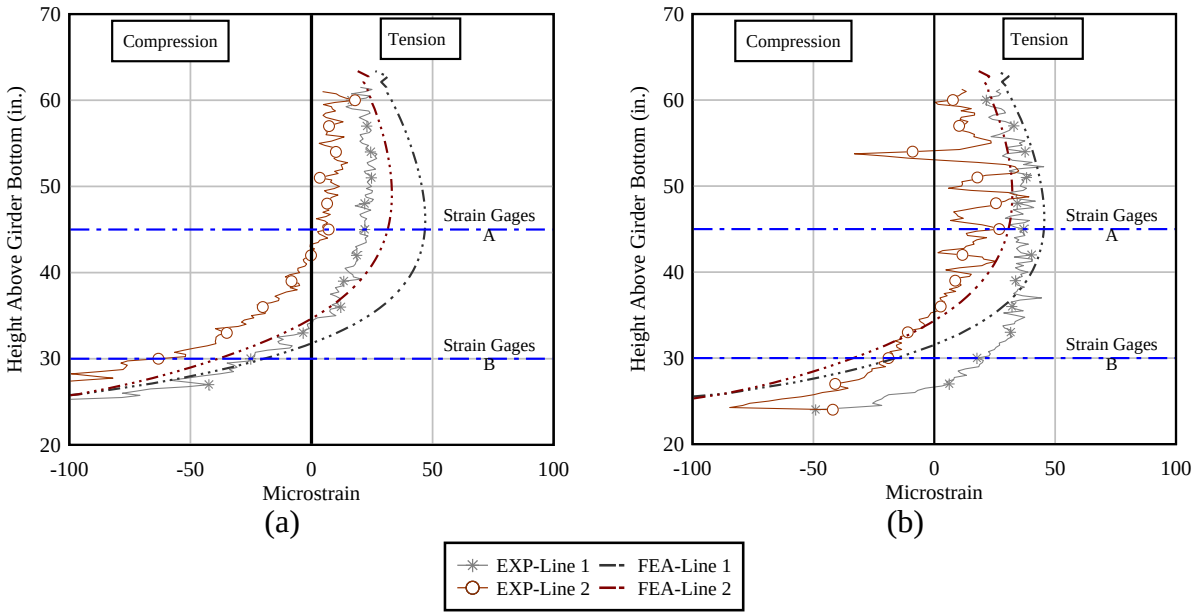

Figure 7-19 Concrete strain at 35% prestress transfer of G4: (a) E1 and (b) E2

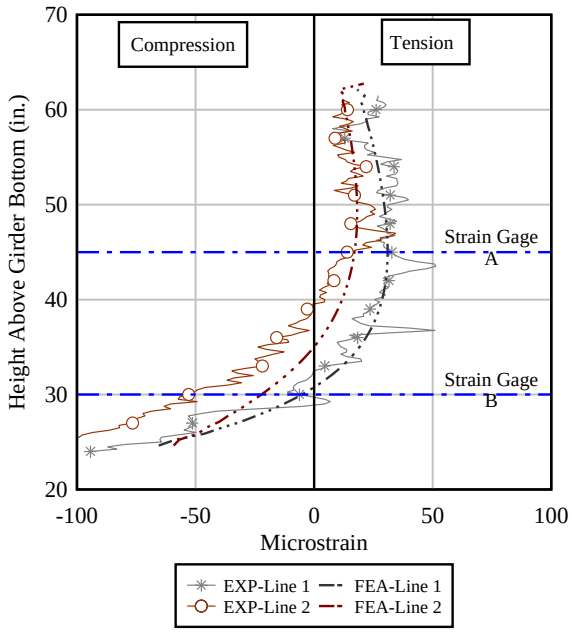

Figure 7-20 Concrete strain at 35% prestress transfer of G5-E2

Figure 7-21 shows the location of the strain gages installed on the two rebar bundles nearest the girder end. Four strain gages were installed to measure strain in different rebar bundles and rebar heights.

Figure 7-22 through Figure 7-26 show a comparison of measured mild-steel reinforcement strain with FEA strain results. Experimental strain measured by strain gages "A" increase with the percent of transferred prestressing force. FEA strain results show similar trends to those measured on strain gage A1 and A2 for all mockups. Both experimental and analytical strain gage A results exhibit positive (tension) strains during prestress transfer. Similarly, FOS Line 1 and Line 2 show tension strains at the location of the strain gage. For instance, Figure 7-16b shows the FOS measurements of G1-E2 (UHPC) where strain gage A is located at a girder height of 45 in. At this location, FOS strains for Line 1 and Line 2 are 31με and 16 με respectively. Moreover, Figure 7-22b shows that at 35% of prestress level, strain gage A-1 and A-2 measured 38 με and 16 με respectively. The agreement of experimental and analytical strain values at the concrete surface and on the mild-steel reinforcement demonstrates the validation of the modeling approach.

Strain measured with gages B1 and B2 exhibit negative strain (compression). At a prestress level of approximately 25%, measured strain begins to shift towards tension. This trend was also observed in the FEA results; however, the experimental strains exhibited higher compression strains. Furthermore, FOS measurements of Line 1 and Line 2 show that at the girder height where strain gages B were located, strains are also in compression. For instance, Figure 7-16b shows the FOS measurements of G1-E2 (UHPC), where strain gage B is located at a girder height of 30 in. At this location, FOS strains for Line 1 and Line 2 are -10με and -37με respectively. Moreover, Figure 7-22b shows that at 35% of prestress level, strain gage B-1 and B-2 measured -8με and -37με respectively. Therefore, both experimental measurements and analytical results show agreement between the concrete and steel reinforcement strains.

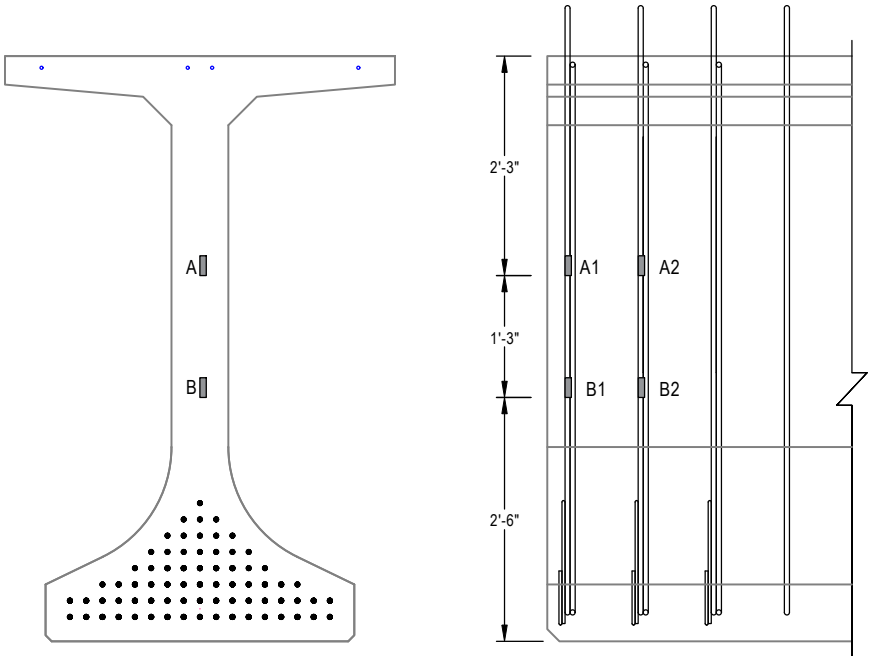

Figure 7-21 Strain gages used for validation of FIB analytical model

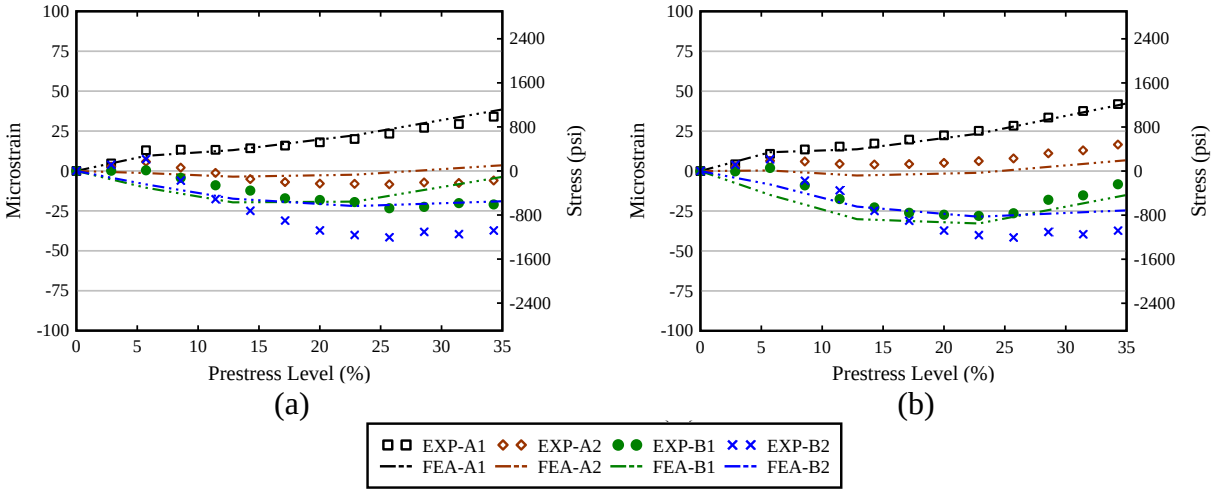

Figure 7-22 Mild-steel reinforcement strain during prestress transfer: (a) G1-E1 and (b) G1-E2

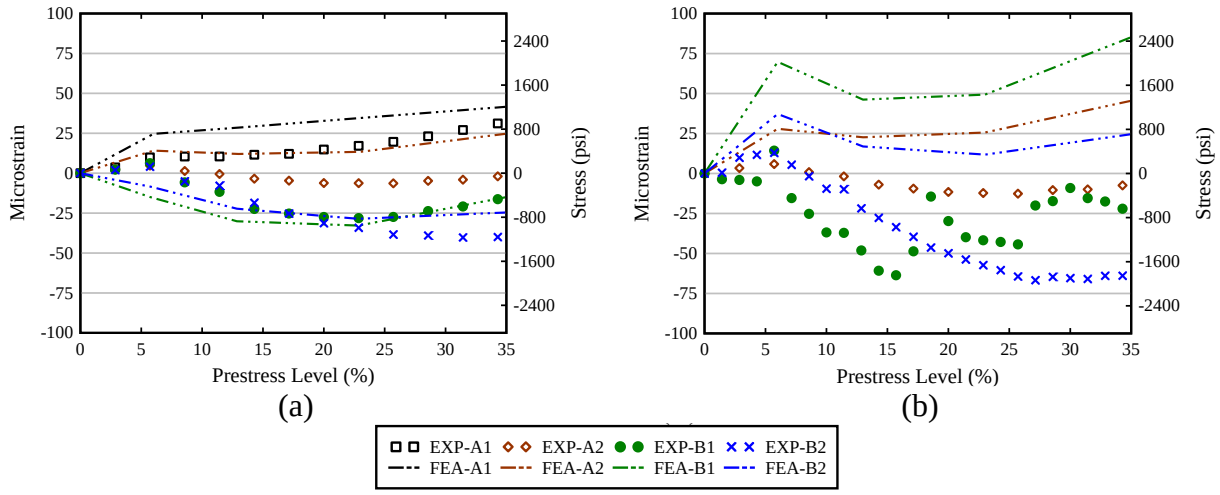

Figure 7-23 Mild-steel reinforcement strain during prestress transfer: (a) G2-E1 and (b) G2-E2

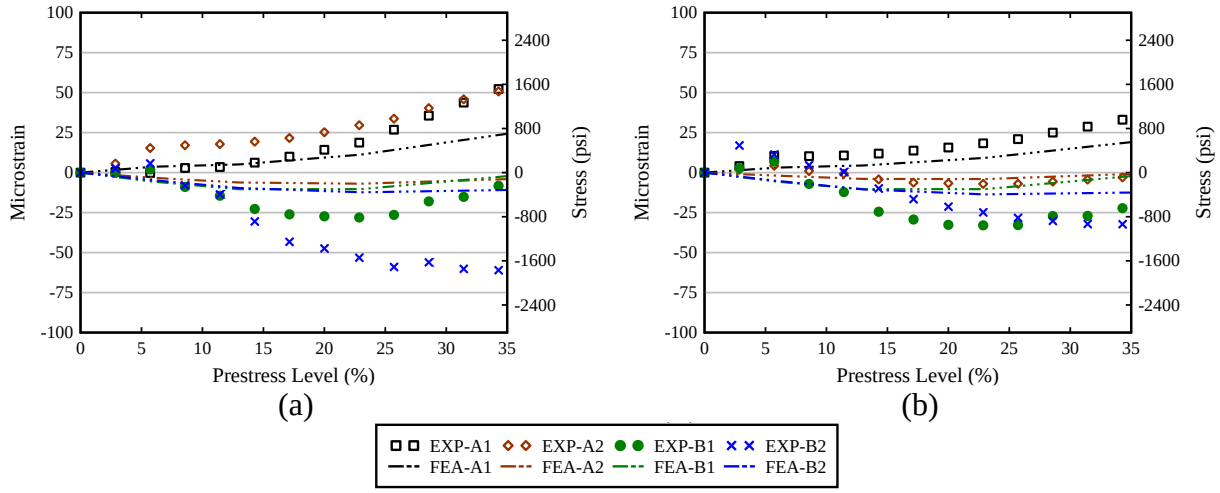

Figure 7-24 Mild-steel reinforcement strain during prestress transfer: (a) G3-E1 and (b) G3-E2

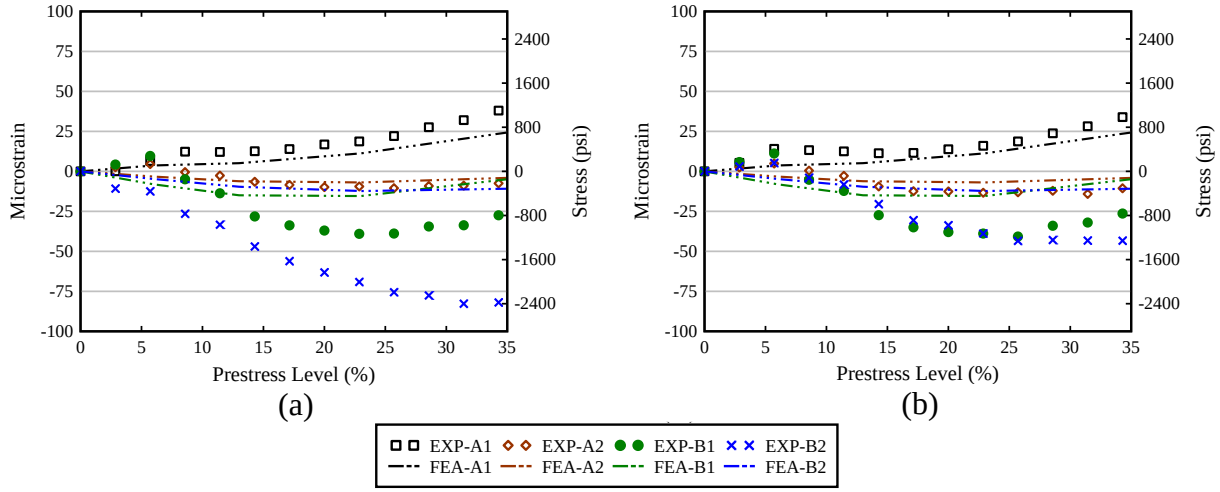

Figure 7-25 Mild-steel reinforcement strain during prestress transfer: (a) G4-E1 and (b) G4-E2

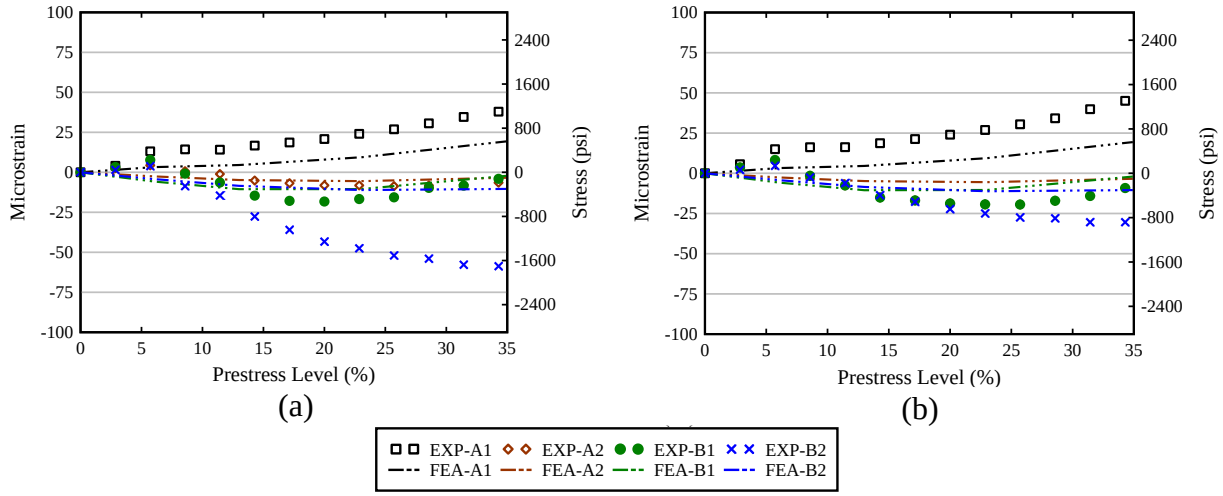

Figure 7-26 Mild-steel reinforcement strain during prestress transfer: (a) G5-E1 and (b) G5-E2

7.3.3 Validation within Inelastic Range

Validation of the FEA results in the inelastic range was performed by comparing crack information generated by the Winfrith model to crack width measurements made on the FIB 72 mockups after prestress transfer. Details of the procedure used to measure crack widths in the field were discussed in Section 3.5.1. Generally, the end regions mockups were inspected with the naked eye immediately after prestress transfer. Inspection consisted of spraying the concrete surface with acetone to identify cracks, then measuring crack widths with a crack width microscope. Crack data from the analytical model were extracted from the concrete solid elements along the surface of the cross-section. A minimum crack width of 0.0005 in. was established for comparison based on the smallest crack widths measured on the experimental mockups. For model validation, two metrics were used: maximum crack width and average crack width. Maximum crack width is the maximum crack width taken on either side of the web on the experimental mockups and determined from the analytical models. Average crack width is defined as the average of all the crack widths measured in each end of the experimental mockups, and those determined from the analytical models.

Figure 7-27 through Figure 7-31 show a comparison of the end region crack patterns visible on the mockups immediately after prestress transfer for both analytical and experimental mockups. FEA crack pattern results were similar to the cracks observed on the SCC ends of both G1 and G2. During visual inspection of the mockups, the UHPC end did not exhibit crack widths larger than 0.0005 in. Considering UHPC tendency to develop micro-cracks, it is possible that fine cracks were overlooked. Nevertheless, FEA and mockup crack patterns of G1 and G2 — both heavily reinforced mockups — compared well. FEA crack patterns of G3-G5 exhibited cracks with an average width of 0.001 in. that were not visible in the experimental mockups.

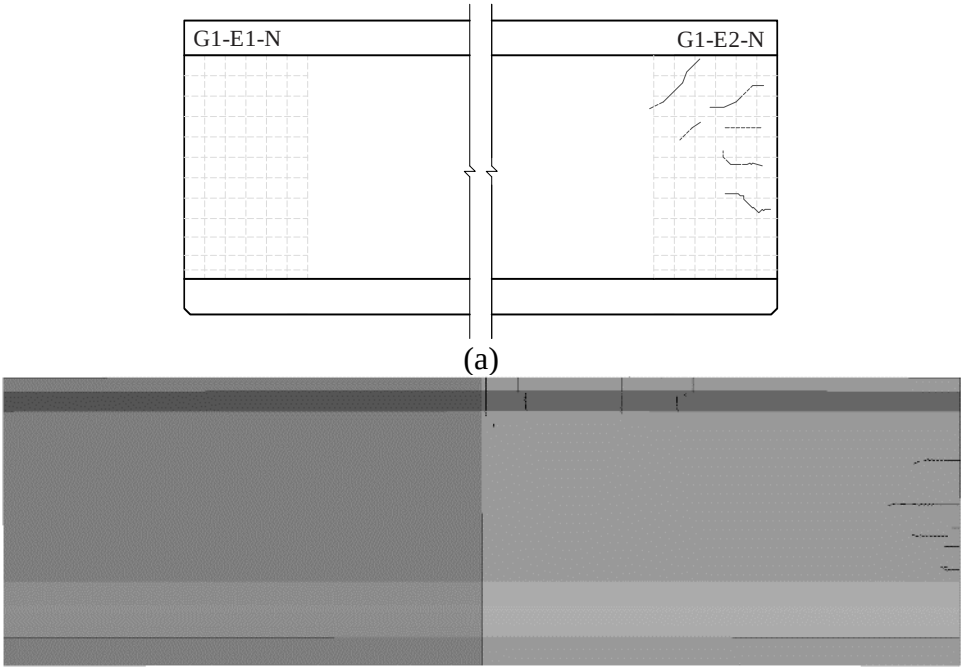

Figure 7-27 End region cracking of G1 after release: (a) experimental and (b) analytical

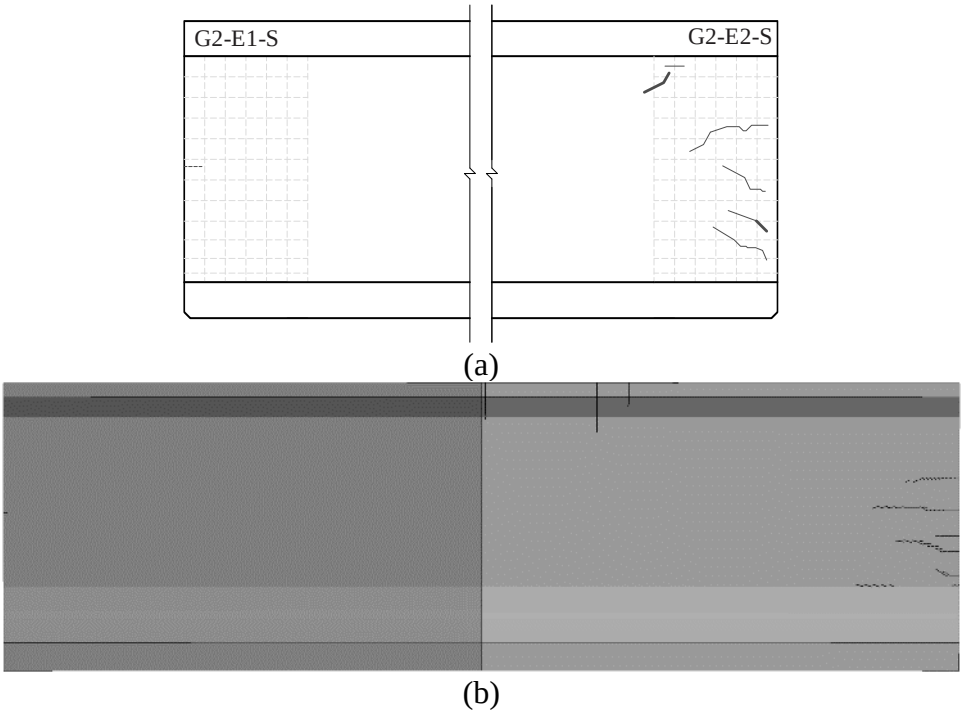

Figure 7-28 End region cracking of G2 after release: (a) experimental and (b) analytical

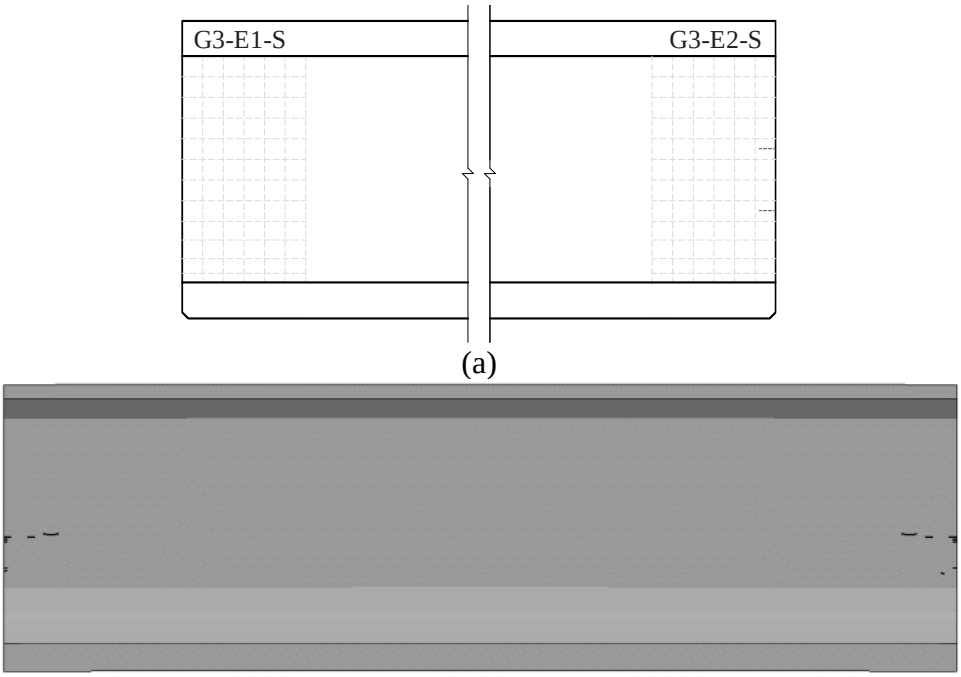

Figure 7-29 End region cracking of G3 after release: (a) experimental and (b) analytical

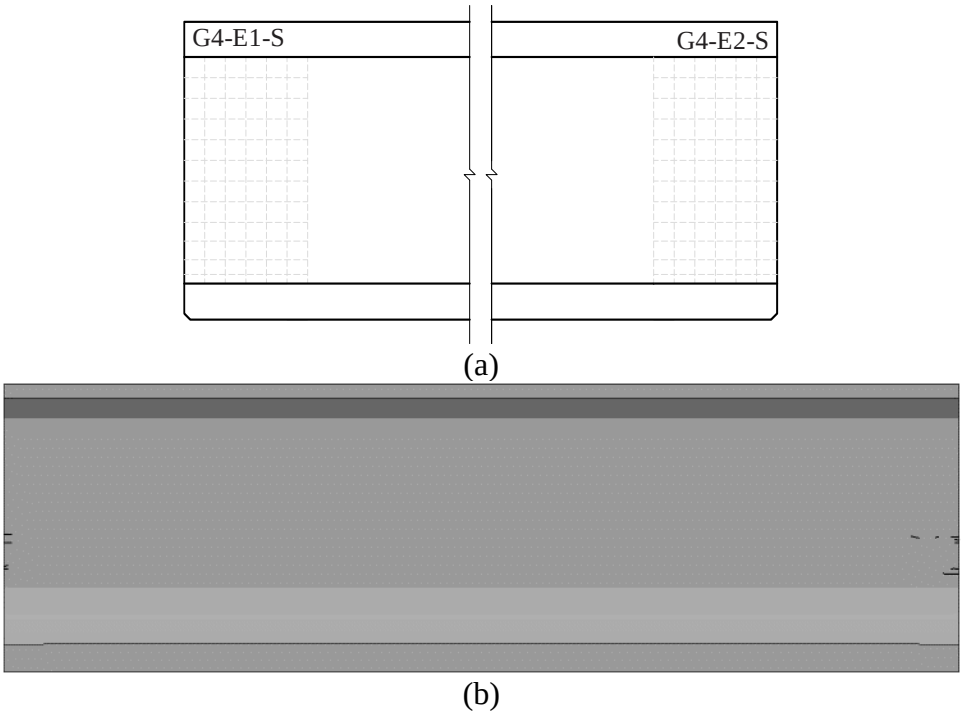

Figure 7-30 End region cracking of G4 after release: (a) experimental and (b) analytical

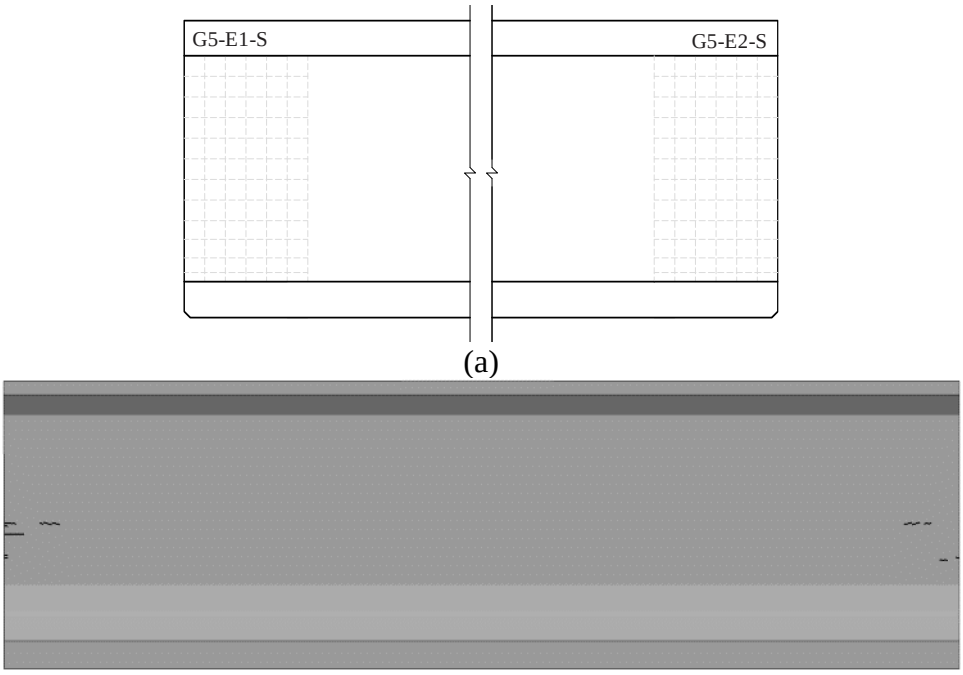

Figure 7-31 End region cracking of G5 after release: (a) experimental and (b) analytical

Figure 7-32 through Figure 7-36 show comparisons of average experimental crack widths and maximum crack widths to those determined from the FEA results. Crack width measurements at 7 days after prestress transfer were also included in the comparison in case cracks were overlooked in the first crack width measurements. Generally, the analytical model shows good agreement with the SCC ends, while it overestimates UHPC crack widths and average crack width. The main difference between the analytical model and the experimental measurements is that for the UHPC ends having a single bar (G3-E1, G3-E2, G4-E2, G5-E1 and G5-E2) the analytical model has maximum crack widths slightly above 0.002 in., while maximum crack widths of 0.001 in. were observed on those mockup ends. Nevertheless, given the dark surface color of UHPC and the tendency of fibers to keep cracks closed, it is possible that cracks under 0.0005 in. were overlooked during field measurements.

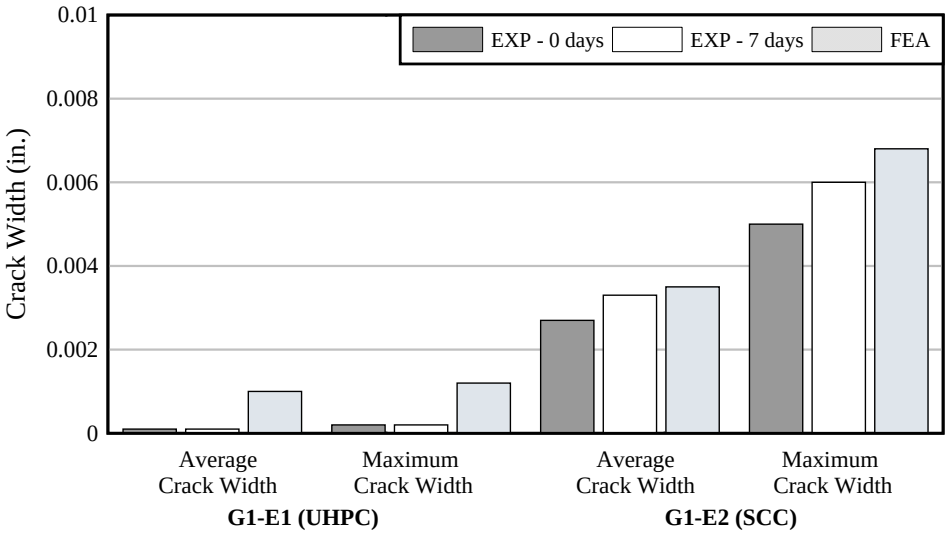

Figure 7-32 Comparison of average and maximum crack width for G1 obtained experimentally and analytically

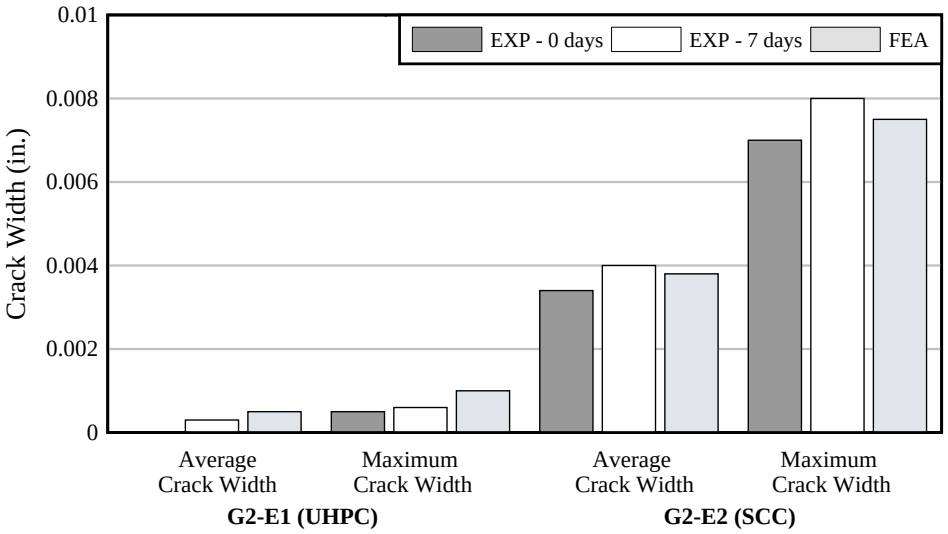

Figure 7-33 Comparison of average and maximum crack width for G2 obtained experimentally and analytically

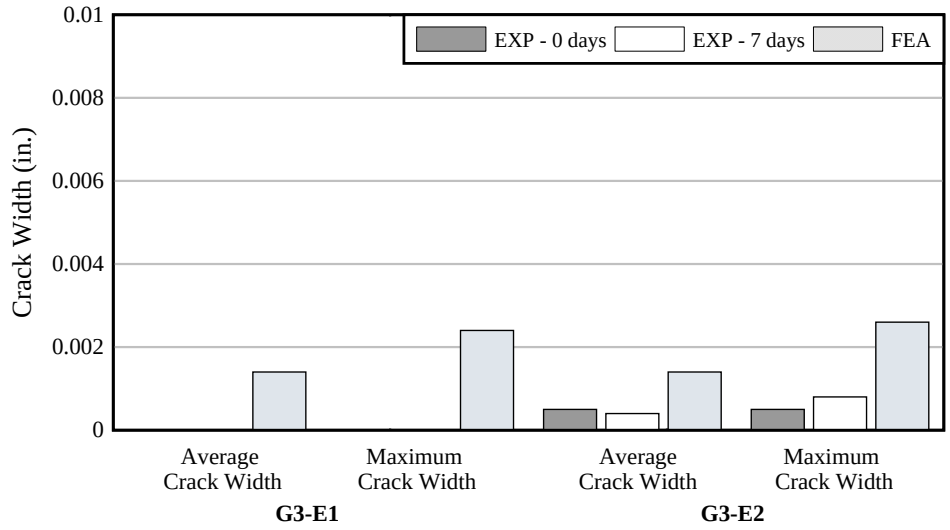

Figure 7-34 Comparison of average and maximum crack width for G3 obtained experimentally and analytically

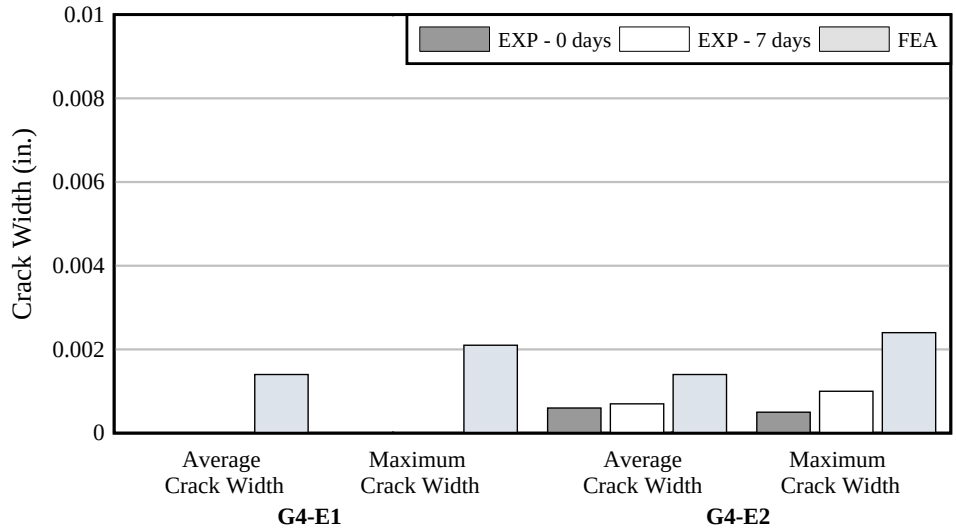

Figure 7-35 Comparison of average and maximum crack width for G4 obtained experimentally and analytically

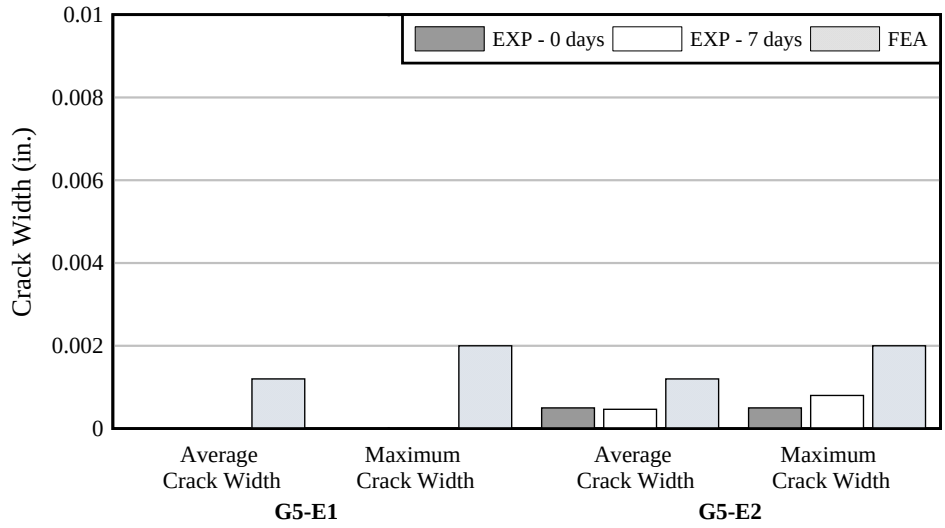

Figure 7-36 Comparison of average and maximum crack width for G5 obtained experimentally and analytically

Current end region design guidelines limit rebar stresses to 20 ksi to limit crack widths. The analytical model was used to determine maximum rebar stresses at 100% prestress level to compare to the 20 ksi limit. Figure 7-37 shows the rebar stresses obtained from the analytical model. The bar chart differentiates the stresses based on the detailing configuration. For instance, the SCC ends having reinforcement bundles are shown in light gray. Furthermore, UHPC ends having a rebar bundle or a single bar are shown in medium-dark gray and black respectively. Note that the SCC ends exceed the 20 ksi limit, which was expected because the number of strands was increased compared to typical FIB 72 strand pattern.

UHPC ends with rebar bundles remained under the 20 ksi limit regardless of the spacing between bundles, while UHPC ends having a single bar exhibited stresses between 25 ksi and 30 ksi. In addition, the figure also shows the crack length index at 1-day and 90-days. Crack length index was computed using the field crack length measured on all mockups and normalized by the crack length on the SCC end in G1, which had typical FDOT reinforcement detailing. The data shown in the figure indicates that UHPC ends with a single rebar are likely to have stresses exceeding 20 ksi, which in SCC is associated with excessive cracking or crack widths in need of repair. However, UHPC ends did not exhibit excessive cracking or crack widths in need of repair. Thus, the 20 ksi limit may not be applicable for end region design when using UHPC.

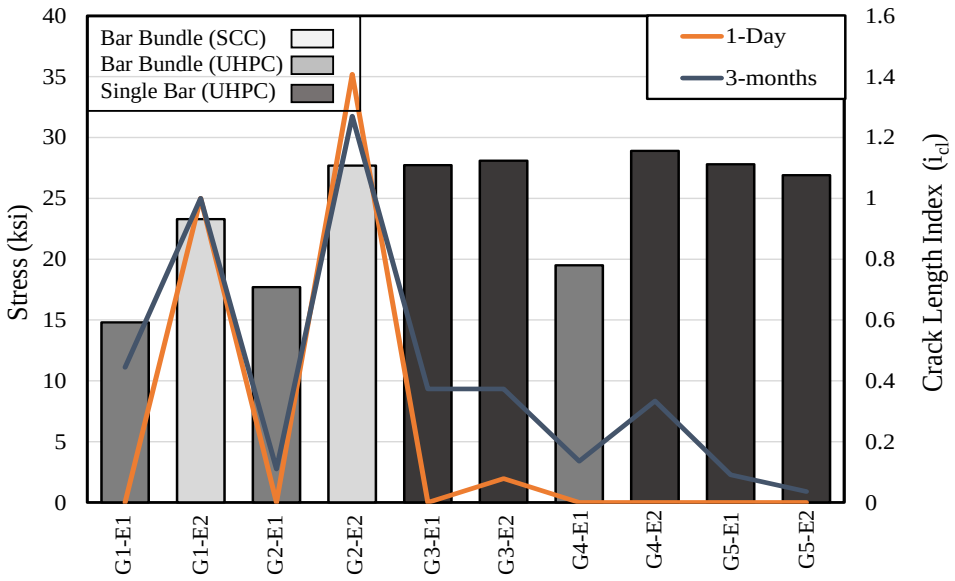

Figure 7-37 Comparison of FEA rebar stresses to crack length index

7.3.4 FIB 96 Model

After validation of the FEA results for the FIB 72 mockups, the same FEA modeling techniques were then used to analyze a FIB 96, which, due to slenderness, is most prone to developing cracks. The modeling approach was maintained to model prestress transfer on a FIB 96. Figure 7-38 shows a schematic of the end region reinforcement schemes used to evaluate the behavior of the FIB 96 end region following prestress transfer.

The first model used typical FDOT detailing with SCC on one end and UHPC on the opposite end. The second model was similar to G2, with the spacing of the rebar bundles increasing from 3.5 in. in G1 to 7 in. in G2. The increase in spacing resulted in 43% reduction in reinforcement cross-sectional area. The third model aimed to evaluate UHPC ends with the lightest possible rebar configuration. One end had a single bar with a spacing of 7in. and 9in., which results in a reduction in reinforcement cross-sectional area of 85 % and 89%, respectively.

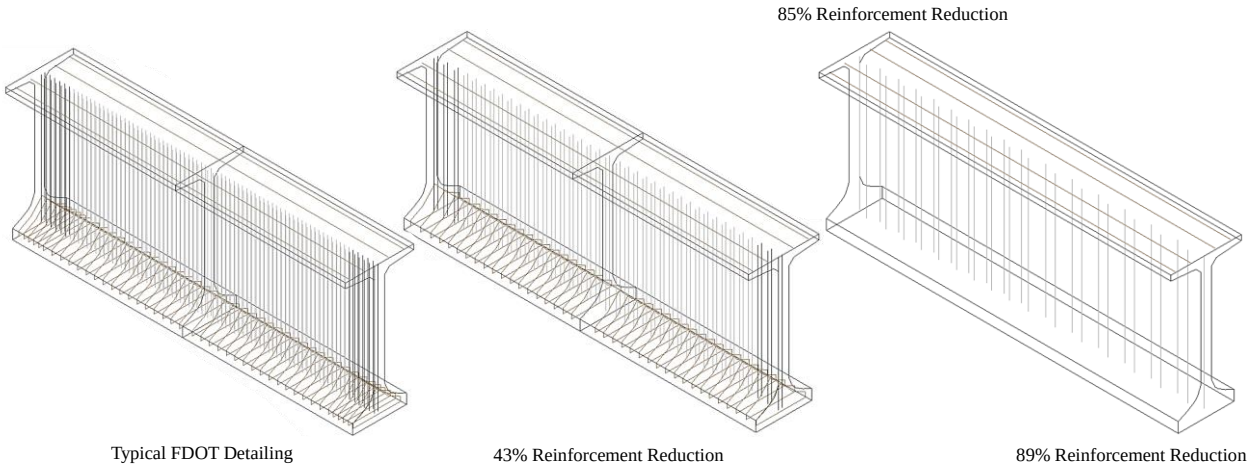

Figure 7-38 Overview of FIB 96 mild-steel reinforcement

Figure 7-39 shows the FEA crack pattern results from the parametric study. As expected, the SCC exhibited severe cracking, while the UHPC exhibited very little cracking. Similar to the FIB 72 discussion, UHPC ends having single rebar resulted in light cracking.

Figure 7-40 shows a comparison of maximum crack widths and average crack widths obtained from all FIB 96 models. SCC ends exhibited maximum crack widths between 0.0067 in. and 0.0075 in., and average crack widths between 0.004 in. and 0.005 in. FDOT crack repair criteria would require that a penetrant sealer be applied at the location of maximum width cracks. UHPC ends, however, exhibited maximum crack widths between 0.001 in. and 0.0028 in., and average crack width between 0.0002 in. and 0.0018 in. These results suggest that the use of UHPC at the girder ends has the potential to significantly reduce the cracking intensity caused by prestressing. These are promising results that should be confirmed by field testing prior to full implementation.

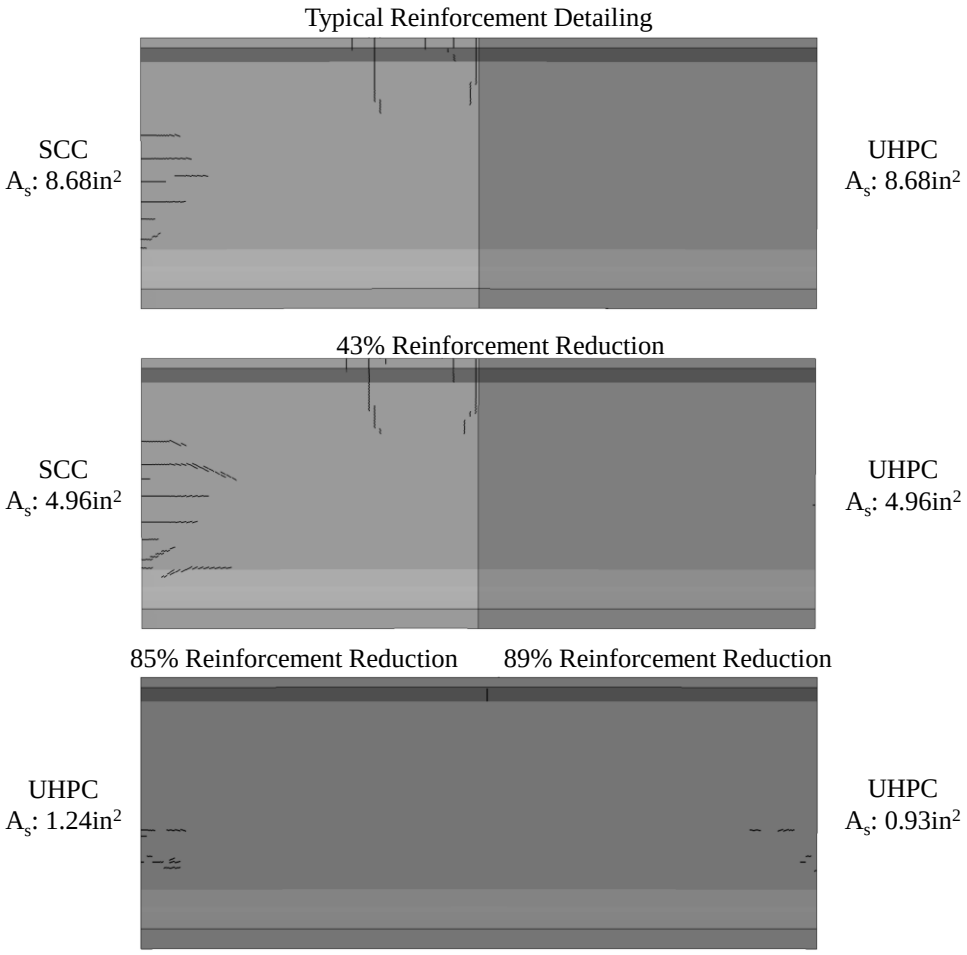

Figure 7-39 Model cracking after release

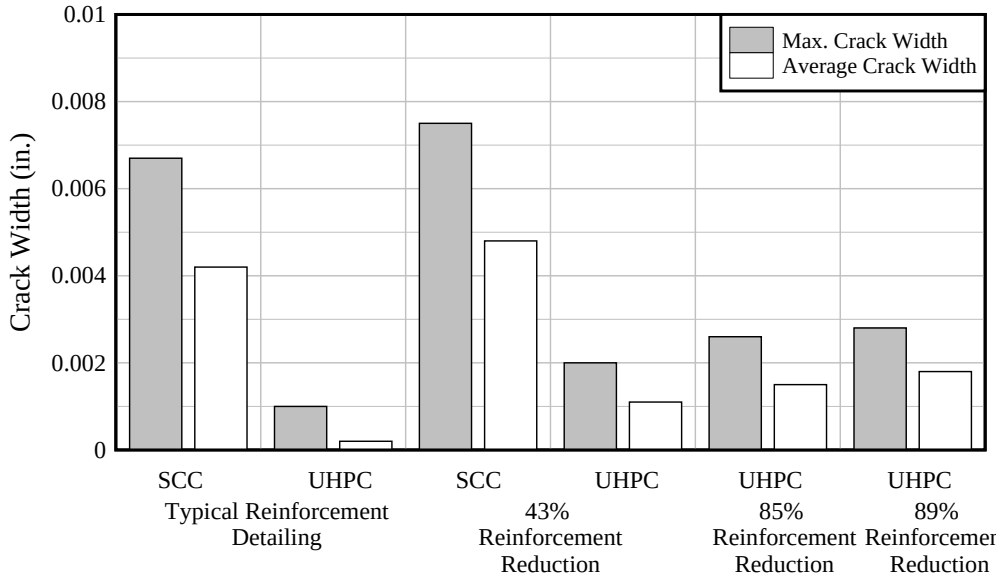

Figure 7-40 Maximum and average crack widths for varying end region reinforcement

7.4 FIB 54 Shear Models

FEA models of the UHPC-SCC hybrid FIB 54 girders were developed to evaluate the behavior under applied shear. Recall that two girders were constructed to investigate the effect of the UHPC length at the ends, and a reduced amount of reinforcement. These girders are named G6 and G7 following the nomenclature used in Section 4. Development of the analytical model was divided into three stages. The first stage was calibration of the material model to simulate the tensile behavior of UHPC. The second stage consisted of simulating the prestress transfer field conditions of the 70 fully bonded strands. Finally, the third stage consisted of adding the concrete deck and applying load. Figure 7-41 shows a schematic of the FIB 54 model.

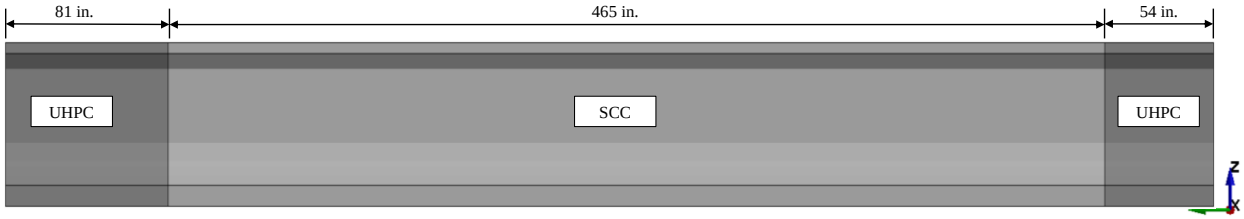

Figure 7-41 Overview of the UHPC-SCC hybrid girder model

The concrete beam, concrete deck and precast bed components of the FEA model were formulated using 8-node 3D solid elements. The shape of the concrete solid elements was devised to minimize the difference between side dimensions of the element, while still accommodating the curved geometry of the bottom flange. Mild-steel reinforcement and prestressing strands were modeled using the same approach as the FIB 72 mockup FEA models.

Construction staging is a feature of LS-DYNA used to account for the different construction events in the life of a model. Two stages were created to account for detensioning and load application (Figure 7-42).

During the detensioning stage the stiffness of the deck and the deck reinforcement are omitted to prevent these components from having an effect during the detensioning stage. At the end of the first stage, the precast bed stiffness is removed, and the girder is supported by newly added spring elements having the same stiffness as bearing pads. Spring axial stiffness used to represent the bearing pads was determined from the experimental load tests using the measurements of the displacement transducers above the supports. Lateral stiffness was computed using the geometry of typical FDOT bearing pads type F and Equation 2. Bearing pad type F dimensions are 10 in. × 32 in. × 2 $^{9}/_{16}$ in., with elastomer layer thicknesses of 0.25 in. and 0.5 in. for the external and internal elastomer layers, respectively. Shear stiffness was determined as:

$$k_s = \frac{A_b G}{l_e} \qquad \text{Equation 7-2}$$

where k_s is the shear stiffness of the bearing pad (lbf/in), A_b is the cross-sectional area of the bearing pads (in.^{2}), G is the shear modulus of the bearing pad type (psi) and l_e is the total thickness of all elastomer layers.

In the second stage, the concrete deck and deck reinforcement stiffness are activated. Finally, during stage 2 the load button starts to move downward at the specified displacement rate.

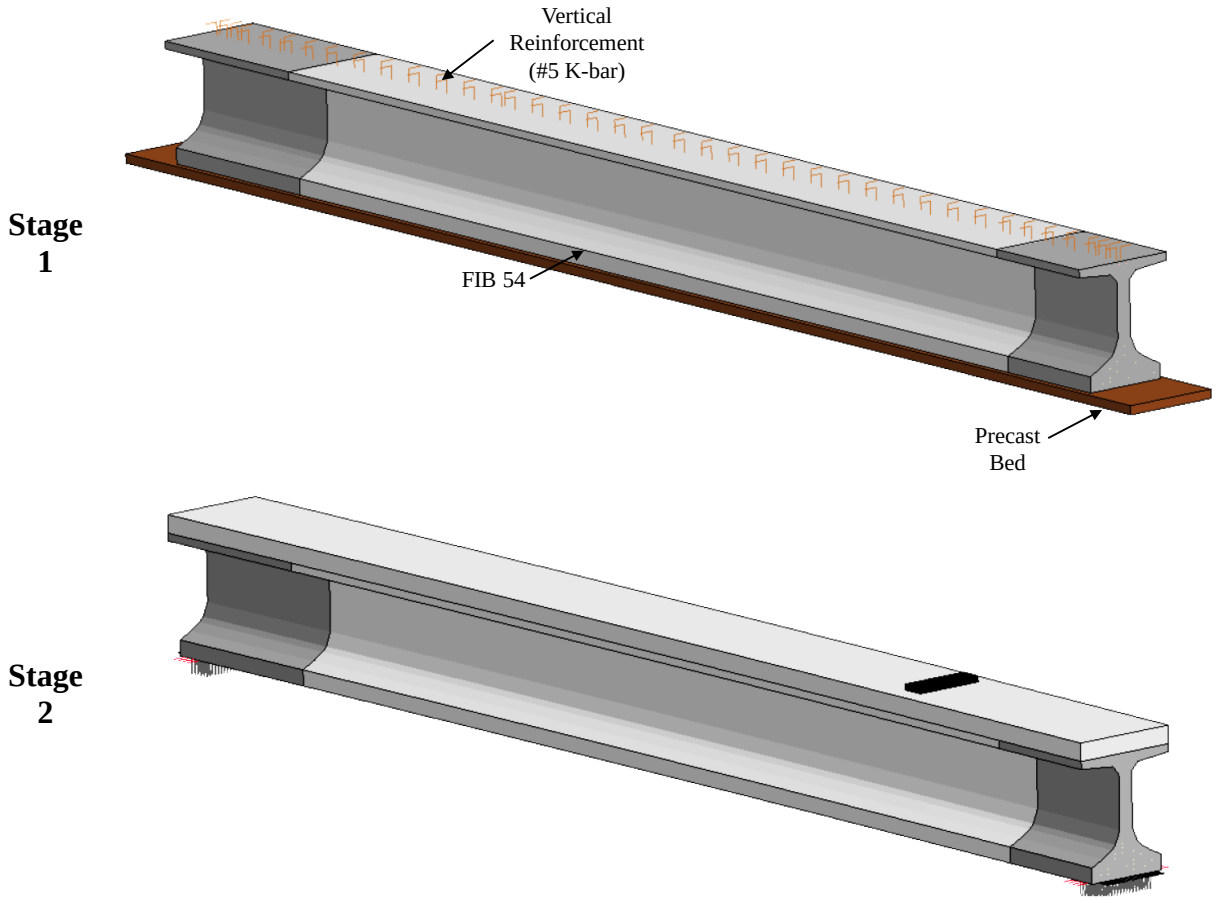

Figure 7-42 FEA construction stages

7.4.1 Concrete Damage Material Calibration

To model the behavior of FIB 54 girders under shear loading, it was important to accurately represent the post-cracking behavior of UHPC. As discussed in section 7.1, the MAT_ CONCRETE_DAMAGE_REL3 (K&C Concrete model) material model was selected to model both SCC and UHPC. In contrast to the MAT_WINFRITH_CONCRETE model, the K&C material model can be used when large deformations of the elements are expected. The K&C model has the capability of automatically generating all necessary parameters solely based on the unconfined concrete compression strength.

MAT_72R3 is not explicitly capable of modeling fibers in concrete; however, the model offers parameters that can be adjusted to distinguish between compression and tension damage, and to approximate the residual tensile strength. These parameters are b1 and b2, which govern the compressive and tensile softening as the stress point moves from the maximum strength surface to the residual strength surface (Liu, Wu, and Chen 2017). For conventional concrete both parameters can be computed using Equation 7-3 and Equation 7-4.

$$b_1 = 0.34h + 0.79 \qquad \text{Equation 7-3}$$

$$b_2 = (0.09W_{lz}^2 - 0.98W_{lz} + 3.06)(1 - 0.004f'^2_c + 0.097f'_c - 0.484 \qquad \text{Equation 7-4}$$

where h is the characteristic element size, W_{lz} is the crack localization width, and f_c is the unconfined compressive strength of SCC or UHPC.

SCC was modeled using the automatic parameter generator based on the unconfined compressive strength obtained experimentally from the average of three cylinders tested on the same day of shear testing. However, several studies (Crawford et al., 2011, Crawford et al., 2013, Wu and Crawford, 2015, and Xu and Wen 2016) have reported that the automatic parameter generator defines the fractional dilatancy parameter (OMEGA) as 0.5, which tends to underestimate the compressive strength of concrete used currently. Recommended OMEGA values for conventional concrete vary from 0.7 to 0.9 depending on the amount of confinement, however, for UHPC the recommended OMEGA value is 0.9.

UHPC was also modeled using the automatic parameter generator, but the tensile strength, parameters b2 and OMEGA were manually calibrated to approximate UHPC tensile behavior. Magallanes et al. (2010) and Yin et al. (2019) reported that specifying a value of -10 for b2 parameter is sufficient to simulate UHPC tensile behavior. The only remaining parameter was the tensile strength of UHPC, which was manually calibrated based on the behavior observed on the DTT and FB models. Figure 7-43 compares the final calibrated model under different loading conditions (axial, bending). Table 7-3 summarizes the parameters used to model both SCC and UHPC.

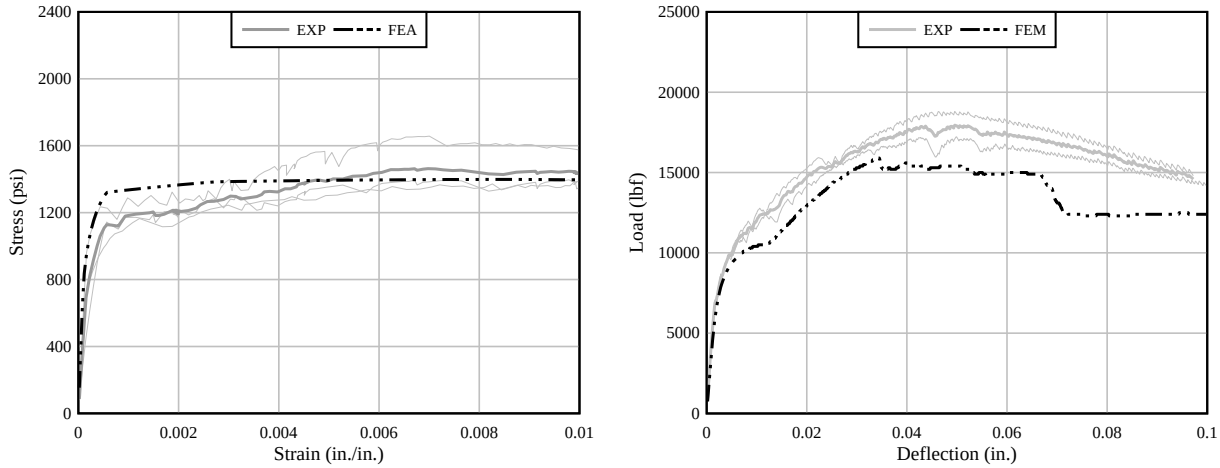

Figure 7-43 K&C material calibration comparison: (a) DTT and (b) FB ASTM C1609

Table 7-3 Summary of key material model parameters

	SCC	UHPC
Unconfined Compressive Strength (psi)	11,200	21,000
Tensile Strength (psi)	790	1400
b1	3	Default
b2	Default	-10
OMEGA	0.9	0.9

7.4.2 Prestress Transfer Validation

Validation of the prestress transfer stage of the FIB 54 shear model consisted of comparing the experimentally measured concrete strains to those obtained from the analytical model. Figure 7-44 shows the location of the fiber optic sensors (FOS) installed on the concrete surface. FOS Line 1 was placed approximately one inch from the girder end, while FOS Line 2 was 3 in. from Line 1.

Figure 7-45 shows the FOS measurements of G6 and G7 compared to the strain obtained from the analytical model. FOS measurements were averaged for one minute once all strands were released. Strains from the analytical model were computed from vertical displacements of the solid element nodes. For both Line 1 and Line 2, it was observed that the analytical model matched the experimental FOS microstrain measurements over the girder height (Figure 7-45). Furthermore, the analytical model matches the high-tensile strain levels at a girder height between 25 in. and 35 in. Note, however, that Figure 7-45a shows sudden peaks in strain associated with crack formation, which is not represented with the MAT_72R3 concrete damage model.

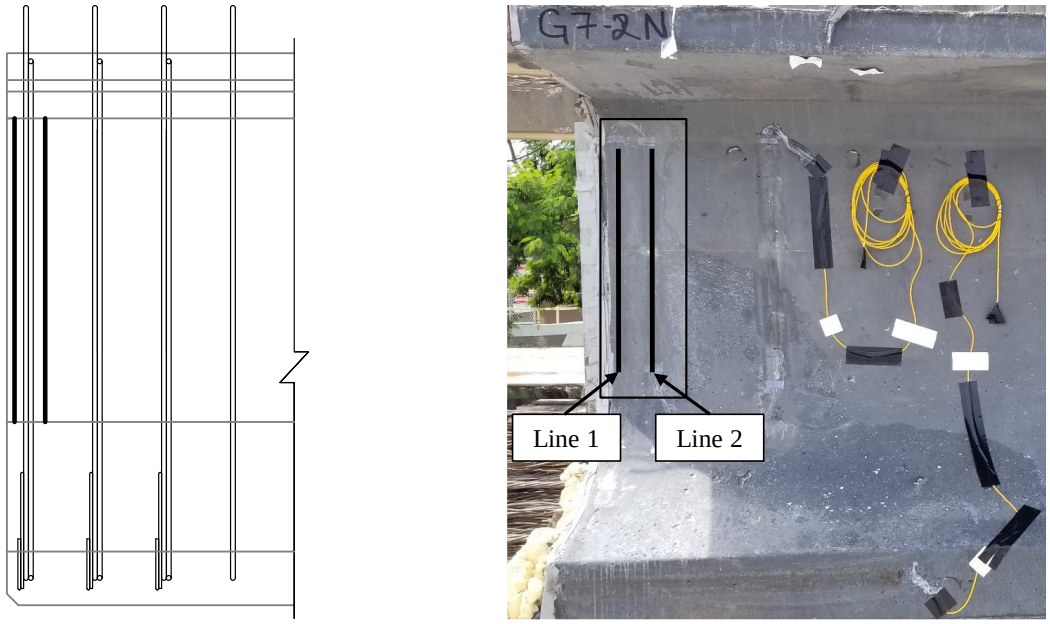

Figure 7-44 FOS installed on the FIB 54 girders

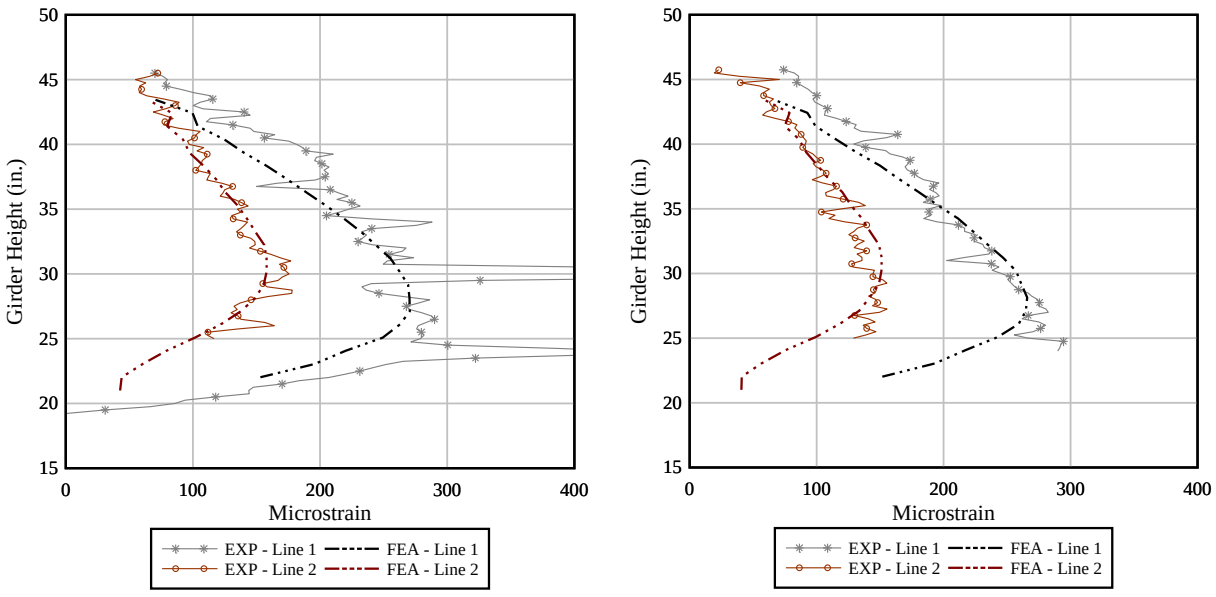

Figure 7-45 Comparison of concrete strain at the end of prestress transfer: (a) G6 and (b) G7

7.4.3 Validation of Load Testing

Validation of the loading stage was performed by comparing the horizontal and vertical concrete strains measured using FOS to those obtained from the analytical model, and by comparing the experimental and analytical load-displacement behaviors up to 1,000 kip. Figure 7-46 shows a schematic of the location of both horizontal and vertical FOS used for validation.

Comparison of strains measured experimentally to those obtained from the analytical model were performed at loads of 250 kip and 500 kip to evaluate the behavior before and after cracking. Based on the FOS measurements, it was estimated that cracking began after 250 kip. Furthermore, 500 kip was the highest load for which reliable FOS data were measured. Beyond this load level, the crack widths were large enough to begin damaging or debonding the FOS glued to the concrete surface.

Figure 7-47 through Figure 7-49 show the experimental and analytical concrete strains at 250 kip (before cracking) and 500 kip (after cracking). In general, the analytical model shows a similar strain pattern to the experimental strain suggesting that the model is able to approximate the behavior of UHPC-SCC hybrid girders under shear loading. Moreover, the model clearly shows the difference in stiffness between UHPC and SCC.

Finally, agreement between the experimental and analytical horizontal strains, suggests that the finite element approach of using nodal merging to model the UHPC-SCC interface was valid because it allowed the model to match the strain transition between concrete types.

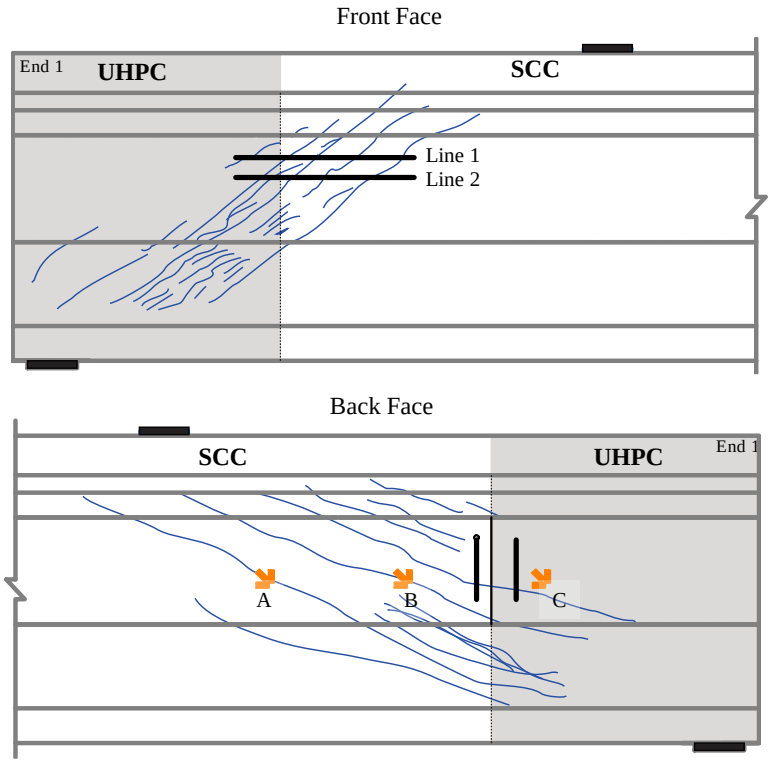

Figure 7-46 Schematic of FOS locations and damage during loading

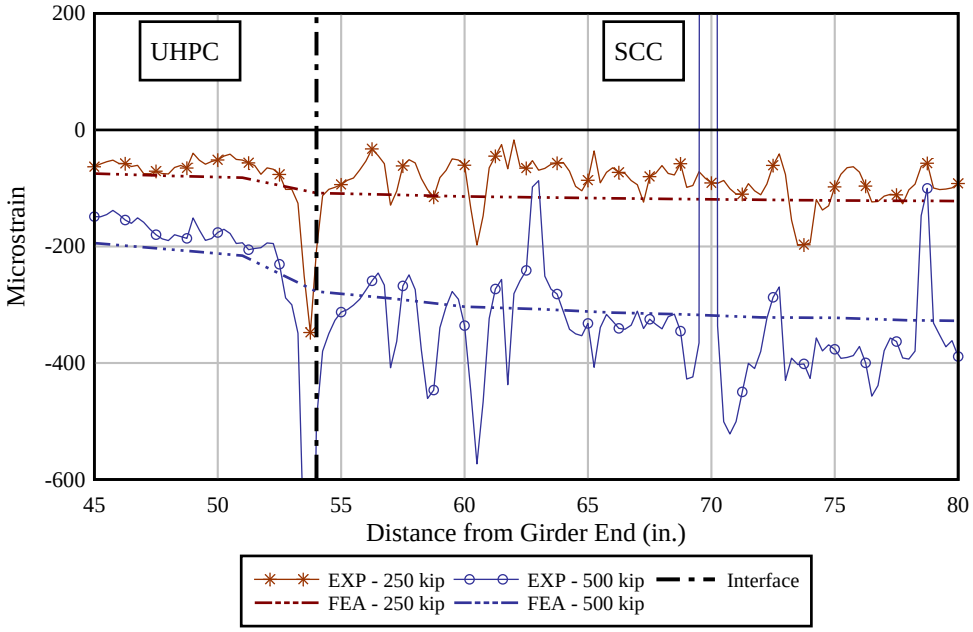

Figure 7-47 Comparison of horizontal concrete strains from Line 1 obtained experimentally and from the analytical model at 250 kip and 500 kip

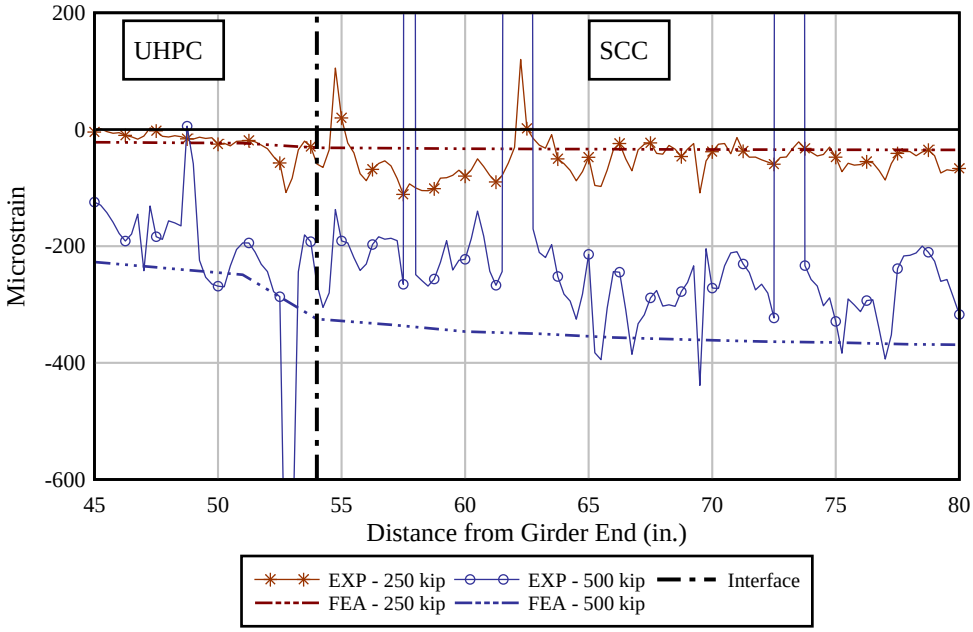

Figure 7-48 Comparison of horizontal concrete strains from Line 2 obtained experimentally and from the analytical model at 250 kip and 500 kip

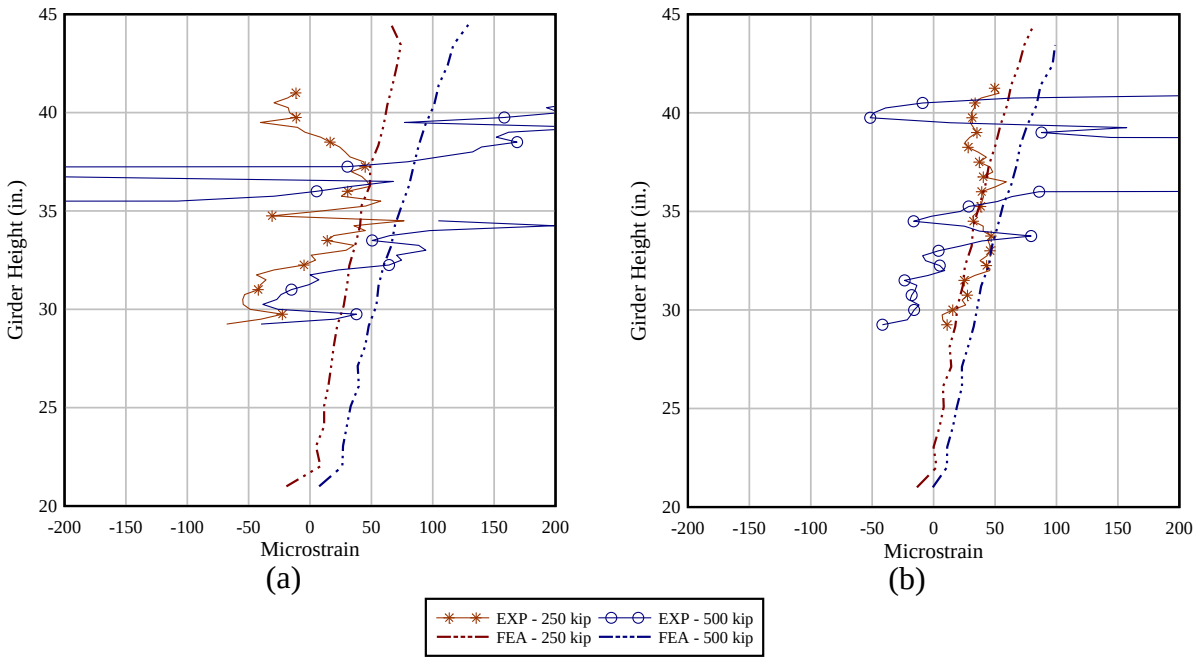

Figure 7-49 Comparison of vertical concrete strains at 250 kip and 500 kip: (a) SCC side and (b) UHPC side

Figure 7-50 shows a comparison of the load-deflection results obtained experimentally and analytically for all four girder ends. The analytical model shows good agreement with the precracked stiffness from the experimental tests. However, the model does not exhibit the same decrease in stiffness after cracking, as was observed experimentally. Recall from Section 4.6 that the experimental tests began to exhibit nonlinear stiffness at approximately 450 kip. Still, the analytical model provided a good approximation to the overall behavior and can be adjusted to match failure once those results become available in future testing.

Results shown in Figure 7-50 indicate that having UHPC for a length of 1.5D increases the shear capacity by ~40 kip. Also, the effect of increasing the spacing between vertical rebar from 7 in. to 9in. does not seem to have affected the shear capacity but the overall deflection increased by 0.1 in. for the ends having 9in. spacing.

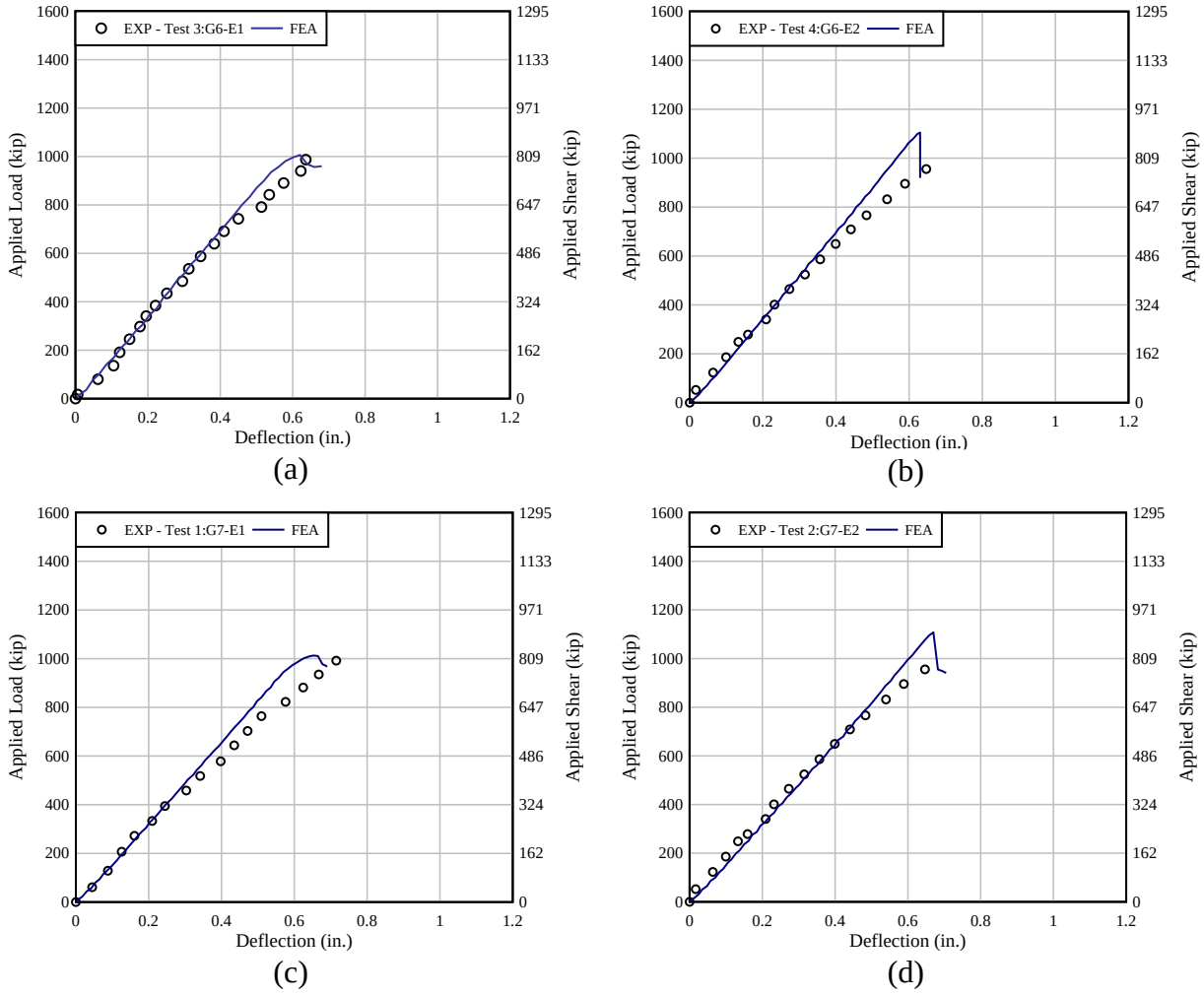

Figure 7-50 Comparison of experimental and analytical shear test results

8 Summary and Conclusions

The objective of this study was to evaluate the effectiveness of using UHPC in the reduction or elimination of visible end region cracking after prestress transfer. To evaluate the effectiveness of UHPC, experimental and analytical investigations were conducted.

The experimental program was divided in two phases. In the first phase, five 20-ft-long FIB 72 mockups were fabricated; the mockups were used to compare end region cracking behavior of UHPC and SCC. Additionally, UHPC mockups were constructed with reduced end region steel reinforcement to further evaluate the crack control capability of UHPC. These mockups were instrumented with linear strain gages and fiber optic sensors (FOS) to measure strain during prestress transfer. Also, all mockups were inspected and monitored for one year to document crack width growth.

The second phase consisted of constructing and load testing two 50-ft-long FIB 54 UHPC-SCC hybrid girders to determine the capacity and behavior of the UHPC-SCC interface under applied shear. A total of four load tests were performed to investigate the effect of UHPC length from the girder end and amount of end region reinforcement. Due to limited capacity of the strong floor supporting the frame, the specimens were not loaded to failure but to a maximum load of 1000 kip.

Direct tension test (DTT) specimens were molded during the fabrication of the FIB 72 mockups and the FIB 54 girders. Results of all DTT testing were compiled to assess the consistency of the UHPC mix in terms of tensile behavior.

Finite element modeling of the FIB 72 mockups and FIB 54 hybrid girders was conducted to better understand the contribution of UHPC in terms of end region behavior and shear response. Using the validated modeling parameters from these FEA models, a follow-up parametric study was conducted on FIB 96 girders to determine the potential benefits of using UHPC end regions on larger girder sections. The FEA investigation was divided into three stages: (1) Material model identification and calibration, (2) Development and validation of FIB 72 mockup model for end region evaluation, and (3) development and validation of FIB 54 hybrid girder model under shear loads.

Finally, implementation of UHPC for precast girder production was considered using two examples of UHPC-SCC hybrid FIB 54 and FIB 96 bridge girder design; the design calculations focused on determining the maximum possible span length that could be attained when using UHPC at the girder ends. These examples considered current FDOT FIB design criteria for a beam spacing of 12 ft.

Key observations and conclusions of FIB 72 mockup testing are as follows:

- At approximately 90-days following release, UHPC FIB 72 mockups exhibited maximum end region crack widths of 0.003 in, which were approximately ~25% of the maximum crack widths measured in the SCC FIB 72 mockups
- UHPC FIB 72 crack widths did not increase with reduction in the quantity of end region mild steel reinforcement

Key observations and conclusions of FIB 54 hybrid girder shear tests are as follows:

- SCC-UHPC interface was able to transfer stress without exhibiting damage during the applied load.
- Increasing the length of UHPC from the end increased the overall stiffness of the girder by reducing crack width and number of cracks in the SCC region.

- The reduction in shear reinforcement did not affect the behavior of the girders up to the maximum applied load. In fact, these specimens carried at least 25% higher superimposed shear without reaching failure than past SCC FIB 54 girders with typical FDOT reinforcement detailing.

Key observations and conclusions of DTT are as follows:

- Cracking strength from DTT results was determined using two methods. Method 1 considers cracking strengths as the first discontinuity from the elastic stiffness. Method 2 defines cracking strength as an average of the multi-cracking region. From these two methods, Method 2 was found to be the most reliable approach to determine the cracking strength of UHPC, with a maximum coefficient of variation of 10.3%
- UHPC cracking strength and peak strength were found to increase by at least 17% from age of detensioning to 28 days.

Key findings from FEA material model calibration:

- The MAT_84 Winfrith concrete model was used to simulate the behavior of UHPC for service conditions. It was shown that by calibrating the material parameters, this material model agreed well with the elastic stiffness and multi-cracking behavior of UHPC measured during DTT tests.
- The MAT_72R3 concrete damage model was shown to be adequate to model FIB 54 hybrid girder behavior up to the maximum load level that was simulated. The parameters in the material model were jointly calibrated using experimental results from DTT and FB tests.

Key findings from FIB 72 Mockup FEA:

- The analytical model of the FIB 72 mockups developed to evaluate end region behavior agreed well with the measured maximum crack widths and effective crack widths of SCC but tended to overestimate the maximum crack widths and effective crack widths of UHPC by 0.0005 in. and 0.0015 in. respectively.
- The analytical model of all UHPC FIB 72 mockups resulted in a maximum crack width of 0.0023 in. immediately after prestress transfer. This maximum crack width is approximately three times lower than the FEA results for cracking in SCC FIB 72 mockups.
- In FEA models of UHPC FIB 72 mockups in which the vertical reinforcement stress exceeded 20 ksi, maximum crack width was less than 0.0023 in. and effective crack width was less than 0.0012 in.
- FIB 96 FEA model showed that SCC can develop maximum crack widths of at least 3.75 times greater than those of UHPC.

Key findings from FIB 54 hybrid girder FEA

- The finite element approach of enforcing nodal compatibility was found to be an appropriate means of modeling the UHPC-SCC interface.
- The FIB 54 model was validated up to 500 kip of load and will need further calibration once the experimental failure strengths are determined.

Key findings from the UHPC-SCC hybrid girder span length study:

- FIB 54 girder span can be extended by 10% from a maximum of 118 ft for all SCC to 130 ft for UHPC-SCC hybrid girder.
- With the increase in span length, the maximum expected shear load is half (430 kip) of the applied shear of the tested FIB 54.
- FIB 96 girder span can be extended by 6.7% from a maximum of 178 ft for all SCC to 190 ft for UHPC-SCC hybrid girder. With the increase in span length, the expected shear increases from 550 kip to 588 kip.

9 Implementation

Based on the experimental and analytical work detailed in this report the following can be considered for implementation:

UHPC Material Testing:

- Compressive strength cylinder tests were performed with three curing methods, room temperature, ambient temperature, and match-curing. Cylinders cured at ambient temperature provided the most reliable results to determine detensioning strength. Match-curing was found suitable; however, it requires sensitive equipment that can be faulty at times.
- UHPC contribution to end region behavior was estimated from the cracking strength of DTTs. Two methods were used to determine cracking strength. Based on the testing conducted for this research, Method 2 appeared to be more consistent; therefore, may be the better choice for end region design

Hybrid Girder Construction Process:

- The cold joint construction process used in this research resulted in good bond between both concrete types. While this method resulted in an additional day of construction, it allowed for more control of the bond quality.
- A more effective use of UHPC in the end region could be realized if the SCC compressive strength at release was increased to 8 ksi; this would allow the SCC to withstand stresses of the increased prestress force allowed by the UHPC use at the end of the girder.

End Region Reinforcement:

- Independent of the amount of reinforcement, none of the crack widths measured in UHPC ends would require crack repair or engineering evaluation. However, based on results from the analytical model, when rebar bundles are not installed the stresses may exceed 20 ksi. Therefore, it is recommended to maintain the first bundle of reinforcement used in typical FDOT detailing.
- UHPC ends with no confinement and no embedded steel bearing plate did not exhibit any splitting or bursting cracks in the bottom flange or in the bottom surface. It is believed that UHPC is able to resist those stresses.

10 Future Work

This study investigated the effectiveness of UHPC as an alternative to reduce or eliminate end region cracking. FIB 72 mockups were monitored for one year after prestress transfer. Even when it is not expected that end region cracks continue to grow after this period, the authors recommend continuing with long-term monitoring to determine if durability of the UHPC-SCC interface or steel fibers corrosion is of concern.

The selected construction method for the UHPC-SCC interface was to create a construction joint with the necessary surface preparation to provide adequate bond between SCC and UHPC. Testing indicated that this method was shown to be structurally sufficient. Further evaluation of the wet cast joint is needed, however, if faster production rate is necessary to make this approach economically feasible.

Fibers distribution within the FIB cross-section should be evaluated to ensure the quality of the UHPC mix. Specimens for DTT or FB can be extracted from the web — in between rebar bundles— to perform tensile testing. Specimens are recommended to be extracted at different heights to determine if fiber segregation or bleeding occurred.

The present study increased the number of prestressing strands to the maximum allowed by the FDOT strand pattern. Experimental crack measurements of the FIB 72 mockups indicated that UHPC may be capable of resisting even higher prestress force without resulting in crack widths in need of repair. Therefore, to increase the structural performance of FIB girders the authors recommend that using 0.7 in. diameter strands for higher prestress force be evaluated. This can be accompanied with the implementation of higher strength SCC mixtures.

Finally, increasing the number of strands and consequently the transferred prestress force, the shear strength of the girder increased. Current design codes do not provide a method to compute the shear contribution from horizontal prestressing strands (V_p). The authors recommend that this contribution be evaluated to optimize shear design of FIBs.

11 References

Abbas, Y. M., & Iqbal Khan, M. (2016). “Fiber–Matrix Interactions in Fiber-Reinforced Concrete: A Review”. Arabian Journal for Science and Engineering, 41(4), 1183–1198. https://doi.org/10.1007/s13369-016-2099-1

Ahlborn, T.M.; Mission, D.L.; Peuse, E.J.; Gilbertson, C.G. (2008). Durability and Strength Characterization of Ultra-High Performance Concrete under Variable Curing Regimes. In Proceedings of 2nd International Symposium on Ultra High Performance Concrete, Kassel, Germany, 5–7, pp. 197–204

Alireza, M., and Rafic, E. (2020). “End Zone Design and Behavior of Prestressed UHPC Girders”. Federal Highway Administration. International Accelerated Bridge Construction Conference

American Association of State Highway and Transportation Officials. (2017). AASHTO LRFD Bridge Design Specification (8th ed.). Washington, DC: AASHTO.

Association Francaise de Genie Civil (AFGC) – Service d’etudes techniques desroutes et autoroutes (SETRA), Bétons fibrés à ultra-hautes performances – ultrahigh performance fibre-reinforce concretes, recommandations provisoires –Interim recommendations; January 2002. p. 153

ASTM C39. (2020). “Standard Test Method for Compressive Strength of Cylindrical Concrete Specimens, PA.

ASTM C1069.(2018). “Standard Test Method for Flexural Performance of Fiber-Reinforced Concrete (Using Beam With Third-Point Loading). West Conshohocken, PA. https://doi.org/10.1520/E1012-14E01.2.

ASTM C1437. (2015). “Standard Test Method for Flow of Hydraulic Cement Mortar. West Conshohocken, PA.

ASTM C1856. (2017). “Standard Practice for Fabricating and Testing Specimens of Ultra-High Performance Concrete, West Conshohocken, PA. https://doi.org/10.1520/E1012-14E01.2

Bahij, S., Adekunle, S. K., Al-Osta, M., Ahmad, S., Al-Dulaijan, S. U., & Rahman, M. K. (2018). “Numerical investigation of the shear behavior of reinforced ultra-high-performance concrete beams”. Structural Concrete, 19(1), 305–317. https://doi.org/10.1002/suco.201700062

Banthia, N., & Trottier, J. F. (1991). “Deformed steel fiber-cementitious matrix bond under impact”. Cement and Concrete Research, 21(1), 158–168. https://doi.org/10.1016/0008-8846(91)90042-G

Crawford, J.E., Wu, Y, Choi, H.J., Magallanes, J.M., & Lan, S.(2011).“User’s manual and documentation for release III of the K&C concrete material model in LS-DYNA.” Technical Rep. TR-11-36.6, Karagozian & Case, Glendale, CA.

Crawford, J. E., Wu, Y., Magallanes, J. M., & Choi, H. J. (2013). “The importance of shear-dilatancy behaviors in RC columns.” Int. J. Prot. Struct., 4(3), 341–377.

Crawford, John, Joseph Magallanes, Andrew Whittaker, & Timothy Richard Brewer. (2016). “Modeling of Pristine and Damaged UHPFRC Materials for Use in Performing Blast and Projectile Penetration Analyses Modeling of Pristine and Damaged UHPFRC Materials for Use in Performing Blast And Projectile,”. 4th International Conference on Protective Structures (ICPS4). Beijing, China.

Diaz, G., & Hamilton, H. (2020). “Macro Synthetic Fiber Reinforcement for Improved Structural Performance of Concrete Bridge Girders”. Florida Department of Transportation Research Report BDK31 977-41. Gainesville, FL.

Dunkman, D. A., Hovell, C. G., Moore, A. M., Avendaño, A., Bayrak, O., & Jirsa, J. O. (2010). “Bursting and Spalling in Pretensioned Concrete Beams”. Master Thesis. The University of Texas at Austin

Eide, M. & Hisdal, J. (2012). Ultra High Performance Fibre Reinforced Concrete (UHPFRC) – State of the Art. *SINTEF Building and Infrastructure*. Oslo, Norway.

Florida Department of Transportation (FDOT). (2012). Index 200010. Florida Department of Transportation, Tallahassee, FL.

Florida Department of Transportation (FDOT). (2016). Structures Design Guidelines (Vol. 1). Florida Department of Transportation, Tallahassee, FL.

Florida Department of Transportation (FDOT). (2018). Standard Specifications for Road and Bridge Construction. Concrete. Florida Department of Transportation, Tallahassee, FL.

FHWA. (2017). “Ultra-High Performance Concrete.” U.S. Department of Transportation/Federal Highway Administration, www.fhwa.dot.gov/research/resources/uhpc/bridges.cfm.

Gowripalan, N., &" Gilbert, R. I. (2000). “Design Guidelines for Ductal Prestressed Concrete Beams”. The University of New South Wales, Australia

Graybeal, B. (2006). “Structural Behavior of Ultra-High Performance Concrete Prestressed I-Girders”. Federal Highway Administration, FHWA-HRT-06-115, McLean, VA.

Graybeal, B. (2007). “Compressive Behavior of Ultra-high-Performance Fiber Reinforced Concrete”. *ACI Mater. J.*,104, 146-152,

Graybeal, B. (2010). “Finite Element Analysis of UHPC : Structural Performance of an AASHTO Type II Girder and a 2nd Generation Pi-Girder,” 1–6. https://doi.org/HRDI-40/11-10(150)E.

Graybeal, B. (2011). “Ultra-High Performance Concrete, TechNote”. FHWA-HRT-11-038, Federal Highway Administration, McLean, VA.

Graybeal, B., & Baby, F.(2014). “Development of Direct Tension Test Method for Ultra-High-Performance Fiber-Reinforced Concrete,” no. 110: 177–86.

Graybeal, Bejamin, & Baby, F. (2019). “Tension Testing of Ultra-High Performance Concrete,” no. February

Graybeal, B. A., and Rafic E.H. (2019). “Development of an AASHTO Guide Specification for UHPC”. International Interactive Symposium on Ultra-High Performance Concrete, 2(1), 1–9.

Guo, W., Fan, W., Shao, X., Shen, D., & Chen, B. (2018). “Constitutive Model of Ultra-high-performance Fiber-reinforced Concrete for Low-Velocity Impact Simulations”. Composite Structures, 185(March 2017), 307–326. https://doi.org/10.1016/j.compstruct.2017.11.022

Haber, Z. B., De la Varga, I., Graybeal, B. A., Nakashoji, B., & El-Helou, R. (2018). “Properties and Behavior of UHPC-Class Materials.” FHWA-HRT-18-036.

Ishii, T.; Nishio, H.; Matsuyama, T.; Miyajima, A.; Yokohata, K.; Gotou, M.; Xin, J.; and Hirai, Y. (2008). “Manufacture and Construction of a PC Through Girder Type Pedestrian Bridge using Ultra High Strength Fiber Reinforced Concrete”. In Proceedings of 8th International Symposium on Utilization of High-Strength and High-Performance Concrete, Tokyo, Japan, 27–29 October 2008;

pp. 1270–1275Japan Society of Civil Engineers (JSCE). (2008). “Recommendations for Design and Construction of High Performance Fiber Reinforced Cement Composites with Multiple Fine Cracks”. March 2008. p. 113.

JCI-S-003-2005. (2006). “Method of Test for Bending Moment-Curvature Curve of Fiber Reinforced Cementitious Composites,” Journal of Advanced Concrete Technology, 4(1), pp. 73–78, Japan Concrete Institute, Tokyo, Japan.

Kang, S., Choi, J., Koh, K., Seok, K., & Yeon, B. (2016). Hybrid effects of steel fiber and microfiber on the tensile behavior of ultra-high performance concrete. Composite Structures, 145, 37–42. https://doi.org/10.1016/j.compstruct.2016.02.075

Kim, D. J., El-Tawil, S., & Naaman, A. E. (2008). Loading Rate Effect on Pullout Behavior f Deformed Steel Fibers. ACI Materials Journal, 105(6), 576–584. https://doi.org/10.14359/20199

Livermore Software Technology Corporation (LSTC). (2016). Keyword User Manual. Livermore, California: Livermore Software Technology Corporation.

Lim, W. Y., & Hong, S. G. (2016). “Shear Tests for Ultra-High Performance Fiber Reinforced Concrete (UHPFRC) Beams with Shear Reinforcement”. International Journal of Concrete Structures and Materials, 10(2), 177–188. https://doi.org/10.1007/s40069-016-0145-8

Liu, J., Chengqing, W., & Xiaowei, C. (2017). “Numerical Study of Ultra-High Performance Concrete under Non-Deformable Projectile Penetration.” Construction and Building Materials 135. Elsevier Ltd: 447–58. https://doi.org/10.1016/j.conbuildmat.2016.12.216.

Maca, P., Zatloukal, J., & Konvalinka, P. (2012). “Development of Ultra High Performance Fiber Reinforced Concrete Mixture”. 2012 IEEE Symposium on Business, Engineering and Industrial Applications, Prague, Czech, 861-866.

Magallanes, J., Wu, Y., Morrill, K. B., & Crawford, J. E. (2010). “Feasibility Studies of a Plasticity-Based Constitutive Model for Ultra-High Performance Fiber-Reinforced Concrete”. MABS 21, International Symposium on Military Aspects of Blast and Shock, Jerusalem, Israel, 12

Markovic, I. (2006). “High-Performance Hybrid-Fibre Concrete: Development and Utilization”. PhD thesis, Technische Universiteit Delft, The Netherlands.

Marshall, W. T., & Mattock, A. H.(1962). “Control of Horizontal Cracking in the Ends of Pretensioned Prestressed Concrete Girders,” PCI JOURNAL, V. 7, No. 5, October 1962, pp. 56-74.

Malvar, L., Crawford, J., Wesevich, J., & Simons, D. (1997). “DYNA3D” 19 (97): 847–73.

Mobasher, B., Mehdi B., & Barsby, C. (2014). “Backcalculation of Residual Tensile Strength of Regular and High Performance Fiber Reinforced Concrete from Flexural Tests.” Construction and Building Materials 70. Elsevier Ltd: 243–53. https://doi.org/10.1016/j.conbuildmat.2014.07.037

Naaman, A. E., and Najm, H. (1991). “Bond-slip mechanisms of steel fibers in concrete”. ACI Materials Journal, 88(2), 135–145. https://doi.org/10.14359/1896

NF P18-710. (2016). “National addition to Eurocode2— Design of concrete structures: specific rules for Ultra-high performance Fibre-reinforced concretes (UHPFRC)”. AFNOR, France standard institute.

Nguyen, D. L., Ryu, G. S., Koh, K. T., & Kim, D. J. (2014). “Size and Geometry Dependent Tensile Behavior of Ultra-High-Performance Fiber-Reinforced Concrete”. Composites Part B: Engineering, 58, 279–292. https://doi.org/10.1016/j.compositesb.2013.10.072

PCI Design Handbook 7th Edition. (2010). Precast/Prestressed Concrete Institute. Chicago, Illinois.

Qian, S., & Li, V. C. (2008). "Simplified inverse method for determining the tensile properties of strain hardening cementitious composites (SHCC)". Journal of Advanced Concrete Technology, 6(2), 353–363. https://doi.org/10.3151/jact.6.353

Qi, J., Wu, Z., Ma, Z. J., & Wang, J. (2018). "Pullout Behavior of Straight and Hooked-End Steel Fibers in UHPC Matrix with Various Embedded Angles". Construction and Building Materials, 191, 764–774. https://doi.org/10.1016/j.conbuildmat.2018.10.067

Rigaud, S., Chanvillard, G., & Chen, J. (2011). "Characterization of Bending and Tensile Behaviors of Ultra-High Performance Concrete Containing Glass Fibers," Proceedings of High Performance Fiber Reinforced Cement Composites 6, pp. 359–366, Ann Arbor, MI.

Ronanki, V., Burkhalter, D., Aaleti, S., Song, W., & Richardson, J. (2017). "Experimental and Analytical Investigation of End Zone Cracking in BT-78 Girders." Engineering Structures 151: 503–17. https://doi.org/10.1016/j.engstruct.2017.08.014.

Ross, B., Hamilton, H., & Consolazio, G. (2013). End Region Detailing of Pretensioned Concrete Bridge Girders (Florida Department of Transportation Research Report BDK75 977-05). Gainesville, FL.

Russell, B. & Burns, N. (1996), "Measured Transfer Lengths of 0.5 and 0.6 in. Strands in Pretensioned Concrete," PCI Journal, Sept.-Oct., pp. 44-54.

Russell, Henry, & Benjamin Graybeal. (2013). "Ultra-High Performance Concrete : A State-of-the-Art Report for the Bridge Community," no. June.

Singh, M., Sheikh, A. H., Ali, M. S. M., Visintin, P., & Griffith, M. C. (2017). "Experimental and Numerical Study of the Flexural Behavior of Ultra-High Performance Fiber Reinforced Concrete Beams". Construction and Building Materials, 138, 12–25. https://doi.org/10.1016/j.conbuildmat.2017.02.002

Soetens, T., Van Gysel, A., Matthys, S., & Taerwe, L. (2013). "A Semi-Analytical Model to Predict the Pull-Out Behaviour of Inclined Hooked-End Steel Fibres". Construction and Building Materials, 43, 253–265. https://doi.org/10.1016/j.conbuildmat.2013.01.034

Tadros, M. K., Badie, S. S., & Tuan, C. Y. (2010). "Evaluation and Repair Procedures for Precast/Prestressed Concrete Girders with Longitudinal Cracking in the Web". National Cooperative Highway Research Program, Report 654. Washington, DC.

Tran, T. K., & Kim, D. J. (2013). "Investigating Direct Tensile Behavior of High Performance Fiber Reinforced Cementitious Composites at High Strain Rates". Cement and Concrete Research, 50, 62–73. https://doi.org/10.1016/j.cemconres.2013.03.018

Voit, K., & Kirnbauer, J. (2014). “Tensile Characteristics and Fracture Energy of Fiber Reinforced and Non-Reinforced Ultra High Performance Concrete (UHPC)”. International Journal of Fracture, 188(2), 147–157. https://doi.org/10.1007/s10704-014-9951-7

Voo, Y., Poon, W. K., & Foster, S. J. (2010). “Shear Strength of Steel Fiber-Reinforced Ultrahigh- Performance Concrete Beams without Stirrups”. (November), 1393–1400.

Wang, H., & Abdeldjelil, B. (2010). “Ductility Characteristics of Fiber-Reinforced-Concrete Beams Reinforced with FRP Rebars”. Construction and Building Materials, vol. 25, no. 5, Elsevier Ltd, 2011, pp. 2391–401, doi:10.1016/j.conbuildmat.2010.11.040.

Wille, K., Naaman, A., & Parra-Montesinos, G. (2011). Ultra-High Performance Concrete with Compressive Strength Exceeding 150 MPa (22ksi): A simpler Way. ACI Mater. J., 108, 46-54.

Wille, K.; & Naaman, A. (2013) “Bond Stress-Slip Behavior of Steel Fibers Embedded in Ultra High Performance Concrete”. In: ECF18, Dresden

Wille, K., El-Tawil, S., & Naaman, A. E. (2014). “Properties of Strain Hardening Ultra High Performance Fiber Reinforced Concrete (UHP-FRC) Under Direct Tensile Loading”. Cement and Concrete Composites, 48, 53–66. https://doi.org/10.1016/j.cemconcomp.2013.12.015

Winkelbauer, B. J. (2016). “Phase I Evaluation of Selected Concrete Material Models in LS-DYNA”. Thesis, (118). University of Nebraska, Lincoln.

Wu, Y., & Crawford, J. E. (2015). “Numerical Modeling of Concrete Using a Partially Associative Plasticity Model”. Journal of Engineering Mechanics, 141(12), 04015051. https://doi.org/10.1061/(asce)em.1943-7889.0000952

Wu, Z., Caijun S., Wen, H., & Linmei W. (2016). “Effects of Steel Fiber Content and Shape on Mechanical Properties of Ultra High Performance Concrete.” Construction and Building Materials 103. Elsevier Ltd: 8–14. https://doi.org/10.1016/j.conbuildmat.2015.11.028

Xia, J., Mackie, K. R., Saleem, M. A., & Mirmiran, A. (2011). “Shear failure analysis on ultra-high performance concrete beams reinforced with high strength steel”. Engineering Structures, 33(12), 3597–3609. https://doi.org/10.1016/j.engstruct.2011.06.023

Xu, M., & Wille, K. (2014). “Calibration of K&C Concrete Model for UHPC in LS-DYNA”. Advanced Materials Research, 1081, 254–259. https://doi.org/10.4028/www.scientific.net/amr.1081.254

Xu, M., Hallinan, B., & Wille, K. (2016). “Effect of Loading Rates on Pullout Behavior of High Strength Steel Fibers Embedded in Ultra-High Performance Concrete”. Cement and Concrete Composites, 70, 98–109. https://doi.org/10.1016/j.cemconcomp.2016.03.014

Yang, I. H., Joh, C., & Kim, B. S. (2010). “Structural Behavior of Ultra High Performance Concrete Beams Subjected to Bending”. Engineering Structures, 32(11), 3478–3487. https://doi.org/10.1016/j.engstruct.2010.07.017

Yin, Hor, Kazutaka Shirai, & Wee Teo. 2019. “Finite Element Modelling to Predict the Fl Exural Behaviour of Ultra-High Performance Concrete Members.” Engineering Structures 183 (September 2018). Elsevier: 741–55. https://doi.org/10.1016/j.engstruct.2019.01.046.

Yudenfreund, M., Odler, I., & Brunauer, S. (1972). “Hardened Portland Cement Pastes of Low Porosity”. Materials and Experimental Methods. *Cement and Concrete Research*, 2, 313-330.

Yuliarti, K., Fehling, E., Ismail, M., & Aboubakr, A. A. M. (2015). “Tensile Strength Behavior of UHPC and UHPFRC”. Procedia Engineering, 125, 1081–1086. https://doi.org/10.1016/j.proeng.2015.11.166

Zagon, Raul, & Kiss Zoltan. (2016). “Shear Behaviour of UHPC Concrete Beams.” Procedia Technology 22: 122–26. https://doi.org/10.1016/j.protcy.2016.01.019.

Zheng, H., & Fang, Z. (2016). “Experimental Study on Shear Behavior of Prestressed Ultra-high Performance Concrete I-girders”. IABSE Conference, Guangzhou 2016: Bridges and Structures Sustainability - Seeking Intelligent Solutions - Report, (June), 775–785. https://doi.org/10.2749/222137816819259149

Zhou, Z., & Qiao, P. (2019). “Direct Tension Test for Characterization of Tensile Behavior of Ultra-High Performance Concrete”. https://doi.org/10.1520/JTE20170644

Zile, E., & Zile, O. (2013). “Effect of the Fiber Geometry on the Pullout Response of Mechanically Deformed Steel Fibers”. Cement and Concrete Research, 44, 18–24. https://doi.org/10.1016/j.cemconres.2012.10.014

Zollo, R. F. (1996). “Fiber-Reinforced Concrete: An Overview After 30 Years of Development. Cement and Concrete Composites”. 19(2), pp. 107-122.

12 Appendix A — Construction Drawings of FIB 72 Mockups

General Notes:

Materials

Concrete shall be:
1. FDOT class VI with f'c (28 day) = 8500 psi and f'ci (release) = 6000 ksi
2. UHPC mix provided by the fabricator

Mild reinforcement shall be grade 60 (fy 60 ksi)

Prestressing strand shall be 270 ksi Lo-Lax

Fabricator shall provide data sheets from concrete, strand, and rebar suppliers.

Fabricator shall provide material samples to UF/FDOT as follows:

(6) 4" dia. x 8" cylinders from each concrete batch
(5) 4"x4"x12" beams from each concrete batch
(9) 2"x2"x17" beams from each concrete batch

Fabricator shall provide material report of strand stressing.

Fabricator shall provide results of all testing performed for fresh and hardened concrete properties.

Girder denomination is as follows:

Girder details	
Denomination	Concrete Type
G1	UHPC/SCC
G2	UHPC/SCC
G3	UHPC
G4	UHPC
G5	UHPC

Schedule

A coordination meeting will be held with the fabricator and UF at least two (2) weeks prior to beginning fabrication.

Eduardo Torres at UF at least (1) week prior to beginning fabrication.
352-872-1082 or edu1291@ufl.edu

Research Instrumentation

UF/FDOT will provide and install research instrumentation in each of the concrete girders in coordination with the fabricator. Internal instrumentation will be mounted to prestressing strands and rebar prior to casting concrete. Therefore, fabricator should provide stirrups at least two weeks before fabrication start. Instruments on rebar will be installed prior to placement of the rebar in the girder.

Other

Fabricator will transport girders from the fabrication facility to:
FDOT Structures Research Center
2007 East Paul Dirac Drive
Tallahassee, FL 32310

Delivery time to be coordinated with FDOT.

Inspections will be provided by on-site FDOT personnel and/or by UF prior to and after concrete casting.

No patchwork or finishing is required.

Proposed Timeline:

Day 1 (Monday)	Day 2 (Tuesday)	Day 3 (Wednesday)	Day 4 (Thursday)	Day 5 (Friday)
- Lay down the strands - Place mesh in Girders 1 and 2 (UF)	- Place steel reinforcement - Install instrumentation (UF) - Place formwork	- Pour UHPC and SCC on all Girders	- Remove formwork - Install external instrumentation (UF) - Draw gridlines (UF)	- Strand release - Relocate Girders for temporary storage.

Precast Bed Layout

Bar Bending Diagrams

Handling & Dunnage

1	General Notes	University of Florida Dept. of Civil and Coastal Engineering 352.872.1082	FDOT Research Hybrid UHPC Girder

Bill of material: G1				
Piece	Size	Qty.	Length	Notes
6A	#6	4	20'-0"	Straight bar
3C	#3	44	6'-7"	See Sheet 1
3D	#3	88	4'-11 3/4"	See Sheet 1
4M	#4	39	3'-8"	Straight bar
5K	#5	77	8'-1"	See Sheet 1
5Y	#5	16	5'-6"	Straight bar
5Z	#5	12	7'-6 1/2"	See Sheet 1
4L	#4	7	4'-0"	Straight bar

2	Girder G1	University of Florida Dept. of Civil and Coastal Engineering 352.872.1082	FDOT Research Hybrid UHPC Girder

3	Girder G2	University of Florida Dept. of Civil and Coastal Engineering 352.872.1082	FDOT Research Hybrid UHPC Girder

Bill of material: G3				
Piece	Size	Qty.	Length	Notes
6A	#6	4	20'-0"	Straight bar
3C	#3	20	6'-7"	See Sheet 1
3D	#3	40	4'-11¾"	See Sheet 1
4M	#4	38	3'-8"	Straight bar
5K	#5	27	8'-1"	See Sheet 1
5Y	#5	-	5'-6"	Straight bar
5Z	#5	-	7'-6½"	See Sheet 1

4	Girder G3	University of Florida Dept. of Civil and Coastal Engineering 352.872.1082	FDOT Research Hybrid UHPC Girder

Bill of material: G4				
Piece	Size	Qty.	Length	Notes
6A	#6	4	20'-0"	Straight bar
3C	#3	13	6'-7"	See Sheet 1
3D	#3	26	4'-11 3/4"	See Sheet 1
4M	#4	38	3'-8"	Straight bar
5K	#5	27	8'-1"	See Sheet 1
5Y	#5	6	5'-6"	Straight bar
5Z	#5	3	7'-6 1/2"	See Sheet 1

5	Girder G4	University of Florida Department of Civil and Coastal Engineering 352.872 1082	FDOT Research Hybrid UHPC Girder

Bill of material: G5				
Piece	Size	Qty.	Length	Notes
6A	#6	4	20'-0"	Straight bar
3C	#3	13	6'-7"	See Sheet 1
3D	#3	26	4'-11 3/4"	See Sheet 1
4M	#4	38	3'-8"	Straight bar
5K	#5	27	8'-1"	See Sheet 1
5Y	#5	-	5'-6"	Straight bar
5Z	#5	-	7'-6 1/2"	See Sheet 1

6	Girder G5	University of Florida Dept. of Civil and Coastal Engineering 352.872.1082	FDOT Research Hybrid UHPC Girder

13 Appendix B — Instrumentation Drawings of FIB 72 Mockups

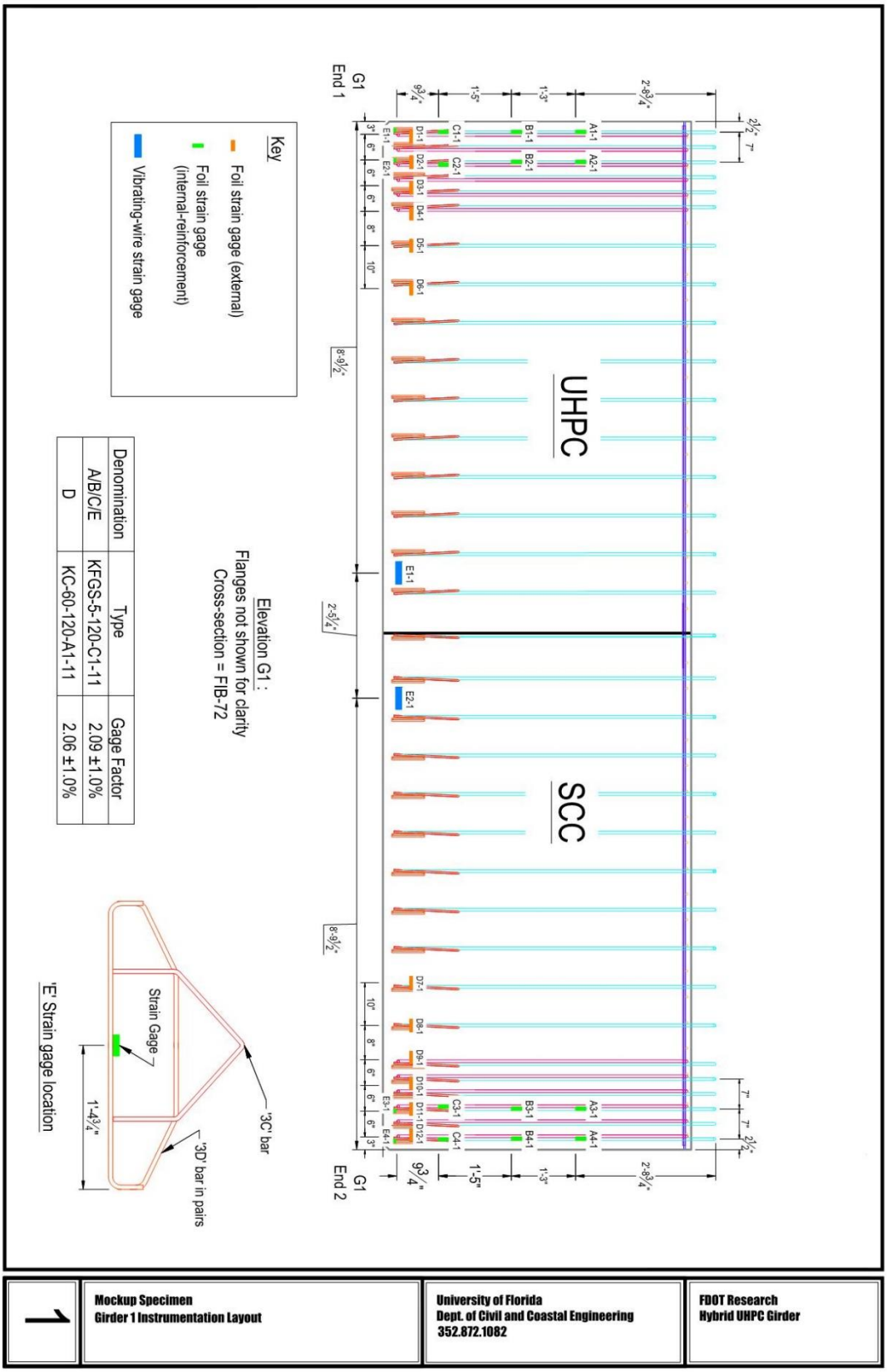

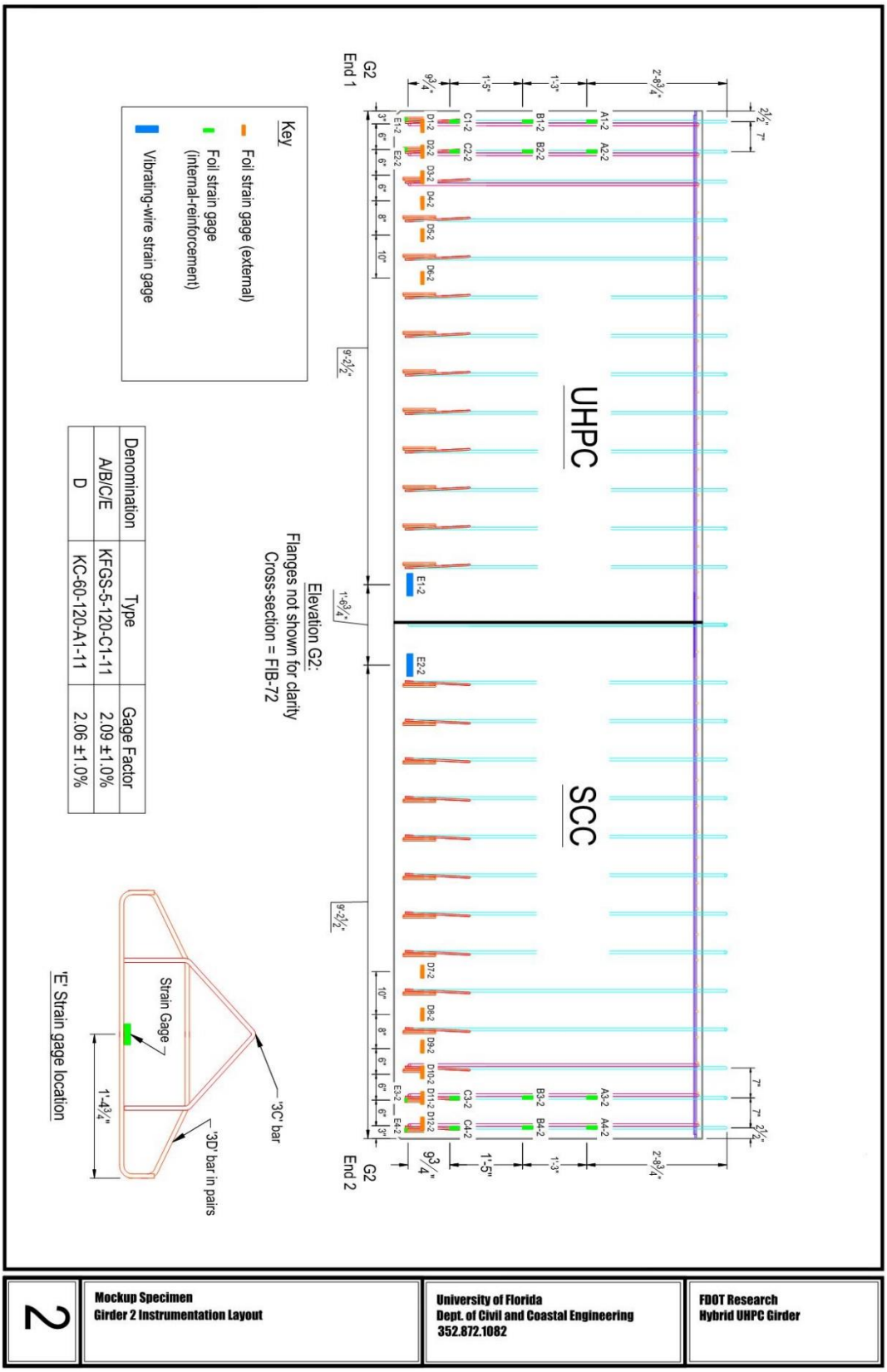
Key
Foil strain gage (external)
Foil strain gage (internal-reinforcement)
Vibrating-wire strain gage
UHPC
SCC
G2 End 1
G2 End 2
Elevation G2:
Flanges not shown for clarity
Cross-section = FIB-72
Denomination | Type | Gage Factor
A/B/C/E | KFGS-5-120-C1-11 | 2.09 ±1.0%
D | KC-60-120-A1-11 | 2.06 ±1.0%
'E' Strain gage location
Strain Gage
'3C' bar
'3D' bar in pairs
2
Mockup Specimen
Girder 2 Instrumentation Layout
University of Florida
Dept. of Civil and Coastal Engineering
352.872.1082
FDOT Research
Hybrid UHPC Girder

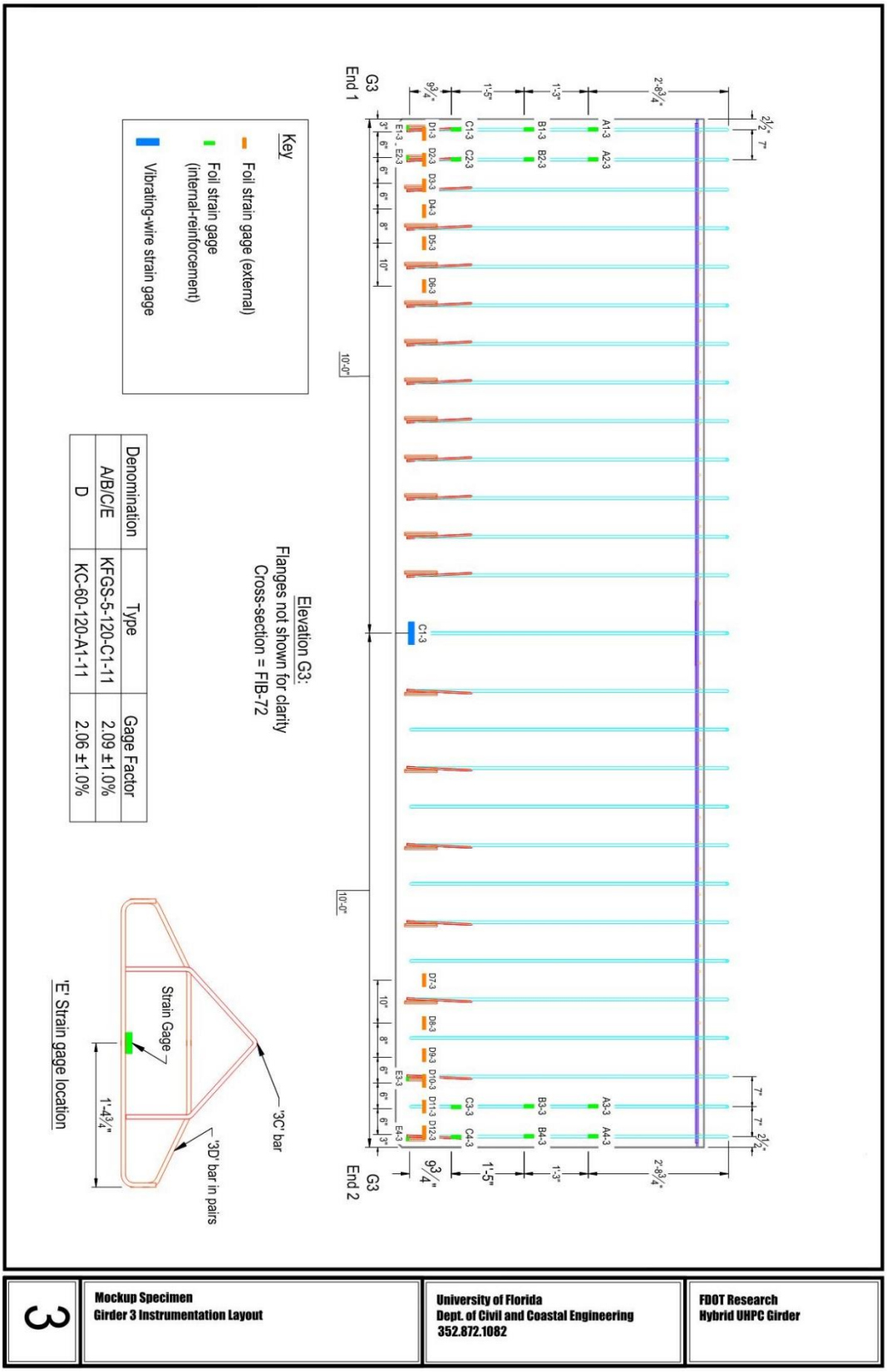

Denomination	Type	Gage Factor
A/B/C/E	KFGS-5-120-C1-11	2.09 ±1.0%
D	KC-60-120-A1-11	2.06 ±1.0%

3	Mockup Specimen Girder 3 Instrumentation Layout	University of Florida Dept. of Civil and Coastal Engineering 352.872.1082	FDOT Research Hybrid UHPC Girder

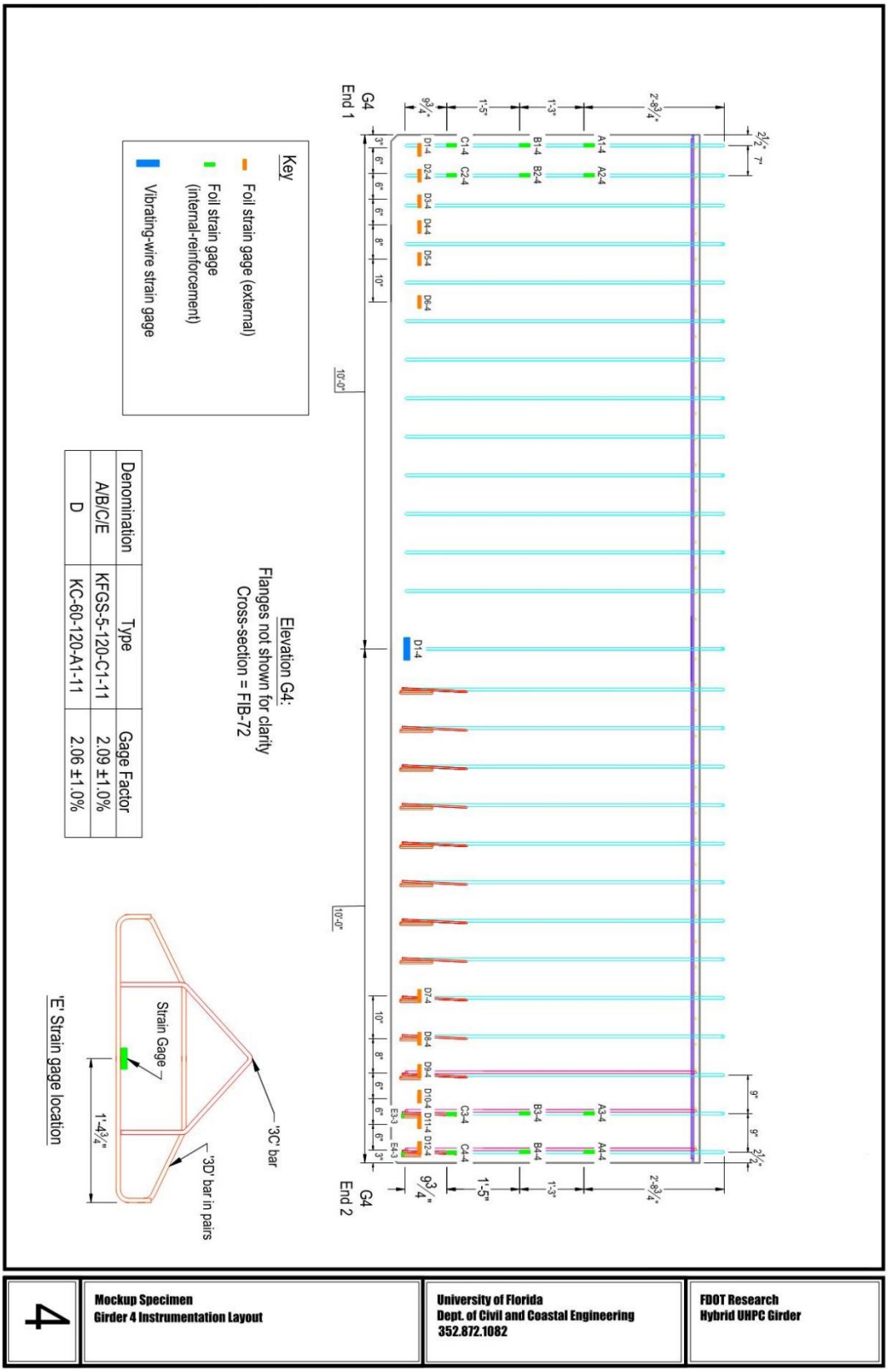

4	**Mockup Specimen** **Girder 4 Instrumentation Layout**	**University of Florida** **Dept. of Civil and Coastal Engineering** **352.872.1082**	**FDOT Research** **Hybrid UHPC Girder**

G5
End 1
G5
End 2
10'-0"
10'-0"
Key
Foil strain gage (external)
Foil strain gage
(internal-reinforcement)
Vibrating-wire strain gage
Elevation G5:
Flanges not shown for clarity
Cross-section = FIB-72
Denomination
Type
Gage Factor
A/B/C/E
KFGS-5-120-C1-11
2.09 ±1.0%
C
KC-60-120-A1-11
2.06 ±1.0%
'E' Strain gage location
Strain Gage
1'-4¾"
'3C' bar
'3D' bar in pairs
5
Mockup Specimen
Girder 5 Instrumentation Layout
University of Florida
Dept. of Civil and Coastal Engineering
352.872.1082
FDOT Research
Hybrid UHPC Girder

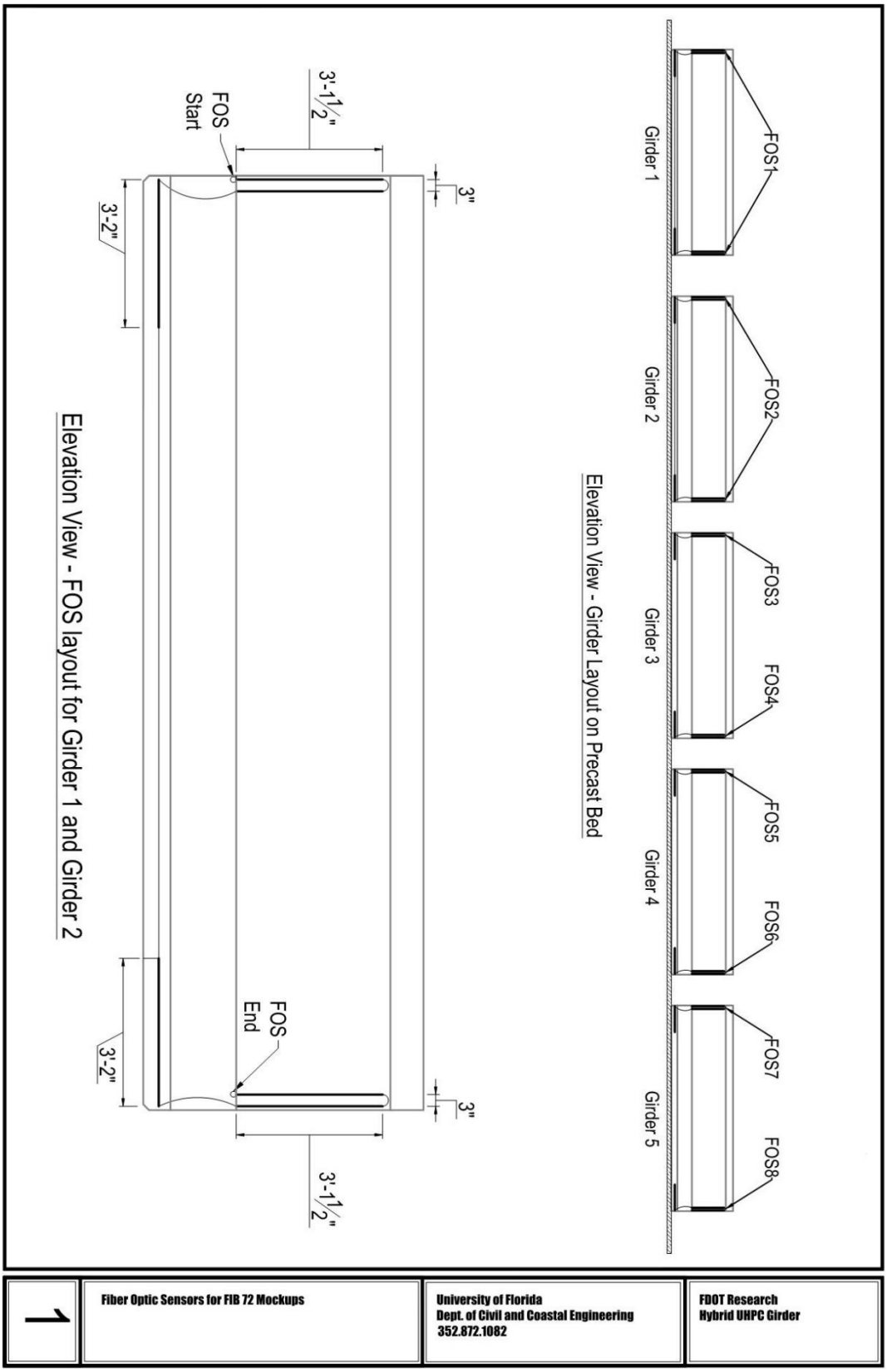
Girder 1
Girder 2
Girder 3
Girder 4
Girder 5
FOS1
FOS2
FOS3
FOS4
FOS5
FOS6
FOS7
FOS8
Elevation View - Girder Layout on Precast Bed
3'-1 1/2"
FOS Start
3"
3'-2"
FOS End
3'-2"
3"
3'-1 1/2"
Elevation View - FOS layout for Girder 1 and Girder 2
1
Fiber Optic Sensors for FIB 72 Mockups
University of Florida
Dept. of Civil and Coastal Engineering
352.872.1082
FDOT Research
Hybrid UHPC Girder

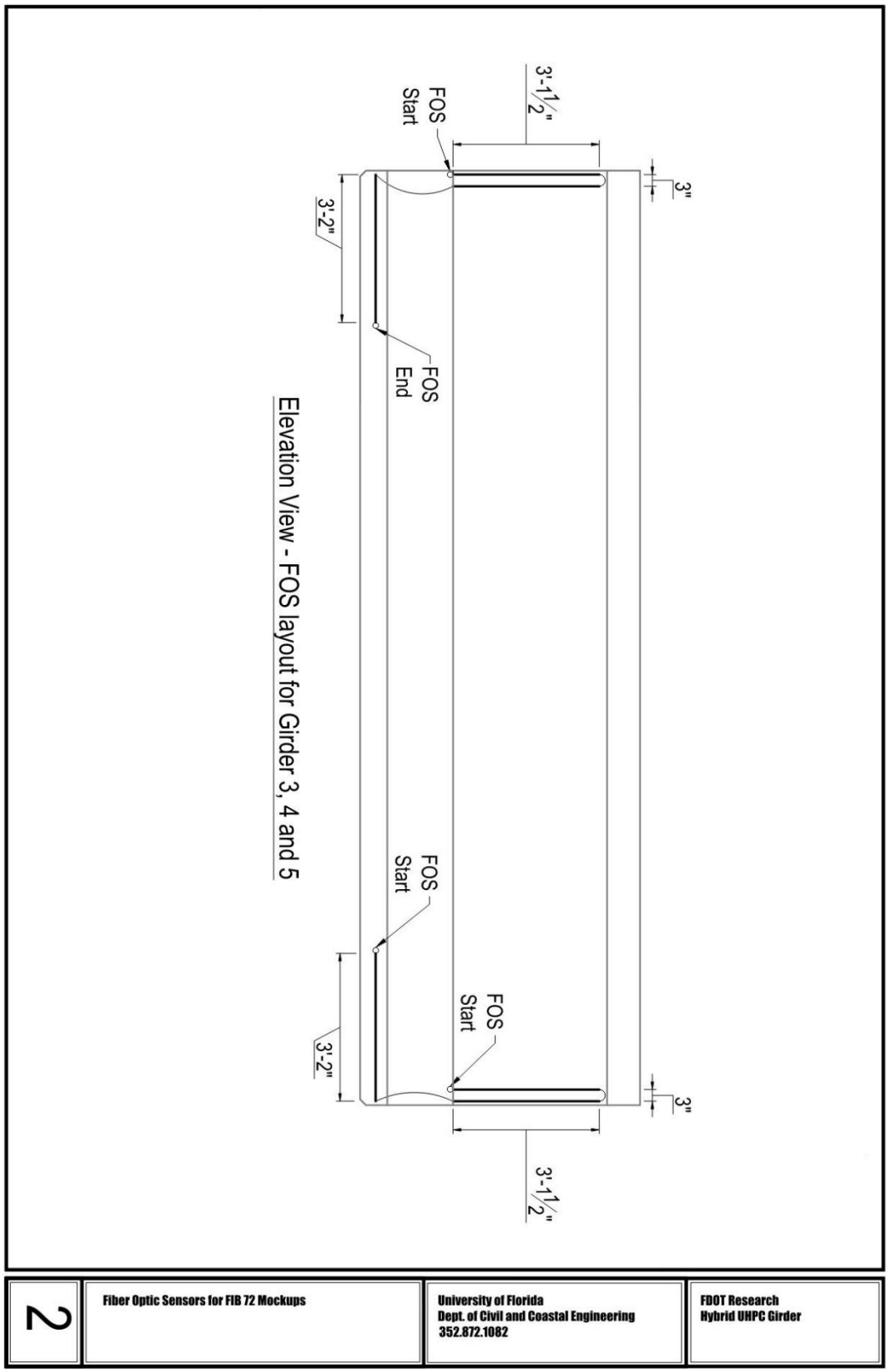

Elevation View - FOS layout for Girder 3, 4 and 5

2	Fiber Optic Sensors for FIB 72 Mockups	University of Florida Dept. of Civil and Coastal Engineering 352.872.1082	FDOT Research Hybrid UHPC Girder

14 Appendix C — Construction Drawings of FIB 54 Hybrid UHPC-SCC Girder

General Notes:

Materials

Concrete shall be:
1. FDOT class VI with f'c (28 day) = 8500 psi and f'ci (release) = 8000 ksi
2. UHPC mix provided by the fabricator

Mild reinforcement shall be grade 60 (fy 60 ksi)

Prestressing strand shall be 270 ksi Lo-Lax

Fabricator shall provide data sheets from concrete, strand, and rebar suppliers.

Fabricator shall provide material samples to UF/FDOT as follows:

(6) 4" dia x 8" cylinders from each concrete batch
(5) 4"x4"x12" beams from each concrete batch
(9) 2"x2"x17" beams from each concrete batch

Fabricator shall provide material report of strand stressing.

Fabricator shall provide results of all testing performed for fresh and hardened concrete properties.

Girder denomination is as follows:

Girder details	
Denomination	Concrete Type
G6	UHPC/SCC/UHPC
G7	UHPC/SCC/UHPC

Schedule

A coordination meeting will be held with the fabricator and UF at least two (2) weeks prior to beginning fabrication.

Contact Eduardo Torres at UF at least (1) week prior to beginning fabrication. 352-872-1082 or edu1291@ufl.edu

Research Instrumentation

UF/FDOT will provide and install research instrumentation in each of the concrete girders in coordination with the fabricator. Internal instrumentation will be mounted to prestressing strands and rebar prior to casting concrete. Instruments on rebar will be installed prior to placement of the rebar in the girder.

Other

Fabricator will transport girders from the fabrication facility to:
FDOT Structures Research Center
2007 East Paul Dirac Drive
Tallahassee, FL 32310

Delivery time to be coordinated with FDOT.

Inspections will be provided by on-site FDOT personnel and/or by UF prior to and after concrete casting.

No patchwork or finishing is required.

Proposed Timeline:

Day 1 (Monday)	Day 2 (Tuesday)	Day 3 (Wednesday)	Day 4 (Thursday)	Day 5 (Friday)
- Lay down the strands - Place mesh in Girders 1 and 2 (UF)	- Place steel reinforcement - Install Instrumentation (UF) - Place formwork	- Pour UHPC and SCC on all Girders	- Remove formwork - Install external instrumentation (UF) - Draw girdlines (UF)	- Strand release - Relocate Girders for temporary storage.

Precast Bed Layout

Bar Bending Diagrams

Handling & Dunnage

1	General Notes	University of Florida Dept. of Civil and Coastal Engineering 352.872.1082	FDOT Research Hybrid UHPC Girder

Elevation: G6
Strands and flanges are not shown for clarity
50'-0" overall length
End 1
End 2
UHPC
SCC
Girder 6 End
Girder 6 Section A/3
Girder 6 Strand Pattern
Girder 6 Detensioning Sequence
Section A/1
Showing 5Ks', 5Z', & 5Y'
Section A/2
Showing 5Ks', 5Z', & 5Y'
Shielding Legend
No shielding
FIB 54 Girder 6
University of Florida
Dept. of Civil and Coastal Engineering
352.872.1082
FDOT Research
Hybrid UHPC Girder

Elevation: G7
Strands and flanges are not shown for clarity
50'-0" overall length
End 1
End 2
UHPC
SCC
SCC
UHPC
Girder 7 End
Girder 6 Section A/3
Girder 7 Strand Pattern
Section A/1
Showing '5Ks', '5Z', & '5Y'
Section A/2
Showing '5Ks', '5Z', & '5Y'
Girder 7 Detensioning Sequence
Shielding Legend
• — No shielding
FIB 54 Girder 7
University of Florida
Dept. of Civil and Coastal Engineering
352.872.1082
FDOT Research
Hybrid UHPC Girder
3

Bill of material: G6				
Piece	Size	Qty.	Length	Notes
5A	#5	4	50'-0"	Straight bar
3C	#3	68	3'-2"	See Sheet 1
3D	#3	136	4'-11 3/4"	See Sheet 1
4M	#4	52	3'-8"	Straight bar
5K	#5	68	8'-1"	See Sheet 1
5Y	#5	12	5'-6"	Straight bar
5Z	#5	6	7'-6 1/2"	See Sheet 1
4L	#4	10	4'-0"	Straight bar

Bill of material: G7				
Piece	Size	Qty.	Length	Notes
5A	#5	4	20'-0"	Straight bar
3C	#3	36	3'-2"	See Sheet 1
3D	#3	72	4'-11 3/4"	See Sheet 1
4M	#4	52	3'-8"	Straight bar
5K	#5	67	8'-1"	See Sheet 1
5Y	#5	12	5'-6"	Straight bar
5Z	#5	6	7'-6 1/2"	See Sheet 1
4L	#4	10	4'-0"	Straight bar

4	**Bill of Materials**	**University of Florida** **Dept. of Civil and Coastal Engineering** **352.872.1082**	**FDOT Research** **Hybrid UHPC Girder**

15 Appendix D — Instrumentation Drawings of FIB 54 Hybrid UHPC-SCC Girder

15.1 Instrumentation During Prestress Transfer

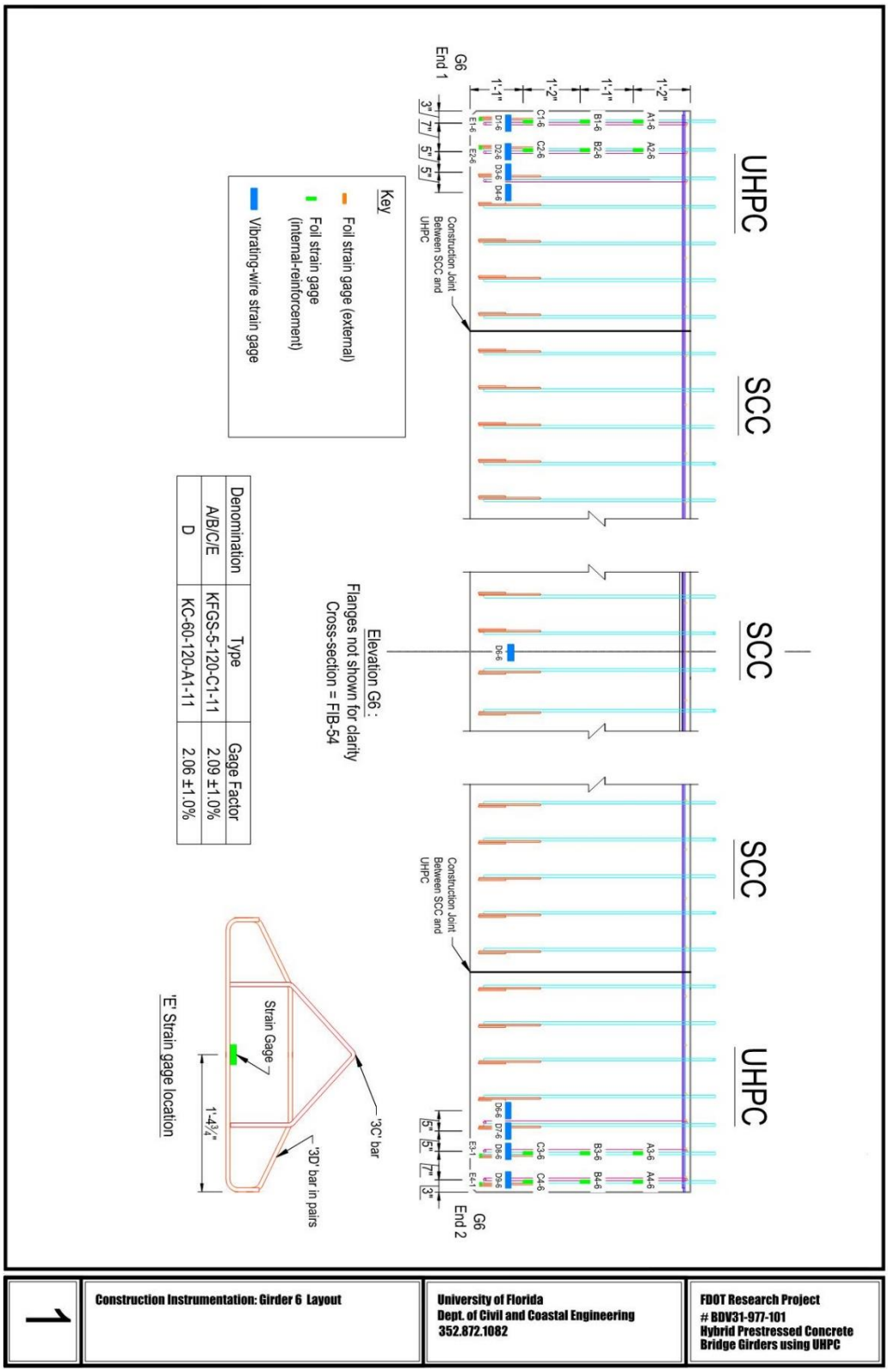

Denomination	Type	Gage Factor
A/B/C/E	KFGS-5-120-C1-11	2.09 ±1.0%
D	KC-60-120-A1-11	2.06 ±1.0%

2	Construction Instrumentation: Girder 7 Layout	University of Florida Dept. of Civil and Coastal Engineering 352.872.1082	FDOT Research Project # BDV31-977-101 Hybrid Prestressed Concrete Bridge Girders using UHPC

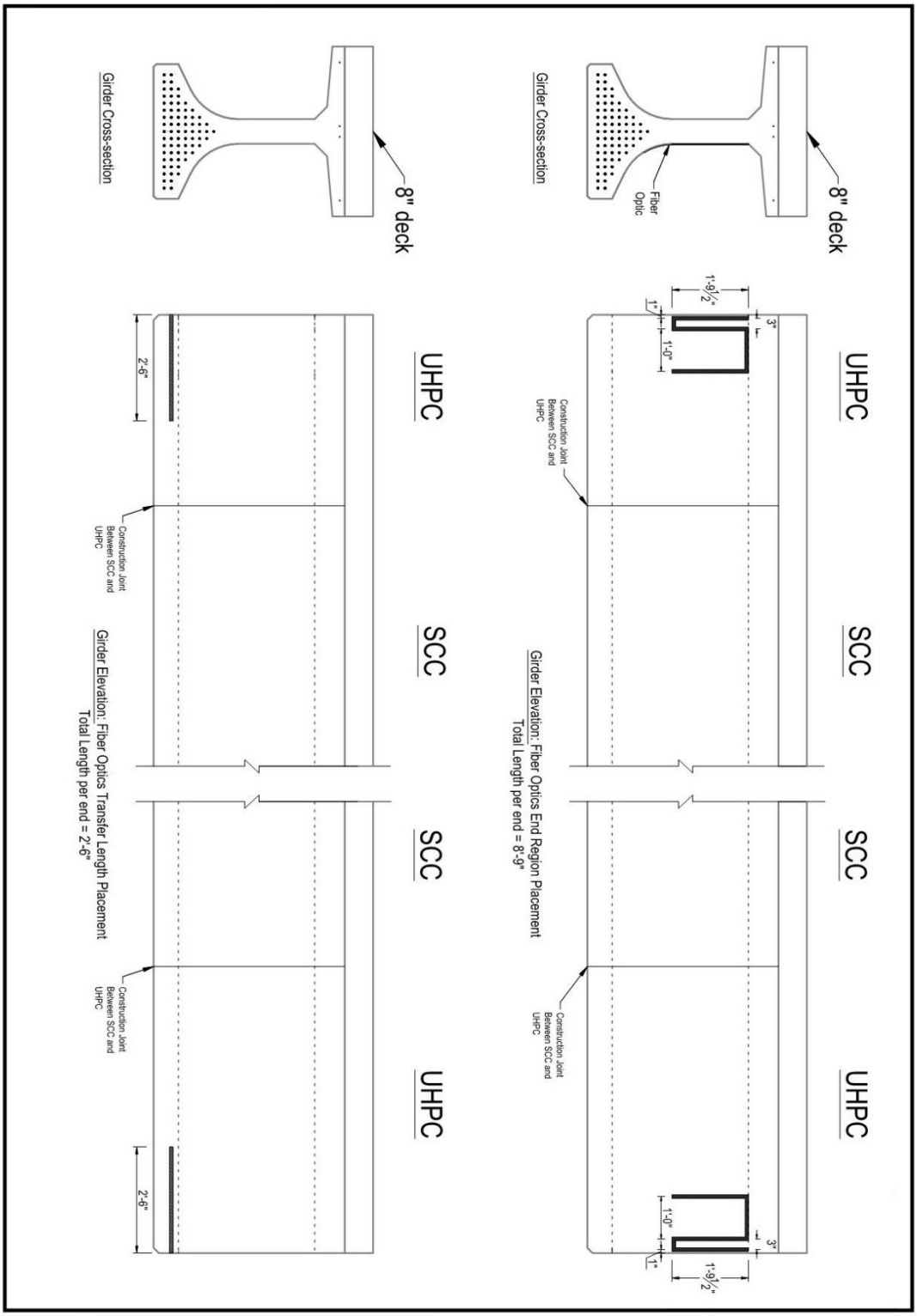

3	Construction Instrumentation: Fiber Optics Layout for Girder 6 and Girder 7	University of Florida Dept. of Civil and Coastal Engineering 352.872.1082	FDOT Research Project # BDV31-977-101 Hybrid Prestressed Concrete Bridge Girders using UHPC

Side View - Deck Reinforcement

Summary of Rebar

Piece	Size	Qty.	Length	Notes
Longitudinal	#5	27	12'-00"	Straight bar
Transversal	#5	102	3'-10"	Straight bar

1	Deck Reinforcement	University of Florida Dept. of Civil and Coastal Engineering 352.872.1082	FDOT Research Hybrid UHPC Girder

15.2 Instrumentation for Load Test

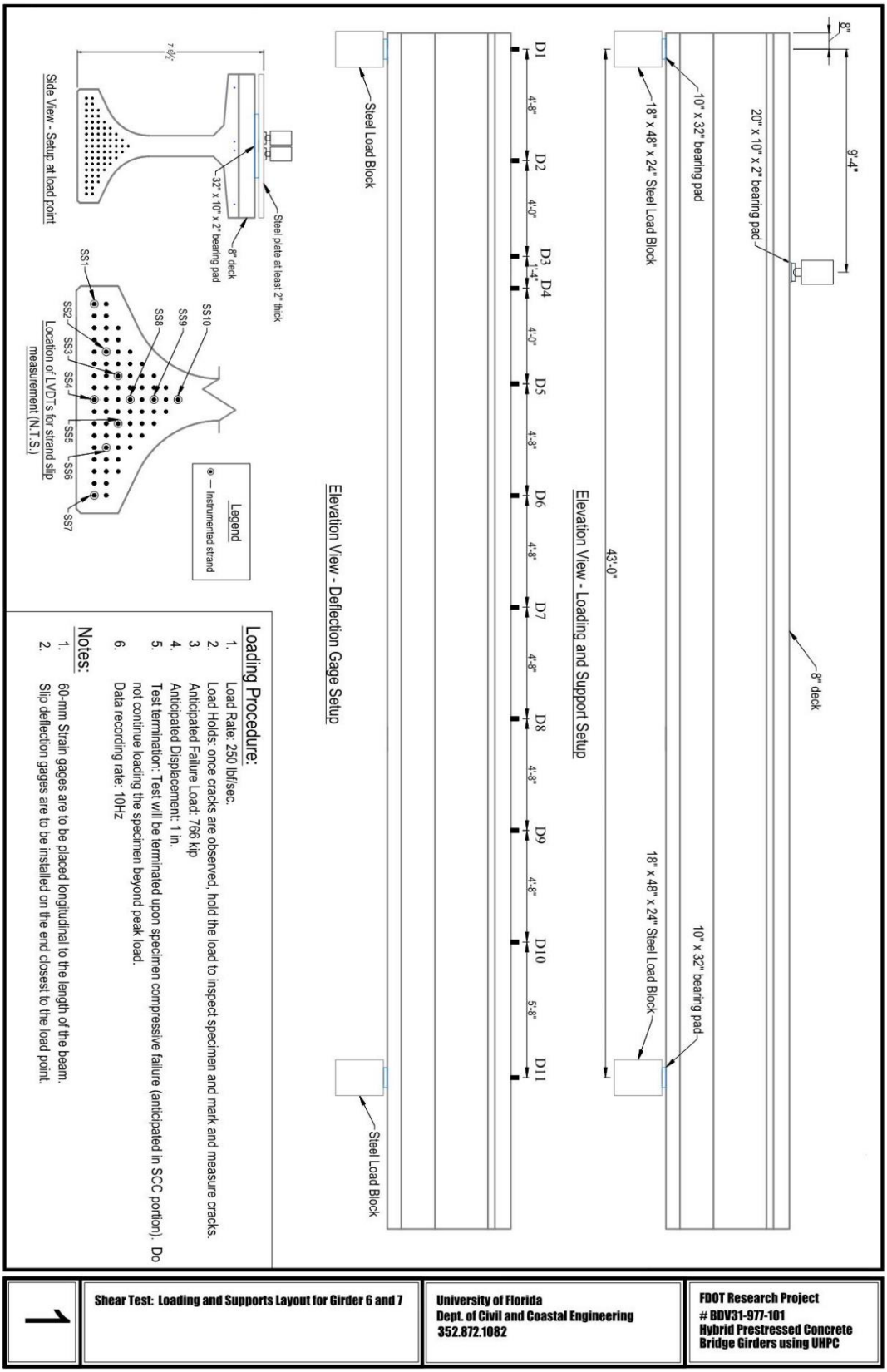

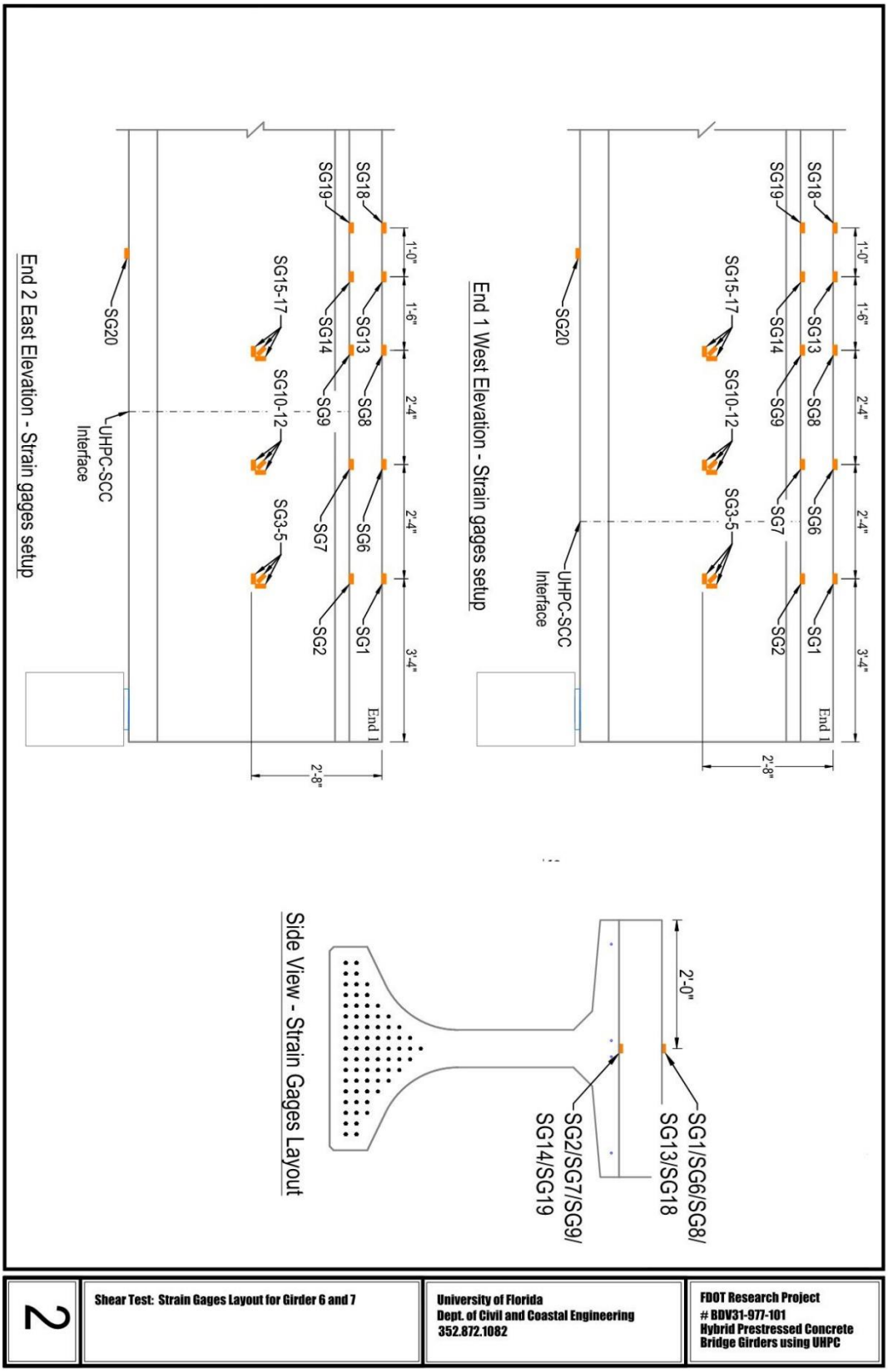
End 1 West Elevation - Strain gages setup
SG18
SG19
SG15-17
SG20
SG13
SG14
SG10-12
SG8
SG9
SG3-5
SG6
SG7
SG1
SG2
UHPC-SCC Interface
End 1
1'-0"
1'-6"
2'-4"
2'-4"
3'-4"
2'-8"
End 2 East Elevation - Strain gages setup
SG18
SG19
SG15-17
SG20
SG13
SG14
SG10-12
SG8
SG9
SG3-5
SG6
SG7
SG1
SG2
UHPC-SCC Interface
End 1
1'-0"
1'-6"
2'-4"
2'-4"
3'-4"
2'-8"
Side View - Strain Gages Layout
2'-0"
SG1/SG6/SG8/
SG13/SG18
SG2/SG7/SG9/
SG14/SG19
2
Shear Test: Strain Gages Layout for Girder 6 and 7
University of Florida
Dept. of Civil and Coastal Engineering
352.872.1082
FDOT Research Project
BDV31-977-101
Hybrid Prestressed Concrete
Bridge Girders using UHPC

1'-5"
1'-8"
Steel plates to support LVDTs (see detail A)
LVDTs mounted to concrete surface
UHPC-SCC Interface
End 1 East Elevation - LVDT location
1'-5"
1'-8"
Steel plates to support LVDTs (see detail A)
LVDTs mounted to concrete surface
UHPC-SCC Interface
End 2 West Elevation - LVDT Location setup
3"
2"
6"
LVDT mounted to concrete surface
Front View - Detail A
3"
2"
Angle 3"x2"x3/16"
1/4" bolt
Steel plate 6"x1 1/2"x1/4"
Side View - Detail A
3
Shear Test: LVDT Layout for Girder 6 and 7
University of Florida
Dept. of Civil and Coastal Engineering
352.872.1082
FDOT Research Project
BDV31-977-101
Hybrid Prestressed Concrete
Bridge Girders using UHPC

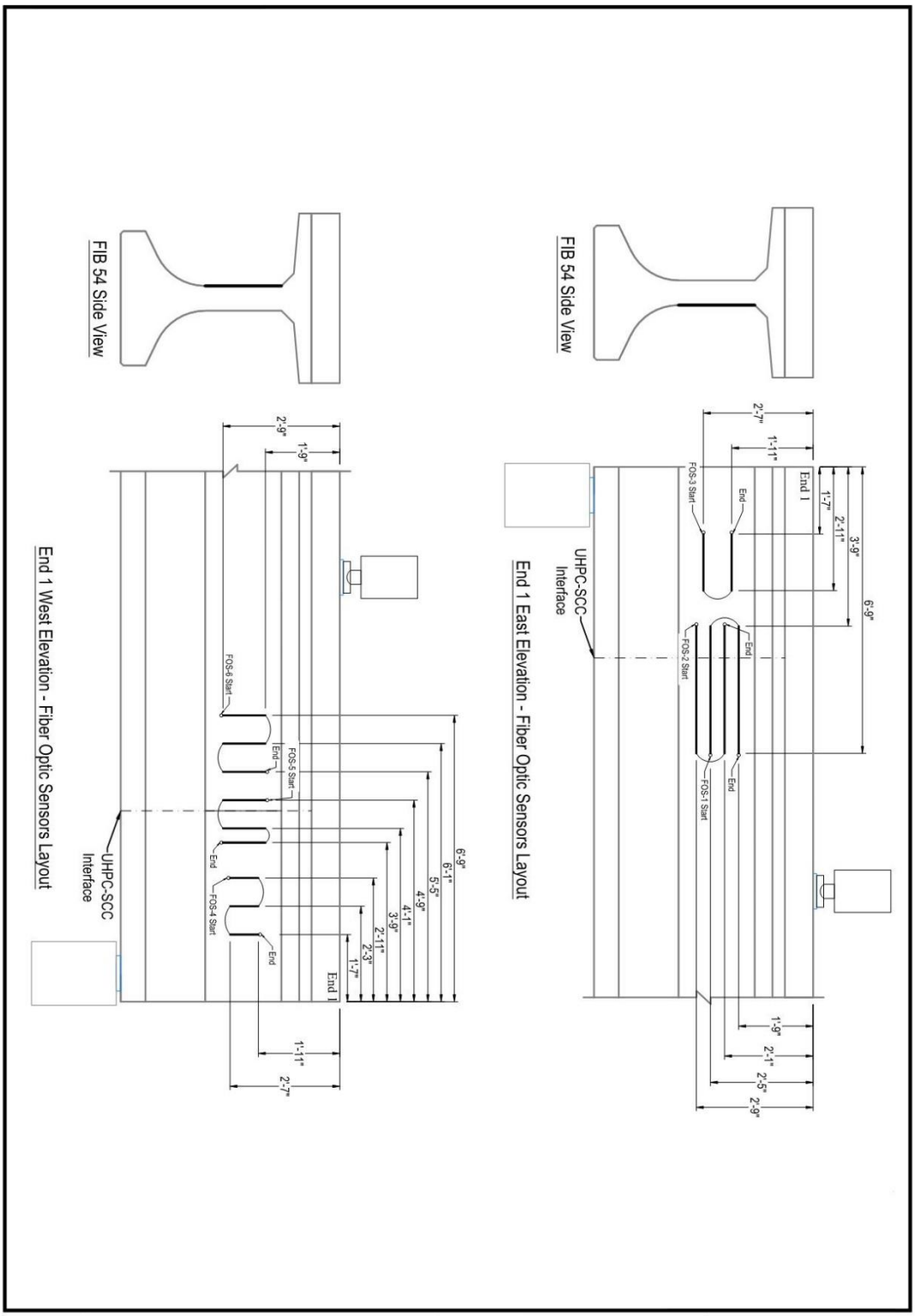

4	Shear Test: Fiber Optics Layout for Girder 6 and 7	University of Florida Dept. of Civil and Coastal Engineering 352.872.1082	FDOT Research Project # BDV31-977-101 Hybrid Prestressed Concrete Bridge Girders using UHPC

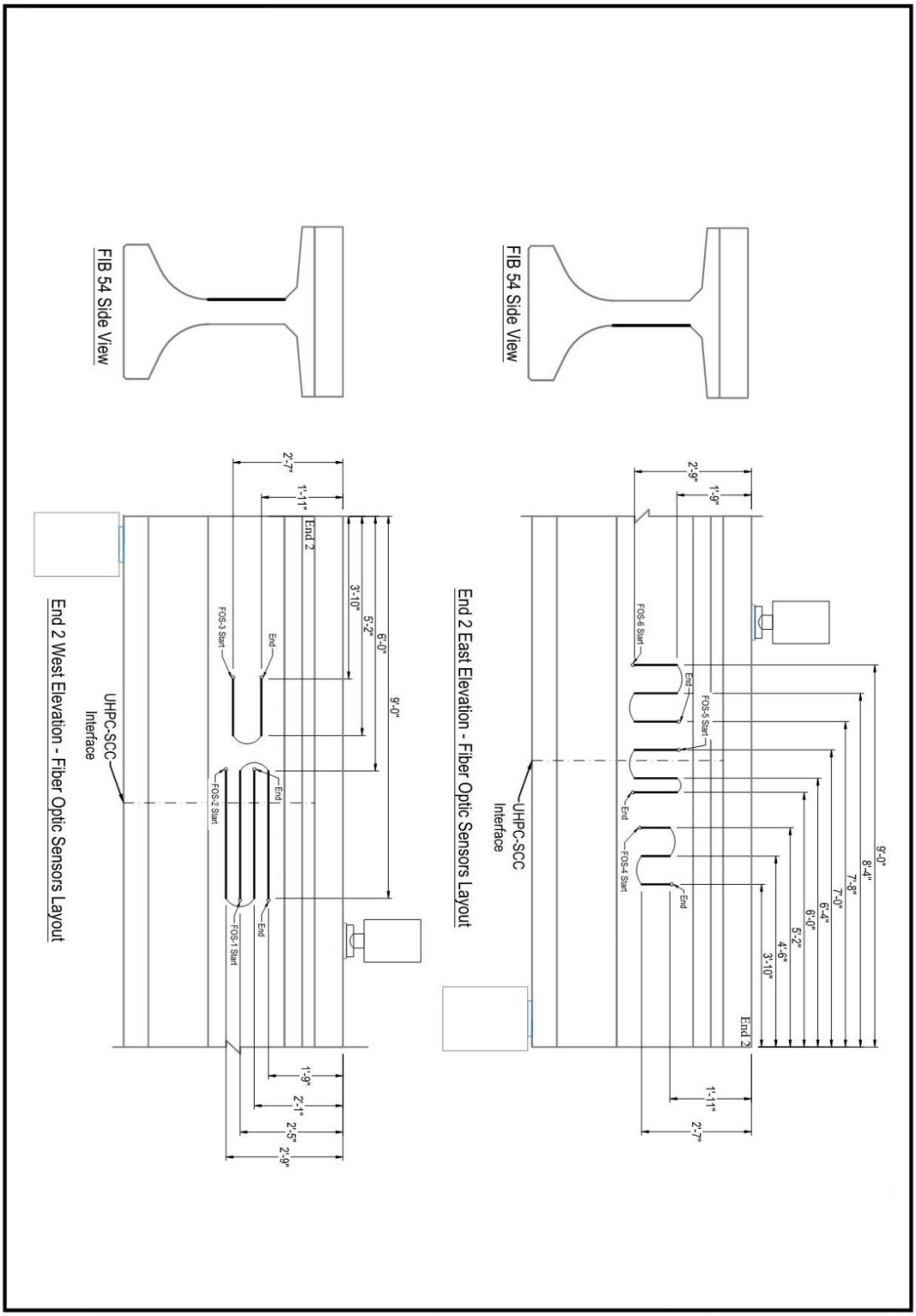

5	Shear Test: Fiber Optics Layout for Girder 6 and 7	University of Florida Dept. of Civil and Coastal Engineering 352.872.1082	FDOT Research Project # BDV31-977-101 Hybrid Prestressed Concrete Bridge Girders using UHPC

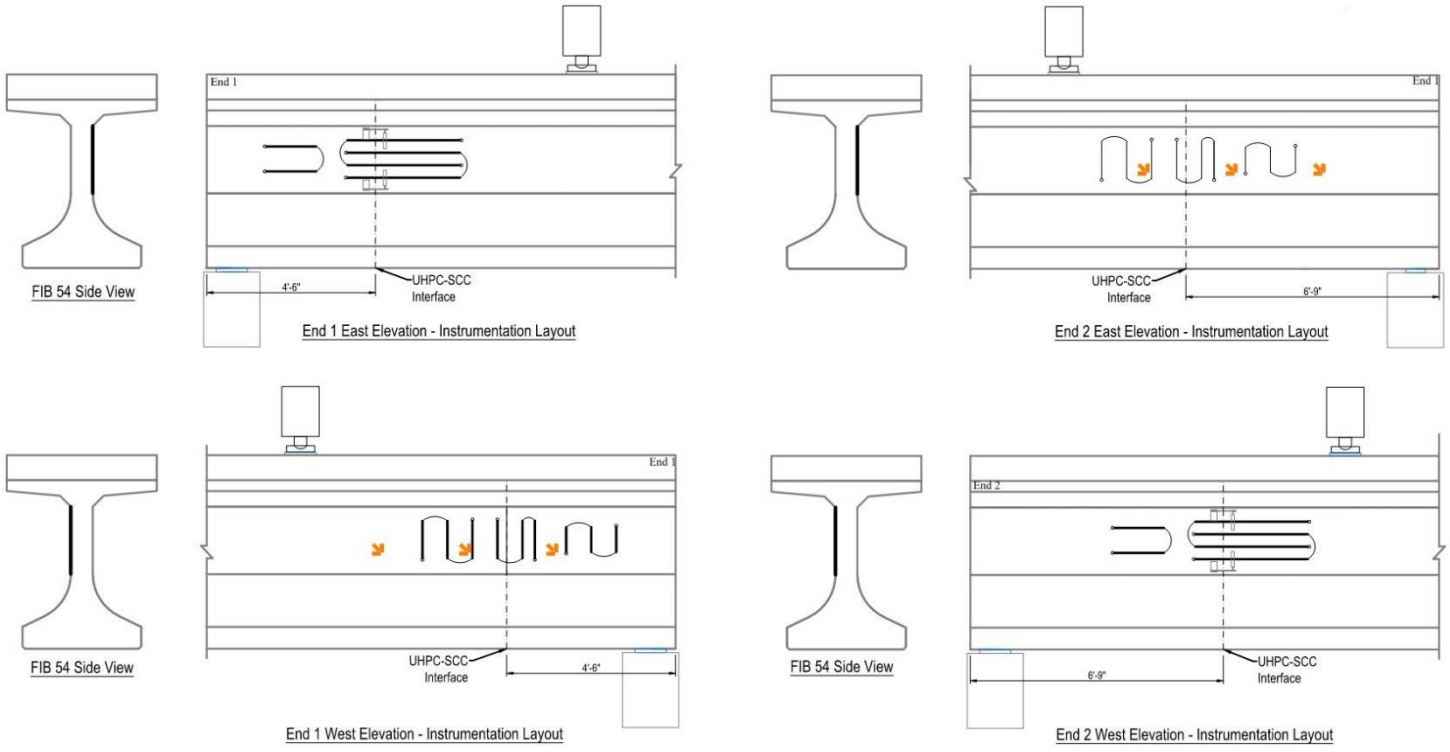

Instrumentation Installation Procedure:

1. Locate strain gages position
2. Smooth concrete surface using grinder
3. Place LVDTs holder and steel angle at interface.
4. Install fiber optics
5. Install strain gages on concrete surface

FDOT Research Project
BDV31-977-101
Hybrid Prestressed Concrete Bridge Girders using UHPC

University of Florida
Dept. of Civil and Coastal Engineering
352.872.1082

Shear Test: Summary of Instrumentation for Girder 6 and Girder 7

6

16 Appendix E — Construction Methods for UHPC-SCC Interface

The fabrication of these girders requires the development of a method that will allow UHPC placement in the girder ends and SCC in the remaining section. The researchers selected a polyethylene mesh with a grid size opening of 0.25 in. and a thickness of 0.08 in to retain the UHPC prior to SCC placement.

A short mockup was used to test the feasibility of the mesh and evaluate any difficulty that could arise. Two FIB sections were selected for the trial a FIB 45 and FIB 63. The mockup had a length of 4 ft and was cast during normal girder production at Standard Concrete Products. The mesh was placed at 3 ft from one of the bulkheads to form a partition to retain the UHPC (Figure E-1).

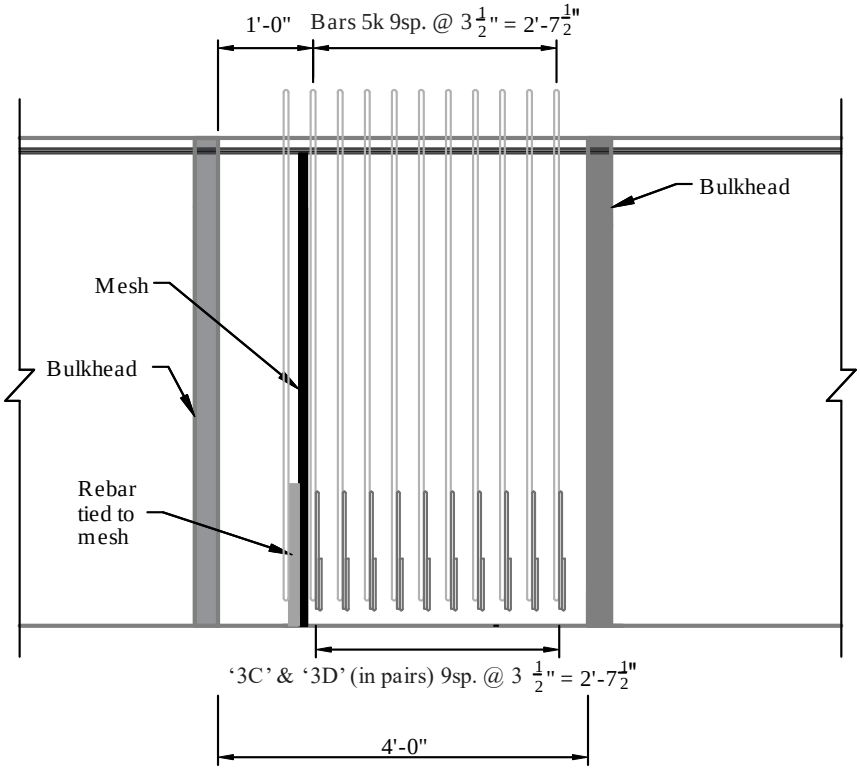

Figure E-1 Elevation view of mockup in precast bed

Prior to installation, the mesh for the FIB 45 was cut in three pieces and assembled together with high strength glue to obtain the geometry shown in Figure E-2. For the second trial, a plywood mold with the FIB shape was fabricated to approximate the desired cross-section. Then, the mesh was cut using the mold to create better approximation of the FIB shape and facilitate placement in the precast bed. Fiberglass rebar was used to support the mesh inside the formwork. Fiberglass can be used to support the mesh through the entire cross-section, without concern about clear cover requirements specified for steel rebar. Therefore, the rebar was cut in specific lengths to match the shape of the FIB. Figure E-3 shows the mesh placed in the precast bed with the respective support. Lastly, SCC was poured on one side of the mockup.

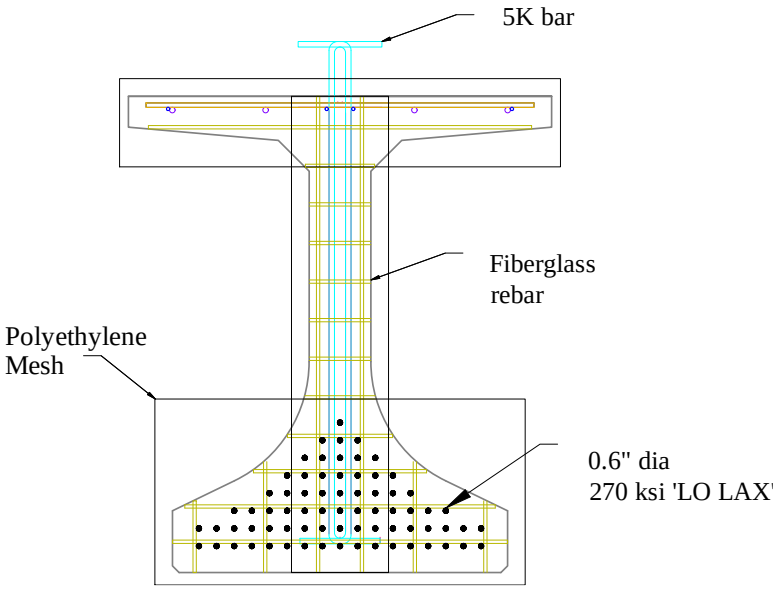

Figure E-2 Polyethylene mesh installation plan

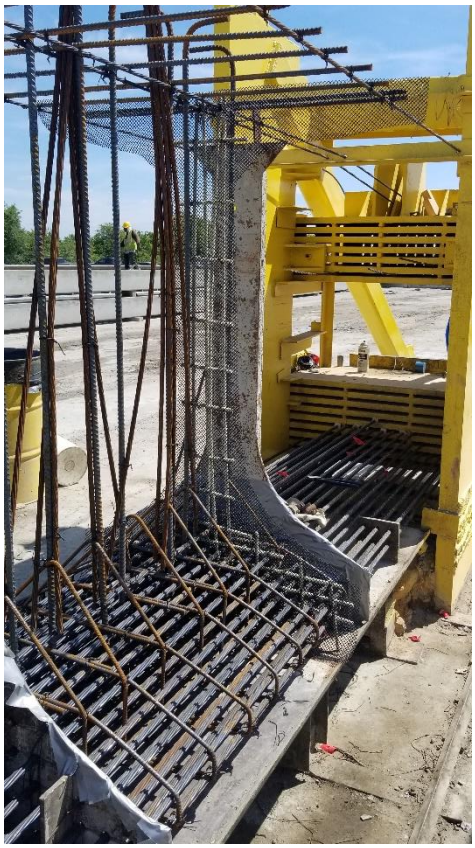

Figure E-3 Polyethylene mesh after installation

In both trials, the polyethylene mesh was able to retain the SCC in one side, and after an hour of the pour, only bleeding was observed in the empty space behind the mesh (Figure E-4). Once the forms were removed, the researchers observed that the mesh had retained the SCC

resulting in a rough surface, which can be beneficial for the bond of the subsequent pour (Figure E-5).

Figure E-4 Material that passed through the mesh after one hour of pour

Figure E-5 Mesh surface after concrete pour